Physics Reports 898 (2021) 1–114

Contents lists available at ScienceDirect

Physics Reports

journal homepage: www.elsevier.com/locate/physrep

Chimeras

Fatemeh Parastesh [a], Sajad Jafari [a], Hamed Azarnoush [a], Zahra Shahriari [b], Zhen Wang [c], Stefano Boccaletti [d,e,f], Matjaž Perc [g,h,i,*]

[a] Department of Biomedical Engineering, Amirkabir University of Technology, 424 Hafez Ave., Tehran 15875-4413, Iran
[b] Complex Systems Group, Department of Mathematics and Statistics, The University of Western Australia, Crawley, Western Australia 6009, Australia
[c] School of Mechanical Engineering and Center for OPTical IMagery Analysis and Learning, Northwestern Polytechnical University, Xi'an, 710072, China
[d] CNR – Institute of Complex Systems, Via Madonna del Piano 10, 50019 Sesto Fiorentino, Italy
[e] Unmanned Systems Research Institute, Northwestern Polytechnical University, Xi'an 710072, China
[f] Moscow Institute of Physics and Technology, Dolgoprudny, Moscow Region, 141701, Russia
[g] Faculty of Natural Sciences and Mathematics, University of Maribor, Koroška cesta 160, 2000 Maribor, Slovenia
[h] Department of Medical Research, China Medical University Hospital, China Medical University, Taichung, Taiwan
[i] Complexity Science Hub Vienna, Josefstädterstraße 39, 1080 Vienna, Austria

ARTICLE INFO

Article history:
Received 28 September 2020
Accepted 19 October 2020
Available online 31 October 2020
Editor: I. Procaccia

Keywords:
Synchronization
Complex network
Oscillator
Spatiotemporal dynamics
Chaos
Nonlinearity
Complexity

ABSTRACT

Chimeras are this year coming of age since they were first observed by Kuramoto and Battogtokh in 2002 in a one-dimensional network of complex Ginzburg–Landau equations. What started as an observation of a peculiar coexistence of synchronized and desynchronized states, almost two decades latter turned out to be an important new paradigm of nonlinear dynamics at the interface of physical and life sciences. Chimeras have been observed in uni-hemispheric sleep of aquatic mammals and migratory birds, in electrocorticographic recordings of epileptic seizures, and in neural bump states that are central to the coding of working memory and visual orientation. Chimera states have also been observed experimentally in physical systems, for example in liquid crystal light modulators, and they have been linked to power grids outages and optomechanics. Here we present a major review of chimeras, dedicated to all aspects of their theoretical and practical existence. We cover different dynamical systems in which chimera states have been observed, different types of chimeras, and different mathematical methods used for their analysis. We also review the importance of network structure for the emergence of chimeras, as well as different schemes aimed at controlling the symmetry breaking spatiotemporal pattern. We conclude by outlining open challenges and opportunities for future research entailing chimeras.

© 2020 Elsevier B.V. All rights reserved.

Contents

1. Introduction 2
2. Chimeras in different dynamical systems 4
   2.1. Phase oscillators 4
   2.2. Mechanical oscillators 8
   2.3. Chemical oscillators 17
   2.4. Optical oscillators 19

* Corresponding author at: Faculty of Natural Sciences and Mathematics, University of Maribor, Koroška cesta 160, 2000 Maribor, Slovenia.
E-mail address: matjaz.perc@gmail.com (M. Perc).

https://doi.org/10.1016/j.physrep.2020.10.003
0370-1573/© 2020 Elsevier B.V. All rights reserved.

2.5. Map lattices ... 20
2.6. Neuronal networks ... 25
3. The mathematics of chimeras ... 30
3.1. Stability analysis of phase oscillators ... 30
3.1.1. Continuum limit and the Ott–Antonsen approach ... 30
3.1.2. Stability of chimeras ... 34
3.2. Characterizing chimeras in dynamical systems ... 44
3.2.1. Kuramoto global order parameter ... 44
3.2.2. Local order parameter ... 45
3.2.3. Strength of incoherence and the discontinuity measure ... 45
3.2.4. Mean phase velocity ... 45
3.2.5. The size of coherent and incoherent clusters ... 45
3.2.6. Root-mean-square deviation ... 46
3.2.7. Normalized coefficient of mutual correlation ... 46
3.2.8. Finite-time Lyapunov exponents for chimeras ... 46
3.2.9. Correlation measures for spatial and temporal coherence ... 46
4. Different types of chimeras ... 48
4.1. Breathing chimeras ... 49
4.2. Multi-headed chimeras ... 49
4.3. Alternating chimeras ... 50
4.4. Traveling chimeras ... 52
4.5. Amplitude mediated chimeras ... 55
4.6. Amplitude chimeras ... 58
4.7. Chimera death ... 60
4.8. Imperfect chimeras ... 61
4.9. Spiral wave chimeras ... 63
5. Chimeras and network topology ... 66
5.1. Two-dimensional networks ... 66
5.2. Three-dimensional networks ... 68
5.3. Multilayer networks ... 70
5.4. Complex structures ... 73
5.5. Coupling schemes ... 77
5.5.1. Global coupling ... 77
5.5.2. Local coupling ... 81
5.5.3. Time-varying coupling ... 83
5.5.4. Hierarchical connections ... 87
6. Control of chimeras ... 91
6.1. Proportional feedback ... 91
6.2. Gradient dynamics ... 92
6.3. Modification of system parameters ... 94
6.4. Pinning control ... 95
6.5. Tweezer control ... 97
6.6. Time-delayed coupling ... 99
6.7. Coupling modifications ... 102
6.8. Control of virtual chimeras ... 104
7. Summary ... 105
8. Future research and outlook ... 106
Declaration of competing interest ... 107
Acknowledgments ... 107
References ... 107

1. Introduction

Complex networks and their collective behaviors have attracted great attention in recent years and opened a new branch in science [1–7]. In most of these studies, the relationships between network components and their impact on the overall behavior have been investigated. All of the natural systems and how they communicate can be modeled as a set of interconnected elements that affect each other's behavior bi-directionally. Therefore, studying complex systems and their mathematical modeling helps in understanding the nature and real life.

The synchronization phenomenon is an emerging collective behavior in complex systems [8–11]. In this state, a large number of elements, which are coupled together, behave coherently. The synchronous patterns have been extensively observed in chemistry, physics, and biology. Thus, it plays a significant role in different sciences. In many situations, synchronization does not mean exactly the same behavior in the network oscillators. Rather, it refers to a process in which the elements have similar behavior, or there is a function that can express each component's behavior compared

with the others. There are many different forms of synchronization such as complete synchronization [12,13], generalized synchronization [14,15], phase synchronization [16], projective synchronization [17], anti-synchronization [18], and lag synchronization [19]. Due to this diversity, synchronization has attracted much attention in recent years, and many numerical and analytical studies have focused on different types of synchronous patterns [20–27].

Along with the synchronization patterns, the collective behaviors which occur in the transition from asynchrony to synchrony, such as partial synchronous states, have also received a great deal of interest. One of the special spatiotemporal patterns in this regard is the situation when some network's elements oscillate synchronously, and the others behave asynchronously. For the first time by Kuramoto et al. [28] in 2002, this phenomenon has been observed in a network of non-locally coupled phase oscillators. They found a pattern composed of two domains of coherent oscillations with unique frequency, and incoherent oscillations with distributed frequencies. This peculiar pattern was called the "chimera state" by Abrams and Strogatz in 2004 [29]. The word "Chimera" refers to a beast with a lion's head, a goat's body, and a snake's tail in Greek mythology. Since this novel interesting dynamical state was composed of incongruous parts, the name "chimera" was chosen to highlight the possibility of coexistence of coherence and incoherence in one network [29].

The discovery of the chimera state launched a wave of new research in the field of coupled nonlinear systems. Besides the phase oscillators, this phenomenon has also been observed in chemical [30–33], mechanical [34–36], optical [37–39], electrical [40] and other systems [41–44] in recent years. However, there is no experimental verification done on chimera state in neurobiology, a piece of evidence exists which supports the association of the chimera state with neuronal evolutions [45]. This association has led to allocating a large proportion of chimera studies to the neuronal networks [46–52]. Apart from the chimera-related neuronal activities, experimental studies have also revealed the chimera state's existence in physical oscillators, verifying that the chimeras are characteristic of natural systems. However, there is about a decade gap between discovering the chimera state and its observation in experiments. These experimental studies demonstrate the applicability of chimera studies in natural systems. For example, the survey of Martens et al. [34] on coupled mechanical systems can interpret the theoretical studies of synchronization in power grids. Therefore, when the power grid networks develop to contain increasing renewable power sources, they may be challenged with a chimera state, leading to large-scale partial blackouts.

About the foundation of the chimera state, a question may arise that why this phenomenon was discovered so late despite its abundance. The response is that the chimera state's basin of attraction is usually smaller than the other stable states in a network. Actually, the chimera phenomenon's occurrence or non-occurrence is sensitive to the initial conditions of the systems [53–58]. In most cases, the observation of this phenomenon is possible only with certain initial conditions. Therefore, the probability that the chimera appears as the steady-state is less than in other cases. The mathematical calculations and experimental evidence indicate that the chimera state's lifespan depends on the size of the network and increases exponentially with the increment of the network size.

The former studies of the chimera state were devoted to the ring network of oscillators. However, with the development of the networks theory and the expansion of chimera studies, the researchers found chimera in more complex network frameworks. Thus, the chimeras have been reported in two- and three-dimensional structures [59–62], multilayer networks [50,63–70], and even small-world and scale-free networks [70,71]. Furthermore, from the coupling scheme's perspective, the chimera states have been investigated considering diverse connection arrangements, ranging from simple nearest-neighbor coupling to time-varying and hierarchical topologies [72–77]. The chimera surveys' growth led to the detection of various types of chimera, other than the initially observed chimera composed of phase-locked and phase distributed groups [78–88]. Different factors, such as the local dynamics of the elements, the coupling scheme and parameters, the time delay and noise, influence on the emergence of different chimera types. Therefore, the scientists began to classify the chimera states based on the spatial properties, the systems' temporal dynamics, and the type of synchronization in the coherent group.

Consequently, the chimera states have drawn considerable attention from different scientists in recent years. Therefore, our motivation in this paper is to present an extensive review of the recent progress in chimera studies. In general, a network of coupled identical systems is defined by,

$$\dot{\mathrm{x}}_i(t) = \mathbf{F}(\mathrm{x}_i(t)) + \sigma \sum_{j=1}^{N} A_{ij}\mathbf{H}[\mathrm{x}_j(t) - \mathrm{x}_i(t)],$$

where $\mathrm{x}_i(t) \in \mathbb{R}^n$ denote the state variables of the system, $\mathbf{F}(\mathrm{x}_i(t))$ describes the dynamics of the individual nodes, and σ and N are the coupling strength and the number of nodes. The network's topology is applied by the connectivity matrix $\{A_{ij}\}$, such that $A_{ij} = 1$ if the nodes i and j are connected and $A_{ij} = 0$ otherwise. Therefore, adjusting the elements of A leads to a different configuration, including local (connection to the nearest neighbor), non-local (connection to several nearest neighbors) and global (all-to-all connection) coupling, or other arbitrary connections. The coupling function between the elements, which can be linear or nonlinear, is determined by H. The chimera studies can be classified into different categories according to the used local dynamics ($F(x)$), the connectivities (A), and coupling function (H). In the following sections, we aim to review the previous researches based on these categories.

At the beginning of the next section, we review chimeras in phase oscillators, in which the chimera state was first discovered. Then, we discuss mechanical, chemical, and optical dynamical systems that have been investigated in chimera's research, and after that, we take a brief look at the chimera in discrete maps. At the end of Section 2, the chimera

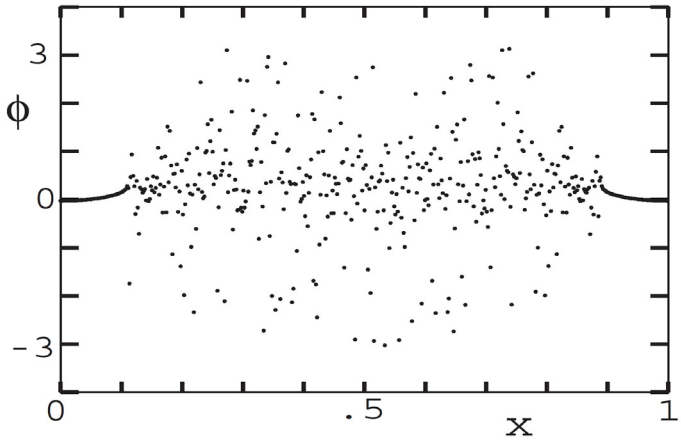

Fig. 1. The time snapshot of the phase oscillator described by CGLE (Eq. (1)) with periodic boundary conditions. The parameters are $a = -1.0$, $b = 0.88$ and $\kappa = 4.0$.
Source: Figure reproduced with permission from [28].

state in neuronal networks is mentioned. Section 3 is devoted to the theoretical and mathematical methods which are used in the chimera research. Firstly, the continuum limit and the Ott–Antonsen approach applied to the phase oscillators are presented. Next, the quantitative measures that have been used for stability analysis and characterizing chimeras in time and phase space are introduced. In Section 4, different types of chimera states are described. The chimera states are named based on the steadiness of the chimera state (e.g., breathing chimera), the number of coherent and incoherent clusters (e.g., multi-headed chimera), the spatial position of coherent and incoherent groups in time (e.g., alternating chimera and traveling chimera), the involvement of amplitude of oscillators (e.g., amplitude chimera, amplitude mediated chimera and chimera death), etc. Section 5 reviews the works by considering different network structures in two and three dimensions and multilayer networks. Then, there is a comprehensive overview of various coupling schemes in networks. Section 6 discusses the presented techniques for controlling the chimera states' existence, stability, and lifetime. Finally, the summary and an outline for future research are presented in Sections 7 and 8.

2. Chimeras in different dynamical systems

Following the study of the chimera state by Kuramoto et al. [28] in the complex Ginzburg–Landau equation, most of the earlier works of chimera state were done on the phase oscillators. Later on it was found that the chimeras are not limited to the phase oscillators, rather are also observable in a variety of systems. Thus, in this section, we discuss the different systems which were considered in chimera studies.

2.1. Phase oscillators

The complex Ginzburg–Landau equations (CGLE) have been widely used in different fields, such as physics. The CGLE in one-dimensional space is described by the following equation

$$\begin{aligned}\frac{\partial}{\partial t}A(x,t) &= (1+i\omega_0)A - (1+ib)|A|^2A \\ &\quad + K(1+ia)\big(Z(x,t) - A(x,t)\big),\end{aligned} \tag{1}$$

where $Z(x,t)$ is the mean-field, which for the non-local coupling is described by

$$Z(x,t) = \int G(x-x')A(x',t')dx'. \tag{2}$$

Here G represents the kernel function. Kuramoto and Battogtokh [28] considered an exponential kernel as

$$G(y) = \frac{\kappa}{2}\exp(-\kappa|y|), \tag{3}$$

which decays with the distance between oscillators. They solved Eq. (1) numerically in the interval $x \in [0, 1]$ for periodic boundary conditions. They found a special phenomenon for defined parameter values $a = -1.0$, $b = 0.88$ and $\kappa = 4.0$. In this state, the phases are distributed randomly near $x = \frac{1}{2}$, and uniformly near the boundaries. Therefore, there is a group of coherent oscillators that are phase-locked (near $x = \frac{1}{2}$), and an incoherent group in the middle. The time snapshot of the phases of the oscillators is shown in Fig. 1.

For further analysis of the model, Eq. (1) was reduced to a phase model by assuming a small coupling strength K. Thus, the phase reduced model can be described by

$$\frac{\partial}{\partial t}\phi(x,t) = \omega - \int G(x-x') \times \sin\big(\phi(x,t) - \phi(x',t) + \alpha\big)dx', \tag{4}$$

where $\phi(x,t)$ is the phase of the oscillator at position x at time t, ω is the natural frequency, and α is the phase constant. They demonstrated that for the parameter values used in Fig. 1, the reduced model (Eq. (4)) exhibits a similar pattern.

After the discovery of Kuramoto and Battogtokh, Abrams and Strogatz [29] studied a similar ring of phase oscillators as Eq. (4), in 2004. To simplify the computations, they used a cosine kernel function instead of the exponential one, as

$$G(x) = \frac{1}{2\pi}(1 + A\cos x). \tag{5}$$

A similar coexistence of coherence and incoherence was observed with this kernel function for $A = 0.995$, $\beta = 0.18$, and $N = 256$. These studies found that the chimera state cannot appear for any values of α when $G = 1$ (global coupling), and also for any values of G when $\alpha = 0$ (Sine coupling). The discretized form of the phase-reduced model (Eq. (4)) is as follows

$$\dot{\varphi}_i = \omega + \frac{K}{N}\sum_{j=1}^{N} G_{ij}\sin(\varphi_j - \varphi_i - \alpha). \tag{6}$$

This model has been later used in many chimera studies with different cosine, step-function, or even piecewise linear kernels [89–101]. For the exponential kernel as Eq. (3), the model is known as the Kuramoto–Sakaguchi model, while it is called the Kuramoto model with the step-function kernel. In the majority of the studies, the coupling function is the simple sine coupling. However, a few [102,103] have considered different coupling functions, such as the Hansel–Mato–Meunier coupling. For example, Suda and Okuda [103] investigated the following network

$$\dot{\theta}_j(t) = \omega + \frac{1}{2R}\sum_{k=j-R}^{j+R} \Gamma(\theta_j(t) - \theta_k(t)), \tag{7}$$

$$\Gamma(\phi) = -\sin(\phi + \alpha) + r\sin(2\phi), \tag{8}$$

where $\Gamma(\phi)$ was the Hansel–Mato–Meunier coupling, and R denoted the coupling range, which was set at $\frac{R}{N} = 0.35$. Firstly, the network was solved for a large number of oscillators as $N = 2000$. The parameter α was fixed at $\alpha = 1.46$ at which the network with sine coupling shows chimera state. Then the ratio of the second component was varied. The results demonstrated that the chimera state exists in this network for $r < 0.073$.

In the finite size network of phase oscillators with sine coupling function, the chimera state is transient and changes to an utterly coherent state. In contrast, the Hansel–Mato–Meunier coupling results in stable chimera, even for a finite number of oscillators [103]. The time of persistence of the chimera state in a network is called the lifetime. This time is dependent on the value of r for the Hansel–Mato–Meunier coupling. Fig. 2 shows the lifetime of chimera for $N = 30$ by varying r. For $r = 0$, which refers to the sine coupling, the chimera's lifetime is limited, which means that the state converts to the complete synchronization after a short time. As r increases and the coupling changes to the Hansel–Mato–Meunier, the lifetime of the chimera is increased sharply. When r reaches $r^* = 0.039$, the lifetime diverges almost to infinity. Thus, the chimera can be stable in a finite size network. Besides the Hansel–Mato–Meunier coupling, Wolfrum et al. [104] reported a stable chimera state in the Kuramoto–Sakaguchi phase oscillators with a cosine kernel with using a non-constant phase lag (α) as

$$\alpha(t) = \frac{\pi}{2} - K(1 - r(t)), \tag{9}$$

where $r(t)$ is the global order parameter. This term can be considered as a global feedback loop with parameter K. The stabilization of the chimera state in this network was proved by using the classical finite-dimensional chaos and bifurcation theory.

The chimera states have also been studied in coupled phase oscillators with attractive or repulsive coupling. Maistrenko et al. [105] investigated the network with a step function kernel in which each oscillator is connected to its $2P$ nearest neighbors (P on the left and P on the right) with constant strength, as

$$\dot{\varphi}_i = \omega + \frac{K}{2R}\sum_{j=-P}^{P} \sin(\varphi_{i+j} - \varphi_i - \alpha). \tag{10}$$

The value of the parameter α controls the coupling such that $-\frac{\pi}{2} < \alpha < \frac{\pi}{2}$ provides the attractive coupling and $\frac{\pi}{2} < \alpha < \frac{3\pi}{2}$ leads to the repulsive coupling. Numerical simulations of this network with $K = 1$ and $\omega = 0$ have shown

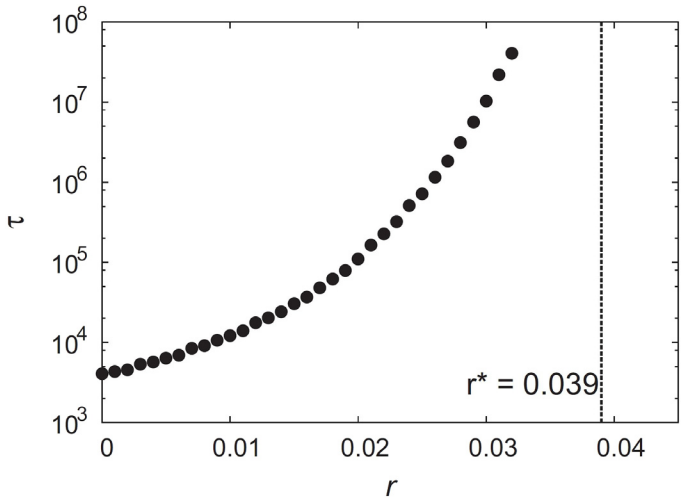

Fig. 2. The lifetime of chimera state in the coupled phase oscillators with the Hansel–Mato–Meunier coupling for $N = 30$ and $\alpha = 1.46$. When r reaches $r^* = 0.039$, the lifetime diverges almost to infinity. The results are the average of simulations of 1000 different initial conditions.
Source: Figure reproduced with permission from [103].

that in the attractive coupling, the chimera appears for α values near $\frac{\pi}{2}$ and intermediate values of the coupling range. For smaller phase shifts or when the coupling is local or global, the chimera is destroyed. In the case of the repulsive coupling, the chimera is formed when the parameter α is far from $\frac{\pi}{2}$ and π. When α approaches $\frac{\pi}{2}$, the spatiotemporal chaos appears in the network, while in $\alpha = \pi$, the network reaches a coherent state, wherein the successive oscillators have a fixed phase difference. In both couplings, changing the value of α causes the increment of the incoherent clusters.

In reality, the oscillators are not identical and may have slight differences. Thus, considering the heterogeneities in the coupled oscillators provides a more realistic model. Many studies have investigated the chimera states under the effects of the heterogeneities in phase oscillators either in the phase lag [106,107] or in the intrinsic frequency [108–111]. By using the bifurcation analysis, Laing demonstrated that the chimera state is also stable in the Kuramoto network with heterogeneous frequencies [108,109]. Xie et al. [111] considered non-uniform inhomogeneity in the natural frequencies of the phase oscillators with the following coupling functions

$$\begin{aligned} G_n^{(1)}(x) &\equiv \cos(nx), \\ G_n^{(2)}(x) &\equiv \cos(nx) + \cos[(n+1)x]. \end{aligned} \tag{11}$$

For applying inhomogeneity in the network, they considered two different distributions: a bump inhomogeneity distribution $\omega(x) = \omega_0 \exp(-\kappa|x|)$, $\kappa > 0$, and a periodic inhomogeneity distribution $\omega(x) = \omega_0 \cos(lx)$ with l being a positive integer. In this study, they investigated the influence of the amplitude (ω_0) and the spatial scale (κ^{-1} or l^{-1}) of the $\omega(x)$. They found that with applying the inhomogeneity, the position of the coherent cluster is fixed to a special location and has very small fluctuations in time. Fig. 3 shows the position of a coherent cluster of the chimera in this network with bump inhomogeneity for different κ values. It is observed that the fluctuations are decreased with the decrement of the bump width. Furthermore, it was revealed that in the chimera state with multiple coherent and incoherent clusters, the width of the coherent clusters is reduced with increasing ω_0, and thus the incoherent domains are merged.

Recently, Frolov et al. [110] reported the occurrence of the chimera-like states, composed of a group of frequency-locked oscillators and an incoherent group with drifting-like frequencies. They considered the Kuramoto oscillators with the form

$$\begin{aligned} \dot{\phi}_i &= \omega_i + \lambda R_i \sum_{l=1}^{N} A_{il} \sin(\phi_l - \phi_i), \\ R_i &= \frac{1}{k_i} \left| \sum_{l=1}^{N} A_{il} e^{j\phi_l} \right|, \end{aligned} \tag{12}$$

where ϕ_i is the phase, ω_i is the natural frequency, and k_i is the degree of each oscillator. λ denotes the total coupling strength, A is the adjacency matrix, and R_i is the local order parameter, which measures the coherence of each node. The heterogeneous natural frequencies are uniformly distributed in the interval $[\omega_0 - \frac{\Delta}{2}, \omega_0 + \frac{\Delta}{2}]$, where ω_0 is the center, and Δ is the width of the distribution. By increasing the coupling strength, the homogeneous network transits from complete

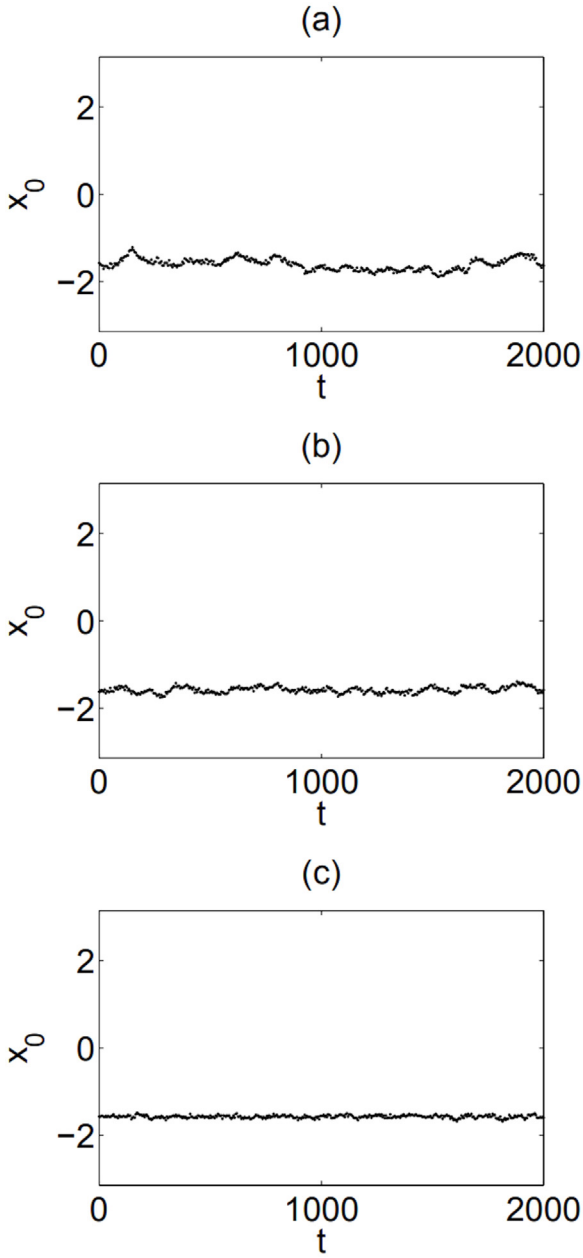

Fig. 3. The position of the coherent cluster of chimera in the heterogeneous phase oscillators with the bump inhomogeneity distribution for natural frequencies. The parameters are $\omega_0 = 0.1$, $\beta = 0.05$, $N = 512$. (a) $\kappa = 10$, (b) $\kappa = 6$ and (c) $\kappa = 2$.
Source: Figure reproduced with permission from [111].

incoherence to coherence in very small coupling strength values. When the inhomogeneity is added to the network, this transition occurs for higher coupling strengths as Δ increases. Moreover, during the transition from incoherence to coherence, there is a region of partially coherent state called the chimera-like state.

To investigate the mechanism of the appearance of this chimera-like state, firstly, the network's equation is rewritten as follows

$$\begin{aligned} \dot{\phi}_i &= f_i = \omega_i + c_i, \\ c_i &= \lambda R_i \sum_{l=1}^{N} A_{il} \sin(\phi_l - \phi_i), \end{aligned} \tag{13}$$

where c_i is the mean coupling term and f_i is defined as the effective frequency. In the case of the frequency-locking state, the mean effective frequency is equal to the mean-field frequency (Ω), which is equivalent to ω_0 for the uniform distribution. Thus, we have $\langle f_i \rangle = \omega_i + \langle c_i \rangle = \Omega = \omega_0$, which results in $\langle c_i \rangle \approx \omega_0 - \omega_i$. Therefore, the difference between each oscillator's natural frequency and the central frequency should be balanced with the coupling term c_i.

When the coupling strength is very small, the network is completely incoherent, and the coupling terms are nearly zero. This state is shown in Fig. 4a, where the left, middle and right panels show the averaged effective frequencies of the oscillators $\langle f_i \rangle$, the averaged effective frequency $\langle f_i \rangle$ vs. the coupling term c_i, and the natural frequency ω_i vs. the coupling term c_i. When the coupling strength increases, the coupling terms try to compensate for the difference $\omega_0 - \omega_i$. Therefore, the oscillators with $\omega_i > -\omega_0$ are coupled attractively with $c_i > 0$, and the ones with $\omega_i < -\omega_0$ are coupled repulsively with $c_i < 0$ (Fig. 4b). Subsequently, the oscillators which are coupled attractively construct a coherent frequency-locked cluster (as shown in Fig. 4c,d). Finally, with more increasing of the coupling strength, all of the oscillators are frequency-locked (Fig. 4e).

A special case of the complex Ginzburg–Landau equations (CGLE) is the Stuart–Landau equation. The Stuart–Landau equation provides a general model for the oscillators which represent the supercritical Hopf bifurcation. Accordingly, this model has been investigated in many chimera studies [112–119]. Premalatha et al. [120] considered a network of globally coupled Stuart–Landau oscillators of the form

$$\dot{w} = w - (1 - ic)|w|^2 w, \tag{14}$$

where $w = x + iy$ is the complex amplitude, and c is the nonisochronicity parameter. They investigated both cases of the symmetric coupling as $\epsilon(\bar{w} - w_j)$ and the symmetry broken coupling as $\epsilon(\overline{\mathrm{Re}(w)} - \mathrm{Re}(w_j))$, where $\overline{w} = (1/N)\sum_{j=1}^{N} w_j$ is the mean-field, and $\overline{\mathrm{Re}(w)} = (1/N)\sum_{j=1}^{N} x_j$ is the mean-field of the real part. It was found that by using the symmetry broken coupling, the irregularity is increased in the network. Furthermore, it leads to the development of different dynamical behaviors. In another study [121], the Stuart–Landau oscillators were considered in two populations described by the following equation

$$\begin{aligned}\dot{z}_j^{(1,2)} &= (1 + i\omega) z_j^{(1,2)} - (1 - ic)|z_j^{(1,2)}|^2 z_j^{(1,2)} \\ &\quad + \frac{\sigma}{2P_1} \sum_{k=j-P_1}^{j+P_1} (z_k^{(1,2)} - z_j^{(1,2)}) \\ &\quad + \frac{\eta}{2P_2} \sum_{k=j-P_2}^{j+P_2} (z_k^{(2,1)} - z_j^{(1,2)}),\end{aligned} \tag{15}$$

where z is the complex variable, ω is the natural frequency, and c is the nonisochronicity parameter. σ and η are the coupling strengths, and P_1 and P_2 are the nearest neighbors in the coupling in two populations. Simulation of this network has shown that for a specific range of the nonisochronicity parameter, the chimera state emerges in both populations with selecting determined initial conditions. An example of this state is shown in Fig. 5. In this dynamics, the synchronized nodes oscillate periodically, while the asynchronized ones are quasiperiodic.

2.2. Mechanical oscillators

To indicate the chimera state in mechanical oscillators, an experiment of coupled metronomes has been done in 2013 [34]. The considered network consists of two populations with a strong coupling within the populations and weaker coupling between populations. When the frequency of the oscillators is increased, the coupling between the oscillators is strengthened due to the growth of momentum. In contrast, the weak coupling between populations is obtained by adjusting the steel springs, which have an effective strength. The metronomes are identical and can move freely in the plane. The setup of this experiment is shown in Fig. 6.

For investigating the behavior of the network, the frequency of the oscillators is kept constant, and the spring strength is varied. When the spring strength is very low, the two populations are anti-phase synchronous, i.e., both populations are synchronized, but have 180° phase difference. For very large spring strength, the populations reach an in-phase synchronized motion. Finally, for intermediate values of spring strength, the chimera state is observed. In this case, one of the populations is synchronous, while the other has asynchronous oscillations. The asynchronous metronomes have different phases and time-averaged frequencies.

The obtained experimental results can be evaluated by a mathematical model. It is assumed that the displacement angles of the swings from equilibrium positions are Φ and Ψ (the metronomes displacement in each population is ϕ_i and Ψ_i). Each metronome is characterized by a self-sustained oscillator with an eigenfrequency ω and damping μ_m, as

$$\ddot{\phi}_i + \sin\phi_i + \mu_m \dot{\phi}_i D(\phi_i) + \frac{\omega^2}{\Omega^2} \cos\phi_i \ddot{\Phi} = 0, \tag{16}$$

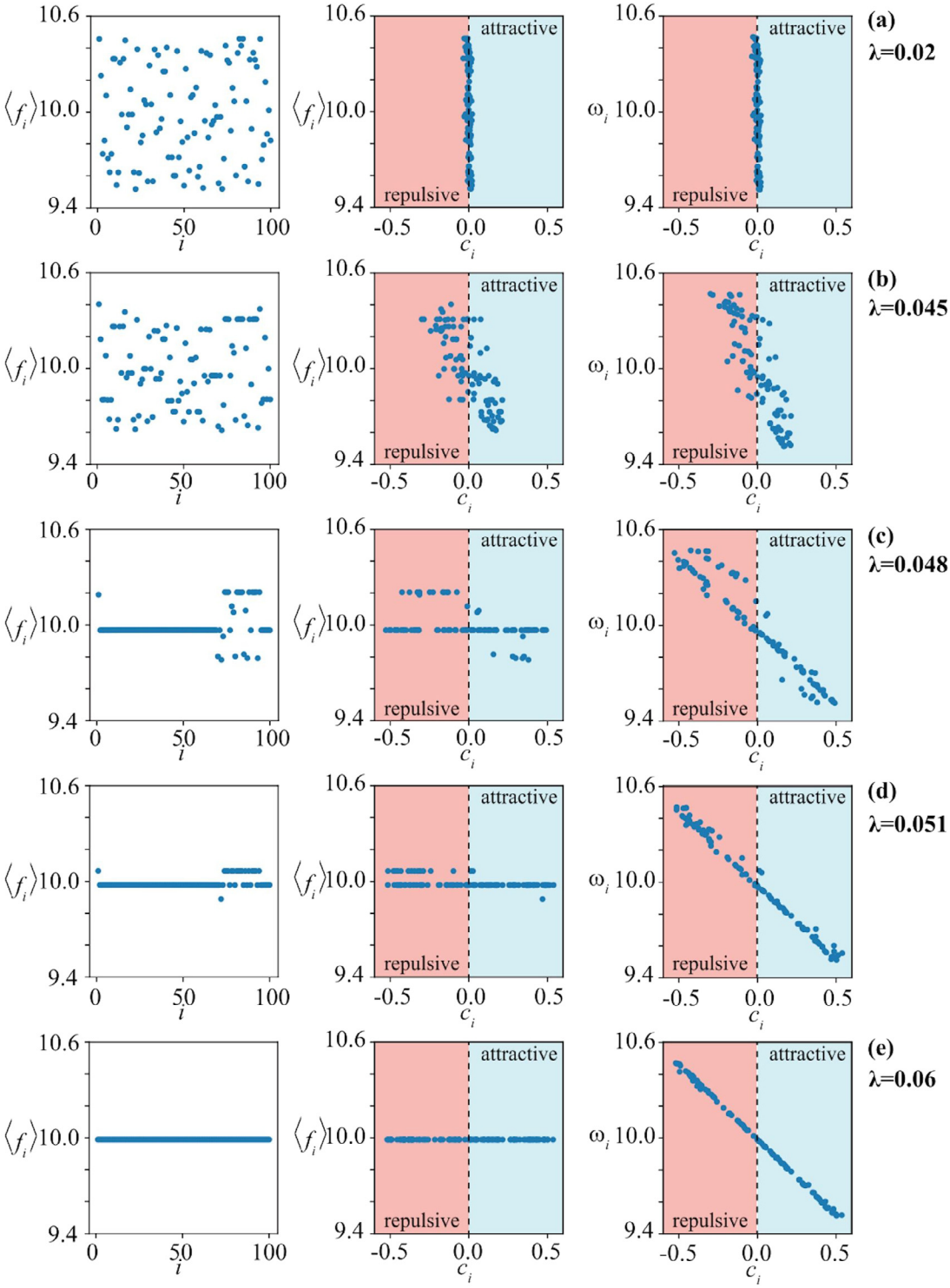

Fig. 4. Mechanism of appearance of chimera-like state in the heterogeneous network of Kuramoto oscillators (Eq. (12)) with $\Delta = 1$, for different coupling strengths (λ). The left, middle and right panels show the averaged effective frequencies of the oscillators $\langle f_i \rangle$, the averaged effective frequency $\langle f_i \rangle$ vs. the coupling term c_i, and the natural frequency ω_i vs. the coupling term c_i. (a) $\lambda = 0.02$, (b) $\lambda = 0.045$, (c) $\lambda = 0.048$, (d) $\lambda = 0.051$, and (e) $\lambda = 0.06$.
Source: Figure reproduced with permission from [110].

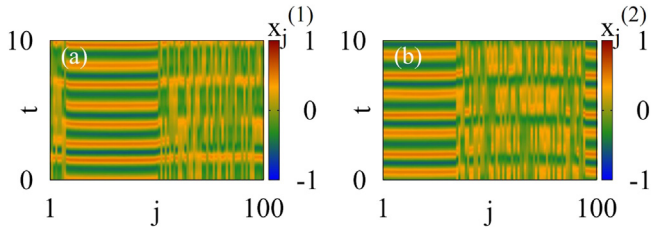

Fig. 5. Spatiotemporal patterns of two populations of the Stuart–Landau oscillators (Eq. (15)), indicating chimera state for specified initial conditions. The parameters are chosen as $c = 5$, $\sigma = 0.1$, $\eta = 0.25$, $\omega = 1.0$ and $r = 0.1$. (a) First population, (b) Second population.
Source: Figure reproduced with permission from [121].

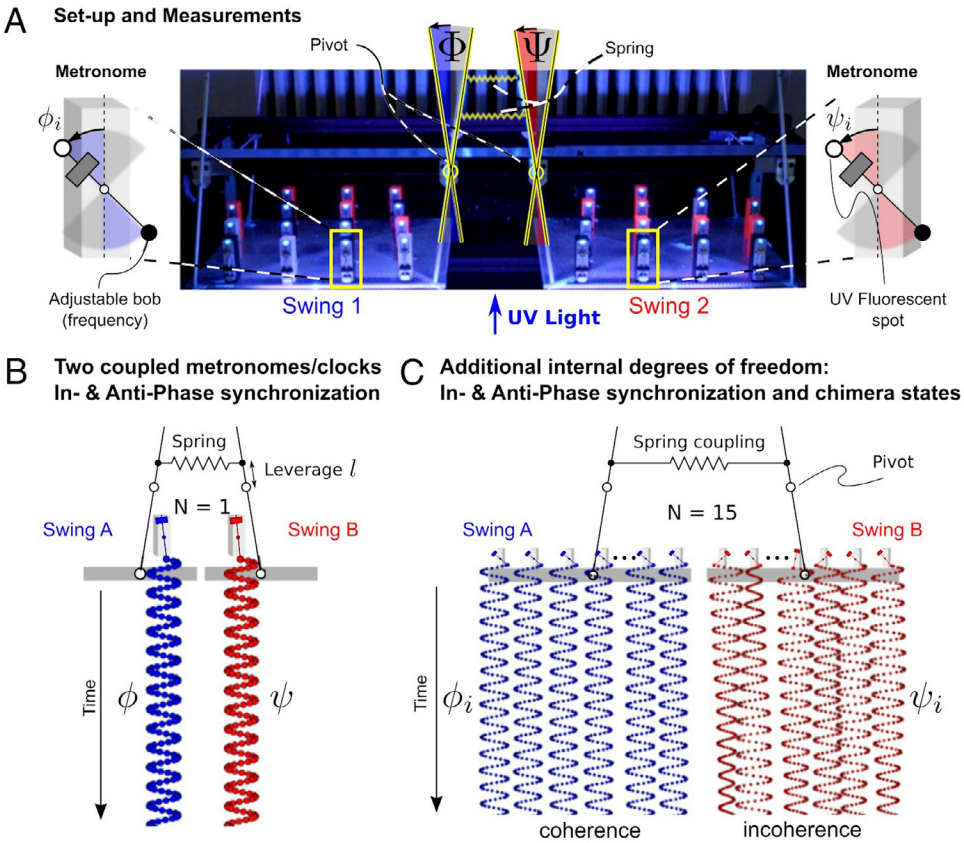

Fig. 6. Experimental setup of coupled mechanical oscillators. There are two populations of N identical metronomes, connected with tunable springs. (a) The experiment schematic. (b) Each population has one metronome, which is in-phase synchronized. (c) Each population has $N = 15$ metronomes. The swing A is synchronous, while swing B is asynchronous, and thus a chimera state is formed. The displacement angles of the metronomes in swing A and B are shown by φ_i and Ψ_i, respectively.
Source: Figure reproduced with permission from [34].

where $\ddot{\phi}_i$ denotes the pendulum inertia, $\sin\phi_i$ is the gravitational force of restitution, $\mu_m\dot{\phi}_i D(\phi_i)$ is the damping with an amplitude-dependent nonlinearity $D(\phi_i)$, and $\frac{\omega^2}{\Omega^2}\cos\phi_i\ddot{\Phi}$ is the driving swing inertia. The derivatives are with respect to $\tau = \omega t$. Each swing is described by the metronomes and the other swing as

$$\ddot{\Phi} + \Omega^2\Phi - \kappa(\Psi - \Phi) + \mu_s\dot{\Phi} + \frac{x_0}{L}\sum_{k=1}^{N}\partial_{\tau\tau}\sin\phi_k = 0, \tag{17}$$

where L is the length of swing, $\Omega = \sqrt{g/L}$ is the eigenfrequency, μ_s is the damping, and κ is the coupling strength between metronomes. Investigating the mathematical model reveals the same results as the experiment. Therefore, a network of basic mechanical elements consisting of inertia, friction, and spring rate, can produce a chimera state.

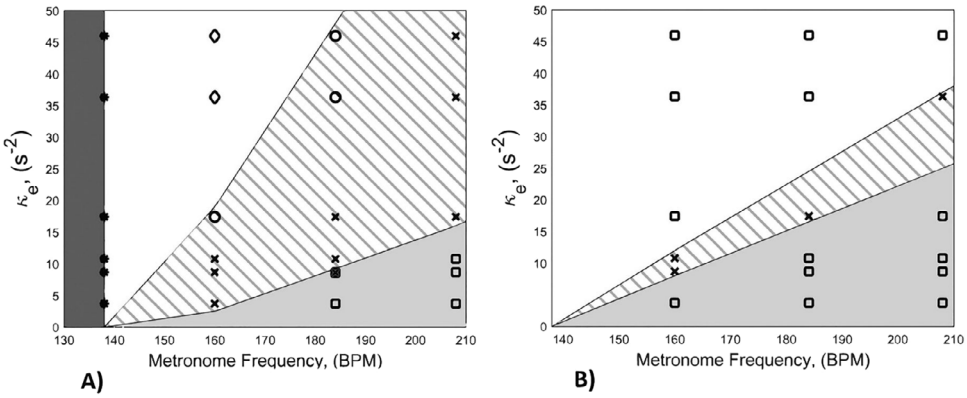

Fig. 7. The phase diagrams of the coupled mechanical oscillators with three platforms in the case of symmetric coupling. (a) The experimental result. (b) The numerical result. ◊: the platforms are in-phase synchronous; ×: the middle platform is asynchronous, and the outer platforms are synchronous; ◯: one of the outer platforms is synchronous, and two others are asynchronous; □: the platforms are anti-phase synchronous; ∗: the platforms are asynchronous.
Source: Figure reproduced with permission from [122].

The chimera state can also emerge in the case of three platforms with either symmetric or asymmetric couplings between them [122]. The experimental setup is the same as the previous case with an additional platform, each consisting of 15 metronomes. Therefore, each metronome motion is described by Eq. (16). The equation for each platform can be an extension of Eq. (17) as follows

$$\ddot{\Phi}_p + \mu_s I_3 \dot{\Phi}_p + \sum_q A_{qp}\Phi_p + \frac{x_0}{L}\sum_{i=1}^{N} \partial_{\tau\tau}\sin(\phi_{i,p}) = 0, \tag{18}$$

where $p = 1,\ 2,\ 3$ is the index of platforms, I_3 is the three-dimensional identity matrix, and A_{qp} is the coupling matrix between p and q platforms, as

$$A = \begin{bmatrix} \kappa_1 + \Omega^2 & -\kappa_1 & 0 \\ -\kappa_1 & \kappa_1 + \kappa_2 + \Omega^2 & -\kappa_2 \\ 0 & -\kappa_2 & \kappa_2 + \Omega^2 \end{bmatrix}.$$

It is assumed that the coupling strength between the left and center platforms is κ_1 and between the right and center platforms is κ_2. When the coupling between platforms is symmetric, i.e., $\kappa_1 = \kappa_2$, by changing the frequency of metronomes and the coupling strength, different synchrony and asynchrony patterns are observed. Thus, the chimera state can be formed in two cases. First, when the middle platform is asynchronous, and the side platforms are synchronous, and second, when one of the side platforms is asynchronous, and the others are synchronous. Fig. 7 shows the phase diagram of this network obtained from experimental (Fig. 7a) and numerical (Fig. 7b) simulations. In the diagrams, the regions marked by the × symbol show the first kind of chimera, and the symbol ◯ represents the second type of chimera. The regions marked by ◊ and □ indicate where all platforms are synchronous, either in-phase (◊) or anti-phase (□). Finally, the asynchronous region is marked by ∗. Comparing Fig. 7a and Fig. 7b shows that the chimera region is very smaller in numerical simulation. This mismatch can be due to the tolerances and inhomogeneities in the physical metronomes, while in numeric, the metronomes are perfectly identical.

In the next step, the couplings are considered asymmetric, i.e., $\kappa_1 \neq \kappa_2$. The phase diagram in this case, is shown in Fig. 8. When the coupling strengths have a significant difference, the chimera state is not formed. The chimera region in the diagram is shown by ×. In comparison to the symmetric coupling, in the asymmetric coupling, only the first kind of chimera, in which the middle platform is asynchronous, appears. The regions marked by ◊ represent the synchronous states.

The chimera state has also been observed in a ring network of coupled pendula [123]. This network consists of coupled pendula, excited by the clock's escapement (Huygens clock). Fig. 9a represents the schematic of pendulums with length l and mass m that are dangled from a fixed disc. The pendula are connected via linear springs and dampers with coefficients k_x and c_x, respectively, and have the distance l_s from the pivot. The displacements of the pendulums are shown by φ_i. The experimental realization of this network is shown in Fig. 9b. In this figure, the nearest neighbor links are shown by green, and the second nearest neighbor links are shown by red lines. The mathematical description of this network can be derived from Newton's laws of dynamics, as

$$\begin{aligned} M_N &= ml^2\ddot{\varphi}_i + c_\varphi\dot{\varphi}_i + mgl\sin\varphi_i \\ &\quad + k_x l_s^2(\varphi_i - \varphi_{i-1}) + k_x l_s^2(\varphi_i - \varphi_{i+1}) \end{aligned}$$

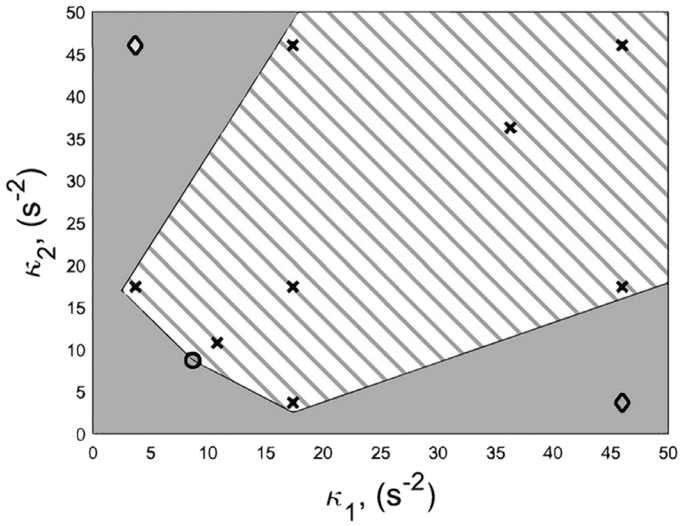

Fig. 8. The phase diagrams of the coupled mechanical oscillators with three platforms obtained from experiment in the case of asymmetric coupling. ◊: two platforms are in-phase synchronous and the third is anti-phase; ×: the chimera state; ◯: bistability.
Source: Figure reproduced with permission from [122].

$$
\begin{aligned}
&+ k_x l_s^2(\varphi_i - \varphi_{i-2}) + k_x l_s^2(\varphi_i - \varphi_{i+2}) \\
&+ c_x l_s^2(\dot{\varphi}_i - \dot{\varphi}_{i-1}) + c_x l_s^2(\dot{\varphi}_i - \dot{\varphi}_{i+1}) \\
&+ c_x l_s^2(\dot{\varphi}_i - \dot{\varphi}_{i-2}) + c_x l_s^2(\varphi_i - \varphi_{i+2}),
\end{aligned} \tag{19}
$$

where i is the pendulum's index, c_φ is the damping coefficient of the linear damper. The escapement mechanism creates the excitation torque M_N for $\varphi_I > \gamma_N$. By adjusting the parameters properly, different patterns of chimera state, which are dependent on the initial displacements, emerge in the pendula.

By reducing the size of the network Eq. (19), the chimera state still exists in the pendula, even for $N = 3$ [124]. In this case, the equations of motion will be the same as Eq. (19), with only considering the nearest-neighbor coupling terms. For a wide range of parameters, the three pendulums are synchronous. For specific values of coupling stiffness $0 < k_x < k_{th}$, by adding a perturbation, the synchronous state is destroyed, and the chimera state is created. The perturbation can be applied by stopping one of the pendulums for an instant.

The time series of the displacement of the pendulums are illustrated in Fig. 10a. At first, all pendulums are synchronized. By applying the perturbation to the pendulum one, the second and third pendulums remain synchronous, while the first one obtains a phase difference with the others. The amplitude of the first pendulum is also decreased. An enlargement of the time series is shown in Fig. 10b. This behavior of the network can be inferred as a small chimera state. The Poincaré maps of the pendulums obtained from numerical and experimental simulations are depicted in Fig. 10c,d, respectively. To confirm the synchrony of the second and the third pendula and their difference with the first one, the snapshots of the phases at the initial and final times, and the normalized mean frequencies are presented in Fig. 10e,f, and Fig. 10g, respectively. In general, the chimera state may appear in this small network of pendula as a result of three factors: the multistability of the pendulums, the existence of the self-excitation, and the proper value of coupling stiffness k_x.

The van der Pol–Duffing and Duffing systems are examples of the simple oscillators which can be used for studying the mechanical systems. In these systems, the external force can be considered as the physical motor, which provides the required force for the system's oscillation. It is generally possible for the motors to fail due to the overloads or defects of some components. Therefore, in a network of coupled mechanical systems, it is of great importance to investigate the effect of the external force failure on the network's behavior. For this study, a network of coupled van der Pol–Duffing oscillators can be considered as [125]

$$
\begin{cases}
\dot{x}_i = y_i + \dfrac{d}{2P} \displaystyle\sum_{j=i-P}^{i+P} [x_j - x_i] \\[2ex]
\dot{y}_i = \alpha(1 - x_i^2)y_i - x_i^3 + F\sin(\omega t) + \dfrac{d}{2P} \displaystyle\sum_{j=i-P}^{i+P} [y_j - y_i],
\end{cases} \tag{20}
$$

where x and y are the position and velocity of ith oscillator, respectively, and $F\sin(\omega t)$ is the external force. The coupling is considered to be non-local, with coupling strength d. It is also assumed that the connections between oscillators occur

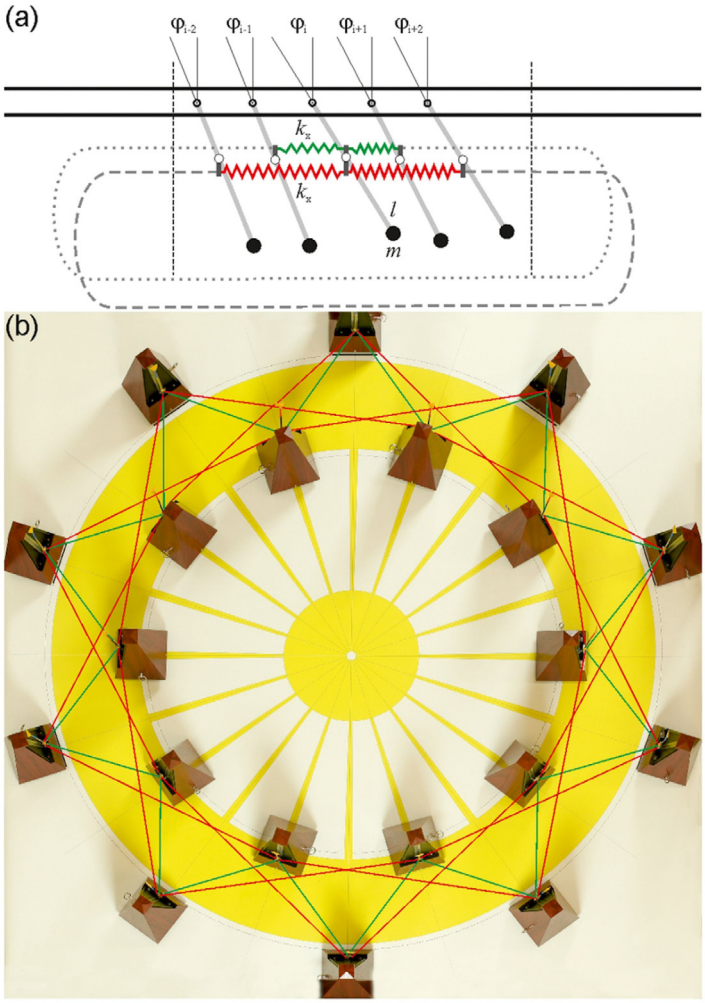

Fig. 9. (a) A ring network of coupled pendula connected via springs and dampers. (b) Experimental realization of the 20 pendula coupled with springs.
Source: Figure reproduced with permission from [123].

through both springs (x variables) and dampers (y variables). Depending on the values of the parameters, the single oscillator exhibits multistability. With considering $\alpha = 0.2$, $F = 1$, and $\omega = 0.94$, it has two coexisting attractors, such that one is chaotic and the other is periodic.

This network (Eq. (20)) shows different spatiotemporal patterns by varying the coupling strength (d). For very small coupling strengths, the oscillators are completely incoherent. With a slight increase in d, some of the oscillators tend to be synchronous, and therefore, the chimera state appears. Depending on the value of the coupling strength, the formed chimera patterns can be divided into two types, where the first type consists of temporal chaos (t-chimera state) and the second one consists of spatial chaos (s-chimera state). For specific values of coupling strength, both chimera types are observed.

Now the case of failure of one motor is considered. This is simulated by turning off one external excitation, i.e., $F_i = 0$. It is assumed that firstly, the network is in the s-chimera state, where the systems have regular oscillations, and the incoherent cluster has spatial chaos. This is shown in Fig. 11a, in which the left and right panels show the snapshot of the x variables, and the mean velocity($\bar{y}_i$)-time plots, respectively. Next, the external excitation of the oscillator $i = 45$ is turned off. The network pattern is depicted in Fig. 11b. It is observed that the dynamics of the disabled oscillator is changed to quasiperiodic and also oscillates with a larger amplitude. This happens due to the existence of the unstable fixed point when $F = 0$. Moreover, the dynamics of the other oscillators are changed to the chaotic oscillations, and thus the s-chimera state transits to the t-chimera state. If the external excitation switches on again, i.e., $F_{45} = 1$, then the oscillators behave regularly, and the network returns to the initial s-chimera state (Fig. 11c). Therefore, the chimera state is not disturbed by the failure of one system, and the only changes are in the systems' dynamics and the length of

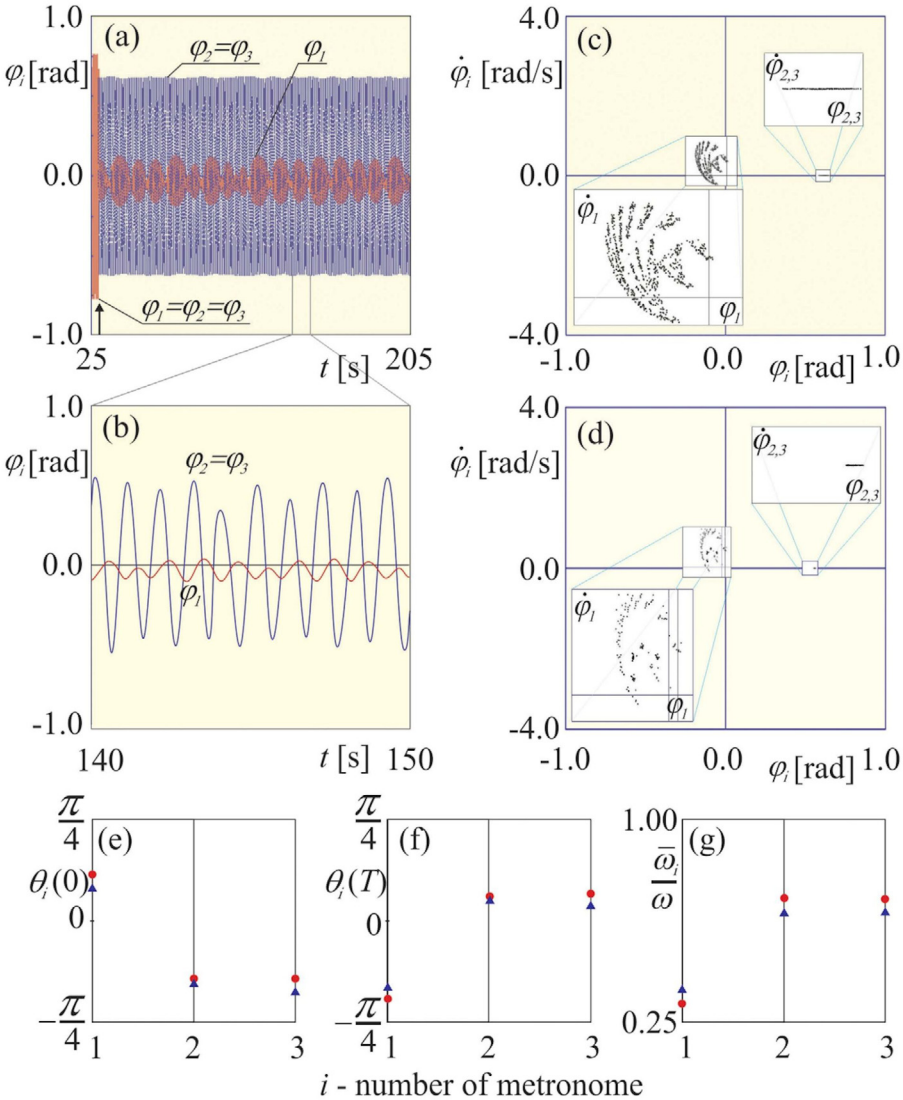

Fig. 10. (a) Time series of the phases of three coupled pendula. The pendulum one is stopped for a moment at the time shown by the arrow. (b) An enlargement of part (a). (c,d) The Poincaré maps of the pendulums obtained from numerical (c) and experimental (d) results. (e,f) The snapshots of the phases at the initial (e) and final (f) times. (g) Normalized mean frequencies of pendula. (the numerical and experimental results are shown by red dots and blue triangles, respectively).
Source: Figure reproduced with permission from [124].

the incoherent/coherent domains. The obtained result is very important in real applications. For example, the process of replacing one motor of the network's units can be done while the network is working, and there is no need to stop the network.

Very recently, an energetic approach was proposed for the analysis of the synchronization and chimera state in a mechanical pendulum-chart network [126]. The network consists of three pendulums that are coupled via their charts. The charts which are linked through linear springs are connected to a rigid wall and to a base that is the energy supplier. The system of coupled pendulums is shown in Fig. 12. Each pendulum has the mass m_i and length l_i, and the mass of each chart is M_i. The displacements of the charts and pendula are denoted by x_i and φ_i. k_j and C_j ($j = 1, 2, \ldots, 9$) are the linear springs and viscous dampers, and C_φ is the linear viscous dissipation of each pendulum. The describing equations of this system are given in Ref. [126].

Investigating this mechanical system for different parameters and analyzing the time series have revealed the formation of six different dynamical patterns: in-phase synchronization, anti-phase synchronization, frequency-locked oscillations, long period synchronization (the frequency of one oscillator is multiple of the synchronized ones), chimera state, and asynchronization. The procedure for identifying these patterns is as follows:

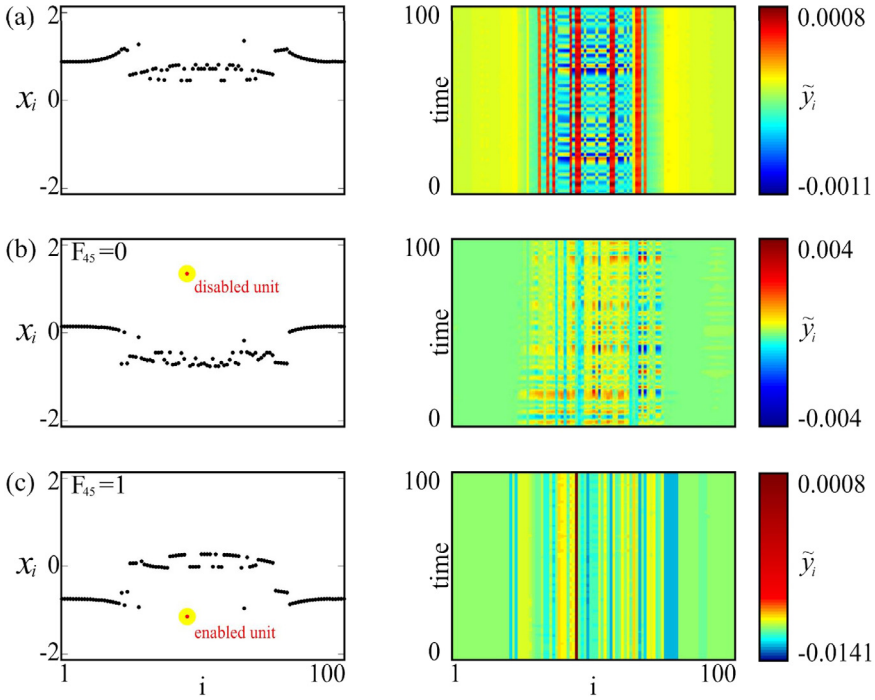

Fig. 11. The effect of the failure of one oscillator, in the van der Pol–Duffing network. The left and right panels show the snapshots of the x variables and the mean velocity ($\tilde{y}_i$)-time plots, respectively. (a) The s-chimera state is observed for $r = 0.3$ and $d = 0.01$, when all excitations are on. (b) The oscillator $i = 45$ is failed, and the pattern changes to the t-chimera state. (c) The external excitation of the oscillator $i = 45$ is turned on again, and the network returns to the initial s-chimera state.
Source: Figure reproduced with permission from [125].

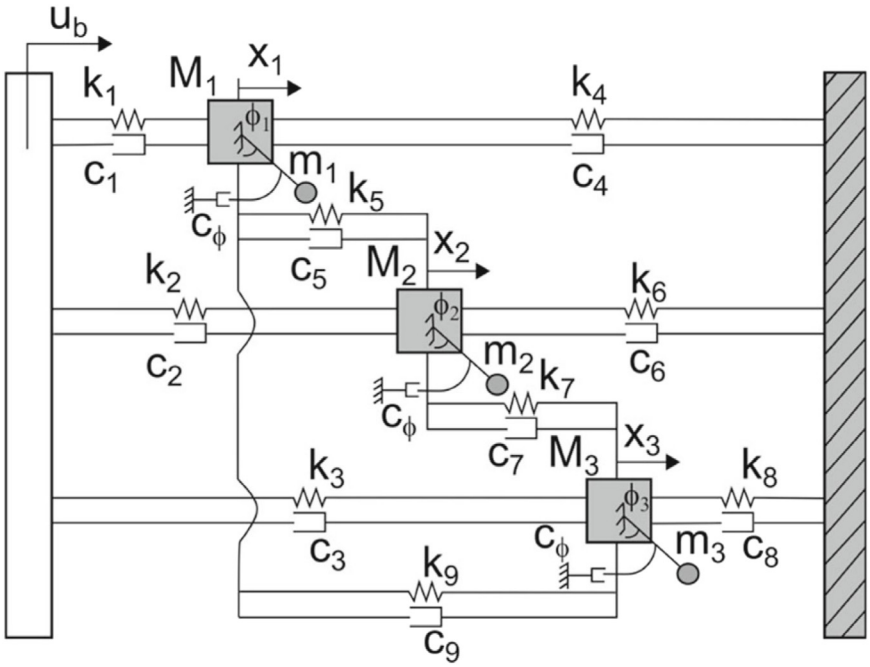

Fig. 12. The schematic of the pendulum-chart system consisting of three pendula.
Source: Figure reproduced with permission from [126].

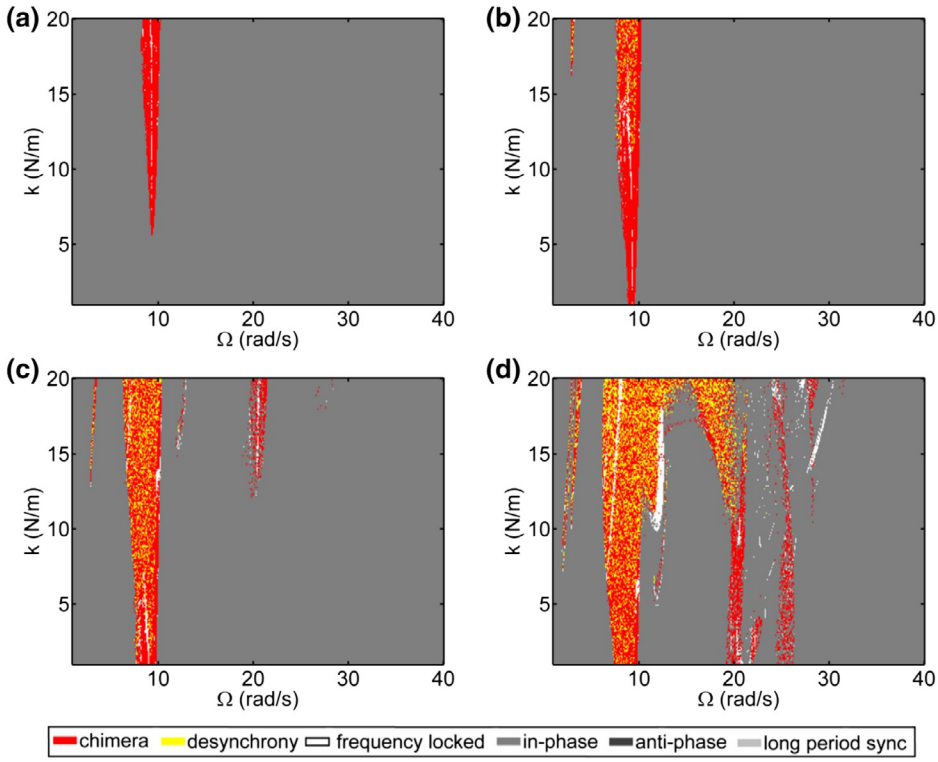

Fig. 13. The regions of different patterns of the pendulum-chart network, with analyzing the charts, for different excitation amplitudes (u). (a) $u = 0.1$ m, (b) $u = 0.2$ m, (c) $u = 0.5$ m, (d) $u = 1$ m.
Source: Figure reproduced with permission from [126].

- Firstly, the position of one oscillator is selected as a reference, and then the other oscillators' positions are subtracted from this reference. In case all subtractions are zero, the network is in in-phase synchronization.
- The next step, when all subtractions are not zero, is to add the subtracted signal with the double of the reference. In case this summation becomes zero for one of the oscillators, the network is in anti-phase synchronization.
- Finally, the peaks of the subtracted signal are computed. If consecutive peaks have the same distance, the pattern is frequency-locked, and otherwise, the long period synchronization is observed.

In case the pattern is not classified with this procedure, another oscillator is chosen as the reference. Subsequently, if the procedure with the new reference results in synchronization, then the network's pattern is the chimera state. Eventually, if no special pattern is identified by taking all oscillators as the reference, the oscillators are asynchronous. Fig. 13 represents the regions of the different patterns of the pendulum-chart network, with analyzing the position of the charts, for different excitation amplitudes. It is observed that for a low excitation amplitude, the oscillators mostly behave in a synchronized motion. As the excitation amplitude increases, the synchronous region is lessened, and more asynchrony patterns emerge in the network. Analyzing the pendulums or the complete chart-pendula system leads to the same results.

The patterns of the mechanical system have some relations with the system's energy. To find this relation, the potential energy of the elastic and also the pendulums are computed. The energy provided by the base is received by k_1, k_2, and k_3, and is transmitted through k_5, k_7, and k_9. Thus, the increment of the excitation amplitude results in receiving higher energy. The energy can be calculated through the charts as

$$E_{F,c} = \frac{1}{t}\int_0^1 \Big(\frac{k_5(x_2-x_1)^2 + k_9(x_3-x_1)^2}{k_1x_1^2 + k_4x_1^2} + \frac{k_5(x_2-x_1)^2 + k_7(x_3-x_2)^2}{k_2x_2^2 + k_6x_2^2} + \frac{k_7(x_3-x_2)^2 + k_9(x_3-x_1)^2}{k_3x_3^2 + k_8x_3^2}\Big)dt, \tag{21}$$

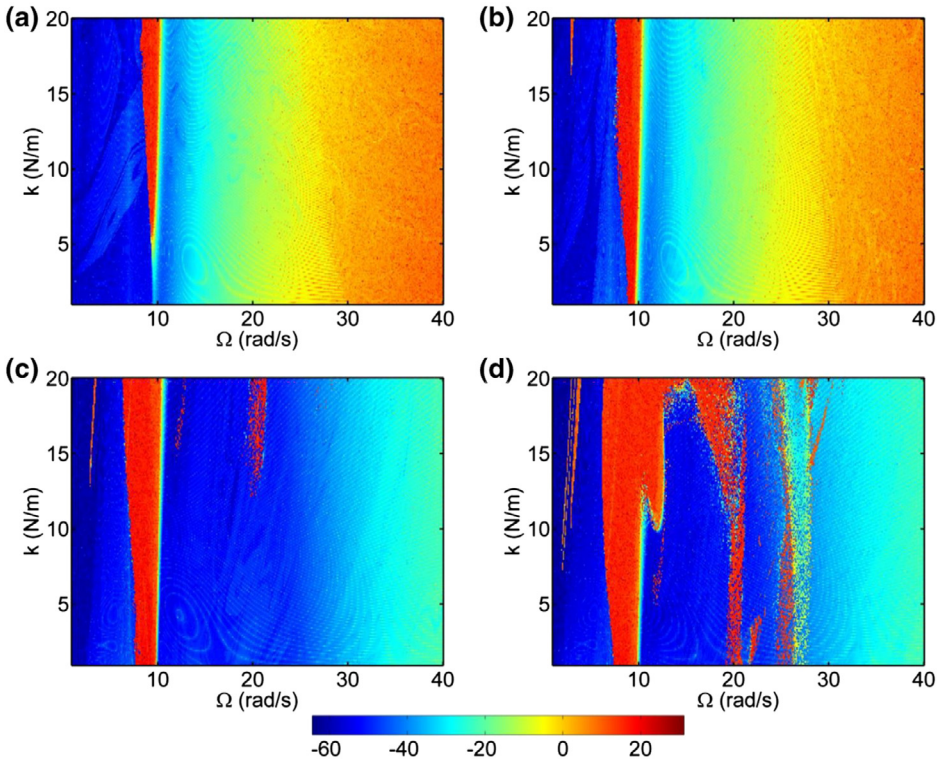

Fig. 14. The diagram of the energy calculated through the charts by Eq. (21) in the logarithmic scale, for different excitation amplitudes. $u = 0.1$ m, (b) $u = 0.2$ m, (c) $u = 0.5$ m, (d) $u = 1$ m.
Source: Figure reproduced with permission from [126].

or by the pendula as

$$E_{F,p} = \frac{1}{t}\int_0^1 \Big(\frac{mgl(1-\cos\phi_1)}{k_1x_1^2+k_4x_1^2} + \frac{mgl(1-\cos\phi_2)}{k_2x_2^2+k_6x_2^2} + \frac{mgl(1-\cos\phi_3)}{k_3x_3^2+k_8x_3^2}\Big)dt. \tag{22}$$

The diagram of the energy calculated through the charts is shown in Fig. 14 for different excitation amplitudes. Comparing this diagram with the dynamical patterns presented in Fig. 13 indicates that the higher energy is related to the asynchronous regions. Thus the system exhibits asynchronous or chimera states when it acquires more energy.

2.3. Chemical oscillators

Tinsley et al. [30] reported the chimera state and its relation to other synchronization states in a network of Belousov–Zhabotinsky oscillators based on an experimental study. Their experiment was relying on the photosensitive Belousov–Zhabotinsky reaction. In this experiment, the N oscillatory particles are separated into two different groups with the same population, A and B. Each particle i in the group σ encounters the feedback of light intensity P_i^σ

$$\begin{aligned} P_i^\sigma &= P_0 + k_\sigma P_{max}(\hat{I}_\sigma(t-\tau) - I_i(t)) \\ &\quad + k_{\sigma\sigma'} P_{max}(\hat{I}_{\sigma'}(t-\tau) - I_i(t)), \end{aligned} \tag{23}$$

where $\sigma = A$ and B, and $\sigma' = B$ and A. $\hat{I}_\sigma$ is the mean intensity of the oscillators in group σ. K_σ and $K_{\sigma\sigma'}$ are the intra- and the inter-group coupling coefficients, respectively. P_{max} is the maximum light perturbation which is equal to 3 mW cm^{-2}. $P_0 = 1.4$ mW cm^{-2} describes the background light intensity. It is considered that the intra-group coupling is stronger than the inter-group coupling, and each particle is globally coupled in each group out of the mean of the signal of its own group and another group. This experiment shows various types of synchronization. In all instances group A

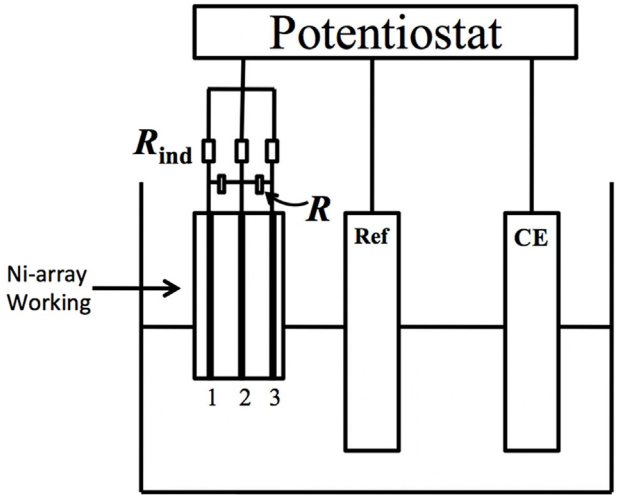

Fig. 15. The schematic of an electrochemical cell for nickel working electrodissolution experiment. *Ref*: $Hg/HgSo_4/Sat \cdot K_2SO_4$ reference electrode, *CE*: Pt electrode, R_{ind}: Individual resistors, R: Coupling resistors. Three elements are coupled by the cross resistors.
Source: Figure reproduced with permission from [127].

stays fully synchronous, but group *B* shows different basic states such as fully synchronized, *n*-cluster, asynchronized and semi-synchronized.

This experiment can be modeled with defining the chemistry of oscillators by

$$\begin{cases} \frac{dX_i}{dt} = f(X_i, Z_i, q_i) + \phi_i^\sigma \\ \frac{dZ_i}{dt} = g(X_i, Z_i, q_i) + 2\phi_i^\sigma, \end{cases} \tag{24}$$

where X_i, Z_i and q_i denote $[HBrO_2]$, $[Ru(bpy)3^{3+}]$ and the stoichiometric coefficient, respectively, and f and g describe the non-photochemical components of the Belousov–Zhabotinsky reaction. ϕ_i^σ is the photo-excitatory feedback of each oscillator and is computed as follows

$$\begin{aligned} \phi_i^\sigma &= \phi_0 + k_\sigma \phi_{max}(\hat{Z}_\sigma(t-\tau) - Z_i(t)) \\ &\quad + k_{\sigma\sigma'} \phi_{max}(\hat{Z}_{\sigma'}(t-\tau) - Z_i(t)), \end{aligned} \tag{25}$$

where the parameters are the same as Eq. (23). The numerical simulations of the model can generate all four types of basic states, which were seen in the experimental system. This network was investigated in both cases of homogeneous and heterogeneous oscillators. The effect of the frequency of the heterogeneous system and the system size was studied in the experiments as well as the simulations. It was revealed that by increasing the system size, the lifetime of the chimera state is increased exponentially. Besides, at very low levels of frequency heterogeneity, the network exhibits asymptotically stable chimera.

The synchronization and chimera pattern has also been investigated experimentally in the network of nickel electrodissolution [127]. The standard electrochemical cell is made up of a nickel electrode array, Hg, $HgSo_4$, saturated K_2SO_4 reference electrode and platinum counter electrode. Fig. 15 shows the schematic of this experimental setup. Each member of the network is an oscillatory reaction on the surface of a nickel electrode. The resistance R plays the role of creating the network by coupling the electrodes. Thus, it is known as the coupling resistance. The coupling strength of the network is determined by $K = 1/R$.

In this study, it was shown that the network of globally coupled six oscillators, which are organized in an extended triangle, demonstrates a Kuramoto transition to synchronization. This synchronization is specified by the natural frequencies. The partial synchronization is observed for a range of coupling strength $0.01 < K < 0.04$. For the coupling strength $K > 0.067$, the network exhibits a completely synchronous state. For investigating the chimera, the network was composed of 20 electrodes organized in a ring, and non-locally coupled by 14 neighboring electrodes. Regarding the previous study [128], a requirement for the emergence of the chimera is a phase delay about $\pi/2$. To apply the phase delay to the network, the coupling resistance was combined with a capacitance, and the combination was considered as the coupling element. The chimera states were observed when the phase delay was in a range of $[-\pi, \pi]$.

For the existence of a chimera state, only two diffusively coupled identical chemical oscillators are enough, such that one of them behaves almost periodically (coherently), and the other chaotically (incoherently) [129]. To demonstrate this chimeric behavior, a four-variable system made up of two coupled Lengyel–Epstein (LE) chemical oscillators have been

Table 1
The behaviors of the network Eq. (26) for different β values[129].

β	Period of 1st oscillator	System behavior
<0.001	1	In-phase
0.0010–0.0017	2	Antiphase
0.0018–0.0078312	1	In-phase
0.0078313–0.01085	3	Reverse canard
0.01086–0.01093	Multi	Complex periodicity
0.01094–0.0116107	Chaos	Chimera
0.0116108	1	In-phase
>0.101	Fixed point	Supercritical Hopf

used. Two oscillators were coupled symmetrically by diffusion. The equation of this four-variable system is as follows

$$\begin{aligned}
\frac{du_1}{dt} &= a - u_1 - \frac{4u_1v_1}{1+u_1^2} + d_u(u_2 - u_1),\\
\frac{dv_1}{dt} &= \beta\big(u_1 - \frac{u_1v_1}{1+u_1^2}\big) + d_v(v_2 - v_1),\\
\frac{du_2}{dt} &= a - u_2 - \frac{4u_2v_2}{1+u_2^2} - d_u(u_2 - u_1),\\
\frac{dv_2}{dt} &= \beta\big(u_2 - \frac{u_2v_2}{1+u_2^2}\big) - d_v(v_2 - v_1),
\end{aligned} \tag{26}$$

where the variables u and v act as an activator and deactivator, respectively. The variable u represents the iodine-containing species, and v describes the chlorine-containing species. Parameter α presents the reactant concentrations, and β describes both the reactant concentrations and the concentration of an immobile indicator. Parameter d_x is a coupling strength for species x. This system behaves periodically for the most values of the parameters and initial conditions. In other words, the oscillators are synchronized with the same amplitude, period, and phase. The system can exhibit the bi-stability, which is termed as the chimera states, in a limited range. The behavior of the system for different β values can be found in Table 1.

Fig. 16 represents how the fixed point of the system loses stability by increasing the β parameter through the supercritical Hopf bifurcation. u-nullcline and v-nullcline are plotted by green and yellow, respectively. Fig. 16a shows the in-phase large amplitude oscillations for $\beta = 0.0078312$. For $\beta = 0.0078313$, the dynamics of one of the oscillators changes to 3-periodic with small amplitude (Fig. 16b). With more increasing of β, the dynamics becomes more complex, and finally, one oscillator becomes chaotic (Fig. 16c). Thus, the chimera emerges through a supercritical torus bifurcation. As β increases more, the oscillators again reach in-phase synchronization with large amplitudes and then with small amplitudes (Fig. 16d,e). Finally, the stability is lost through a supercritical Hopf bifurcation (Fig. 16f).

2.4. Optical oscillators

The experimental realization of a coupled-map lattice with using a liquid-crystal spatial light modulator has been mainly investigated in the past three decades. Due to this importance, the spatiotemporal dynamics of this network were studied by Hagerstrom et al. [130] in both 1D and 2D configurations. The network contains the optical nonlinearity which is created by the polarization optics. The nonlinear relation ($I(\varphi) = (1 - cos(\varphi))/2$) is between spatial phase shift that is exerted by spatial light modulator, and the light intensity measured by the camera. The phase of the network elements is updated with the following iterative equation

$$\phi_i^{n+1} = 2\pi a\left\{I(\phi_i^n) + \frac{\epsilon}{2R}\sum_{j=-R}^{R}\Big[I(\phi_{i+j}^n) - I(\phi_i^n)\Big]\right\}, \tag{27}$$

where i is the index of the oscillator, R is the number of elements in the coupling, and ϵ characterizes the strength of the coupling. The temporal dynamics of an isolated map is controlled by the parameter a; such that for $a = 0.85$ is chaotic. For the 2D lattice, the phase is updated according to

$$\phi_{i,j}^{n+1} = 2\pi a\left\{I(\phi_{i,j}^n) + \frac{\epsilon}{4R^2}\sum_{k,l=-R}^{R}\Big[I(\phi_{i+k,j+l}^n) - I(\phi_{i,j}^n)\Big]\right\}. \tag{28}$$

The dynamics of the elements can be determined by the temporal entropy. Fig. 17a,b indicate the dynamics of 1D and 2D configurations, respectively, by changing the coupling strength and coupling radius $r = R/N$. The blue region refers to the low entropy and periodicity, while the orange region shows high entropy and chaos. For 1D lattice, the results are obtained by setting $N = 256$, and for 2D, a square of 128×128 is considered. In Fig. 17a, three tongues are

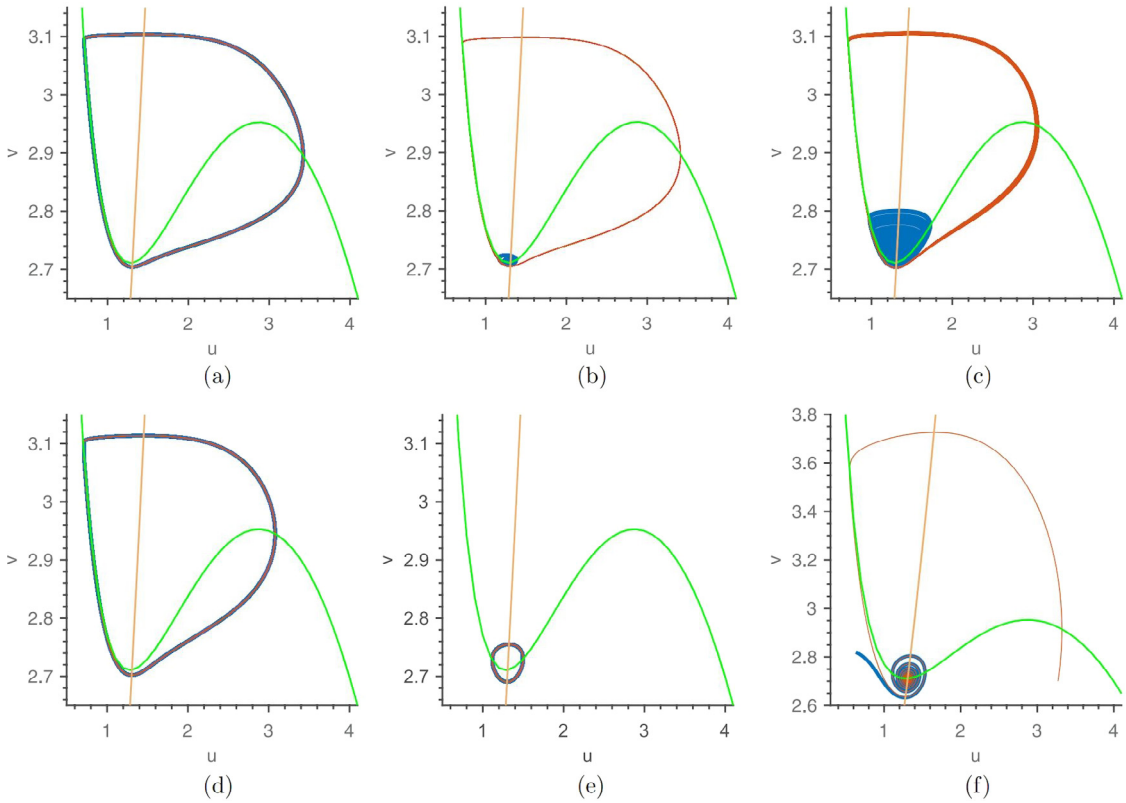

Fig. 16. The dynamics of the chemical oscillators (Eq. (26)) with increasing β. (a) In-phase synchronization with large amplitude for $\beta = 0.0078312$. (b) Anti-phase synchronization for $\beta = 0.0078313$. (c) Chimera state for $\beta = 0.0116107$. (d)) In-phase synchronization with large amplitude for $\beta = 0.0116108$. (e) In-phase synchronization with small amplitude for $\beta = 0.04$. (f) Stable fixed point for $\beta = 0.2$. The initial conditions are $(u_1, v_1) = (0.63, 2.83)$ and $(u_2, v_2) = (3.27, 2.70)$ and parameters are $a = 6.54$, $d_u = 0.00081$, and $d_v = 0.0018$.
Source: Figure reproduced with permission from [129].

observed, marked by $K = 1,\ 2,\ 3$. These regions are periodic in time and have spatial wave numbers of K (the number of maximum). In these regions, by decreasing the coupling strength, the spatial behavior is changed from coherence to incoherence. During this transition, the chimera state is also observed. The snapshots showing this transition are illustrated in Fig. 17c,d, for 1D and 2D lattices, respectively. Both experimental and numerical simulation results are shown. The highlighted parts in the chimera state plots show the incoherent parts. The hatched regions in Fig. 17a,b represent the region of the stable global synchronization.

The chimera state has also been demonstrated in an optical comb experimentally and numerically [131]. In a passively mode-locked laser, each line of the comb is a linear mode of the laser, and each mode is an oscillator. In the passively mode-locked laser, the modes are coupled to each other with different coupling strengths to have a non-local coupling. By varying the pumping current, a coexistence of coherent and incoherent modes is observed in the comb. The coherent modes (oscillators) have a constant phase difference and are phase-locked. While in the incoherent ones, there is no fixed phase difference. The reason for this coexistence may be the nonlinear field–matter interactions. When the chimera state occurs, the coupling is naturally operated by the system, not with a defined preset or feedback adaptive operations.

2.5. Map lattices

The discrete-time systems can be used for the modeling of many processes. The network of discrete-time systems coupled with nearest-neighbor coupling is called the coupled map lattice. Diverse dynamical behaviors and synchronization patterns, such as chimera state, have been observed in the map lattices. A coupled map lattice is described by the following equation

$$z_i^{t+1} = f(z_i^n) + \frac{\sigma}{2P} \sum_{j=i-P}^{i+P} \left[f(z_j^t) - f(z_i^t) \right],\ i = 1, \ldots, N \tag{29}$$

where z_i is the real discrete variable, t shows the discrete-time, and σ and P are the coupling strength and the number of nearest-neighbors in coupling. $f(z_i^t)$ describes the dynamics of the lattice elements. For studying the chimera state in

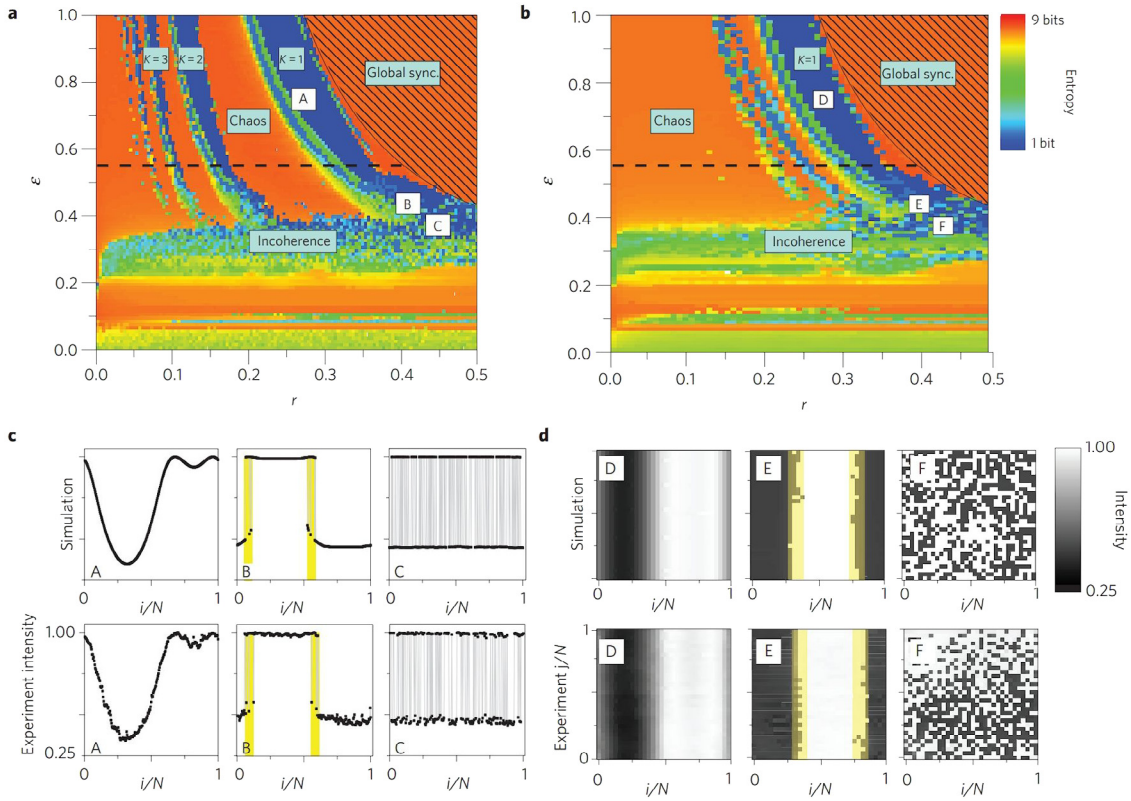

Fig. 17. The dynamics of the optical map lattices in 1*D* (left panel) and 2*D* (right panel) configurations. The temporal dynamics of the lattices by computing the temporal entropy is shown in parts a and b, by varying the coupling range (r) and strength (ε) (blue: low entropy and periodic, orange: high entropy and chaotic). The tongues marked by K are periodic and have spatial wave numbers of K. The experimental and numerical results of different spatial patterns are shown in parts c and d for 1*D* and 2*D*, respectively. A and D: coherence , B and E: chimera state, C and F: incoherence. The highlighted parts show the incoherent regions.
Source: Figure reproduced with permission from [130].

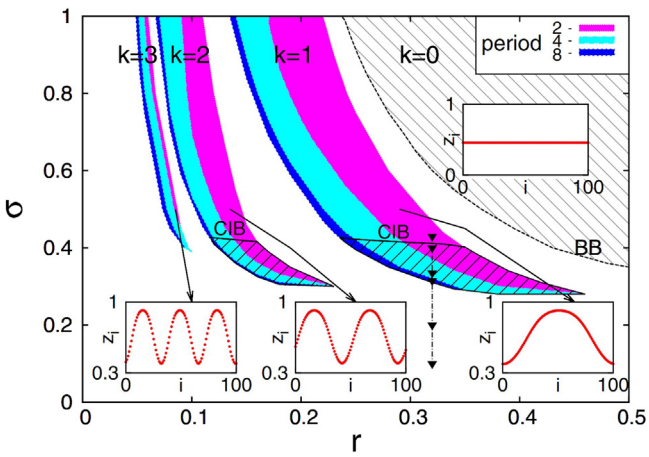

Fig. 18. Different dynamics of the coupled Logistic lattice in the (r, σ) plane. The hatched and colored regions represent coherent states with wave number k. The synchronous state with $k = 0$ is inside the BB bifurcation curve. The coherent and incoherent states in the colored regions are separated by the CIB bifurcation curves, where below CIB, the network is two-cluster incoherent. The parameters are $a = 0.38$ and $N = 100$.
Source: Figure reproduced with permission from [132].

discrete systems, the Logistic map $f(z) = az(1 - z)$ has been widely used [132–139]. Different dynamical behaviors of the coupled Logistic map lattice in the plane of σ and $r = P/N$ are demonstrated in Fig. 18 for $a = 3.8$. When the

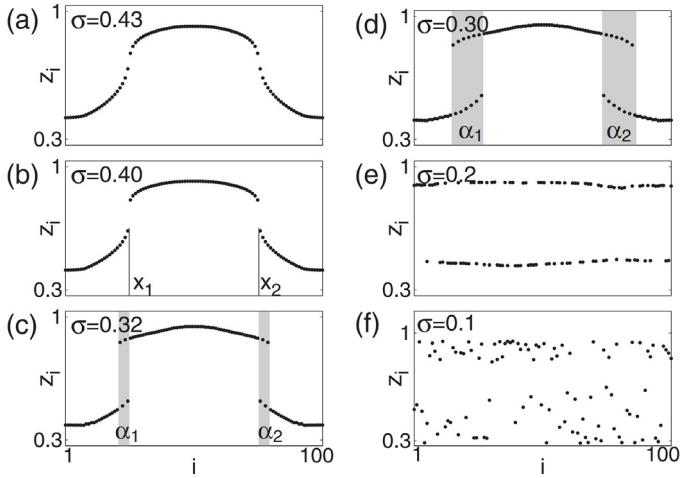

Fig. 19. The time snapshots of the Logistic maps for r=0.32 and different coupling strengths. (a) $\sigma = 0.43$, (b) $\sigma = 0.4$, (c) $\sigma = 0.32$, (d) $\sigma = 0.3$, (e) $\sigma = 0.2$, (f) $\sigma = 0.1$. The gray regions in parts c and d represent incoherent cluster of chimera state.
Source: Figure reproduced with permission from [134].

maps are coupled locally, the network shows spatiotemporal chaos. In contrast, when the coupling is global, a complete, coherent state is formed in the network for sufficient value of coupling strength. The synchronous state appears in the hatched region shown in Fig. 18, and losses its stability after passing the bifurcation curve BB. The colored tongues in this figure show other coherent regions with the wave number k. In these regions, the maps have periodic behavior and are subjected to period-doubling bifurcation with the decrement of σ and r. The insets in Fig. 18 indicate the time snapshots of z variables in each state.

During the transition from coherence to incoherence, firstly, some of the elements loose coherence, and the chimera state is formed. The dynamics of the network for $r = 0.32$ is represented in Fig. 19 for different coupling strengths. In $r = 0.32$, the network is coherent above $\sigma = 0.4$, as can be seen in Fig. 19a. In this case, the profile of z_i constitutes upper and lower branches. With decreasing the coupling strength to $\sigma = 0.4$, two branches separate at the points x_1 and x_2 in Fig. 19b, and further decreasing leads to the formation of incoherent clusters, and thus the chimera state appears (shown by α_1 and α_2 in Fig. 19c,d). For smaller coupling strengths, the incoherent clusters become wider, and finally, the network is incoherent (Fig. 19e,f).

To understand the mechanism of formation of chimera, the dynamics of the coupling function $\frac{\sigma}{2P}\sum_{j=i-P}^{i+P}\left[f(z_j^t)-f(z_i^t)\right]$ is investigated [135]. To this aim, instead of the time snapshot, the space–time plot, which is the accumulated 100 last iterations, is shown for $f(z_i^t)$. Therefore, the dynamics of the systems that is periodic or chaotic can be identified. Fig. 20 shows the space–time plot of $f(z_i^t)$ and the snapshots of the z variables for $a = 3.8$, $r = 0.32$, $N = 1000$, and different coupling strengths. As the coupling strength decreases in parts a–c, the coupling function remains periodic, but its period is duplicated. The corresponding snapshots show that the network is coherent. At $\sigma = 0.35$, the coupling function enters chaos with period-doubling bifurcation, and simultaneously the formation of incoherent regions is observed in the snapshot. The temporal dynamics of the systems in each case are similar to the coupling function. Thus, for $\sigma = 0.43$, the oscillators are periodic and finally reach chaotic behavior by period-doubling bifurcation root to chaos. Consequently, the chimera state is generated by the period-doubling bifurcation in both the coupling function and the local dynamics.

The chimera states in Logistic maps are also robust to the parameter inhomogeneity [136]. The inhomogeneity can be applied by assuming different values for the parameter a of the Logistic maps. Malchow et al. [136] considered that the parameters a of maps are chosen from a Gaussian distribution with the mean value of $\langle a\rangle = 3.8$ and the standard deviation s. Therefore, the non-identical Logistic maps may have different periodic or chaotic dynamics. To investigate the effect of the inhomogeneous parameter, the value of the standard deviation is varied. By introducing inhomogeneity, the behavior of the network is mostly influenced in small coupling strengths. By increasing the standard deviation, the coherent tongues (shown in Fig. 18 for $k = 1, 2, 3$) are affected. Firstly, the tongues with larger k disappear gradually. Moreover, the tongues which are related to $k = 1$ and $k = 2$, shrink and are visible only for higher coupling strengths. The effect of adding the inhomogeneity to the chimera state in the Logistic lattice is shown in Fig. 21, wherein the left panel shows the time snapshot, and the right shows the spatiotemporal pattern. Fig. 21a represents the chimeric behavior of the identical maps ($s = 0$) for $r = 0.32$ and $\sigma = 0.22$. Then, the standard deviation is increased, and the network's behavior is shown in parts b–f. It is observed that the general behavior of the systems is preserved. But, the pattern becomes blurred with increasing s.

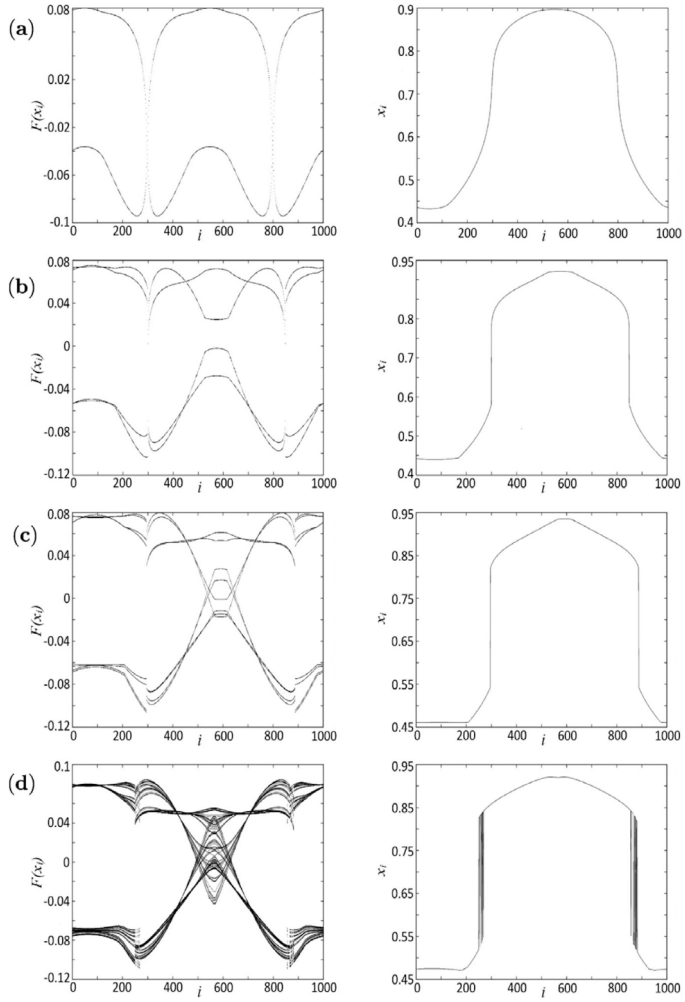

Fig. 20. The space–time plots of the coupling function and the time snapshots of the coupled Logistic maps for different coupling strengths. (a) $\sigma = 0.43$, (b) $\sigma = 0.38$, (c) $\sigma = 0.3574$, and (d) $\sigma = 0.35$. The other parameters are $r = 0.32$, $a = 3.8$, and $N = 1000$.
Source: Figure reproduced with permission from [135].

The coupled sine circle maps have also shown the chimera state [140,141]. This map is described by the following equation

$$\theta_{t+1} = f(\theta_t) = \theta_t + \Omega - \frac{K}{(2\pi)} \sin(2\pi\theta_t) \quad \text{mod } 1, \tag{30}$$

where $0 < \theta < 1$ is the angle, and Ω and K are the winding number and the nonlinearity parameter. With increasing K, the map tends to the mode lock, and Arnold's tongues appear in the $K - \Omega$ space. Nayak and Gupte [140] considered two populations of sine circle maps in which each system was coupled to the other systems in its group with coupling strength ε_1 and also to the systems of the other group with coupling strength ε_2. Thus, the whole network can be described by

$$\begin{aligned}\theta^{\sigma}_{n+1}(i) = {} & (2 - \varepsilon_1 - \varepsilon_2) + (\theta^{\sigma}_n(i) + \Omega - \frac{K}{(2\pi)} \sin(2\pi\theta^{\sigma}_n(i))) \\ & + \sum_{\sigma'=1}^{2} \frac{\varepsilon_{\sigma\sigma'}}{N_{\sigma'}} \sum_{j=1}^{N_{\sigma'}} (\theta^{\sigma'}_n(j)) \\ & + \Omega - \frac{K}{(2\pi)} \sin(2\pi\theta^{\sigma'}_n(j)) \quad \text{mod } 1.\end{aligned} \tag{31}$$

The coupling strengths have the values between 0 and 1, with the condition $\varepsilon_1 + \varepsilon_2 = 1$. They considered similar initial conditions for the first population and the random initial conditions for the second one. With these initial conditions, the

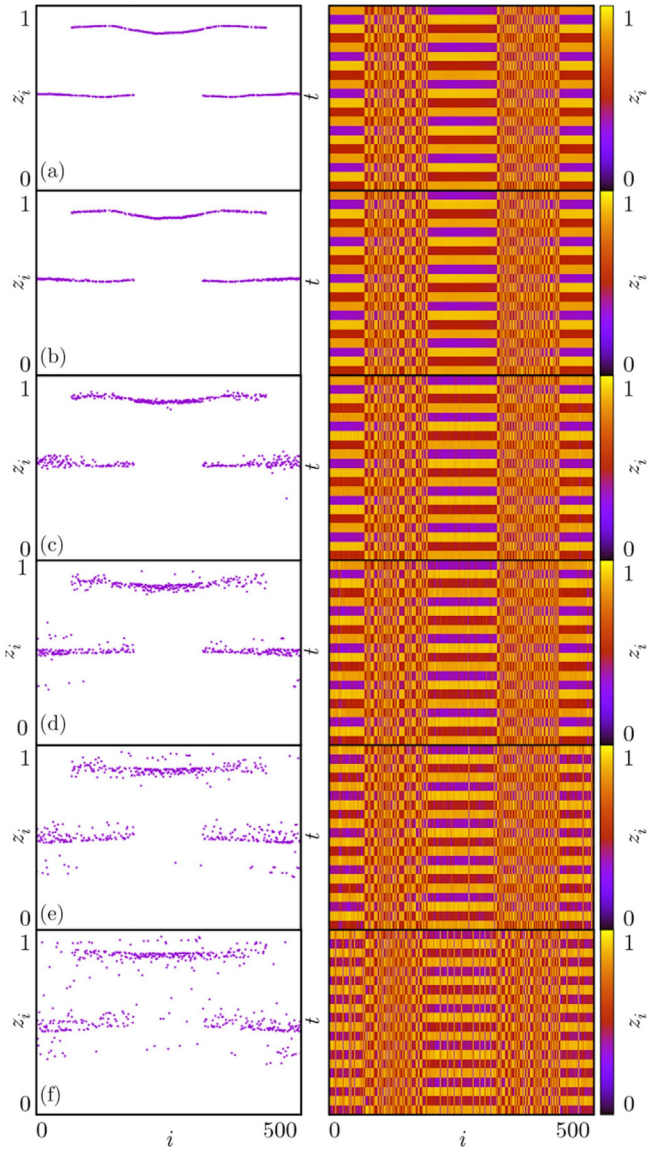

Fig. 21. The chimera state in non-identical Logistic maps. The left and right panels show the snapshots and the spatiotemporal patterns, respectively. The parameter a is selected from a Gaussian distribution with the mean $\langle a \rangle = 3.8$ and the standard deviation s. (a) $s = 0$, (b) $s = 0.01$, (c) $s = 0.05$, (d) $s = 0.1$, (e) $s = 0.15$, (f) $s = 0.2$.
Source: Figure reproduced with permission from [136].

network shows different dynamical behaviors by varying the parameters K and Ω. When the value of K is very large, both groups are completely coherent, but there is a phase difference between them. The snapshot of the maps, in this case, is shown in Fig. 22a. With decreasing K, the oscillators in the second group fall into several synchronous clusters (Fig. 22b). By more decreasing K, the systems of the second population are clustered into two synchronous and asynchronous groups, where the synchronous systems have the same phases as the first population. This state can be called the clustered chimera (Fig. 22c). Finally, further decrement in K leads to the complete asynchrony in the second population, and a chimera state is formed (Fig. 22d). Singha and Gupte [141] represented that the chimera state also arises by selecting completely random initial conditions for both populations. They reported the occurrence of the chimera states with synchronized phases in one group and asynchronized phases in another one. In special cases, the synchronous group was not perfect and consisted of different oscillating oscillators.

The dynamical properties of the elements of the network influence on its collective behavior. Some researches have reported that in the network of non-locally coupled chaotic systems, the chimera state emerges only when the single element has a nonhyperbolic attractor [142–144]. The trajectories of the hyperbolic system are of saddle type.

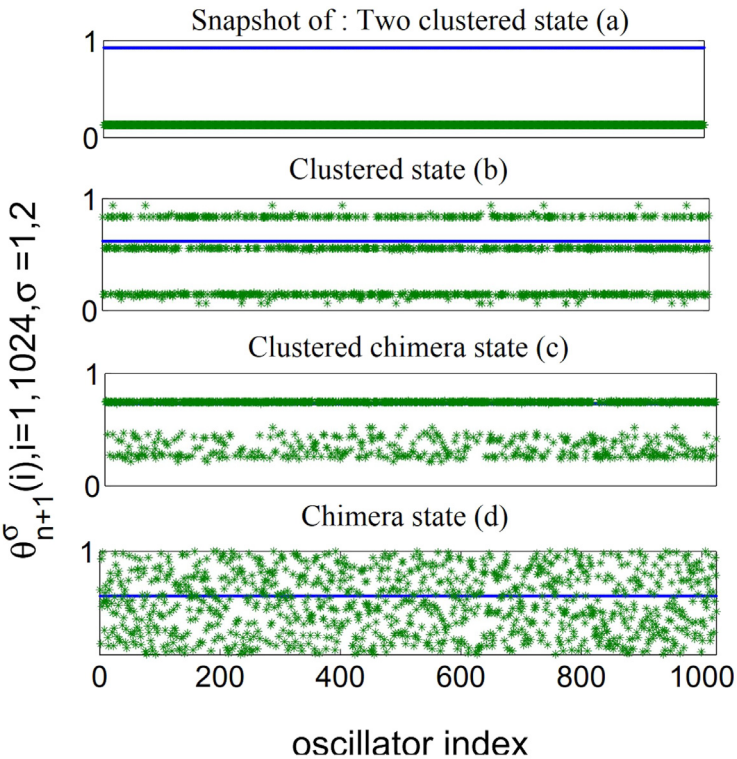

Fig. 22. The time snapshot of the coupled sine circle maps in two populations (Eq. (31)) with different parameter values.
Source: Figure reproduced with permission from [140].

The hyperbolic attractor has a homogeneous structure and is robust to slight changes in parameters. In contrast, a nonhyperbolic system has unstable homoclinic trajectories. The nonhyperbolic system is multistable and has several periodic and chaotic attractors in constant parameters. In these systems, the periodic and chaotic attractors bifurcate by changing the system parameters.

To examine this hypothesis, the Hénon and Lozi maps have been chosen as examples of systems with nonhyperbolic and hyperbolic attractors. These maps can be obtained as the Poincaré sections of the nonhyperbolic class of Rössler oscillators and the hyperbolic class of Lorenz oscillators, respectively. A ring of Hénon (or Lozi maps) with non-local coupling can be considered as

$$\begin{aligned} x_i^{t+1} &= f(x_i^t, y_i^t) + \frac{\sigma}{2P} \sum_{j=i-P}^{i+P} [f(x_j^t, y_j^t) - f(x_i^t, y_i^t)], \\ y_i^{t+1} &= \beta x_i^t, \end{aligned} \tag{32}$$

where for the Hénon map $f(x, y) = 1 - \alpha x^2 + y$, and for the Lozi map $f(x, y) = 1 - \alpha|x| + y$. The dynamical regions of these two maps are shown in Fig. 23. It is observed that the behavior of the Hénon map (Fig. 23a) is very similar to the Logistic map. The regions labeled with D and E represent the spatially incoherent and synchronous states, respectively, and the tongues labeled with A, B, and C refer to the coherent regions with wave numbers $k = 3$, $k = 2$, and $k = 1$. In the transition from coherence to incoherence, the chimera state emerges in the Hénon maps. The dynamics of the Lozi maps, which is demonstrated in Fig. 23b, is completely different from the Hénon map. It consists of a completely synchronous region (shown by purple), an incoherent region (shown by blue), and the traveling waves (shown by white). In contrast to the Hénon maps, the chimera states are not observed in the coherence–incoherence transition of Lozi maps. Instead, this transition occurs through solitary states. In a solitary state, most of the oscillators are synchronized, while some of them escape from the synchronized group and oscillate differently. Therefore, the chimera state emerges only in the systems with nonhyperbolic attractors.

2.6. Neuronal networks

One of the significant steps in the evolution of life was the progression from unicellular to multicellular. This development required the interdependent metabolic activities of cells to get coordinated and controlled [145]. A brain

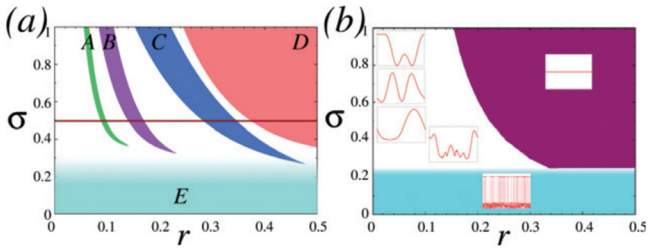

Fig. 23. Dynamical regions in the non-locally coupled Hénon (a) and Lozi (b) maps in the (r, σ) plane. (a) A, B, and C show coherent regions with wave number $K = 3,\ 2,\ 1$. D and E show the complete coherent and incoherent regions. The horizontal line represents the border of the coherence–incoherence transition. (b) The purple, blue and white colors show the coherent, incoherent, and traveling waves regions, respectively. The parameters are $\alpha = 1.4$, $\beta = 0.3$ and $N = 1000$.
Source: Figure reproduced with permission from [142].

neuronal network is a self-organized system consisting of a significant number of interconnected components called neurons [146]. It has been estimated that the human brain network involves more than 86 billion neurons, quadrillion synaptic connections, and a trillion bit/second equivalent processing [147]. Brain networks are represented with graphs in which neurons or brain regions are nodes, and structural or functional interactions are edges (connections) [148]. One of the most exciting features of a neural network is that each neuron behavior is not only dependent on its single activity, but it is also affected by the behavior of its neighboring neurons with electrical and chemical synapses [149]. Therefore, studying the function of the human brain and the mental disorders and any processes in the biological system requires a good understanding of neurons, neuronal activity, and the connectivity of the neuronal network [150–152].

Brain connectivity has three different categories [147,153]:

1. Structural connectivity, which is the connection between the anatomical and physiological structures of the brain. This network can be considered as individual neural nodes linked by synaptic edges connections to other neurons in a microscopic scale. Anatomical and electrophysiological data of the neuronal activity are used for constructing the brain structure. These data provide information about the connectivity patterns and population density of specific cell types within a brain region. By using graph theory, a realistic estimation of the structural connectivity can be produced [154].
2. Functional connectivity, which is usually defined as the statistical dependencies between spatially unconnected or remote neurophysiological regions. Most of the connectivity data for these studies are based on histologic tract-tracing experiments that have been done on different kinds of animals [155,156]. Since tract-tracing on living people is not appropriate, in-vivo structural connectivity data from the human subjects are collected with non-invasive imaging methods such as Magnetic resonance imaging (MRI), diffusion tensor imaging (DTI), and tractography. MRI data can be used for quantifying the volume density of local correlations in cortical thickness or gray matter (GM). DTI and tractography are also useful for calculating interregional white matter connectivity, large-scale brain regions connected by bundles of axons.
3. Effective connectivity, which is the influence one neural system exerts on another. These networks are often generated for multiple frequency bands of the time-series signal and make it possible to study a wide range of time scales.

Communications between neurons and their synchrony determine the functional activity of the brain. In other words, brain functions are based on dynamical interactions between neural assemblies distributed within and across distinct cerebral regions. This connectivity is recorded by high-resolution time series of neural activity such as electroencephalography (EEG) and magnetoencephalography (MEG), or even by imaging methods like functional magnetic resonance imaging (fMRI). Blood-oxygen-level-dependent signals also give information about neuronal activity [157]. The data type specifies the construction of the network and the choice of nodes and edges. For instance, network nodes are surface electrodes in EEG data and the voxels represent anatomical or functional areas in fMRI data. A network edge can also be obtained by tracing white matter tracts through the brain or based on statistical relationships between time series of regional activity, such as interregional correlation, coherence, or phase synchronization in undirected or directed, weighted or unweighted mode [148]. These statistics can help in recognition of pathological brain disorders such as epilepsy, Alzheimer, schizophrenia, multiple sclerosis (MS), etc. [158,159].

Information processing and neuronal collective behavior in the mammalian brain is based on the ionic current flow across neuron membranes. These signaling can be divided into two main groups: chemical synapse and electrical synapses [69,160]. Synapses are the specialized sites of functional interaction between neurons [161]. Electrical and chemical synapses have significant differences in both the molecular mechanisms of information transfer and in their morphological organization. There is no continuity between the cytoplasm of the two cells at the chemical synapse. The synaptic cleft is the distance separating the pre- and post-synaptic membranes that is approximately 20–40 nm in chemical synapses. In contrast, this space in electrical synapses is much smaller, in the order of 2–4 nm between the pre-

and post-synaptic membranes. Through this area of apposition, the two cells communicate with each other. The difference in the distances between pre- and post-synaptic ends in electrical and chemical synapses demonstrates that time delays of electrical synapses are generally shorter than those of chemical ones. It is worth mentioning that electrical synaptic transmission is not appropriate for too complex and complicated processes of higher organisms, while chemical synapses are suitable for providing higher diversity and fine-tuning signals [162]. Although different parts of a nerve cell (dendrites, somata, and axons) can transmit information through both electrical and chemical synapses, the chemical transmission usually occurs between synaptic terminals of axons and dendrites or soma neurons of a second neuron, muscle fiber, or gland cells [163].

The most typical synapses are chemical synapses that release neurotransmitters from synaptic vesicles tonically with a high rate that make information transfer possible [164]. Transmission of information by chemical synapses occurs in all organisms, from unicellular organisms such as bacteria to highly complex mammals [163]. Chemical synapses have two types, excitatory and inhibitory. Spikes of an inhibitory pre-synaptic neuron can prevent the post-synapses neuron connected to it from spiking. In contrast, spikes of an excitatory neuron induce the post-synaptic neuron to spike [165]. One of the most important excitatory neurotransmitters in the mammalian brain that has attracted a lot of attention in the last two decades is glutamate. The Glutamate released from synapses activates ion channel-forming receptors at post-synaptic cells [166]. When the spikes cross the axon of the pre-synaptic neuron and reach the synaptic area causing changes in the ionic permeability of the post-synaptic membrane. Therefore the calcium channels open, and the calcium flows lead into the neuron, which releases neurotransmitters in the synaptic region. This happening activates ligand-gated ion channels and enables data transfer [167]. Therefore, in modeling the chemical synapses in the neuronal networks, a nonlinear coupling function is used. This nonlinear coupling function is mostly the sigmoidal nonlinear input–output function as

$$\Gamma(x) = \frac{1}{1 + e^{-\lambda(x-\Theta_s)}}, \tag{33}$$

where λ defines the slope of the function, and Θ_s is the synaptic threshold.

Electrical synapses are much faster than chemical synapses and can almost do everything that they do. The interesting point is that the chemical synapses can work as modulatory for electrical synapses and create mixed excitatory synapses that can be found in many regions of the mammalian CNS [161]. Electrical synapses discovered in the 20th century [168] are the communication pathways of many nerve cells in the mammalian central nervous system that communicates through bidirectional ionic currents and small organic molecules. Therefore, they can produce changes in the membrane potential of neighboring neurons and provide velocity and reciprocity to the communication allowing the synchronization of neuronal clusters. They play an important role in all the functions of neural circuits of mammalian brains and can be found everywhere in their neuronal system. Transmitting excitation from an active axon to a post-synaptic cell (which can be quite similar in electrical and chemical synapses) and synchronizing the activity of neurons are the main functions of electrical transmission between cells [160]. There is also some evidence of electrical synapses and the gap junctions between neurons in non-mammalian systems. The first evidence was the contacts between the giant axon and the giant motor fiber of the crayfish, which was followed by some other evidence in fishes and birds. These discoveries were made after the advancement of technology and the possibility of combining electrophysiological data and ultrastructural images, which helped to identify the electrical communication and gap junctional coupling [168].

Most of the time, the electrical synapses work as low pass filters. It means that they prefer to transmit low-frequency stimuli typically and transmit high-frequency oscillations in particular circumstances. This feature helps them to transfer a pre-synaptic impulse into an electrical excitatory post-synaptic potential in the post-junctional cell rapidly. Action potentials occur when the voltage-gated ion channels are activated, due to membrane depolarization, followed by sufficient transmitted current to the post-synaptic cell. The easy movement of ionic current between two cells can represent bidirectional transmission via the intercellular channels. Thus, these synapses are usually modeled with a simple diffusive function. One of the benefits of electrical synapses to the chemical neurotransmission is the unique interchange of the stimulus helped by electrical neurotransmission and the transfer of sub-threshold potentials. However, electrical transmission cannot be equated to shared excitation. A more depolarized cell can excite a less depolarized cell and vice-versa. Besides, some electrical synapses are not bi-directional; instead, transmission in only one direction is more significant, i.e., at the motor synapse of the crayfish that was mentioned as the first evidence of gap junctional coupling in non-mammalian systems [162].

As the action potential is the communication path between neurons, understanding the excitability feature, which determines the mechanism of the generation of the action potential, is very important. Excitability can be divided into two parts: type I yields a response of finite amplitude and infinite period through a global bifurcation, and type II gives rise to zero-amplitude and finite period spikes via a Hopf bifurcation. Type II excitability is often modeled by the FitzHugh–Nagumo system. The FitzHugh–Nagumo model is described by the following equations

$$\begin{aligned} \epsilon_0 \dot{u} &= u - \frac{u^3}{3} - v, \\ \dot{v} &= u + \mu, \end{aligned} \tag{34}$$

where u and v are the activator and inhibitor variables, $\epsilon_0 > 0$ is the time scale parameter, and μ is the excitability threshold. For $|\mu| < 1$, the system is in the oscillatory state, while for $|\mu| > 1$, it is in an excitatory state. Another neuron

model is the Hindmarsh–Rose model, which is representative for both type I and type II excitability and exhibits very complex behavior, including spiking, regular and chaotic bursting. The Hindmarsh–Rose model is described by

$$\begin{aligned}\dot{x} &= y + ax^2 - x^3 - z + J,\\ \dot{y} &= 1 - dx^2 - y,\\ \dot{z} &= c(b(x - x_0) - z),\end{aligned} \tag{35}$$

where x, y, z are the membrane potential, fast and slow variables, respectively. J denotes the stimulation current, and a, b, c, d are the control parameters. The chimera states and other collective dynamics have been identified in this model [169]. The level of excitability and its type and also non-local network features can make different types of synchrony in the system [170].

The communication and information exchange among the neurons determine the brain function. During these interactions among an abundance of neurons in a huge neuronal network in behavioral and cognitive tasks, a group of neurons oscillate coherently and get synchronized [171]. Changes in the structure of connections between neurons or the removal of any of the connections can cause the synchronous structure to be asynchronous or, in general, the collective behavior changes from one type to another [172]. The coupling strength also has a remarkable influence on the collective behavior of the neuronal network [173]. Intercellular communication also affects the individual neural behavior, which exhibits spike or burst activities [174].

One of the most important factors for synchronizing neuronal behavior is the electromagnetic radiation (ER), which can be internal or external. The source of internal electromagnetic fields is the charge movement in the cell membrane channel of neurons that can regulate the collective behavior among subnetworks in a positive or negative way. When the effect of ER is positive, it can enhance the synchronous behavior, while negative feedback may suppress it [175]. Membrane potential differences between two adjacent neurons can also produce an electromagnetic induction effect. The electromagnetic induction acts as a memristor synapse to connect the two neurons and can lead to state-dependent collective behaviors such as chimera states [50,176,177]. The external electromagnetic fields from any source outside the system can regulate the dynamical behavior of the neural network according to the intensity and frequency of the electromagnetic radiation [178].

Neuronal synchronization for the coherency of perceptual and cognitive states has critical importance in order to execute behavior and motor action that depend on multiple sources of information [179]. The level of synchrony in different regions of the brain can be measured by the electrophysiological or neuroimaging data. Neuroimaging studies show that in many neurological and psychiatric disorders, network connections and the neurons' synchrony are different from the normal condition. On the other hand, neural synchronization is not desirable for all brain processes. Neurons in a healthy brain also work asynchronously in some situations. The asynchronous population activity can help for efficient information processing, decision making, and regulating some other vital tasks. For example, during waking and REM sleep, the brain cortex operates in a highly asynchronous state. Another example is the subthalamic nucleus, a specific location in the basal ganglia, which exhibits asynchronous electrical activity in the beta frequency band as a measure for movement preparation [180].

Several studies show the occurrence of surprising chimera states in neuronal networks, the situation that the two common synchronous and asynchronous states can coexist within the same neuronal circuitry at the same time [47,181,182]. Recently, Majhi et al. [45] presented a complete review of the chimera studies in neuronal networks. Chimera can potentially explain the so-called "bumps" of neural activity, which is a state that the firing rate is constant at some spatial locations and higher at other spatial positions. Therefore, this state is crucial for the dynamical activity of the brain [183]. For example, it is believed that the neurons are in the chimera state for visual orientation tuning and the head direction system in rats [184]. Another evidence of the coexistence of synchronous and asynchronous states has been seen in the uni-hemispheric slow-wave sleep. This sleep, with one eye open, is seen in some migratory birds [185], ducks [186], lizards [187], and aquatic mammals such as dolphins, eared seals, and manatees, where one cerebral hemisphere sleeps and the other stays in an awake condition. It means that they shut down only one cerebral hemisphere of the brain and close the opposite eye. Meanwhile, the other half of the brain monitors what is going on in the environment (for migratory birds) and controls breathing functions (for aquatic mammals). In this case, the neuronal oscillations in the sleepy part are synchronous, whereas the neurons in the wake part of the cerebral hemisphere oscillate asynchronously. The experimental records of EEG also shows that the electrical activities in the sleeping hemisphere have higher amplitude and lower frequency than the awake hemisphere [188]. Recent studies show that the neuronal behavior in asymmetric sleep in human patients with sleep apnea, is almost the same as uni-hemispheric sleep in animals [189].

Chimera-like state is also strongly connected to various types of pathological brain diseases such as Parkinson's disease, Alzheimer's disease, autism, and schizophrenia [45]. The current theories of autism and schizophrenia emphasize that the main problem in these patients is deficits in the coordination of distributed processes result of reduced neural synchronization that involve multiple cortical areas leading to impaired specific cognitive functions [190]. Another example in this regard is Alzheimer's disease (AD), which is a chronic, progressive neurodegenerative disorder that may cause dementia, has been associated with a reduced proportion of long-distance connections. In the early stages of the disease, a decrease in the beta band synchronization appears and in the more advanced stages, the loss of gamma band synchronization found in AD [191]. Although studies in healthy elderly have shown a decrease in the synchrony of neurons

in cognitive activity (especially in the alpha band frequency spectrum) and a decrease in neuronal activity in general, in some cases, an increase instead of a decrease of synchronization is associated with pathological aging. For instance, researches have reported an increase in the delta band synchronization due to cholinergic deafferentation, and excessive parietal–temporal cortical synchrony has been observed in the preclinical stages of AD [191]. Another example of increased abnormal neural synchronization is the essential tremor (ET) or Parkinson's disease (PD), which is the most frequent movement disorder in terms of prevalence. Studies report the existence of two significant coherencies in patients with ET: first, significant coherence between muscle activity and brain areas at tremor frequency and, second, coherence between distinct brain areas at the same frequency [192]. The results of the experiments on the cells after systemic treatment with 1-methyl-4-phenyl-1,2,3,6-tetrahydropyridine (MPTP) also show that the cells fire less at passive limb movements, which suggests a relationship between excessive beta oscillations and reduced specificity for movements [193].

There is also some relation between chimera state collapses and epileptic seizures [194]. Electrocorticography (ECoG) data from patients with intractable focal epilepsy demonstrate that before the start of seizures, the onset channels are asynchronous, while the other channels are synchronous. By starting the seizures, the non-onset channels become more asynchronous. At the end of the seizure, this synchrony can be observed that might facilitate termination. Delay differential analysis (DDA) of these ECoG data suggests the hypothesis that the asynchrony–synchrony transition, which leads to epileptic seizures, can be explained by the induction and dynamics of chimera states. The analysis results, in some cases, also show that the brain stays in the chimera state for up to 2 h prior to a seizure. Therefore, this feature can be used as a long-term seizure forecasting in some patients [195]. More generally, changes in synchronization can be said to be a promising feature for seizure prediction [194]. Epilepsy has different types. Sometimes it affects the frontal lobe area, sometimes the temporal lobe, and in more advanced cases of the disease, the enhanced synchronization extends to more areas. These remarkable observations suggest that epilepsy may have an anatomical basis rooted in the symmetry of the brain network [196].

Most of the neuronal networks' studies show that the chimera state occurs due to chemical synapses, but there is also some evidence that the electric synapse current can also evoke chimeras [84]. One particular pattern of the chimera state that plays an important role in the brain functions is "mixed oscillatory state" (MOS), in which asynchronous neurons are distributed uniformly among the stable stationary groups of neurons [197]. Two kinds of chimera-like states can be produced in neuronal networks due to interactions among different cortical areas: spiking chimera-like state (SC) with desynchronized spikes, and bursting chimera-like state (BC) with desynchronized bursts [198]. One of the special types of chimera states is coherence-resonance chimera (CR chimera) that is characterized by periodic switching of the position of the coherent and incoherent parts. The interesting point of this kind of chimera it that CR chimera appears only when the noise intensity belongs to a certain space. If the amount of noise is higher or lower than that value, there is no oscillation, or the system becomes completely desynchronized [199,200]. The chimera state can be used for the classification of external stimulus in order to consider a threshold value for the pulse amplitude. If the amplitude of the input signals is above that threshold, they are classified as the first type, whereas pulses whose amplitude is below the threshold, are classified as the second type. Survey results also show that the inhibitory coupling decreases the range of uncertainty in the stimulus amplitude classification [51].

Very recently, Bansal et al. [201] performed an empirical study on the brain network by considering 76 brain regions (nodes). They turned their attention to understand how brain structure influences the dynamical patterns produced by stimulation. Thus, instead of analyzing the recorded brain signals and examining their correlations, they considered nine different cognitive systems for the brain and assigned each part of the network into one of them. The intended systems can be divided into three parts as follows: (1) sensory motor-related systems, including auditory (Aud), visual (V), motor and somatosensory (MS), ventral temporal association (VT) systems that are knowledge-related areas. (2) systems with functional roles, including attention (Att), medial default mode (mDm), cingulo-opercular (CP), and frontoparietal (FP) systems. (3) subcortical system that is related to autonomic and primal functions. For supporting a generalized class of cognitive functions, each of these nine cognitive systems consists of the coactivated regions. Then, they presented a "cognitive chimera states", which cognitively informed a framework to study how large-scale brain structure influences brain dynamics and functions. The results show that due to the correlation of the brain functions and cognitive systems, the contributions to the three states (coherent, chimera, and metastable) are different from one cognitive system to another. The coherent states are mainly from the nodes' stimulation within subcortical and medial default mode systems. Frontoparietal, cingulo-opercular, ventral temporal association, and auditory systems contribute substantially to metastable states. The interesting point is that all nine systems produce chimera states. It means that chimera states have a higher possibility of being observed than either coherent or metastable states. It is also noteworthy that the regions of coherent states, which enable integrated neural processing, are mostly in the middle of the brain. While almost all the entire regions of metastable states, which enable segregated neural processing, are distributed in the surrounding areas. However, the regions of chimera states are relatively uniformly distributed within the brain space. Huo et al. [196] also studied the collective behavior of the brain network, which emerges from the interaction of neuronal population on real data of the human cortex. For better understanding the structure–dynamics relationship, they analyzed the data from both global and local regions and observed that the chimera state appears on both global and local levels.

3. The mathematics of chimeras

This chapter attempts to review some notions in the mathematical analysis of complex chimera phenomenon in networks of spatially extended coupled oscillators. The chapter is organized into two sections. In the first subsection, for a system of spatially extended coupled oscillators, we describe a general stability analysis, the formulation of the continuum limit equation, and its simplification using the Ott–Antonsen manifold reduction technique. Moreover, the stability analysis of chimera states in some different network topologies is discussed. Next, with the aim of quantifying chimera state characteristics, some quantitative measures like the Strength of incoherence, Discontinuity measure, Order parameters, … are introduced in the second subsection.

3.1. Stability analysis of phase oscillators

In this subsection, first, we deliberate the mathematic and stability analysis behind the chimera states in a universal spatially extended oscillator system using Continuum limit and Ott–Antonsen attitude. Following this, we review the stability analysis of chimera states for specific networks including ring network, two-population network, heterogeneous network, and small network.

3.1.1. Continuum limit and the Ott–Antonsen approach

In this part, we explain the continuum limit approach when and suppose there is a probability density function that characterizes the state of the system. To do this, first, we consider a generalization of Eq. (1) that can be in the form of the following stochastic ODE equations [202]

$$\begin{aligned}\frac{d\theta_k}{dt} &= \omega_k - \frac{1}{N}\sum_{j=1}^{N} g(x_k, x_j) f\big(\theta_k(t) - \theta_j(t)\big) \\ &\quad + \xi_k(t),\ \ k = 1, \ldots, N\end{aligned} \tag{36}$$

where ω_k are independently and randomly selected from the distribution $h(\omega)$ defined as

$$h(\omega) = \lim_{N\to\infty} \frac{1}{N}\sum_{k=1}^{N} \delta(\omega - \omega_k). \tag{37}$$

Since $h(\omega)$ is probability measures on $\mathbb{R}$, it satisfies the following condition

$$\int_{-\infty}^{+\infty} h(\omega) d\omega = 1. \tag{38}$$

In this generalized equation, f is a periodic function with a period of 2π, and $\xi_k(t)$ is an uncorrelated Gaussian noise with the following condition

$$\begin{aligned}\langle \xi_k(t)\rangle &= 0, \\ \langle \xi_k(t)\xi_j(t')\rangle &= 2v\delta_{j,k}\delta(t - t').\end{aligned} \tag{39}$$

The coupling function is $g : D \times D \to \mathbb{R}$ and x_k are uniformly distributed in a bounded domain D defined as

$$d(x) = \lim_{N\to\infty} \frac{1}{N}\sum_{k=1}^{N} \delta(x - x_k) = |D|^{-1}, \tag{40}$$

where $d(x)$ satisfies the normalization condition on D

$$\int_D d(x) dx = 1. \tag{41}$$

In the mean-field reduction approach, when $N \to \infty$, instead of individual θ_k, we look for their probability distribution $p(\theta, \omega, x, t)$ as an empirical measure. $p(\theta, \omega, x, t)$ gives the relative number of oscillators with $\theta_k = \theta$, $\omega_k = \omega$, and $x_k = x$ for the time t.

$$p_N(\theta, \omega, x, t) = \frac{1}{N}\sum_{k=1}^{N} \delta(\omega - \omega_k)\delta(x - x_k)\delta(\theta - \theta_k(t)) \tag{42}$$

tends to the solution of the Fokker–Planck equation

$$\frac{\partial p}{\partial t} + \frac{\partial}{\partial \theta}(p\Big[\omega + \int_D dx' \int_{-\infty}^{+\infty} d\omega' \int_0^{2\pi} g(x,x') \times f(\theta'-\theta)p(\theta',\omega',x',t)d\theta'\Big]) = v\frac{\partial^2 p}{\partial \theta^2}. \tag{43}$$

Specifically, when $v = 0$, Eq. (43) describes the dynamics of Eq. (36) in the absence of noise. Since the solution in the noiseless case of Eq. (43) is hyperbolic type, it is irregular and potentially can have some singularities and discontinuities. However, in the presence of noise $v \neq 0$, the solution is parabolic and is more regular.

Usually, to find the solutions to Eq. (43), their Fourier series representation are used as

$$p(\theta,\omega,x,t) = \frac{h(\omega)d(x)}{2\pi}\Big(1 + \sum_{n=1}^{\infty}[\bar{u_n}(\omega,x,t)e^{in\theta} + u_n(\omega,x,t)e^{-in\theta}]\Big). \tag{44}$$

Here, u_n and $\bar{u_n}$ are n-th Fourier coefficient and its complex conjugate, respectively. The Fourier coefficients are obtained by

$$u_n(\omega,x,t) = \int_0^{2\pi} \frac{p(\theta,\omega,x,t)}{h(\omega)d(x)} e^{in\theta} d\theta. \tag{45}$$

In this definition, $u_n(\omega,x,t)$ is a local order parameter and depends on ω and x that can quantify the correlation between oscillators' behavior with the approximately equal ω_k, and x_k. Although u_n is dimensionally infinite and then complicated, in the noiseless case of Eq. (43) with individually selecting function f, the most straight forward analysis will be achieved. To do this if $v = 0$ and, $f(\theta) = \sin(\theta - \alpha)$, the simplification can be done by the help of Ott and Antonsen's discovery of the invariant manifold reduction method [203,204]. Since using this method, the solutions of Eq. (44) reach the invariant manifold; the method is beneficial when the steady-state dynamics of the system is more critical than the transient dynamics.

In this method, it is supposed that with considering $u_n(\omega,x,t) = u^n(\omega,x,t)$ to Eq. (44), the solution will be the solution of Eq. (43) in the absence of noise; where $u : \mathbb{R} \times D \times \mathbb{R} \to \mathbb{C}$ is the solution of the following equation

$$\begin{aligned} \frac{du}{dt} &= i\omega u(\omega,x,t) + \frac{1}{2}e^{-i\alpha}\mathcal{F}u \\ &\quad - \frac{1}{2}e^{i\alpha}u^2(\omega,x,t)\mathcal{F}\bar{u}, \\ \mathcal{F}u(x,t) &:= \int_{-\infty}^{+\infty} d\omega \int_D h(\omega)d(y)g(x,y)u(\omega,y,t)dy, \\ \text{and, } |u(\omega,x,t)| &\leq 1. \end{aligned} \tag{46}$$

More importantly, Eq. (46) potentially can reveal all chimera states existing in Eq. (36). When $\mathcal{F}$ is a bounded operator on $L^\infty(\mathbb{R} \times D; \mathbb{C})$, for $U = \{u \in L^\infty(\mathbb{R} \times D; \mathbb{C}) \ : \ |u| \leq 1\}$, if $u(.,0) \in U$, then $u(.,t) \in U$.

Using the local order parameter, the flow-invariant coherent and incoherent regions can be distinguished as

$$S_{coh}(u,t) = \{(\omega,x) \in \mathbb{R} \times D \ : \ |u(\omega,x,t)| = 1\},$$

and

$$S_{incoh}(u,t) = \{(\omega,x) \in \mathbb{R} \times D \ : \ |u(\omega,x,t)| < 1\}.$$

If we calculate the conditional probability density $P_u(\theta)$, which is a distribution of oscillators' phases in the system with $\omega_k = \omega$, and $x_k = x$, for the incoherent region we obtain

$$P_u(\theta) = \frac{p(\theta,\omega,x,t)}{h(\omega)d(x)} := \frac{1}{2\pi}\frac{1-|u|^2}{1-2|u|\cos(\theta - \arg u) + |u|^2}.$$

This is the Poisson distribution with the center positioning on $\arg u$ and the distribution width and degree of non-uniformity characterized by $|u|$. For the coherent region, the distribution is a delta function centering on $\arg u$ (see Fig. 24). This implies that in the coherent region with $|u| = 1$, the oscillators are phase-locked, $P_u(\theta) = \delta(\theta - \arg u)$.

With considering a system of identical oscillators in the noiseless case $v = 0$, and $h(\omega) = \delta(\omega)$, Eq. (46) will be meaningful only for $\omega = 0$. Therefore, the equation can be rewritten to a new version with $z(x,t) = u(0,x,t)$

$$\frac{dz}{dt} = \frac{1}{2}e^{-i\alpha}\mathcal{F}_0 z - \frac{1}{2}e^{i\alpha}z^2(x,t)\mathcal{F}_0\bar{z},$$

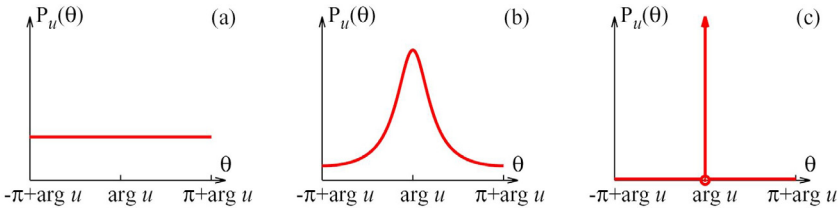

Fig. 24. The Poisson distribution for coherent, and incoherent regions, (a) $|u| = 0$, (b) $0 < |u| < 1$, (c) $|u| = 1$.
Source: Figure reproduced with permission from [202].

$$\mathcal{F}_0 z(x,t) := \int_D d(y)g(x,y)z(y,t)dy, \tag{47}$$

and for the coherent region with $|z(x,t)| = 1$, which can be presented in the form of $z(x,t) = e^{i\Theta(x,t)}$, and $\Theta : D \times \mathbb{R} \to \mathbb{R}$, Eq. (47) is equivalent to Eq. (48). This equation is an integral representation of Eq. (36) for the identical oscillator in the noiseless case

$$\frac{\partial \Theta}{\partial t} = \int_D d(y)g(x,y)\sin\big(\Theta(y,t) - \Theta(x,t) - \alpha\big)dy. \tag{48}$$

3.1.1.1. Chimera states in CGLE model (Eq. (1)). In model Eq. (1), for the identical oscillators $h(\omega) = \delta(\omega)$, distributed in the form of $x_k = -\pi + 2k\pi/N$, in the domain $D = [-\pi, \pi]$, the dynamics on the Ott–Antonsen manifold is obtained as

$$\begin{aligned} \frac{dz}{dt} &= \frac{1}{2}e^{-i\alpha}\mathcal{G}z - \frac{1}{2}e^{i\alpha}z^2(x,t)\mathcal{G}\bar{z}, \\ \mathcal{G}(\varphi)(x) &:= \int_{-\pi}^{+\pi} G_{1D}(x-y)\varphi(y)dy, \end{aligned} \tag{49}$$

where $g(x,y) = 2\pi G_{1D}(x-y)$, and G_{1D} is the coupling function defined in Eq. (1). Finding the solutions of Eq. (49) can determine the probability density $p(\theta, 0, x, t)$ of the Eq. (44).

The linearized form of Eq. (49) around the completely incoherent state $z(x,t) = 0$ is

$$\frac{dz}{dt} = \frac{1}{2}e^{-i\alpha}\mathcal{G}z. \tag{50}$$

Here, if the integral operator has a spectrum on the imaginary axis, the critical spectrum σ_{cr}, the solution of the linearized equation can bifurcate from a completely incoherent state. It is determined that the nonzero critical spectrum for $\alpha = +\frac{\pi}{2}$, and $\alpha = -\frac{\pi}{2}$ is: $\sigma_{cr} = \bigcup_{k=1}^{\infty}\{\pm i\pi g_k\}$, where the g_k are the coefficients of Fourier series of the even coupling function G_{1D} defined as

$$g_k = \frac{1}{2\pi}\int_{-\pi}^{+\pi} G_{1D}(x)\cos(kx)dx. \tag{51}$$

With considering

$$z(x,t) = ae^{i(kx+\Omega t)}, \tag{52}$$

in Eq. (49), a new equation will be obtained as

$$i\Omega = \pi g_k e^{-i\alpha} - \pi g_k a^2 e^{i\alpha}, \tag{53}$$

whose solutions for each $k \in Z$ are

$$\Omega = \begin{cases} -2\pi g_k \sin\alpha, & \text{for } a = 1, \text{ and } \alpha \in \mathbb{R} \\ -\pi g_k(1+a^2)\sin\alpha, & \text{for } a > 0, \text{ and } \alpha = \pm\frac{\pi}{2}. \end{cases} \tag{54}$$

In this analysis, the bifurcation points of solution branches from zero, completely incoherent, are the points ($a = 0$, $\alpha = \pm\pi/2$, $\Omega = \mp\pi g_k$). Furthermore, the points ($a = 1$, $\alpha = \pm\frac{\pi}{2}$, $\Omega = \mp 2\pi g_k$) that undergo complex fold bifurcation are vital in the emergence of chimera states.

It is noteworthy that rather than emerging chimera state on branches bifurcating from zero, chimera states may emerge on the higher-order branches. For instance, for $g_0 \neq 0$ with $k = 0$, and $a \in (0, 1)$, secondary branches are bifurcating from the solutions of Eq. (52) that by performing continuation of them, chimera states can be found [205].

The complex fold bifurcation for $u \in \mathbb{C}$, and $p \in \mathbb{R}$ is defined as $u^2 = p$. Therefore, for Eq. (53) around the points ($a = 1$, $\alpha = \pm\frac{pi}{2}$, $\Omega = \mp 2\pi g_k$), the following transformation can be done

$$u = \left(ae^{i\alpha} + \frac{i\Omega}{2\pi g_k a}\right)\left(1 \mp \frac{\Omega}{2\pi g_k a}\right)^{-1/2}, \quad p = 1 \pm \frac{\Omega}{2\pi g_k a}. \tag{55}$$

The completely coherent state is the solution of this equation for $k = 0$.

It is essential to mention that due to the symmetry of Eq. (49), it has other solutions that bifurcate from zero. Also, it has rotating wave solutions as

$$z(x,t) = a(x)e^{i\Omega t}, \tag{56}$$

where $\Omega \in R$, and $a \in C_{per}([-\pi,\pi];\mathbb{C})$, that C_{per} is a space of complex-valued and periodic function on $[-\pi,\pi]$. The stable rotating waves that satisfy $|z(x,t)| \leq 1$, are given by

$$z(x,t) = H(|w(x)|^2)w(x)e^{i\Omega t}, \tag{57}$$

where

$$H := \begin{cases} \frac{1-\sqrt{1-s}}{s} = \frac{1}{1+\sqrt{1-s}} & \text{for } 0 \leq s < 1 \\ \frac{1-i\sqrt{s-1}}{s} = \frac{1}{1+i\sqrt{s-1}} & \text{for } s \geq 1, \end{cases}$$

and $\omega(x)$, α, and Ω satisfy a self-consistency equation as

$$i\Omega e^{i\alpha}w(x) = \mu w(x) = \int_{-\pi}^{+\pi} G_{1D}H(|w(y)|^2)w(y)dy. \tag{58}$$

After computing the solution branches $(\mu, w(x))$ of Eq. (58), these can be transformed into solutions of Eq. (49).

To analyze the stability of rotating waves (Eq. (57)), Eq. (49) should be linearized concerning the small perturbation. To do this the ansatz, $z(x,t) = (a(x)e^{i\beta} + v(x,t))e^{i\Omega t}$ is considered in Eq. (49) that results in this equation

$$\frac{dv}{dt} = -\Omega\eta(|w(x)|^2)v + \frac{1}{2}e^{-i\alpha}(\mathcal{G}v + a^2(x)\mathcal{G}\bar{v}), \tag{59}$$

where $v(x,t)$ is perturbation and $\eta(s)$ is

$$\eta(s) = \begin{cases} i\sqrt{1-s} & \text{for } 0 \leq s < 1 \\ -\sqrt{s-1} & \text{for } s \geq 1. \end{cases} \tag{60}$$

The equivalent form of Eq. (59) is

$$\frac{dv}{dt} = \mathcal{L}v \text{ where } \mathcal{L} := \mathcal{M} + \mathcal{K}, \tag{61}$$

that $\mathcal{M}$ is a multiplication operator as

$$(\mathcal{M}\mathbf{v})(x) := \mathbf{M}(x)\mathbf{v} \text{ with } \mathbf{M}(x) = -\Omega\eta(|w(x)|^2), \tag{62}$$

and $\mathcal{K}$ is an integral operator as

$$\mathcal{K}(\varphi)(x) = \int_{-\pi}^{+\pi} \mathbf{K}(x,y)\varphi(y)dy, \tag{63}$$

and $\mathbf{K}(x,y)$ is the matrix kernel defined by: $\mathbf{K}(x,y) = \frac{1}{2}\mathbf{QP}(x)G(x-y)$. Here $\mathbf{Q}$, and $\mathbf{P}$ are determined by

$$\mathbf{P} = \begin{pmatrix} \mathrm{Re}(1+(e^{-i\beta}a(x))^2) & -\mathrm{Im}(1-(e^{-i\beta}a(x))^2) \\ \mathrm{Im}(1+(e^{-i\beta}a(x))^2) & \mathrm{Re}(1-(e^{-i\beta}a(x))^2) \end{pmatrix},$$

and

$$\mathbf{Q} = \begin{pmatrix} \sin\beta & \cos\beta \\ -\cos\beta & \sin\beta \end{pmatrix}.$$

The operator $\mathcal{L}$ is a linear operator, and its spectrum consists of the essential spectrum σ_{ess} and point spectrum σ_{pt}. Its essential spectrum is $\sigma_{ess}(\mathcal{L}) = \{-\Omega\eta(|w(x)|^2) \ : \ x \in [-\pi,\pi]\} \cup \{c.c.\} \subset \mathbb{R} \cup i\mathbb{R}$.

A point spectrum is a finite number of eigenvalues. With considering the perturbation

$$v(x,t) = v_+(x)e^{\lambda t} + \bar{v}_-(x)e^{\bar{\lambda}t}, \tag{64}$$

as a solution to Eq. (59), it is obtained that

$$\begin{pmatrix} v_+ \\ v_- \end{pmatrix} = \frac{1}{2}\begin{pmatrix} e^{-i\alpha(\lambda+\Omega\eta(|w|^2))^{-1}(\mathcal{G}v_+ + a^2\mathcal{G}v_-)} \\ e^{i\alpha(\lambda+\Omega\overline{\eta(|w|^2)})^{-1}(\mathcal{G}v_- + \bar{a}^2\mathcal{G}v_+)} \end{pmatrix}. \tag{65}$$

Eq. (65) should be solved numerically, especially in the case of having a first-rank integral operator G, it can be solved as a nonlinear finite-dimensional eigenvalue problem. Generally, the obtained eigenvalues will be real or complex conjugate pairs. Fig. 25a shows the possible spectrum for a chimera solution of Eq. (57). The spectrum has two parts; a solid curve which shows the essential spectrum σ_{ess}, and the dots that are eigenvalues representing point spectrum σ_{pt}. Since the real parts of eigenvalues are non-positive, the spectrum corresponds to a stable chimera-like solution.

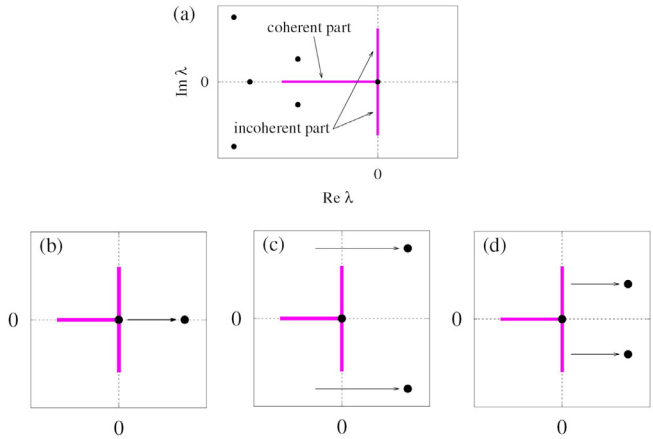

Fig. 25. (a) The schematic of spectrum of a stable chimera-like solution of Eq. (57). The essential and point spectrum is depicted by the solid lines and dots, respectively. The interval along real and imaginary axis corresponds to the coherent and incoherent parts, respectively. (b-d) Destabilization scenarios: (b) Symmetry breaking (c) Hopf bifurcation, (d) Non-standard Hopf bifurcation. In contrast to other scenarios, in non-standard Hopf bifurcation, unstable eigenvalues do not emerge from the neutrally stable essential spectrum.
Source: Figure reproduced with permission from [202].

The real part of eigenvalues determines whether they are stable or not, i.e., when the real parts of λ are negative, they are stable, and when the real part is positive, they are unstable. Therefore, there are three possible scenarios for a chimera state to destabilize: symmetry breaking, Hopf bifurcation, or non-standard Hopf bifurcation. Fig. 25b-d shows these three scenarios. Because of continuous symmetry, the essential spectrum consists of zero eigenvalues.

3.1.2. Stability of chimeras

Below, we reconsider different networks of coupled phase oscillators that Ott–Antonsen ansatz is applied to reduce the partial differential equation number. In these studies, the bifurcation analysis is done on the steady states that provide stability information for chimera states.

3.1.2.1. Ring of oscillators. After the discovery of chimera, Abrams et al. [29] presented an exact solution and stability analysis for chimera state in a ring of oscillators (Eq. (1)) coupled via a cosine kernel (Eq. (5)) that makes the model analytically solvable. They found a close-form and stationary solution (where parameters depend on space only) for the self-consistency equation of the complex order parameter (Eq. (66))

$$\begin{aligned} R(x)\exp[i\Theta(x)] &= e^{i\beta}\int_{-\pi}^{+\pi} G(x-x')\exp[i\Theta(x')] \\ &\quad\times \frac{\Delta-\sqrt{\Delta^2-R^2(x')}}{R(x')}dx' \\ &= c + a\cos x, \end{aligned} \tag{66}$$

where $\beta = \pi/2 - \alpha$, $\Delta = \omega - \Omega$, and Ω is the angular frequency of the rotating frame. Their solution way was finding real and imaginary parts of c, a, and Δ (Eq. (67)), which can be followed in [29]. For $\epsilon \to 0$, and $\beta = \beta_1\epsilon$,

$$\begin{aligned} \Delta &\sim 1 + \Delta_1\epsilon + \Delta_2\epsilon^2, \\ c &\sim 1 + c_1\epsilon + c_2\epsilon^2, \\ a_r &\sim a_{2r}\epsilon^2, \\ a_i &\sim a_{2i}\epsilon^2. \end{aligned} \tag{67}$$

Their approach provides valuable information about the chimera state [29]. Fig. 26 left panel shows the fraction of drifting oscillators $f_{drift} = \frac{1}{\pi}\cos^{-1}\frac{\delta}{u(\delta)}$ as a function of β_1, where

$$u = a_{2r} = -\mathrm{Re}\left[\sqrt{2}\left\langle\cos x\sqrt{\delta - u\cos x}\right\rangle\right], \tag{68}$$

with $\delta = \Delta_2 - c_2$. The figure indicates the solutions as two branches. The upper branch is stable, and bifurcates from a pure drifting state with $\beta_1 = 0$. By increasing the control parameter, drifting oscillators alter to a locked group. The minimum fraction of drifting is about 44% that corresponds to a stable chimera state. This occurs at the largest value of the control parameter β_1, and this is a point that the upper and lower branches of solutions colloid. The lower branch is an unstable solution that appears at $\beta_1 = 0$ from a homoclinic lock state.

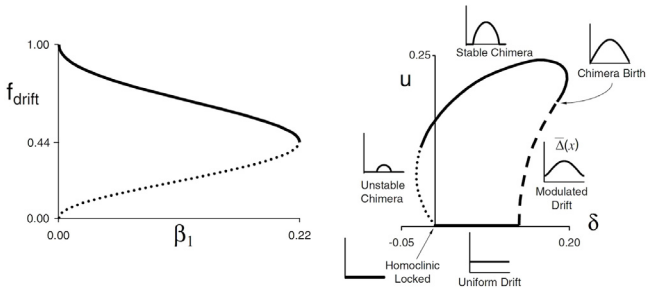

Fig. 26. Left panel: The fraction of oscillators f_{drift} as a function of control parameter β_1. The solid and dotted lines indicate stable and unstable chimera state, respectively. Right panel: Display of u as a function of δ. Different dash styles indicate a different state. The shape of the corresponding $\bar{\Delta}(x)$ vs. x for each state is plotted in the inset panels.
Source: Figure reproduced with permission from [29].

In Fig. 26 right panel, there is a complete representation of results that is a plotting of $u(\delta)$ as a function of the relevant parameter δ. Although in this case δ cannot be considered as a valid control parameter to signify bifurcations, it helps to present some significant events that were not possible in Fig. 26 left panel, e.g., two critical events in the genesis of chimera states happen in the $f_{drift} = 0$, $\beta_1 = 0$ point that will be seen as a single point in Fig. 26 left panel. In Fig. 26 right panel, different states are indicated with different dashing styles of the branches. The solid zero branches along the horizontal axis represents a group of spatially uniform drift states. More than uniform drift states, modulated drift states appear just with $\beta = 0$. This is the first crucial event occurring at $\delta = \frac{1}{8}$, where in this point a spatially drift state emerges. In this case, for states that are on the dashed branches all oscillators are drifting with the same average phase and different amounts of coherence based on the values of x. The stable chimera state is created when the first locked oscillators emerge. This occurs at the intersection of the dashed branch with the line $u = \delta \approx 0.18$. Furthermore, in Fig. 26 right panel, the time averaged frequency $\bar{\Delta}(x)$ as a function of x is plotted too. For locked oscillators, the time-averaged frequency is equal to zero, and for drifting oscillators, it is equivalent to $\epsilon\sqrt{\delta - u\cos x}$, to leading order in ϵ. Hence, $\bar{\Delta}(x)$ for the homoclinic locked state is zero, for uniform drift states is a fixed line, for modulated drift states is positively modulated, and for chimera states contains both zero and nonzero parts. Totally, one can conclude that the time-averaged frequency is decreased when circulating back toward the origin.

A comprehensive analysis of the infinite-dimensional nonlinear eigenvalue problem (NEVP) corresponding to standing wave solutions was further presented by Omelchenko et al. [205]. They indicated that every nonzero harmonic in the Fourier series of G function leads to solution curves as primary and secondary branches that bifurcate from a trivial solution. Each branch can be interpreted as a phased-lock solution or coherence–incoherence pattern. In their study, they presented the continuum limit equation form of Eq. (1) as

$$\begin{aligned} &\tfrac{\partial f}{\partial t} + \tfrac{\partial}{\partial t}(fJ) = 0, \\ &J(\theta, x, t) = \omega + \mathrm{Im}\left(Z(x,t)e^{-i(\theta+\alpha)}\right). \end{aligned} \tag{69}$$

Then using Ott–Antonsen invariant manifold method by supposing that $z(x,t)$ is a solution of the equation

$$\frac{dz}{dt} = i\omega z(x,t) + \frac{1}{2}e^{-i\alpha}\mathcal{G}z - \frac{1}{2}e^{i\alpha}z^2(x,t)\mathcal{G}\bar{z}, \tag{70}$$

the solution of the continuum limit equation (Eq. (69)) is obtained as

$$f(\theta, x, t) = \frac{1}{2\pi}\left(1 + \sum_{n=1}^{\infty}[\bar{z}^n(x,t)e^{in\theta} + z^n(x,t)e^{in\theta}]\right). \tag{71}$$

Furthermore, they reached nonlinear eigenvalue problems (NEVP), the same as Eq. (58), where

$$\mu := (\omega - \Omega)e^{-i\beta} = (\omega - \Omega)e^{-i(\pi/2-\alpha)}, \tag{72}$$

$$w(x) := (\omega - \Omega)^{-1}(\mathcal{G}a)(x). \tag{73}$$

It should be mentioned that every solution (μ, w) of NEVP corresponds to a solution of Eq. (70) (with Eq. (56) as ansatz).

Nonlinear eigenvalue problem Eq. (58) can be rewritten in the form of

$$\mathcal{F}(\mu, w) := \mu w - \mathcal{G}\mathcal{H}(w) = 0, \tag{74}$$

where $\mathcal{G}$ is defined as Eq. (49), and $\mathcal{H}(\omega) = H(|w|^2)w$. Some solutions of Eq. (74) are as follows

$$w(x) = pe^{ikx}, \tag{75}$$

where $k \in \mathbb{Z}$ and $p \in (0, \infty)$, and by considering Eq. (75) into Eq. (74), this is obtained

$$\mu = 2\pi g_k H(p^2), \tag{76}$$

that is equivalent to

$$\begin{aligned} p < 1 \text{ and } \mu &= \frac{2\pi g_k}{1+\sqrt{1-p^2}}, \\ p \geq 1 \text{ and } \mu &= \frac{2\pi g_k}{1-i\sqrt{p^2-1}}. \end{aligned} \tag{77}$$

In order to find the primary solution branches, Eq. (74) is linearized around the trivial solution $w = 0$, thus

$$\partial_w \mathcal{F}(\mu, 0) = \mu\mathcal{I} - \mathcal{G}\mathcal{H}'(0) = \mu\mathcal{I} - \frac{1}{2}\mathcal{G}. \tag{78}$$

The derivative in the left-hand side is invertible for $\mu = \mu_k = \pi g_k$, $k = 0, 1, \ldots$. And for each nonzero μ_k, $\ker \partial_w \mathcal{F}(\mu_k, 0) = \text{span}\,\{e^{ikx}, e^{-ikx}\}$.

Using Eq. (76), it is achieved that $2\pi g_k \mathcal{H}(0) = \mu_k$ means all solutions of Eq. (74) bifurcate from zero at critical values of $\partial_w \mathcal{F}(\mu, 0)$. In addition, it was proved that for $(\mu - \mu_k)g_k > 0$, and for all sufficiently small $\mu - \mu_k \in R$, a non-trivial asymptotically solution of Eq. (74) is

$$w(x) = 4\sqrt{\frac{1}{3\pi g_k}(\mu - \mu_k)}\sin(kx) + O(|\mu - \mu_k|) \text{ for } \mu \to \mu_k. \tag{79}$$

Since all Fourier coefficient g_k are different and nonzero, Eq. (79) demonstrates that there is an infinite number of primary branches that bifurcate from the trivial solution and can be continued numerically. Besides, there are secondary bifurcation points that appear as a result of numerical continuation of primary branches. For $(\mu - \nu_k)C_0/C_1 > 0$, and for all sufficiently small $\mu - \nu_k \in R$, a non-trivial asymptotically solution of Eq. (74) is

$$w(y) = p_0(\nu_k)\sqrt{\frac{C_0}{C_1}(\mu - \nu_k)}\cos(kx) + O(|\mu - \nu_k|), \tag{80}$$

where for $\mu \to \nu_k$

$$\nu_k := \frac{2\pi g_0^2}{g_0 + g_k}.$$

Here it is supposed to have $g_0 \neq 0$, $\frac{g_k}{g_0} \in (0, 1]$ for some $k \geq 1$, and

$$\begin{aligned} C_0 &= 1 - 2\pi g_k c_2 p_0'(\nu_k), \\ C_1 &= \frac{1}{4}\pi g_k\left(c_3 + \frac{4\pi g_0 c_2^2}{\nu_k - 2\pi g_0 c_1} + \frac{4\pi g_{2k} c_2^2}{\nu_k - 2\pi g_{2k} c_1}\right), \end{aligned}$$

and

$$c_m := \mathcal{H}^{(m)}(p_0(\nu_k)) = \frac{d^k}{du^k}\left(\frac{u}{1+\sqrt{1-u^2}}\right)\Bigg|_{u=p_0(\nu_k)}. \tag{81}$$

There is a main difference between secondary and primary branches, i.e., just for the condition $\frac{g_k}{g_0} \in (0, 1]$, the bifurcation occurs. In other words, the emergence of secondary branches is related to both the absolute value and sign of g_k. As an example, Eq. (74) is considered with the coupling function Eq. (5). In this case, nonzero Fourier series coefficients are: $g_0 = \frac{1}{2\pi}$ and, $g_1 = g_{-1} = \frac{A}{4\pi}$.

Therefore, there exist two primary solutions bifurcating at $\mu = \mu_0$, and $\mu = \mu_1$. The secondary solution branch bifurcates at $\mu = \nu_1$ that exists only for $\frac{g_k}{g_0} \in (0, 1]$ or equivalently $A \in (0, 2)$. The solution for $A = 0.9$ is displayed in Fig. 27. In this figure, the thick black line is a branch of a spatially uniform solution; the thick blue line is the second primary solution, and the thick red line is the secondary solution. The solid blue line denotes a coherence–incoherence pattern with two coherent regimes, and the solid red line denotes a coherence–incoherence pattern with one coherent regime. Thin lines are the projection of thick lines in the plane $|w(x)| = 0$. In the figure, the right panel shows $|w(x)|$ for each solution, before and after bending bifurcation point. In this panel $|w(x)| \geq 1$ indicates coherent regions and $|w(x)| < 1$ indicates incoherent regions.

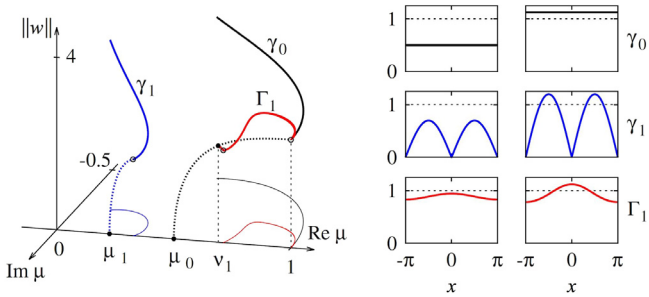

Fig. 27. The solution of Eq. (74) for cosine coupling function with $A = 0.9$. The left panel displays primary branches with solid black and blue lines and a secondary branch with a solid red line. The right panel is $|w(x)|$ before and after empty circles (bending bifurcation point).
Source: Figure reproduced with permission from [205].

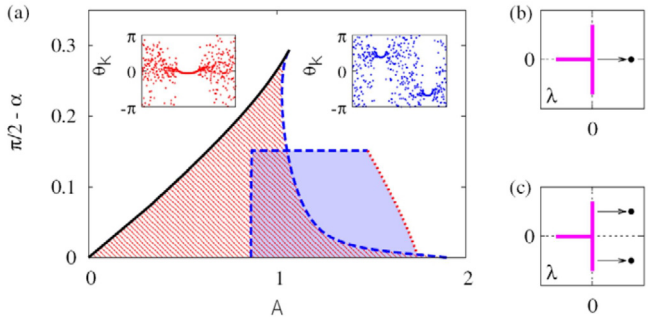

Fig. 28. (a) The bifurcation diagram of the solutions of Fig. 27. The shaded and hatched regions represent the stability regions of the primary and secondary solutions, respectively. The solid line shows the fold bifurcation and the red and blue lines correspond to the appearance of single real eigenvalue (b) and pair of complex conjugate eigenvalues (c) from the essential spectrum.
Source: Figure reproduced with permission from [205].

The bifurcation diagram for solution branches of Eq. (74), corresponding to Fig. 27, for two different patterns, is shown in Fig. 28. One of the solutions (blue pattern) is stable in the blue region, and another (red pattern) is stable in the hatched region. The black line indicates fold bifurcation; the red line corresponds to the case of single real eigenvalue emerging from the essential spectrum, and the blue line corresponds to the case where a pair of complex conjugate eigenvalues emerges from the essential spectrum.

3.1.2.2. Network with two populations. The chimera states arise from a completely symmetric partially synchronized state of the Kuramoto model within a symmetry-breaking pitchfork bifurcation [206]. To show this, a network of two clusters is considered as

$$\dot{\theta}_i^\sigma = \omega_i^\sigma - \sum_{\sigma'=1}^{2} \frac{K_{\sigma\sigma'}}{N_{\sigma'}} \sum_{j=1}^{N_{\sigma'}} \sin(\theta_i^\sigma - \theta_j^{\sigma'} + \alpha). \tag{82}$$

Here, $\sigma \in \{1, 2\}$ identifies the clusters, ω_i^σ are selected from $g(\omega)$, and N_σ is the number of oscillators in cluster σ. $K_{\sigma\sigma'}$ is the coupling strength with $K_{11} = K_{22} = \mu > K_{12} = K_{21} = \nu > 0$, where $\mu + \nu = 1$, and $\mu - \nu = A$ are considered.

The Ott–Antonsen ansatz is used as

$$f^\sigma(\theta, t; \omega) = \frac{g(\omega)}{2\pi}\left(1 + \left(\sum_{n=1}^{\infty}(a_\sigma(\omega, t)e^{i\theta})^n + \text{c.c.}\right)\right), \tag{83}$$

where f is the probability density function, $g(\omega)$ is a Lorentzian distribution with scale parameter D and mean zero as $\pi g(\omega) = \frac{D}{D^2+\omega^2}$, and c.c. stands for complex conjugate. Therefore, the corresponding continuity equation is written in

$$\frac{\partial a_\sigma}{\partial t} + i\omega a_\sigma + \frac{1}{2}\sum_{\sigma'=1}^{2} K_{\sigma\sigma'}(z_{\sigma'} a_\sigma^2 e^{-i\alpha} - \bar{z}_{\sigma'} e^{i\alpha}) = 0, \tag{84}$$

where $z_\sigma(t) = \int_{-\infty}^{+\infty} g(\omega)\bar{a}_\sigma(\omega, t)d\omega = \bar{a}_\sigma(-iD, t)$. As a result, Eq. (84) is a two-dimensional complex ODEs describing the order parameter of the clusters. By rewriting Eq. (84) in polar coordinates, with $z_1 = r_1 e^{i\varphi_1}$, $z_2 = r_2 e^{i\varphi_2}$, and $\varphi = \varphi_1 - \varphi_2$,

the three-dimensional real ODEs are obtained as

$$\begin{aligned}\dot{\phi} &= \left(\frac{1+r_1^2}{2r_1}\right)[\mu r_1 \sin\alpha - \nu r_2 \sin(\phi-\alpha)],\\ &\quad - \left(\frac{1+r_2^2}{2r_2}\right)[\mu r_2 \sin\alpha + \nu r_1 \sin(\phi+\alpha)],\\ \dot{r_1} &= -Dr_1 + \left(\frac{1-r_1^2}{2}\right)[\mu r_1 \cos\alpha + \nu r_2 \cos(\phi-\alpha)],\\ \dot{r_2} &= -Dr_2 + \left(\frac{1-r_2^2}{2}\right)[\mu r_2 \cos\alpha + \nu r_1 \cos(\phi+\alpha)].\end{aligned} \tag{85}$$

The bifurcation analysis is done with considering $\mu = \frac{1+A}{2}$, $\nu = \frac{1-A}{2}$, and $\beta = \pi/2 - \alpha$. In the study [29], by selecting $D = 0$, it was revealed that the chimera state disappears through a saddle–node bifurcation. Now, the problem is to find the connection between the fully synchronized state and stable chimera state. Plotting the bifurcation diagram of A vs. β shows that in contrast to the case $D = 0$, for $D > 0$ a pitchfork bifurcation is obtained and the saddle–node bifurcation does not reach the origin. If the bifurcation is plotted with fixed A, the pitchfork bifurcation is balloon-like where inside of the balloon is a region of stable chimera state. The region between saddle–node bifurcation and pitchfork bifurcation is the bistability region.

From Fig. 29, it is obtained that for $D = 0$, the bifurcation type is just saddle–node. With increasing D from 0, the heterogeneity among the natural frequency of oscillators increases, which results in decreasing in the order parameter of spatially symmetric synchronous states. Moreover, as D increases ($D = 0.003$), the horizontal line alters, and a new intersection with saddle–node branch shifts to supercritical and subcritical pitchfork bifurcations. When D increases to $D = 0.001$, the subcritical pitchfork bifurcation, and saddle–nodes bifurcations collide to a supercritical pitchfork bifurcation. Therefore, it is found that the chimera states are connected to the synchronous state through a pitchfork bifurcation, a connection that was not observable in the $D = 0$ case.

Laing considered a network of two populations with uniform intra-populations and different inter-populations coupling [207]. It was assumed that in a network supporting chimera states, the oscillators in the incoherent population are in a smooth and closed curve C. For the analysis of the dynamics of the curve C, and the probability density on this curve, the Stuart–Landau oscillators are reconsidered. In [208], a network of N oscillators is considered, and the state of the jth oscillator is described by the complex variable z_j as

$$\frac{dz_j}{dt} = f(z_j, \bar{z}; K), \tag{86}$$

and the mean field $\bar{z}$ is

$$\bar{z} = \frac{1}{N}\sum_{k=1}^{N} z_k. \tag{87}$$

Moreover, K is the coupling strength between an oscillator and $\bar{z}$. It is observed that, by plotting the state of oscillators in a complex plane, the points lie on closed smooth curve C. This curve is parametrized by ϕ as the angle, and $R(\phi; t)$ is the distance from the origin, and $P(\phi; t)$ is the density at the angle ϕ. Eq. (87) with using $z_j = r_j e^i$, could be rewritten as

$$\frac{dr_j}{dt} = F(r_j, \phi_j, \bar{z}), \tag{88}$$

$$\frac{d\phi_j}{dt} = G(r_j, \phi_j, \bar{z}), \tag{89}$$

and the dynamics of R and P are determined by

$$\frac{\partial R}{\partial t}(\phi, t) = F(R, \phi, \bar{z}) - G(R, \phi, \bar{z})\frac{\partial R}{\partial \phi}, \tag{90}$$

$$\frac{\partial P}{\partial t}(\phi, t) = -\frac{\partial}{\partial \phi}[P(\phi, t)G(R, \phi, \bar{z})], \tag{91}$$

where

$$\bar{z} = \int_0^{2\pi} P(\phi, t)R(\phi, t)e^{i\phi}d\phi. \tag{92}$$

This approach is used in a network of Stuart–Landau oscillators to study the splay state in a single population of all-to-all coupling oscillators. However, it can be used to study the chimera state in a network of two populations where

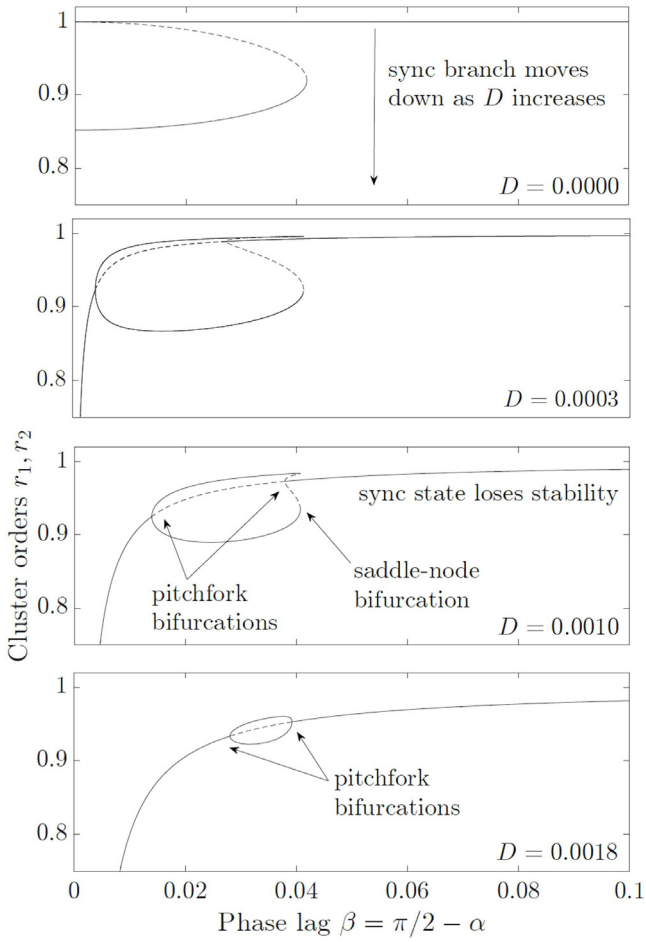

Fig. 29. Cluster order parameters (r_1, r_2) as a function of phase lag parameter (β). Stable and unstable branches are displayed with solid and dashed curves, respectively. Center branch corresponds to the symmetric extension of the synchronous state with $r_1 = r_2$. In the top panel, chimera states have $r_1 = 1, r_2 < 1$ or $r_2 = 1, r_1 < 1$, and in other panels, symmetric pairs of chimera states have $r_1 = a, r_2 = b$ and $r_1 = b, r_2 = a$.
Source: Figure reproduced with permission from [206].

one is perfectly synchronous, and the other lies on smooth closed curve C. It should be mentioned that this approach is valid if oscillators do lie on curve C that should be examined by solving the original equations.

Considering the definition mentioned above, for a network of two populations, supposing that the population one $(j = 1, \ldots, N)$ is asynchronous, and population two is completely synchronous $(j = N + 1, \ldots, 2N)$, the equations governing the dynamics are

$$\frac{\partial R}{\partial t}(\phi, t) = F(R, \phi, \bar{X}, Y) - G(R, \phi, \bar{X}, Y)\frac{\partial R}{\partial \phi}, \tag{93}$$

$$\frac{\partial P}{\partial t}(\phi, t) = -\frac{\partial}{\partial \phi}[P(\phi, t)G(R, \phi, \bar{X}, Y)] + D\frac{\partial^2}{\partial \phi^2}P(\phi, t), \tag{94}$$

$$\frac{dY}{dt} = i\omega Y + \epsilon^{-1}\{1 - (1 + \delta\epsilon i)|Y|^2\}Y + e^{-i\alpha}(\mu Y + \nu\bar{X}), \tag{95}$$

$$\bar{X} = \int_0^{2\pi} P(\phi, t)R(\phi, t)e^{i\phi}d\phi, \tag{96}$$

where $Y = X_j$ describes the identical dynamics of oscillators in the coherent population. The intra-group and inter-group couplings are assumed as $\mu = \frac{1+A}{2}$, $\nu = \frac{1-A}{2}$, respectively, and $\beta = \frac{\pi}{2}$. One of the solutions of Eqs. (93) to (96) for the

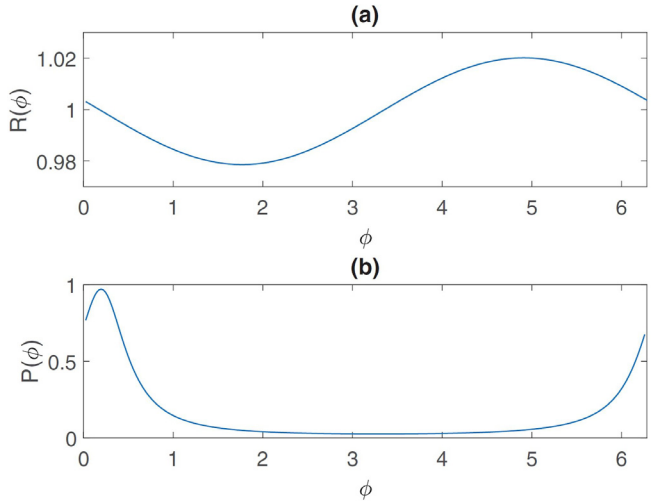

Fig. 30. The snapshot of a solution of Eqs. (93) to (96). (a) and (b) show $R(\varphi)$, $P(\varphi)$, respectively.
Source: Figure reproduced with permission from [207].

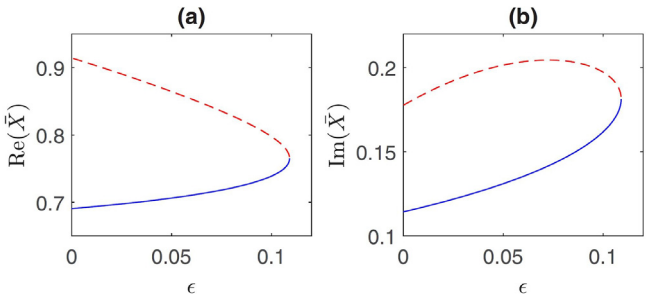

Fig. 31. (a,b) The steady-state of Eqs. (93) to (96) as a function of ϵ with unstable dashed line and stable solid line.
Source: Figure reproduced with permission from [207].

parameters $\epsilon = 0.05$, $\omega = 0$, $\delta = -0.01$, $A = 0.2$, $\beta = 0.08$, and $D = 10^{-8}$ is shown in Fig. 30. This solution is obtained by numerically integrating Eqs. (93) to (96) in time. Here, the stability in the steady-state is derived from eigenvalues of the linearization of Eqs. (93) to (96). The eigenvalues are two clusters, one cluster is around $\mathrm{Re}(\lambda_j) = -40$, and the other cluster is around $\mathrm{Re}(\lambda_j) = 0$. The first cluster is related to linearizing F with respect to R, and the second group is related to the dynamics of p, presumably. Fig. 31 shows the following of the solution in Fig. 30 by varying ϵ and using pseudo-arclength continuation.

The steady-state of Eqs. (93) to (96) can be obtained by integrating the equations in time to find a periodic solution of these equations. This steady-state as a function of ϵ is presented in Fig. 31 for parameters $\omega = 0$, $\delta = -0.01$, $A = 0.2$, $\beta = 0.08$, and $D = 10^{-8}$. For all of the points in figure, Eqs. (93) to (96) have a stable and periodic solution. Fig. 32 is obtained by following the saddle–node bifurcation in Fig. 31a,b as A varies. For $\epsilon = 0.05$, as A increases, a supercritical Hopf bifurcation appears that the oscillation created in this bifurcation is destroyed within a homoclinic bifurcation. It should be mentioned that this bifurcation is obtained by following the algebraic equations that define the bifurcation, not by direct simulation. Furthermore, this approach is not valid in the case that a completely coherent group becomes incoherent.

3.1.2.3. Heterogeneous network. The stability of chimera states in networks of identical Kuramoto oscillators has been examined in numerous studies. However, real systems can be adequately modeled with the networks having heterogeneity. Therefore, investigating the robustness of chimera states that corresponded to the network's heterogeneity is worthwhile. Laing considered several networks of heterogeneous phase oscillators [108,109]. In this part, the analytical investigation of the robustness of chimera states in a model of two coupled networks (Eq. (85)) is done concerning the heterogeneity in the natural frequencies of oscillators. The natural frequencies of oscillators are chosen from a Lorentzian distribution

$$\pi g_\sigma(\omega^\sigma) = \frac{D_\sigma}{(\omega^\sigma - \Omega_\sigma)^2 + D_\sigma^2}, \tag{97}$$

where ω_i^σ are from a distribution that is centered at Ω_σ with half-width at half maximum D_σ, and Ω_1 is set to zero.

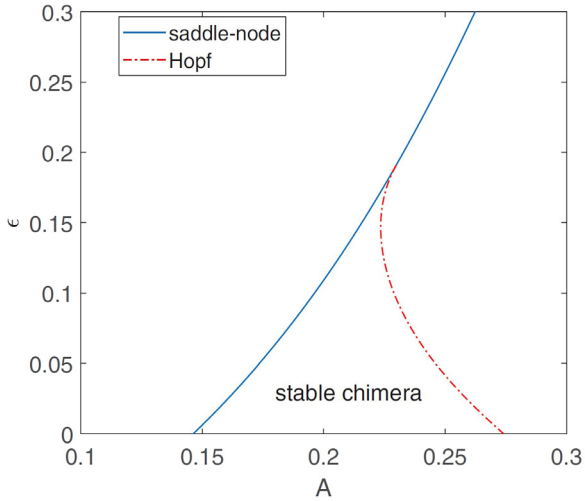

Fig. 32. The continuation of the saddle–node bifurcation in Fig. 31a,b.
Source: Figure reproduced with permission from [207].

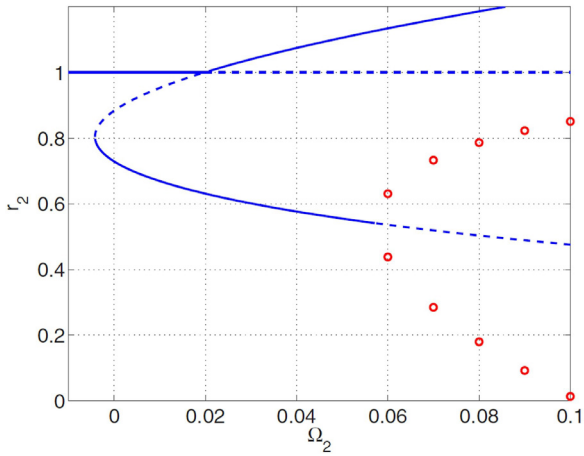

Fig. 33. The figure shows r_2 as a function of Ω_2 for $r_1 = 1$ ($r_2 > 1$ is not physically meaningful). The circles are minimum and maximum of stable periodic oscillations. The solid and dashed lines show the stable and unstable fixed points of Eq. (85). $A = 0.2$, $\beta = 0.1$. Figure reproduced with permission from [109].

The first case is varying the frequency offset Ω_2 with $D_1 = D_2 = D = 0$. It is considered that one region is wholly synchronized with $r_1 = 1$. When $\Omega_2 = 0$, then $(r_2, \phi) = (1, 0)$, which is a completely synchronized state. Fig. 33 indicates that as Ω_2 increases from zero, a state corresponding to a completely synchronized state, the $r_2 = 1$ bifurcates through a transcritical bifurcation involving saddle chimera. Further, with increasing Ω_2, the stable chimera bifurcates within a supercritical Hopf bifurcation that results in an oscillation in r_2; the minimums and maximums of stable oscillation are depicted with circles in Fig. 33. If Ω_2 decreases from zero, the stable chimera destroys soon, concluding that the stable chimera is much more robust to speeding up than slowing the asynchronous oscillators in the network.

The second case to examine is varying the distribution width $D_1 = D_2 = D$. The system described by Eq. (85) has a symmetry, i.e. $(r_1, r_2, \phi) \rightarrow (r_2, r_1, -\phi)$. For this system with $A = 0.2$, $\beta = 0.7$, and D=0, five fixed points are 1) $(r_1, r_2, \phi) = (1, 1, 0)$ as the perfect synchrony, 2) one stable chimera for $(r_1 = 1, r_2 \neq 1, \phi \neq 0)$, 3) its symmetrical state, 4) one saddle chimera for $(r_1 = 1, r_2 \neq 1, \phi \neq 0)$, 5) its symmetrical state. Increasing the control parameter D as the heterogeneity parameter can destabilize and restabilize the symmetric state. Moreover, increasing the heterogeneity causes a decrease in the width of the angular distribution of the incoherent region in the chimera state.

Fig. 34, represents the third studied case with modifying one distribution width D_2, with no frequency offset. In this case $D_1 = \Omega_2 = 0$. Since the system is not symmetric, the effect of varying D_2 on the chimera state with $(r_1 = 1, r_2 \neq 1)$

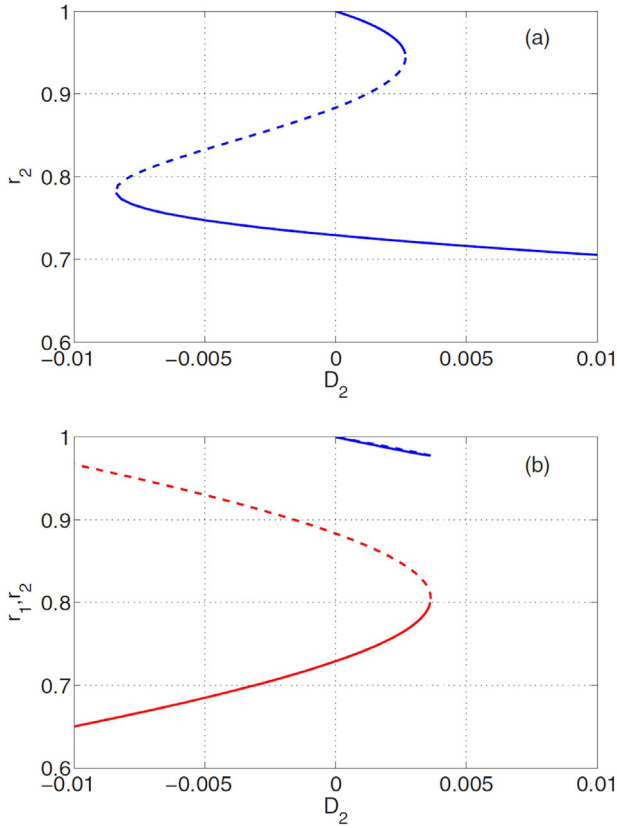

Fig. 34. The fixed points of Eq. (85) for $D_1 = \Omega_2 = 0$. (a) r_2 as a function of D_2, when $r_1 = 1$. (b) r_1 (red curve) and r_2 (blue curve) as a function of D_2. In this figure, dashed lines are unstable and solid lines are stable. $A = 0.2$, $\beta = 0.1$.
Source: Figure reproduced with permission from [109].

is not the same for the chimera state with ($r_1 \neq 1, r_2 = 1$). When $D_2 = 0$, there exist five fixed points for Eq. (85). When $r_1 = 1$, as D_2 increases the perfect solution is destroyed in a saddle–node bifurcation; however, a chimera with desynchronization in region 2 persists (Fig. 34a). Fig. 34b indicates that as D_2 increases, both stable chimera and saddle chimera are destroyed in a saddle–node bifurcation. Therefore, when one region is sufficiently heterogeneous, the only chimera with desynchronization in its population persists.

3.1.2.4. Small network. The chimera states not only occur in systems with large numbers of oscillators, but also may appear in systems with a small number of oscillators. Since the order parameter is not stationary in small networks, the chimera states are challenging to characterize. Therefore, fewer improvements have been made to analyze chimera states in small networks, and often a continuum approach is replaced with a given finite network. This approach leads to solving an eigenvalue problem that makes the opportunity of characterizing chimera states. In the study [209], It is found that in a network with $2N$ phase oscillators with two groups, chimera states emerge even for two oscillators per group. In this study, two groups of N phase oscillators with unique natural frequencies are considered as

$$\begin{aligned}
\frac{d\theta_i}{dt} &= \omega - \left(\frac{1+A}{2N}\right)\sum_{j=1}^{N}\cos(\theta_i - \theta_j - \beta) \\
&\quad - \left(\frac{1-A}{2N}\right)\sum_{j=1}^{N}\cos(\theta_i - \phi_j - \beta), \\
\frac{d\phi_i}{dt} &= \omega - \left(\frac{1+A}{2N}\right)\sum_{j=1}^{N}\cos(\phi_i - \phi_j - \beta) \\
&\quad - \left(\frac{1-A}{2N}\right)\sum_{j=1}^{N}\cos(\phi_i - \theta_j - \beta),
\end{aligned} \tag{98}$$

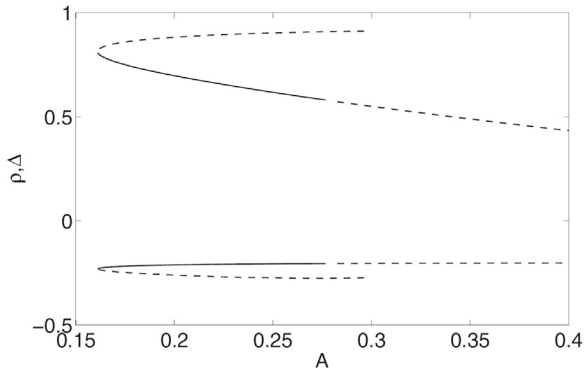

Fig. 35. The positive and negative curves are the values of ρ and Δ, respectively, on the Poincaré section $\Psi = \pi$ of Eq. (99). The solid line is stable, and the dashed line is unstable. $\beta = 0.1$, and $N = 4$.
Source: Figure reproduced with permission from [209].

where θ and ϕ are phases of oscillators in group 1, and 2. The intra-group and inter-group coupling is assumed as $\mu = \frac{1+A}{2}$, $\nu = \frac{1-A}{2}$, respectively, and $\beta = \frac{\pi}{2} - \alpha$. To reduce the system's dimensionality, the Pikovsky and Rosenblum method can be used. Thus, the network in chimera state can be described with the following three equations (see [209])

$$\begin{aligned}
\frac{d\rho_2}{dt} &= \left(\frac{1-\rho_2^2}{4}\right)[(1+A)\Gamma\sin(\xi+\beta) \\
&\quad +(1-A)\sin(\Delta+\beta)], \\
\frac{d\Delta}{dt} &= \frac{1+A}{2}\left[-\cos\beta + \Gamma\left(\frac{1+\rho_2^2}{2\rho_2}\right)\cos(\xi+\beta)\right] \\
&\quad + \frac{1-A}{2}\left[-\Gamma\cos(\xi-\Delta+\beta)\right. \\
&\quad \left. + \left(\frac{1+\rho_2^2}{2\rho_2}\right)\cos(\Delta+\beta)\right], \\
\frac{d\Psi_2}{dt} &= -\left(\frac{1-\rho_2^2}{4\rho_2}\right)[(1+A)\Gamma\cos(\xi+\beta) \\
&\quad +(1-A)\cos(\Delta+\beta)].
\end{aligned} \tag{99}$$

These equations describe the chimera state in a network having two groups, i.e., group 1 is completely synchronized, and group 2 is asynchronized. ρ_2 is a degree of synchronization in group 2 and this measure for the completely synchronized group is $p_1 = 1$. $\Delta = \phi_1 - \phi_2$ that ϕ_i is related to the mean phase of group i for $i = 1, 2$. Ψ_2 is the spread of the phases of oscillators in group 2 and for the completely coherent region, this variable is equal to $\Psi_1 = 0$.

For a network of $N = 4$ oscillators in each group, a Poincaré section $\sum$, in the flow at $\Psi \mod 2\pi = \pi$ is placed, and as Ψ decreases through $\sum$, the values of ρ, and Δ are recorded. The results are shown in Fig. 35. The figure indicates that with increasing control parameters from zero, stable and unstable chimera states appear through a saddle–node bifurcation. By increasing A further, the stable chimera becomes unstable via Hopf bifurcation. This kind of bifurcation is similar to the continuum limit case that is compared in Fig. 36.

This study [209] ascertains that stable chimera states exist even for $N = 2$. For $N = 4$, and $N = 3$, they obtained the bifurcation qualitatively the same as $N = \infty$ case. Fig. 36 shows that in $N = \infty$ case, as A increases for small β, one stable and one saddle chimera states appear in a saddle–node bifurcation. As A increases repeatedly, the stable chimera bifurcates to a supercritical Hopf bifurcation that commences with emerging a breathing chimera. By further increasing the control parameter A, the solution collides with the saddle chimera in a homoclinic bifurcation, and stable chimera states die. In $N = 3$ and $N = 4$ cases, similarly, as A increases from zero, stable, and unstable chimera states arise in a saddle–node bifurcation. The stable chimera state becomes unstable within a supercritical Hopf bifurcation, as A increases further. Furthermore, for the more considerable value of A, the stable solution created from Hopf bifurcation is destroyed via a global bifurcation. In the $N = 2$ case, first, stable periodic orbits appear through a global bifurcation. As A increases,

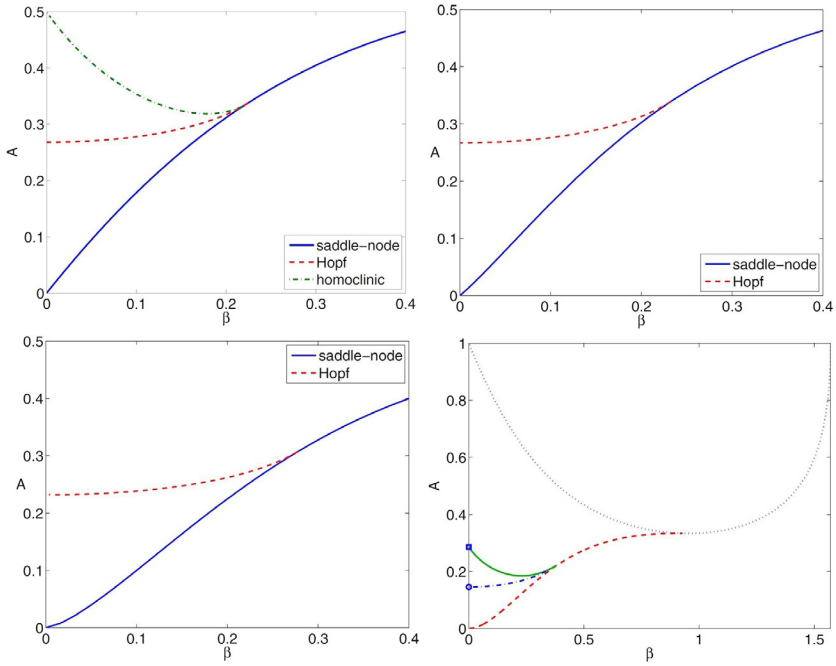

Fig. 36. Bifurcations of A vs. β for different number of network oscillators. Top left: $N = \infty$, Top right: $N = 4$, Bottom left: $N = 3$, Bottom right: $N = 2$. For $N = 2$ case, the black, blue, red, and green curves are saddle–node of fixed points, pitchfork of chimera, heteroclinic connection and homoclinic connection between fixed points, respectively. The stable chimera exists in the region between red and green curves and $\beta = 0$ axis.
Source: Figure reproduced with permission from [209].

the supercritical Hopf bifurcation occurs, and the stable periodic orbits bifurcate to an unstable orbit and two stable orbits. When the second global bifurcation occurs, both stable chimera states disappear; however, the unstable periodic orbit insists. Although the bifurcation is different and contains global and pitchfork bifurcations, stable chimeras exist in wedge again.

3.1.2.5. Turbulent chimeras. In a homogeneous chain of non-locally coupled oscillators, a supercritical bifurcation from a coherent state leads to a self-emerging chimera state [210]. This chimera state emerges from the general initial conditions without necessitating specific initial conditions. Near the bifurcation point, the chimera state is stable, but it becomes turbulent with increasing fluctuations in parameters. Thus, an irregular merging of synchronous and partially synchronous regions occurs. Further, a turbulent state occurs beyond the instability of the stationary chimera state. In this case, although the synchronous regions are persistent, they appear at various locations. So the pattern is called a turbulent chimera.

3.2. Characterizing chimeras in dynamical systems

In this section, we discuss some quantitative statistical measures to characterize chimera States.

3.2.1. Kuramoto global order parameter

The global order parameter is defined as [28,206,211,212]

$$R(t) = \frac{1}{N}\left|\sum_{k=1}^{N} e^{i\theta_k(t)}\right|, \tag{100}$$

where θ_k is the phase of oscillator k, and N is the number of oscillators in the network. The continuum limit analog of the global order parameter is determined by

$$r(t) = \frac{1}{2\pi}\left|\int_{-\pi}^{\pi} z(x,t)dx\right|. \tag{101}$$

Here, $z(x,t)$ is the complex local order parameter [205]. For a completely incoherent state with $z(x,t) = 0$, the global order parameter is $r = 0$, and for completely coherent states, it is $r = 1$. This parameter takes a time-independent constant value of $0 < r < 1$ for chimera states.

3.2.2. Local order parameter

The local order parameter is another notion that can characterize the coherent and incoherent regions of chimera [61,213–215]. This method signifies the local ordering of oscillators and indicates the coherence degree defined as

$$L_i = \left| \frac{1}{2\nu} \sum_{|i-k|\leq\nu} e^{j\Phi_k} \right|, \ i = 1, 2, \ldots, N. \tag{102}$$

Here, $j = \sqrt{-1}$, and the oscillators are supposed to be on a ring having ν nearest-neighbors on each side. Φ_k is the geometric phase of ith oscillator. For coherent regions of chimera states $L_i \approx 1$, and for the oscillators belonging to incoherent regions of chimera states $L_i < 1$.

3.2.3. Strength of incoherence and the discontinuity measure

To describe the strength of incoherence (SI) [216], firstly, it is needed to introduce the new variable $z_i = (z_{1,i}, \ldots, z_{d,i}) = x_i - x_{i+1}$, where x_i represents the state vector of ith oscillator for $i = 1, 2, \ldots, N$. The variable $z_{l,i}$, $l = 1, 2, \ldots, d$ has its minimum value when oscillators i, and $i+1$ are coherent. For incoherent neighboring oscillators i and $i+1$, $z_{l,i}$ has a value between $\pm|x_{l,i,max} - x_{l,i,min}|$. For chimera state, some of $z_{l,i}$ have the same value, however some others have distributed values between $\pm|x_{l,i,max} - x_{l,i,min}|$. Thus, the standard deviation is used to quantify the synchronization level

$$\sigma_l = \left\langle \sqrt{\frac{1}{N}\sum_{i=1}^{N}[z_{l,i} - \langle z_l\rangle]^2} \right\rangle_t, \tag{103}$$

where $\langle z_l\rangle = \frac{1}{N}\sum_{i=1}^{N} z_{l,i}(t)$. For a coherent state, σ_l is zero, and for both incoherent and chimera states, it has a nonzero value. Therefore, to distinguish between the incoherent and chimera states, the local standard deviation is used as

$$\sigma_l(m) = \left\langle \sqrt{\frac{1}{n}\sum_{i=n(m-1)+1}^{mn}[z_{l,j} - \langle z_l\rangle]^2} \right\rangle_t, \ m = 1, 2, \ldots, M \tag{104}$$

where M is an even number, and oscillators in the network are divided into M bins. Thus, σ_l is calculated for every bin having $n = \frac{N}{M}$ oscillators. Using local standard deviation, the SI is introduced as

$$SI = 1 - \frac{\sum_{m=1}^{M} s_m}{M}, \tag{105}$$

where $s_m = \Theta(\delta - \sigma_l(m))$. Here, Θ is the Heaviside step function with a small threshold δ. When σ_l is less than δ, $s_m = 1$, otherwise $s_m = 0$. Therefore, for coherent states $SI = 0$, for incoherent states $SI = 1$, and for chimera states $0 < SI < 1$.

The measure that can distinguish between chimera states and multi-chimera states is the discontinuity measure, that is based on the distribution of s_m calculated as

$$\eta = \frac{\sum_{m=1}^{M} |s_i - s_{i+1}|}{2}, \ (s_{M+1} = s_1). \tag{106}$$

The discontinuity measure $\eta = 1$ specifies the chimera state, and integer discontinuity measure $\eta > 1$ shows the multi-chimera states.

3.2.4. Mean phase velocity

The mean phase velocity approach also verifies the existence of a chimera state in coupled systems. It is defined as [217]

$$\omega_i = \frac{2\pi M_i}{\Delta T}, \ i = 1, 2, \ldots, N. \tag{107}$$

Here ΔT is a sufficiently long time interval, and M_i is the number of oscillation during ΔT for ith oscillator. For coherent states, ω_i are constant values and for incoherent states ω_i are randomly distributed. For chimera states ω_i have values on a continuous curve such that constant values correspond to the coherent regions of phase-locked oscillators.

3.2.5. The size of coherent and incoherent clusters

Two measures can be applied to quantify the relative size of the coherent region of the chimera state. First, the relative size of the incoherent regions can be calculated as [218]

$$N_{\text{incoh}} = \frac{1}{N}\sum_{k=1}^{N} \Theta(\omega_k - \omega_{\text{coh}} - c), \tag{108}$$

where Θ is the step function, ω_k is the mean phase velocity of the element k, ω_{coh} is the mean phase velocity of the coherent part and c is a small tolerance. When the argument of the function Θ is positive, it takes the value of 1; otherwise it takes the value of zero.

Another measure is the extensive cumulative size of the incoherent parts, M_{incoh}, which is defined by

$$M_{\text{incoh}} = \sum_{k=1}^{N} |(\omega_k - \omega_{\text{coh}})|. \tag{109}$$

This measure determines the area below the arcs in the mean phase velocity profiles and demonstrates the degree of the incoherence of chimera states. For purely coherent states, this extensive measure is zero.

3.2.6. Root-mean-square deviation

In this method to quantify the chimera states, the root-mean-square deviation of oscillators is defined by [47,219,220]

$$\Delta_i = \left\langle (2x_i(t) - x_{i+1}(t) - x_{i-1}(t))^2 \right\rangle, \tag{110}$$

where $x_i(t)$ describes the dynamic of ith oscillators in the network, and $\langle\cdot\rangle$ is time averaging. Using Δ_i, the average difference between the instantaneous states of adjacent oscillators can be estimated. Since Δ_i has significant local maximum in incoherent clusters, the boundaries of synchronous and asynchronous clusters can be determined.

3.2.7. Normalized coefficient of mutual correlation

To quantify the degree of oscillation disorder in the chimera states, the normalized coefficient of mutual correlation (CMC) of oscillators is employed [221]. The CMC can provide measurable characteristics of chimera states and describe features of the amplitude, phase, and intermittent chimeras. The CMC is defined by

$$\Psi_{1,i} = \frac{\left\langle \tilde{x}_1(t)\tilde{x}_i(t) \right\rangle}{\sqrt{\left\langle \tilde{x}_1^2(t) \right\rangle \left\langle \tilde{x}_i^2(t) \right\rangle}}, \tag{111}$$

where $(1, i)$ denotes the first and the ith oscillators at the same time, the brackets define the average in time and $\tilde{x}(t) = x(t) - \langle x(t) \rangle$ is the fluctuation relative to the mean value. In the phase chimera region, the CMC is close to unity, and for incoherent phase chimera regions, its sign changes from negative to positive.

Using this method, for phase and amplitude chimera, a difference of correlation is revealed. The CMC has a value below unity for all elements of the incoherent region. Therefore, decreasing of CMC in an amplitude chimera indicates an incoherence in oscillations that conform to the chimera state definition. Further, the intermittency phenomenon is characterized by the random alternation of time intervals. In this case, the oscillator with the fixed number i can correspond to either phase or amplitude chimera regions.

3.2.8. Finite-time Lyapunov exponents for chimeras

For the general Kuramoto system that supports chimera states, by calculating the probability distribution of the local Lyapunov exponents, a specific shape of the distribution is observed. This shape has an asymmetric Gaussian-like peak, with a shoulder on each side. In general, the central peak is positioned near the left shoulder of the distribution shape. Therefore, the knowledge of expected shape can be a characteristic for chimera state identification in the case there is the possibility to measure the phases of all oscillators directly or in the case that the systems are possible but not directly measurable [222]. Fig. 37a represents the local Lyapunov exponents distribution as the number of oscillators increases. It is observed that by increasing N, the distribution shape has an expected shape, however, shoulders and the main peak become more pronounced. Fig. 37b shows the distribution shape for different phase-lag parameters. It is observed that the location of the central peak shifts from the left side extreme to the center extreme as α changes. However, the central peak never moves away from extremes, since the chimera becomes unstable for marginally larger or smaller value.

3.2.9. Correlation measures for spatial and temporal coherence

3.2.9.1. Correlation in space. In this method, local curvature is used as a measure of spatial coherence. Generally, the local curvature is quantified with Laplacian for any point in the spatial dimension [223]. For one snapshot in time t with spatial data f, the discrete Laplacian D in one spatial dimension system is defined as

$$\begin{aligned} \hat{D}f &= \Delta x^2 Df \\ &= f(x + \Delta x, t) - f(x, t) + f(x - \Delta x, t). \end{aligned} \tag{112}$$

In this definition, each data in f can have a real, complex, or higher dimension values. Following this concept, for a chimera state observed in the Kuramoto model, the local curvature values at each point are depicted in Fig. 38. This figure indicates that the chimera state is mapped onto a new function using D_m as the maximum of $|\hat{D}|$. Here, D_m is the curvature of an oscillator on the circuit with neighboring oscillators located in the opposite position. For a ring network with constant amplitude A, D_m converges to $4A$ in the continuum limit. In the synchronous regions $\lim_{N\to\infty} |\hat{D}| = 0$, while in the incoherent regions $|\hat{D}|$ has a finite value. By considering the normalized probability density function of $|\hat{D}|$ as $g(|\hat{D}|)$, the $g(|\hat{D}| = 0)$ determines the relative size of spatially coherent regions. When the system is completely synchronized

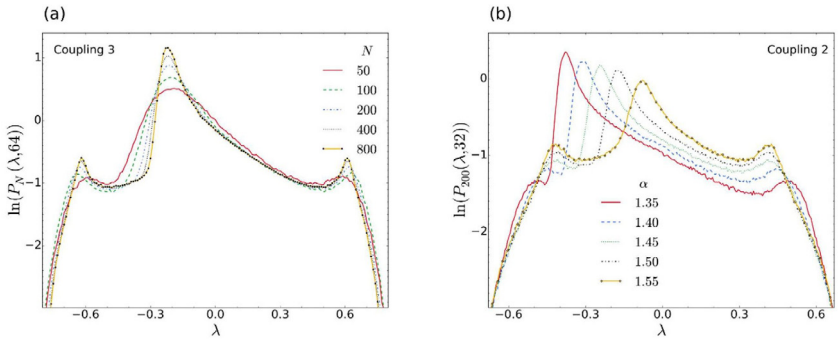

Fig. 37. The local Lyapunov exponents distribution for chimera state. (a) For the different number of oscillators (N). (b) For the different phase-lag parameter (α).
Source: Figure reproduced with permission from [222].

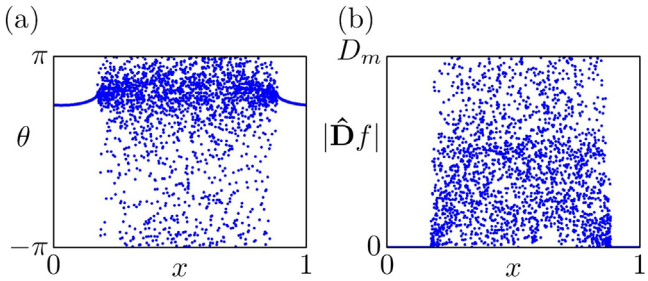

Fig. 38. (a) The snapshot of the chimera state in the Kuramoto model. (b) The values of the local curvature calculated using discrete Laplacian D.
Source: Figure reproduced with permission from [223].

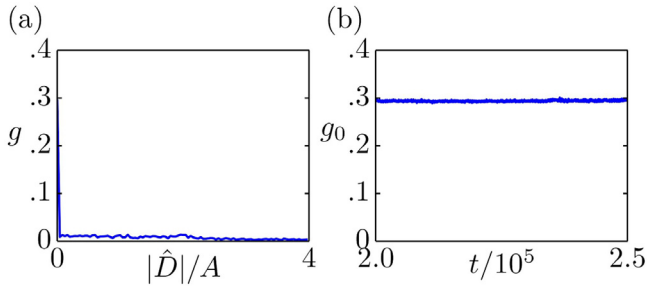

Fig. 39. (a) The probability distribution function $g(|\hat{D}|)$ for the Kuramoto model corresponding to Fig. 38. (b) The $g_0(t)$ for a longer time series.
Source: Figure reproduced with permission from [223].

$g(|\hat{D}| = 0) = 1$, while for a completely incoherent system $g(|\hat{D}| = 0) = 0$. Therefore, the values of $0 < g(|\hat{D}| = 0) < 1$ correspond to the coexistence of coherent and incoherent regions.

It is proposed that for a spatially extended system, a point $\delta = 0.01D_m$ should characterize the system as coherent or incoherent. Therefore, the correlation measure

$$g_0(t) := \int_0^{\delta} g(t, |\hat{D}|)d|\hat{D}|, \tag{113}$$

is useful to describe the spatial extent of the coherent region. Fig. 39a displays an example of g for a Kuramoto model. Fig. 39b indicates $g_0(t)$ as a function of time. In this case, $g_0 \approx 0.3$ corresponds to the chimera state.

3.2.9.2. Correlation in time. The temporal correlation of oscillators can provide valuable information for distinguishing chimera states, too [18]. For oscillators with X_i, and X_j time series, that their means and standard deviations are μ_i, μ_j, and σ_i, σ_j, respectively, the pairwise correlation coefficient is

$$\rho_{ij} = \frac{\langle (X_i - \mu_i) * (X_j - \mu_j) \rangle}{\sigma_i \sigma_j}. \tag{114}$$

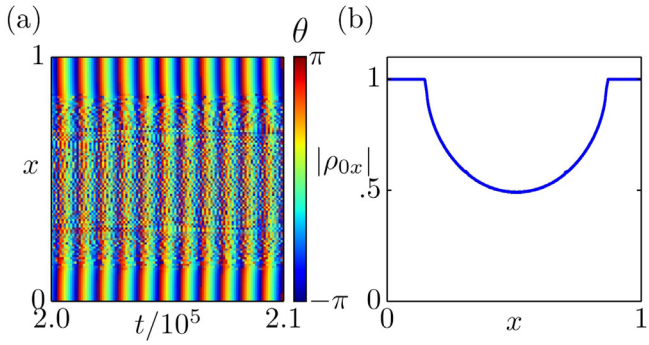

Fig. 40. (a) Spatiotemporal pattern of a chimera state in the Kuramoto model. (b) Pairwise correlation coefficients $\{\rho_{0x}\}$.
Source: Figure reproduced with permission from [223].

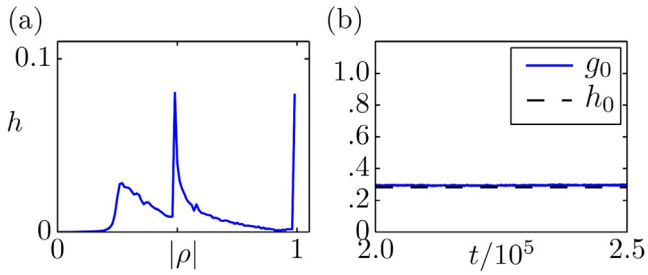

Fig. 41. (a) The distribution function h for a chimera state in the Kuramoto model. (b) The comparison of time series of $g_0(t)$, and time-independent h_0.
Source: Figure reproduced with permission from [223].

Here, $\langle\cdot\rangle$, and $*$ indicate temporal mean and complex conjugate, respectively. For linearly correlated time series $\rho_{ij} = 1$, and for linearly anti-correlated time series $\rho_{ij} = -1$. For complex time series $|\rho_{ij} = 1|$, $\angle\rho_{ij} = \alpha$ and α is a constant phase shift. Therefore, the normalized distribution function h of

$$\hat{\mathbf{R}} = \{|\rho_{ij}|\}, i \neq j, \tag{115}$$

can measure the correlation in time. For static chimera state with the coherent cluster localized at a specified position over time, the normalized distribution function $h(|\rho_{ij}| \approx 1)$ is nonzero. For instance, for the chimera in Fig. 40a, the first row of the correlation matrix $\hat{\mathbf{R}}$, $\{\rho_{0x}\}$, that is the correlation between oscillator positioning at $x = 0$ and the rest of the oscillators, is shown in Fig. 40b.

The distribution function h is displayed in Fig. 41. The distinct peak at $\rho = 1$ demonstrates that the majority of oscillators are positioning at the same positions that correspond to a static chimera. Another peak is at $\varrho \approx 0.5$ that corresponds to partial linear correlation between synchronous oscillators and oscillators positioning at $x \approx 0.5$. The percentage of oscillators that are correlated in time is quantified with

$$h_0 := \sqrt{\int_{\gamma}^{1} h(|\rho|)d|\rho|}. \tag{116}$$

It should be noted that h_0 does not always indicate the size of the coherent region, spatially for non-static chimera, that the regions are changing their positions over time. Moreover, if and only if the chimera is static with no spatial coherence in the synchronous cluster, h_0 coincides with g_0.

4. Different types of chimeras

The development of the chimera studies to various oscillatory systems has led to discovery of different types of chimeras, including breathing chimera, amplitude chimera, chimera death, etc. The chimera types although consisting of coherent and incoherent regions, have different properties in space and time. These chimera states are described in this section with detail.

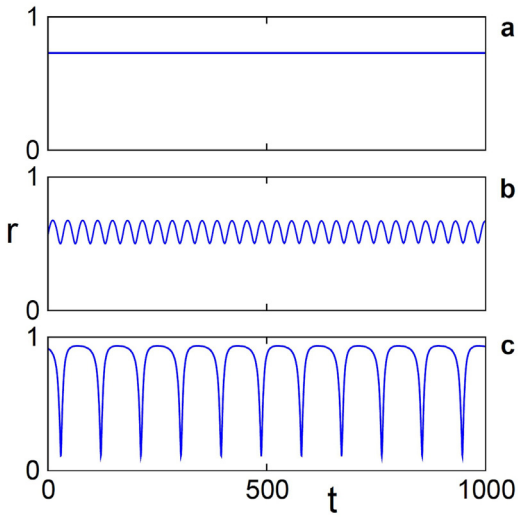

Fig. 42. The order parameter of the network of phase oscillators with two populations. The coupling strength between the groups is ν and within the groups is μ. (a) The stationary chimera for $\mu - \nu = 0.2$. (b) The breathing chimera for $\mu - \nu = 0.28$. (c) The breathing chimera with longer breathing for $\mu - \nu = 0.35$.
Source: Figure reproduced with permission from [224].

4.1. Breathing chimeras

Before the study of Abrams et al. [224], it was assumed that the chimera states are statistically stationary, i.e., the positions of the coherent and incoherent domains are static in time. In 2008, Abrams et al. [224] investigated a network of phase oscillators and found that the chimeras can also be non-stationary and called this state breathing chimera. The network they considered consisted of two populations, with stronger within groups coupling strength than the between groups coupling strength. It is possible to detect the stationary and breathing chimera states by calculating the order parameter in time. In fact, in the stationary chimera, the order parameter is constant, while in the breathing one, the order parameter changes periodically. The order parameter of the second population of the phase oscillators network is shown in Fig. 42. Fig. 42a shows the existence of a stationary chimera with a constant order parameter. By increasing the difference of the within and between groups coupling strength, the chimera is changed to the breathing, which is shown in Fig. 42b. More increasing of this difference gives rise to breathers with a longer period (Fig. 42c), and finally, leads to the appearance of complete synchronization.

The emergence of breathing chimera has also been revealed in ring networks [108,225]. As discussed in the previous section, Laing [108] studied a ring network of phase oscillators with heterogeneity in the frequencies of the oscillators. By using the OA ansatz, this network was analyzed, and the formation of the breathing chimera was investigated. A similar study has been done on a network of identical phase oscillators with nonlinear coupling. In contrast to most studies, Bolotov et al. [225] considered the phase shift of the force acting on oscillators to be non-constant and claimed that probably this factor is necessary for the emergence of breathing chimera.

4.2. Multi-headed chimeras

Strengthening the coupling between the phase oscillators can lead to the appearance of multiple coherent clusters within the incoherent region [217]. This state was firstly reported by Omelchenko et al. [217] and called the multi-headed chimera or multi-chimera. They considered a ring of non-locally coupled FitzHugh–Nagumo (FHN) oscillators with direct and cross-couplings. This network exhibits classical chimera state (with one coherent and incoherent domain) for small values of coupling strength. Increasing the coupling strength gives rise to the formation of two incoherent clusters. This can be seen in Fig. 43a–d. In these figures, the left column shows the time-snapshots of the activator variables of the oscillators, and the right column shows their mean phase velocities. The right panel of Fig. 43 shows the transition from classical chimera to three-headed chimera due to increased coupling strength and decreased coupling range.

The local dynamics of the oscillators of the network plays an important role in the emergence of multi-chimeras. The multi-chimera states are also observable in non-locally coupled van der Pol oscillators when their local dynamics is sinusoidal oscillation [226]. Varying the bifurcation parameter of the oscillators leads to the change of the local dynamics to nonlinear relaxation oscillation. In this case, the stability regions of multi-chimeras are strongly influenced. As the

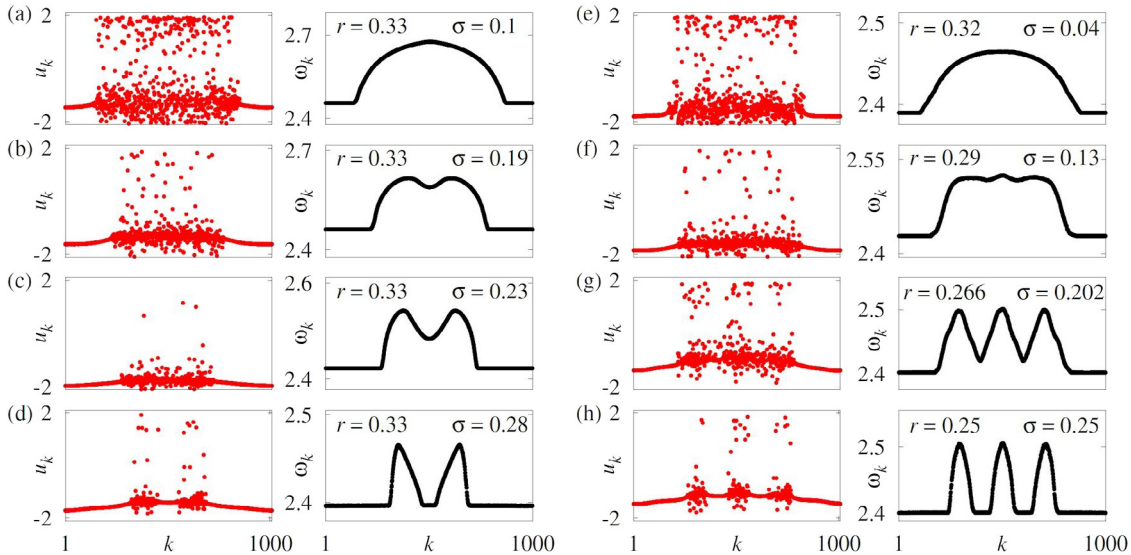

Fig. 43. The time snapshot (left column) and the mean phase velocity (right column) of the network of non-locally coupled FitzHugh–Nagumo oscillators. The left panel (a–d) shows the formation of chimera states with two incoherent clusters by increasing the coupling strength (σ), and the right panel (e–h) shows three incoherent clusters by increasing the coupling strength (σ) and decreasing the coupling range (r).
Source: Figure reproduced with permission from [217].

nonlinearity becomes stronger, the emergence of multi-chimeras is enhanced, and the stability regions in the coupling strength and coupling range plane are extended.

The multi-headed chimera has also been observed in coupled pendula [227]. Jaros et al. [227] reported the existence of the chimera state consisting of the active and the passive pendula, for a specific range of coupling stiffness. With the appearance of passive clusters with chaotic behavior in the large active pendula, which are synchronous, the multi-headed chimera is formed. However, the active pendula in different clusters have different periods. The number of the pendula in each cluster, and the number of their neighboring passive pendula, and also the synchronization type, determine the periods of the active pendula.

Tsigkri-DeSmedt et al. [228] investigated the emergence of multi-chimeras in the network of the Leaky Integrate-and-Fire model. They considered two different cases of absence and presence of a refractory period in neurons' behavior. They realized that the refractory period leads to longer chimera states and also gives rise to the appearance of chimera states with multiple coherent and incoherent clusters. While the value of the refractory period does not affect the number of coherent and incoherent clusters.

4.3. Alternating chimeras

The mechanism of the uni-hemispheric sleep is an alternation in the coherency and incoherency of two cerebral hemispheres [229]. This phenomenon can be related to the alternating chimera, in which the coherent and incoherent groups alternatively change their spatial position in time [230]. To model this phenomenon, Ma et al. [229] used two coupled groups of oscillators with the following equation

$$\frac{d\theta_i^\sigma}{dt} = \omega_i + \sum_{\sigma'=1}^{2} \frac{K_{\sigma\sigma'}}{N_{\sigma'}} \sum_{j=1}^{N_{\sigma'}} \sin(\theta_j^{\sigma'}(t) - \theta_i^\sigma(t) - \alpha) + A\sin(\Omega(t-\tau_\sigma)), \tag{117}$$

where $\sigma = 1, 2$ is the number of the groups and N_σ is the number of oscillators in each group. $K_{\sigma\sigma'}$ denotes the coupling strength from oscillators of σ' to σ. The parameters are set at $K_{11} = K_{22} = \mu = 5$, $K_{12} = K_{21} = \nu = -4$ and $\alpha = \pi/2 - 0.1$. The term $A\sin\Omega(t-\tau_\sigma)$ is an external signal with the amplitude A and the frequency Ω to model the environmental changes, and the τ_σ is the time when the system responds to the environment. Since two cerebral hemispheres have different response times, $\tau_1 = 0$ and $\tau_2 \neq 0$ are assumed. Furthermore, the oscillators are considered to be non-identical with different ω_i, chosen from a uniform random distribution in $[1-\delta, 1+\delta]$, due to the non-identical property of two hemispheres. Therefore, in this network the non-identity of ω_i and also, the existence of the external signal are required for the emergence of alternating chimera. To characterize the chimera states, the authors in [229] used the average of the

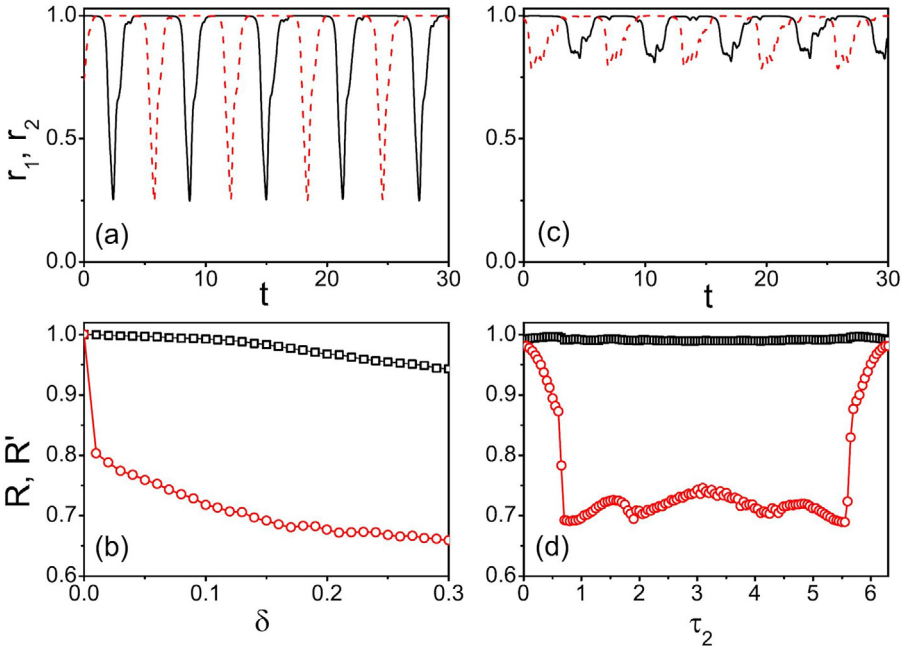

Fig. 44. The alternating chimera state for the network of Eq. (117). The first row shows the variation of r_1 and r_2 in time, for $\delta = 0.01$ and $\tau_2 = 1.5$ in (a), and for $\delta = 0.1$ and $\tau_2 = 0.5$ in (c). The second row shows the variation of R_1 and R_2, with respect to diversity parameter δ, for $\tau_2 = 1.5$ in (b) and with respect to the time delay τ_2, for $\delta = 0.1$ in (d).
Source: Figure reproduced with permission from [229].

order parameter of the synchronized (R) and asynchronized groups (R') as

$$R = \langle max(r_1, r_2)\rangle, \quad R' = \langle min(r_1, r_2)\rangle, \tag{118}$$

where $\langle\cdots\rangle$ denotes the time average, and the order parameter (r) is obtained by

$$r_\sigma(t)e^{i\phi_\sigma(t)} = \frac{1}{N_\sigma}\sum_{j=1}^{N_\sigma} e^{i\theta_j(t)}, \quad \sigma = 1, 2 \tag{119}$$

where $\phi_\sigma(t)$ is the average phase at time t, and $r(t) = 1$ and $r(t) = 0$ show synchronization and asynchronization, respectively.

Fig. 44a shows the order parameter of two groups for $\delta_1 = 0.01$ and $\tau_2 = 1.5$. This figure represents the alternation of synchronization and asynchronization between two groups. For higher diversity parameter values (δ), the alternating chimera still exists but with poor quality synchronization, as is shown in Fig. 44c. To illustrate the dependency of existence of alternating chimera on the diversity parameter, Fig. 44b is presented. As is shown, by increasing δ, the average of the order parameter of the synchronized and asynchronized groups is decreased slowly. Finally, Fig. 44d illustrates the variation of R and R' with respect to the time delay τ_2. Thus, the alternating chimera is robust to both the variation of diversity parameter and the time delay.

As mentioned, the non-identity of the oscillators and the presence of an external signal is required for the emergence of chimera state in the network of Eq. (117). However, the alternating chimera state has also been observed in a two-dimensional network of modified CGLE oscillators with nonlinear global coupling [231]. This network is capable of exhibiting different dynamics such as two-phase cluster state, ordinary and alternating chimera states, and so on by changing the parameters' values. Fig. 45 shows an example of the alternating chimera observed in this network. Initially, the network is composed of two domains of asynchronous and synchronous states (Fig. 45a), similar to the ordinary chimera state. But as time passes, these two domains are exchanged, and the primary synchronous state becomes asynchronous, while the asynchronous one becomes synchronous (Fig. 45a–c). This alternation is firstly disordered in time, and then, becomes regular. Fig. 45d illustrates the one-dimensional spatiotemporal pattern of the network along the x-axis.

Since the most relevant phenomenon to the alternating chimera is the uni-hemispheric sleep, the study of neuronal dynamics in the emergence of this chimera type is of particular importance. In this regard, Majhi and Ghosh [230] investigated a network of Hindmarsh–Rose neurons coupled indirectly through ephaptic coupling (i.e., through the

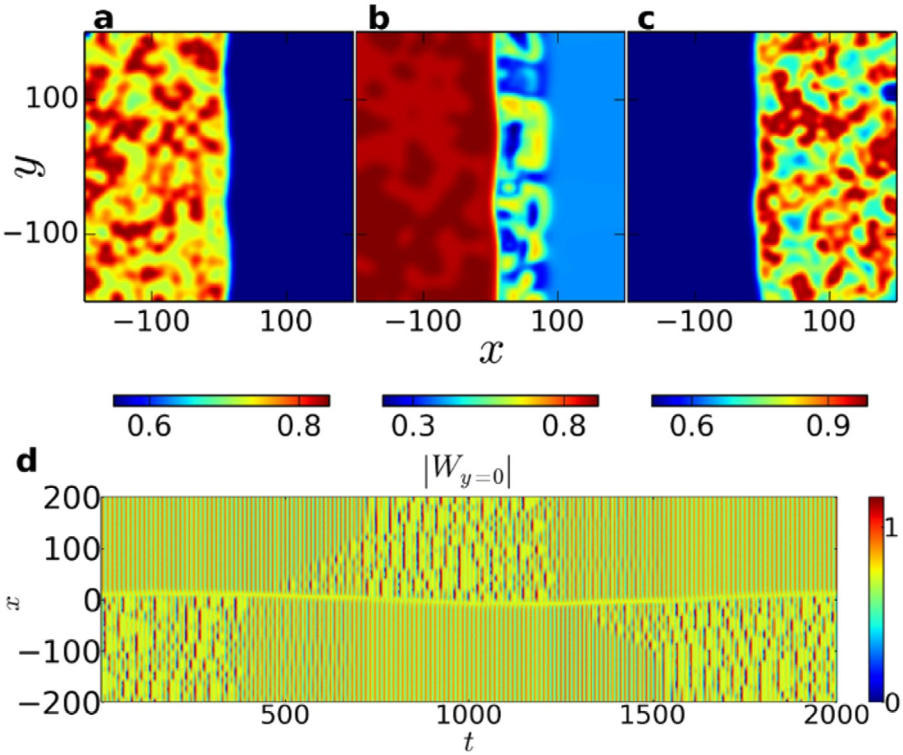

Fig. 45. Alternating chimera state in a two-dimensional modified CGLE network. (a–c) The snapshots of the network after the formation of two synchronous and asynchronous states, at $t = 0$, 600, and 1000. (d) One-dimensional spatiotemporal pattern of the network along the x-axis, showing regular alternations.
Source: Figure reproduced with permission from [231].

electromagnetic field). The equations of this network are described as

$$\begin{aligned}
\dot{x}_i &= y_i + bx_i^2 - ax_i^3 - z_i + I - \epsilon\rho(\phi_i)x_i,\\
\dot{y}_i &= \alpha - dx_i^2 - y_i,\\
\dot{y}_i &= c[s(x_i - e) - z_i],\\
\dot{\phi}_i &= -k_1\phi_i + k_2x_i + \sum_{j=i-P}^{j=i+P}[\phi_j - \phi_i],\\
\rho(\phi_i) &= \beta_1 + 3\beta_2\phi_i^2,
\end{aligned} \tag{120}$$

where the fourth variable (ϕ_i) shows the magnetic flux across the membranes and $\rho(\phi_i)$ is the memristive conductance that provides the coupling between the membrane potential and the magnetic flux. It is clear that the coupling in this network is between the magnetic flux variables through nearest-neighbors. The parameters were set at $b = 3$, $a = 1$, $\alpha = 1$, $d = 5$, $s = 4$, $e = -1.6$, $c = 0.005$, $I = 3.25$, 1.9, $k_1 = 0.5$, $k_2 = 0.9$, $\beta_1 = 0.4$ and $\beta_2 = 0.02$.

In this study, different dynamical behaviors of the neurons, such as chaotic bursting, periodic bursting, and plateau bursting, were considered. Their results showed that in the case of chaotic bursting, the stationary alternating chimera appears in all coupling schemes (local, non-local and global coupling), while in the local coupling the chimeras are transient. Besides the alternating chimera, the oscillation death states also reveal for specific coupling parameters. By changing the local dynamics of the neurons to periodic bursting, the chimera's lifetime is increased in local coupling. Furthermore, in the non-local and global coupling, the alternating chimeras transit directly to the complete, coherent state. Finally, by using the plateau bursting as the local dynamics, the region of the emergence of alternating chimera in the parameter plane is extended.

4.4. Traveling chimeras

The traveling chimera state is formed when the position of the coherent group of the chimera moves at a constant speed in time. This type of chimera was firstly observed in a network of identical phase oscillators similar to Eq. (4) with

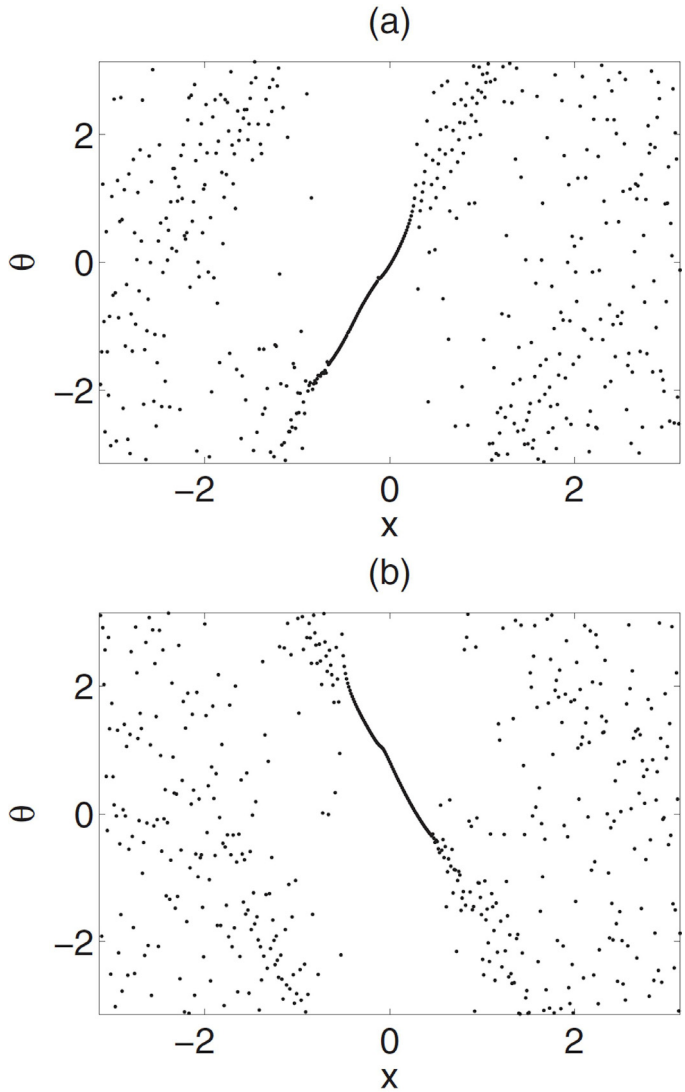

Fig. 46. The snapshot of the phases of coupled phase oscillators with coupling function $G \equiv \cos(2x) + \cos(3x)$ and $\beta = 0.03$, exhibiting traveling chimera state. The coherent cluster in (a) travels to left and in (b) travels to the right.
Source: Figure reproduced with permission from [232].

considering $\alpha \in [0, \frac{\pi}{2}]$ and by defining $\beta = \frac{\pi}{2-\alpha}$ [232]. The coupling function is considered to be as

$$G_n \equiv \cos(nx) + \cos[(n+1)x], \tag{121}$$

where n is a positive integer. An example of the traveling chimera observed in this network is shown in Fig. 46, by setting $n = 2$ and $n = 3$. The gradient of the phase in the coherent group defines the direction of traveling, such that for the positive gradient, the motion is toward the left, and for the negative gradient, the motion is to the right.

To obtain the position of the coherent group, the following function is defined

$$\begin{aligned} F(x^*) &:= \frac{1}{N}\sum_{k}^{N}[\theta_t - f(x_k, x^*)]^2, \\ f(x, x^*) &= -\cos(x - x^*). \end{aligned} \tag{122}$$

The value of x^* at which the Function F is minimized, determines the position of the coherent group. Fig. 47a shows the position of the coherent group in the traveling chimera, which is a periodic function in time and depicts that the coherent group moves with a constant speed (obtained for $N = 512$ and $\beta = 0.03$). Fig. 47b illustrates the speed of traveling for different numbers of oscillators (N). This figure shows that the traveling is inherent and not dependent on

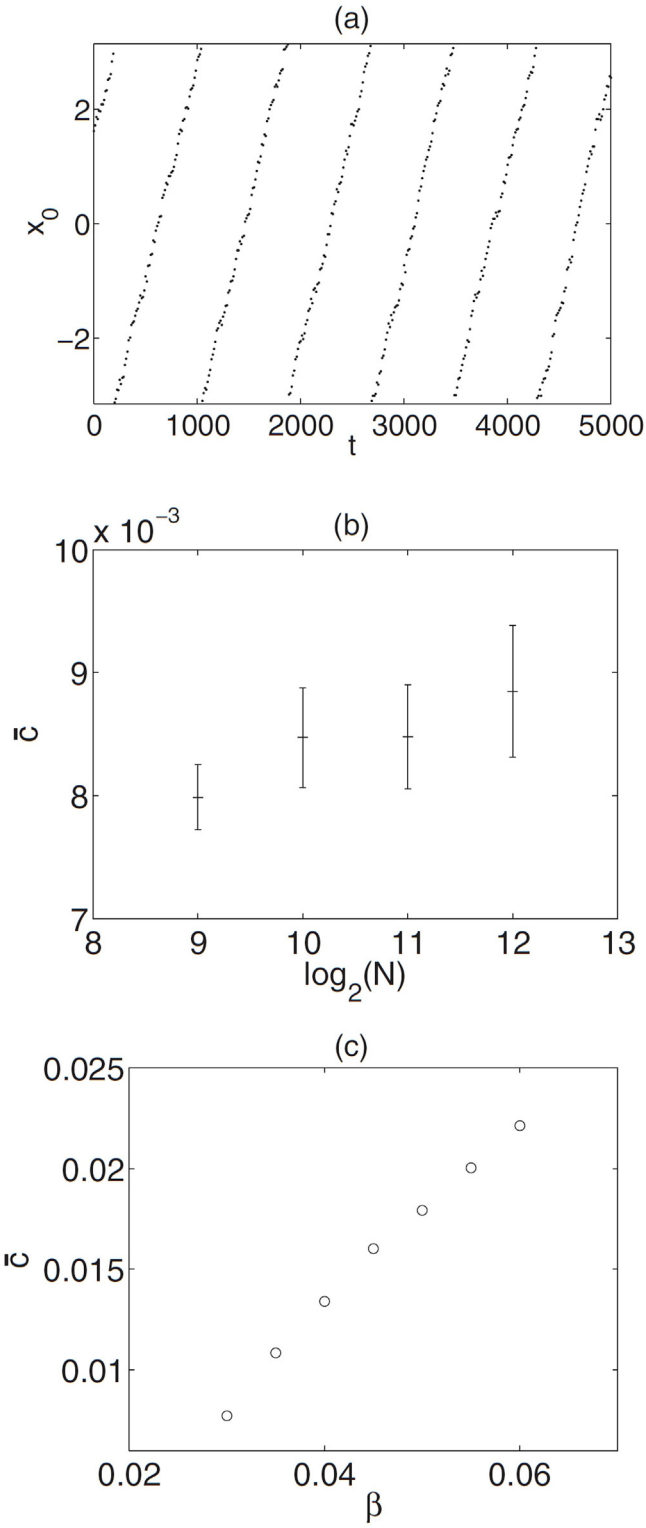

Fig. 47. The traveling chimera properties of the phase oscillators network. (a) The position of the coherent group in time, for $N = 512$ and $\beta = 0.03$. (b) The average speed ($\bar{c}$) of the traveling chimera with respect to the number of oscillators (N) for $\beta = 0.03$. (c) The average speed ($\bar{c}$) of the traveling chimera with respect to β for $N = 512$.
Source: Figure reproduced with permission from [232].

the value of N. Fig. 47c shows the variation of speed with respect to β. It is observed that by increasing β, the traveling chimera state is less probable to appear. The numerical simulations have shown that the traveling chimera is stable for $0.015 < \beta < 0.065$.

Hizanidis et al. [214] represented that the hierarchical coupling topology can cause the emergence of traveling chimera states. Their investigation on a lattice limit cycle (LLC) model demonstrated that based on the topology of the coupling (i.e., the fractal dimension of the limiting set, and the base pattern), different one-cluster or multi-cluster traveling chimeras can emerge. To detect the traveling chimera from the stationary one, they presented a method based on the position of the maximum of the oscillators in time. Since the incoherent region is traveling, therefore the position of the oscillator with the maximum value ($J_{max}(t)$) must change periodically. This period can be attained by the Fourier transform of $J_{max}(t)$. Thus, the speed of the traveling can be obtained by: $v_{tr} = \frac{N}{T_{tr}}$. In the network of LLC, by increasing the coupling strength, the speed of the traveling chimera decreases.

The traveling chimera state has also been found in neuronal networks. Considering a network of Hindmarsh–Rose neurons with both types of synapses, the traveling chimera state was observed in [233]. In this network, the local connections were through the gap junctions, and for the non-local ones, the chemical synapses were used. The describing equations of this network are

$$\begin{aligned}
\dot{x}_i &= y_i + bx_i^2 - ax_i^3 - z_i + I \\
&\quad + k_1(x_{i+1} + x_{i-1} - 2x_i) \\
&\quad - \frac{-k_2}{2P-2}(v_s - x_i)\sum_{j=i-P}^{i+P} \Gamma(x_j), \\
\dot{y}_i &= c - dx_i^2 - y_i, \\
\dot{y}_i &= r[s(x_i - x_R) - z_i],
\end{aligned} \tag{123}$$

where $\Gamma(x)$ denotes the chemical synaptic function.

Fig. 48a shows the spatiotemporal pattern of the formed traveling chimera in which there are two groups of synchronous and asynchronous oscillators. The two groups are not static in time and travel from the bottom left corner to the top right corner. However, the direction of the traveling is not fixed, and by changing the chemical coupling strength, the direction can be reversed. The time snapshots of the neurons' membrane potential are illustrated in Fig. 47b for two different time instants. The snapshots confirm that the position of the synchronous cluster moves in time. The behavior of the neurons in this pattern is chaotic bursting that is shown in Fig. 47c. In the asynchronous part of the network, the neurons are in the bursting state, while in the synchronous part, the neurons are in resting state. Furthermore, the investigations have shown that the pure chemical coupling with higher strengths can also induce traveling chimera, while the pure electrical coupling cannot.

By changing the coupling of the Hindmarsh–Rose neurons to the gradient coupling, the traveling chimera, and the imperfect traveling chimera states are observed [213]. The gradient coupling can represent both the excitatory and inhibitory effects in the neurons' connections. The Hindmarsh–Rose network with gradient coupling is described as follows

$$\begin{aligned}
\dot{x}_i &= ax_i^2 - x_i^3 - y_i - z_i \\
&\quad + (V_s - x_i)((\epsilon + r)\Gamma(x_{i+1}) + (\epsilon - r)\Gamma(x_{i-1})), \\
\dot{y}_i &= (a + \alpha)x_i^2 - y_i, \\
\dot{y}_i &= \mu(bx_i + c - z_i),
\end{aligned} \tag{124}$$

where $\Gamma(x)$ is the chemical synaptic function Eq. (33) with $\lambda = 10$ and $\theta_s = -0.25$. Depending on the values of coupling parameters (ϵ) and (r), different couplings such as the asymmetric excitatory coupling ($\epsilon > r$) with different synaptic strengths for the nearest-neighbors, one-way local excitatory ($\epsilon = r$), and the simultaneous occurrence of excitatory and inhibitory synapses ($\epsilon < r$) can be implemented. The proper selection of the coupling strength in the one-way excitatory coupling, and also the simultaneous excitatory–inhibitory coupling can lead to the emergence of traveling chimera. While the asymmetric excitatory coupling causes the appearance of imperfect traveling chimera state. In this type of chimera, the incoherent part of traveling chimera extends into the coherent domain. Fig. 49 shows the pattern of the imperfect traveling chimera. The spatiotemporal pattern of this chimera is illustrated in Fig. 49a, which shows an irregular traveling. The time snapshots of the membrane potential of the neurons are depicted in Fig. 49b,c for two different time instants. It is observed that at $t = 1750$, there is one incoherent cluster, while at $t = 2250$, there are two incoherent clusters. At this state, the neurons have a chaotic bursting behavior (the combination of square-wave bursting and plateau bursting), as shown in Fig. 49d.

4.5. Amplitude mediated chimeras

In 2013, Sethia et al. [234] studied the Complex Ginzburg–Landau Equation with non-local coupling and exponential kernel, by considering strong coupling strength. While in the past studies, the couplings were investigated to be weak, which led to ignoring the amplitude variations and considering only the phase dynamics. This study revealed that the

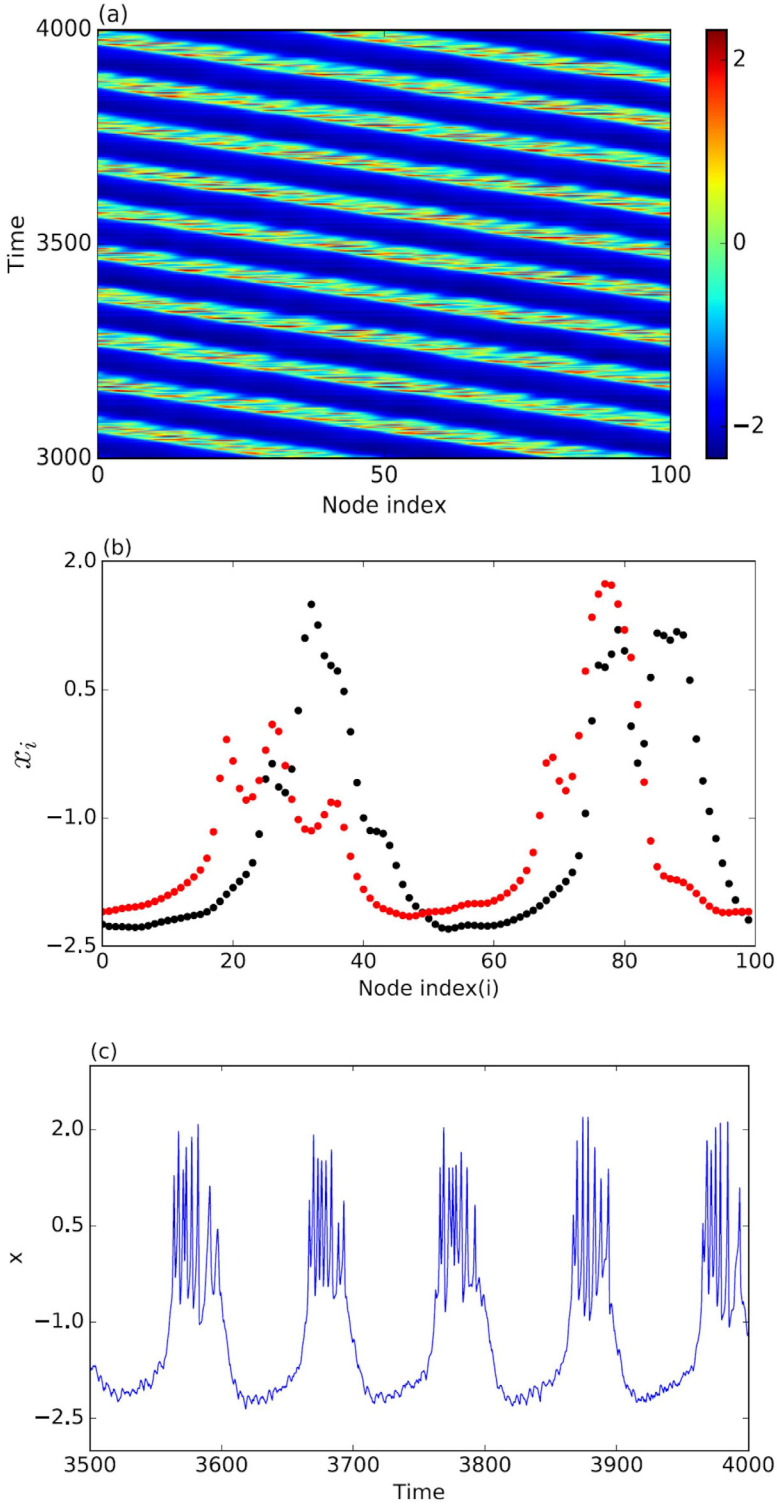

Fig. 48. The traveling chimera state in the network of Hindmarsh–Rose neurons with local gap junctions and non-local chemical synapses. (a) The spatiotemporal pattern of the neurons' membrane potential. (b) The snapshots of the neurons at two different instants. (c) The chaotic behavior of one neuron of the network.
Source: Figure reproduced with permission from [233].

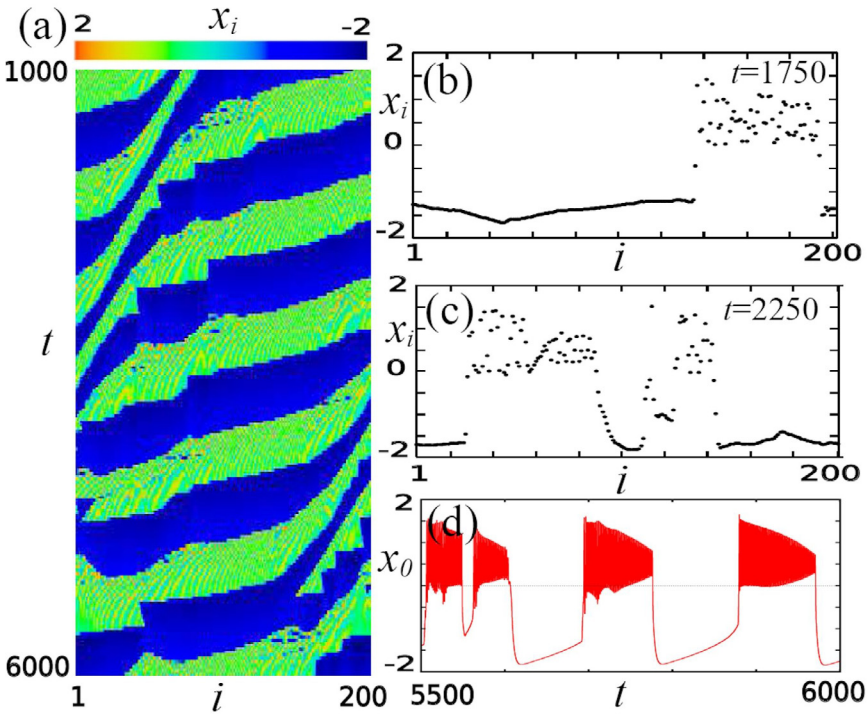

Fig. 49. Imperfect traveling chimera in Hindmarsh–Rose neuronal network with asymmetric excitatory coupling ($r = 0.2$ and $\epsilon = 0.56$). (a) Spatiotemporal pattern of the neurons' membrane potential. (b) The snapshot at $t = 1750$, with one incoherent cluster. (c) The snapshot at $t = 2250$ with two incoherent clusters. (d) The time series of one of the neurons exhibiting a mixed bursting behavior.
Source: Figure reproduced with permission from [213].

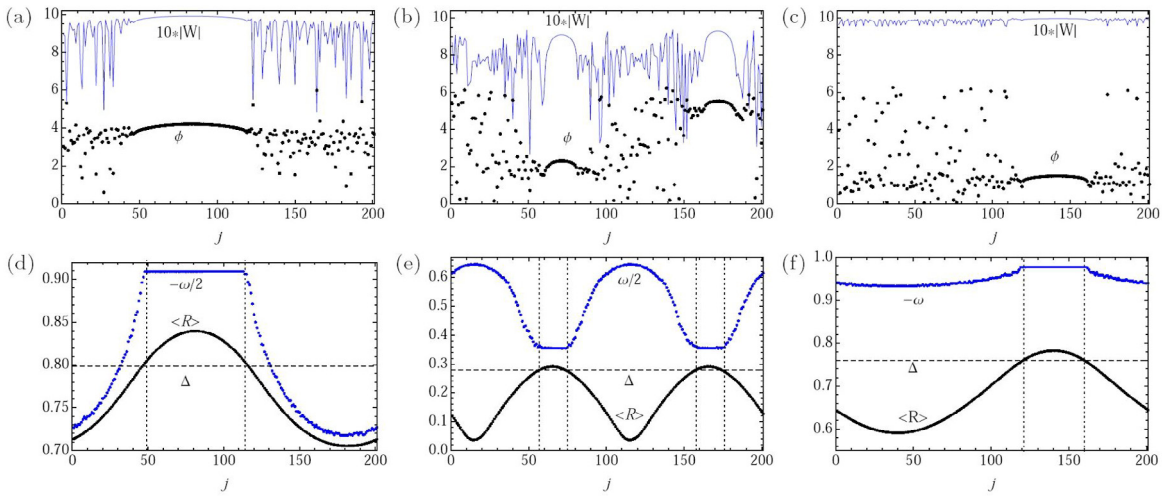

Fig. 50. (a–c) The snapshots of the amplitude ($|W|$ in blue) and phase (ϕ in black) of the network of Complex Ginzburg–Landau Equation. (a) 1-cluster amplitude mediated chimera with $K = 0.4$, $C_1 = -0.5$, $C_2 = 2$. (b) 2-cluster amplitude mediated chimera with $K = 0.4$, $C_1 = -4$, $C_2 = 0.5$. (c) Phase chimera with $K = 0.05$, $C_1 = -0.9$, $C_2 = 1$. (d–f) The time average of the complex order parameter (R in black) and the average frequency (ω in blue) corresponding to parts a–c.
Source: Figure reproduced with permission from [234].

strong coupling causes the oscillators in the incoherent domain to have amplitude differences, in addition to the phase fluctuations. This state was named amplitude mediated chimera. The network of CGLE was investigated in a wide range of parameters (linear and the non-linear dispersion (C_1, C_2) and the coupling strength (K)), and 1-cluster, 2-cluster (stationary and non-stationary) amplitude chimeras were obtained (shown in Fig. 50). Fig. 50a–c illustrate the time snapshots of the phase (black) and amplitude (blue) of the oscillators corresponding to the 1-cluster amplitude mediated chimera, 2-cluster

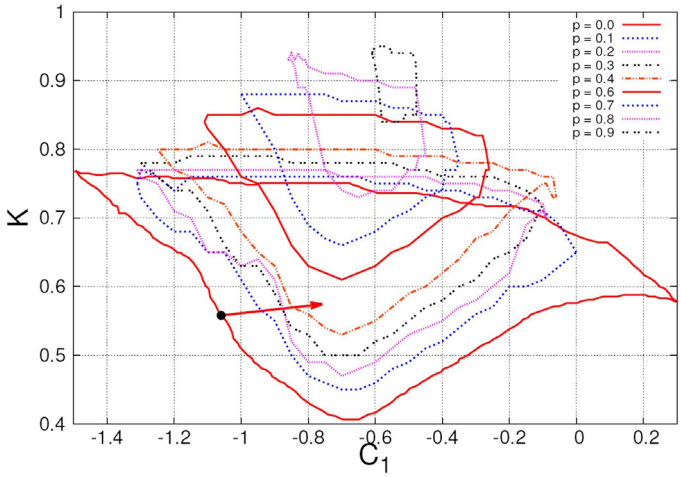

Fig. 51. Region of amplitude mediated chimera in (C_1, K) plane, in the network of globally coupled CGLE for different values of the fraction of the inactive oscillators to the active ones (p). The arrow shows the shift of the region of the chimera from $p = 0$ to $p = 0.1$. The network parameters are $N = 201$, $C_2 = 2$, $a = 1$, $b = 1$.
Source: Figure reproduced with permission from [235].

amplitude mediated chimera and phase chimera, respectively. It is observed that in the amplitude mediated chimera (Fig. 50a,b), there are both amplitude and phase fluctuations, but the amplitude variations in phase chimera (Fig. 50c) are ignorable. The time-averaged of the complex order parameter ($R(x)$ in black), and the averaged frequency of the oscillators (blue) corresponding to the parts a–c are shown in Fig. 50d–f, respectively.

The amplitude mediated chimera has also been studied in the presence of inactive oscillators in a network of globally coupled CGLE [235]. The coupling of the inactive oscillators with the active ones leads to their revival, and they appear in the amplitude mediated chimera as a separate coherent cluster with lower amplitude than the active oscillators. However, they cause a decrement in the overall frequency of the coherent part. Furthermore, the fraction of the inactive oscillators to the active ones (p) significantly affects the region of the emergence of amplitude mediated chimera. Fig. 51 shows the existence area of chimera in the parameter plane (C_1, K) for different p values. This figure represents that by increasing the number of inactive oscillators, the chimera region is lessened and also moves toward larger coupling strength values. The amplitude mediated chimera is also robust to the presence of a large number of inactive oscillators ($p = 0.9$).

4.6. Amplitude chimeras

In amplitude chimera, the chimera occurs in the amplitude of the oscillators rather than their phase. Therefore, in this case, the network consists of two groups of coherent and incoherent oscillators, one with spatially coherent amplitude and the other with spatially incoherent amplitudes. The phases of the oscillators are synchronous [236]. To illustrate this pattern, consider a network of non-locally coupled Stuart–Landau (SL) oscillators as

$$\begin{aligned} \dot{z} &= f(z) \equiv (\lambda + i\omega - |z|^2)z, \\ \dot{z}_j &= f(z_j) + \frac{\sigma}{2P} \sum_{k=j-P}^{j+P} (\mathrm{Re}\, z_k - \mathrm{Re}\, z_j), \end{aligned} \tag{125}$$

where $z = x + iy$, and λ and ω are real. σ is the coupling strength, and P/N is the coupling range. By setting the coupling parameters at $\sigma = 14$ and $P = 4$, and $N = 100$, the amplitude chimera emerges in the network. Fig. 52a shows the distance between the center of mass of each oscillator and the origin ($r_{c.m.}$). It is observed that the center of mass of the coherent oscillators is at the origin, while the incoherent oscillators have different centers of mass. Fig. 52b illustrates the mean phase velocity of the oscillators, which is a flat profile, representing the same phase for all oscillators. The limit cycles of the oscillators in the complex plane are shown in Fig. 52c.

The stability of the amplitude chimeras can be obtained by using the Floquet theory, which determines the local stability of the periodic oscillators [238]. For Floquet analysis, first, consider that a system with describing equation $\dot{x} = F(x(t))$, has a periodic solution as $\chi(t) = \chi(t+T)$. Then, the stability of the periodic solution is obtained by considering the adjacent solutions

$$x(t) = \chi(t) + \delta x(t). \tag{126}$$

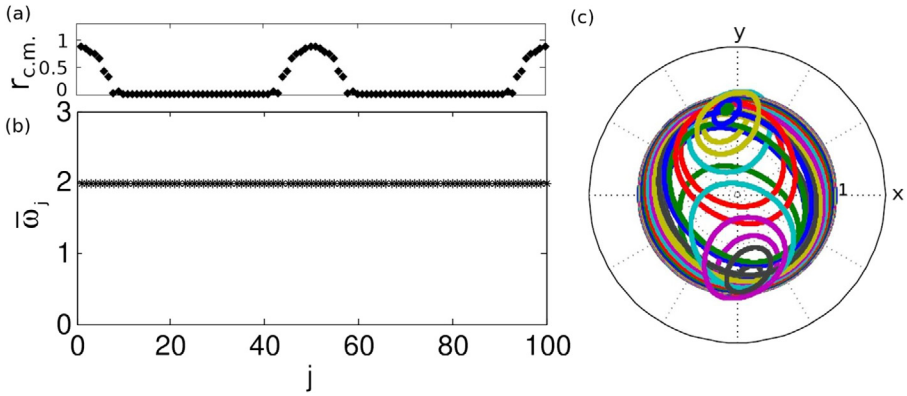

Fig. 52. The amplitude chimera in the network of Stuart–Landau oscillators. (a) The distance between the center of mass of each oscillator and the origin ($r_{c.m.}$). (b) The mean phase velocity which is a flat profile. (c) The phase space of the oscillators in the complex plane, representing the coherent limit cycles centered at the origin and the incoherent limit cycles with different centers of mass. The parameters are $N = 100$, $P = 4$, $\sigma = 14$, $\lambda = 1$ and $\omega = 2$.
Source: Figure reproduced with permission from [237].

The linearized equation, by computing the Jacobean of the system equation at $\chi(t)(D\mathbf{f}(\chi(t)))$, is as follows

$$\delta\dot{x}(t) = D\mathbf{f}(\chi(t))\delta x(t), \tag{127}$$

with the solution

$$\delta x(t) = \mathbf{U}(t)\delta x(0), \tag{128}$$

where $\delta x(0)$ is the initial condition and $\mathbf{U}(t)$ is the monodromy matrix with the property $\mathbf{U}(t+T) = \mathbf{U}(t)\mathbf{U}(T)$, and is obtained from the following equation

$$\dot{\mathbf{U}}(t) = D\mathbf{f}(\chi(t))\mathbf{U}(t), \quad \mathbf{U}(0) = 1. \tag{129}$$

The eigenvalues of the monodromy matrix are called the Floquet multipliers and describe the stability of the periodic solution $\chi(t)$. The Floquet multipliers have the following relation with the Floquet exponents

$$\mu_k = exp(\Lambda_k + i\Omega_k)T. \tag{130}$$

Thus, the periodic solution is unstable if there is only one positive Λ_k.

The results of the Floquet analysis of the Stuart–Landau oscillators, which exhibits amplitude chimera is presented in Fig. 53 [238]. In Fig. 53, the transient time t_{tr} of amplitude chimeras is shown in the coupling parameter plane, (the coupling strength σ and the coupling range r). Therefore, the long-lasting amplitude chimera exists for weak coupling and a large coupling range. The maximum real part of the Floquet exponents Λ of the amplitude chimeras with $t_{tr} > 320$, is illustrated in Fig. 53b. According to this diagram, the amplitude chimera in all of the parameter values has at least one positive Λ. In some cases, there are two positive Λ. The number of Floquet exponents with positive real parts is depicted in Fig. 53c. Therefore, the amplitude chimeras are saddle cycles, which have one or two unstable manifolds.

Bogomolov et al. [135] investigated the spatial transition from the coherence to incoherence in the network of chaotic oscillators with non-local coupling. They studied the bifurcation diagram of the coupled Logistic maps in the plane of coupling strength and coupling range. It was found that the vertical front formation and the chaotic dynamics are necessary and sufficient conditions for the emergence of chimera states. The chaotic dynamics disturbs the phase synchronization of the network and leads to the in-phase and anti-phase oscillations. Therefore, the phase chimera state is formed. Furthermore, the oscillators in the incoherent group have weak chaotic dynamics. While decreasing the coupling strength leads to stronger chaotic behavior in the incoherent domain and creates the amplitude chimera state. The authors have stated that the formation of amplitude chimera is the result of the instability of the chaotic synchronization in the coherent group.

In most of the studies, the patterns of amplitude mediated chimera and amplitude chimera have been observed in distinct networks. However, observation of both amplitude and amplitude mediated chimera has been reported in a network of non-locally coupled Rayleigh oscillators [239]. The increment of the coupling strength leads to the transition of the network's behavior from amplitude mediated chimera to amplitude chimera. This transition occurs at a specific threshold, which is the point of symmetry-breaking pitchfork bifurcations of nontrivial inhomogeneous steady states [239].

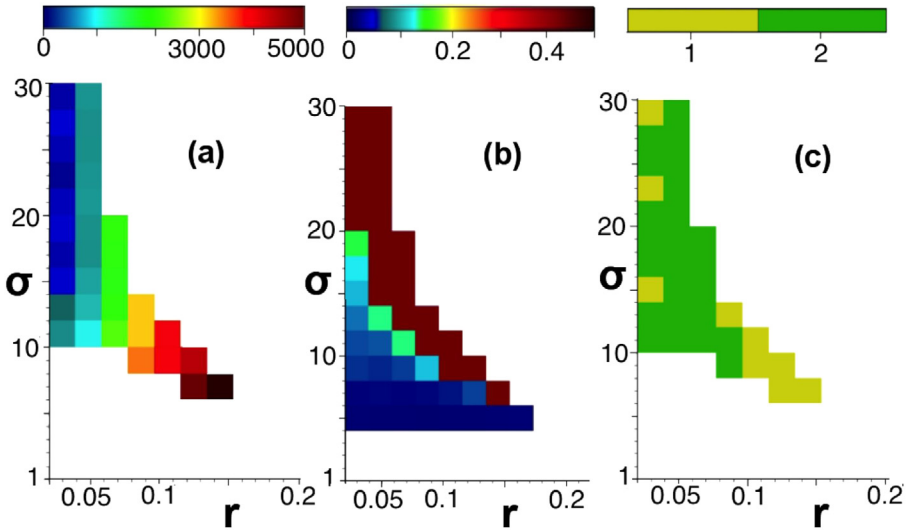

Fig. 53. (a) The transient time of the amplitude chimeras in the network of SL oscillators (Eq. (125)) in the (r, σ) plane. (b) The maximum value of the positive real parts of Floquet exponents (Λ). (c) The number of the positive real parts of Floquet exponents. The parameters are $N = 100$, $\lambda = 1$, and $\omega = 2$.
Source: Figure reproduced with permission from [238].

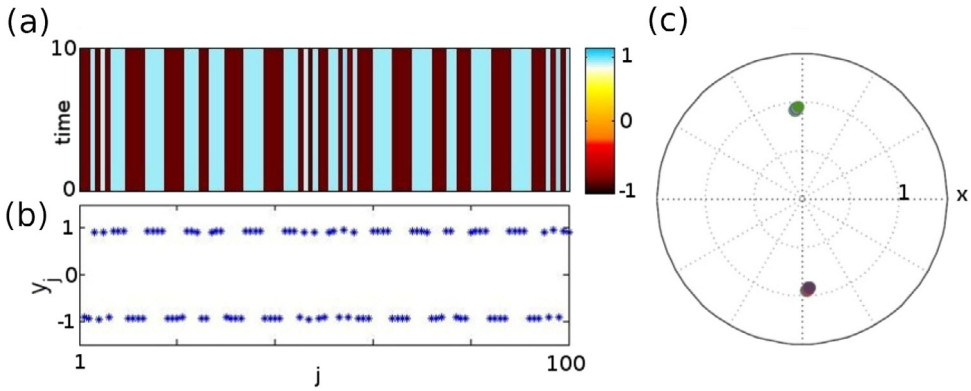

Fig. 54. The chimera death state in the network of Stuart–Landau oscillators (Eq. (125)). (a) The spatiotemporal pattern of the y variables. (b) The time snapshot of the y variables. (c) The phase space of the oscillators in the complex plane, representing two fixed points shifted by a phase π. The parameters are $N = 100$, $P = 5$, $\varrho = 26$, $\lambda = 1$ and $\omega = 2$.
Source: Figure reproduced with permission from [237].

4.7. Chimera death

The oscillation death is a symmetry-breaking phenomenon in the network of coupled self-sustained oscillators. This state is formed by splitting a homogeneous steady state into at least two different branches (upper and lower) [236,237]. Combining the properties of the chimera state and the oscillation death, a new pattern called chimera death is formed. In the chimera death state, there exist two groups of spatially coherent oscillation death (with the same branch of the inhomogeneous steady state) and spatially coherent oscillation death (with random branches in the inhomogeneous steady state) [236].

In the network of the Stuart–Landau (SL) oscillators (Eq. (125)), by varying the coupling parameters, the amplitude chimera disappears, and the chimera death emerges. This state is shown in Fig. 54 for $N = 100$, $P = 5$, and $\sigma = 26$ [236]. The spatiotemporal pattern of the network is shown in Fig. 54a, which represents the existence of multiple clusters of the coherent and incoherent steady states. The time snapshot of the y variables is depicted in Fig. 54b, and the phase portrait of the oscillators in the complex plane is shown in Fig. 54c. Thus, the oscillators are attracted to two fixed points, which are located on the lower and upper branches of the inhomogeneous steady state.

The realistic coupling channels may have dispersion, which leads to behaving as an all-pass filter or has both dissipation and dispersion, which causes a low-pass filtering behavior. Therefore, it is of importance to investigate the appearance of

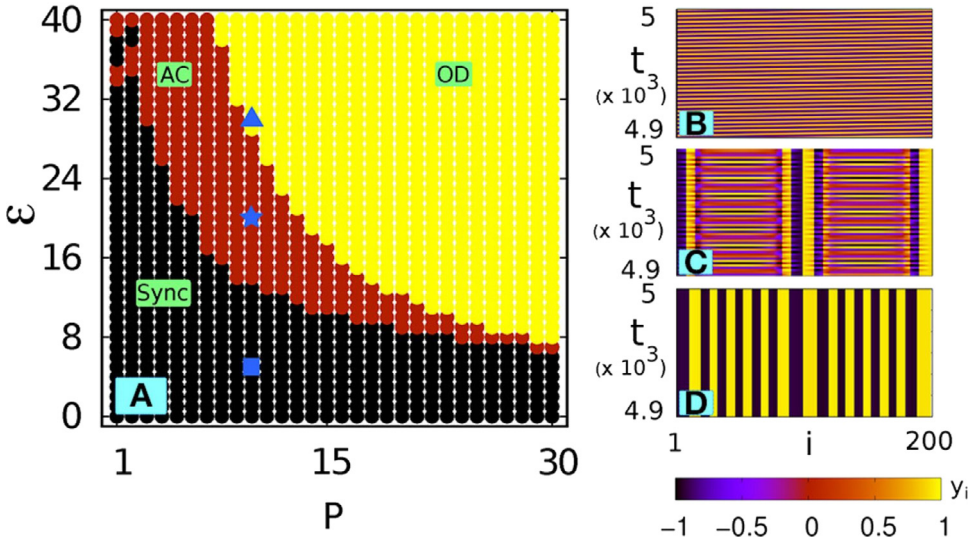

Fig. 55. (A) Different behaviors of the SL network (Eq. (131)) with no filtering in the (P, ε) plane. Sync: synchronization, AC: amplitude chimera, CD: chimera death. (B-D) The spatiotemporal patterns of the network for $P = 10$ exhibiting synchronization for $\varepsilon = 5$ in (B), amplitude chimera for $\varepsilon = 20$ in (C), and chimera death for $\varepsilon = 30$ in (D).
Source: Figure reproduced with permission from [240].

amplitude chimera and chimera death in the presence of local filtering. Considering the network of coupled SL oscillators with non-local symmetry-breaking coupling, the filtering effect can be applied through the self-feedback path in the coupling term [240]. So the equations of the network can be as follows

$$\dot{x}_i = (1 - x_i^2 - y_i^2)x_i - y_i\omega + \frac{\varepsilon}{2P}\sum_{j=i-P}^{i+P}(x_i - \mathbf{U}_i),$$
$$\dot{y}_i = (1 - x_i^2 - y_i^2)y_i + x_i\omega. \tag{131}$$

In the case of $\mathbf{U}_i = x_i$, there is no filtering effect. By setting $\mathbf{U}_i = z_i$, $\dot{z}_i = \alpha(x_i - z_i)$, a low-pass filter will be present in the network, while all-pass filtering can be described by $\mathbf{U}_i = 2z_i - x$, $\dot{z}_i = \alpha(x_i - z_i)$. The parameter α is the cut-off frequency and controls the filtering effects. When there is no filter in the coupling, by increasing the coupling strength and range, the SL network transits from complete synchronization to the amplitude chimera and then to the chimera death. The patterns of the network with no filtering in the (P, ε) plane, is shown in Fig. 55. With considering the filter in the coupling, the regions of the chimeras shrink, and instead, the synchronization appears. Fig. 56 shows the behavior of the network in the presence of low-pass filtering. For larger α values, the network patterns are less affected and the overall behavior of the network is similar to Fig. 55. By decreasing the value of α, the chimera regions are more influenced and the synchronization appears in the wider region. Finally, for very low α values, the chimeras are completely suppressed. Using the all-pass filter instead of the low-pass filter leads to similar results.

The patterns of amplitude chimera and chimera death have also been observed in chaotic oscillators in addition to the limit-cycle oscillators. Xiao et al. [241] studied a network of Lorenz oscillators with repulsive coupling and found that by increasing the coupling strength, the network's behavior changes from spatiotemporal chaos to amplitude chimera, then to the chimera death (or coherent oscillation death), and finally, to the traveling wave states. In this network, the occurrence of the amplitude chimera and the chimera death are also dependent on the initial conditions and coexist in specific coupling strength. In contrast to the coupled Stuart–Landau oscillators, the amplitude chimera and the chimera death states in the Lorenz network are not transient, but stable and long-lasting. Furthermore, the number of coherent clusters in chimeras is related to the number of the nearest-neighbors in coupling with a power law.

4.8. Imperfect chimeras

The imperfect chimera state was firstly observed in a network of the coupled pendula [123]. The network was consisted of N identical pendula, hung from a fixed disc, and coupled non-locally with the two nearest-neighbors. The coupled pendula could show the one-headed and two-headed chimeras. In addition, a special state called imperfect chimera was observed. In this state, a few oscillators (solitaries) in the synchronous cluster of the chimera oscillate differently from the most incoherent oscillators. As an example, the phase space and the frequency spectrum of a solitary pendulum and one pendulum of the synchronous cluster are illustrated in Fig. 57. Fig. 57a shows that the solitary pendulum has a periodic

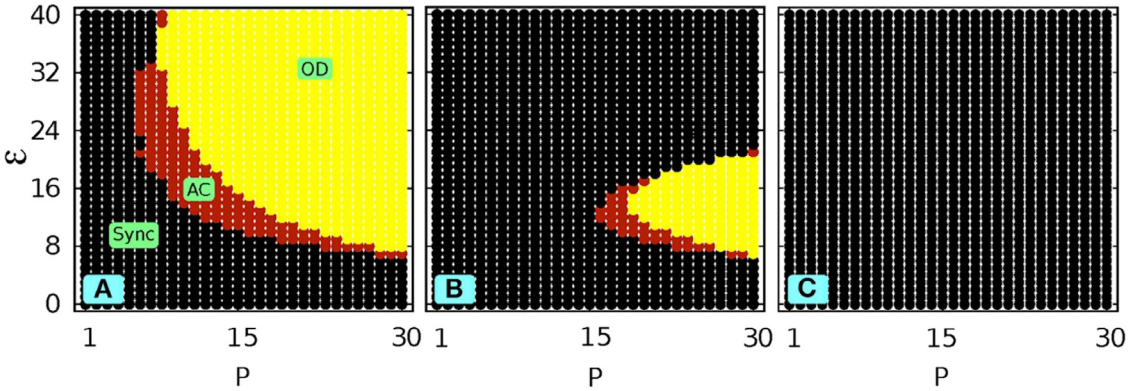

Fig. 56. The phase diagram of the SL network (Eq. (131)) with low pass filtering in the (P, ε) plane for (A) $\alpha = 50$, (B) $\alpha = 20$, (C) $\alpha = 10$. By decreasing α, the amplitude chimera and the chimera death are disappeared.
Source: Figure reproduced with permission from [240].

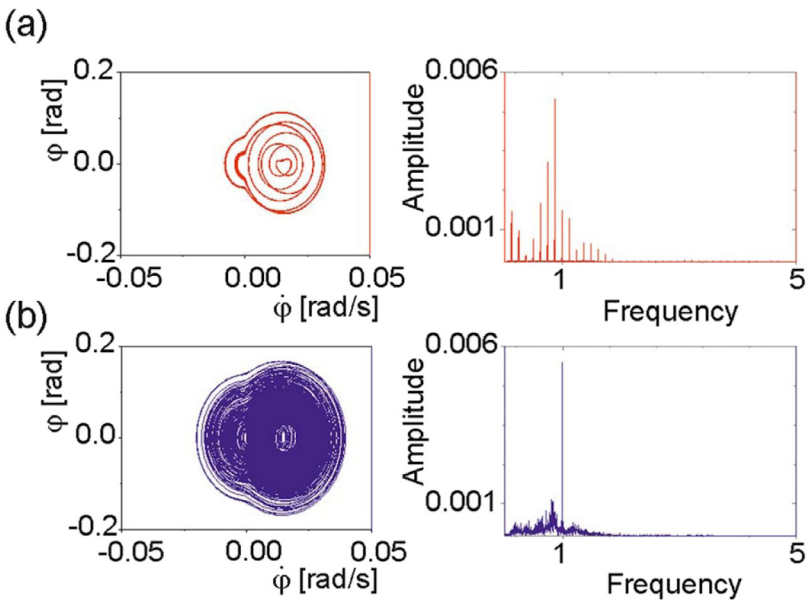

Fig. 57. The phase spaces and the frequency spectra of the pendulums in imperfect chimera. (a) The solitary pendulum. (b) One pendulum of the coherent cluster.
Source: Figure reproduced with permission from [123].

oscillation, while the synchronous pendula have chaotic behavior (Fig. 57b). The existence of the imperfect chimera has also been confirmed experimentally in coupled metronomes.

The imperfect chimera also occurs when some of the oscillators escape from the synchronized cluster of chimera. This type of chimera was found in the network of the Kuramoto model with inertia (pendulumlike elements) [242]. The phase of each element of this network can be given by

$$m\ddot{\theta}_i + \varepsilon\dot{\theta}_i = \frac{\mu}{2P+1}\sum_{j=i-P}^{i+P}\sin(\theta_j - \theta_i - \alpha), \tag{132}$$

where m is the mass of each element, ε denotes the damping coefficient, and μ and α are the coupling strength and the phase lag, respectively. To investigate this network, the parameters were set at $m = 1$, $\varepsilon = 0.1$, $P = 40$ and $N = 100$. The results showed that this network has a transition from a complete synchronous state to a rotating wave by varying the phase lag (α) of oscillators and the coupling strength (μ). But during this transition, the imperfect chimera and multi-headed chimeras appear. Fig. 58 shows the creation of the imperfect chimera in this network. The frequency-time plot (Fig. 58a) shows that initially, the pattern is imperfect synchronization (Fig. 58b), but as time passes, the chimera state is formed, and further, it becomes imperfect (Fig. 58d).

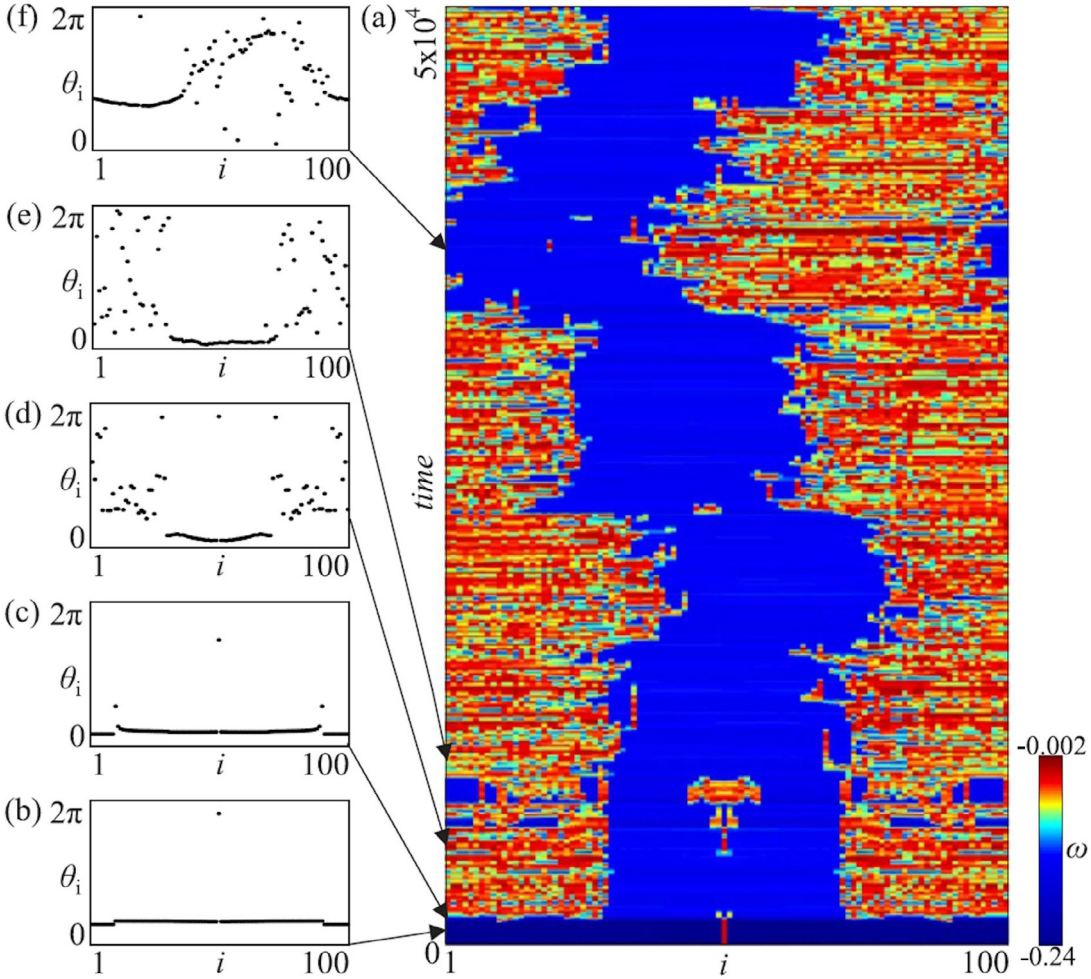

Fig. 58. The formation of the imperfect chimera in the network of the Kuramoto model with inertia, for the phase lag $\alpha = 1.5308$ and coupling strength $\mu = 0.024$. (a) The frequency-time plot. (b–f) The snapshots at different time instants.
Source: Figure reproduced with permission from [242].

4.9. Spiral wave chimeras

The first study of the spiral chimera was done by Kuramoto and Shima on the FitzHugh–Nagumo model [243]. They carried out numerical simulation for different values of coupling strength. They observed that for large values of K, the spiral pattern rotates steadily, and there is nothing anomalous. It means that the center of rotation of the spiral is mapped to a certain fixed point in the phase space. But when the coupling strength K becomes smaller, the overall spiral pattern will change, and the characteristic wavelength, which is comparable with the core radius, becomes smaller. Decreasing K also changes the phase portrait qualitatively. As a result, a neighborhood in the physical space can no longer be mapped to a neighborhood in the phase space. So the spatial continuity of the pattern in the central core will be lost, and some of the oscillators in the core behave individually rather than collectively.

One year later, in 2004, these authors worked on a corrected reduced form of a non-local version of the complex Ginzburg–Landau equation [244]. They noticed that by plotting the mean-field phase on a special cross-section, a critical radius is observable that on its outer domain, the oscillators are coherent, and on the inner domain, they are incoherent. They also realized that the same phenomenon happens in the distribution of the mean frequency. The frequency pattern is clearly separated into two parts. In the outer domain, the frequency of the oscillators is identical, while in the inner field, they have distributed frequencies. Although they did not use the chimera name for describing the observed phenomenon in neither of the two articles, their results showed the existence of spiral waves with a phase-randomized core, which can be called as a spiral chimera.

These spiral patterns were studied further deeply by Kim et al. [245]. They investigated the effect of phase-shifted coupling on the dynamics of a two-dimensional array of coupled oscillators and founded many interesting patterns. They

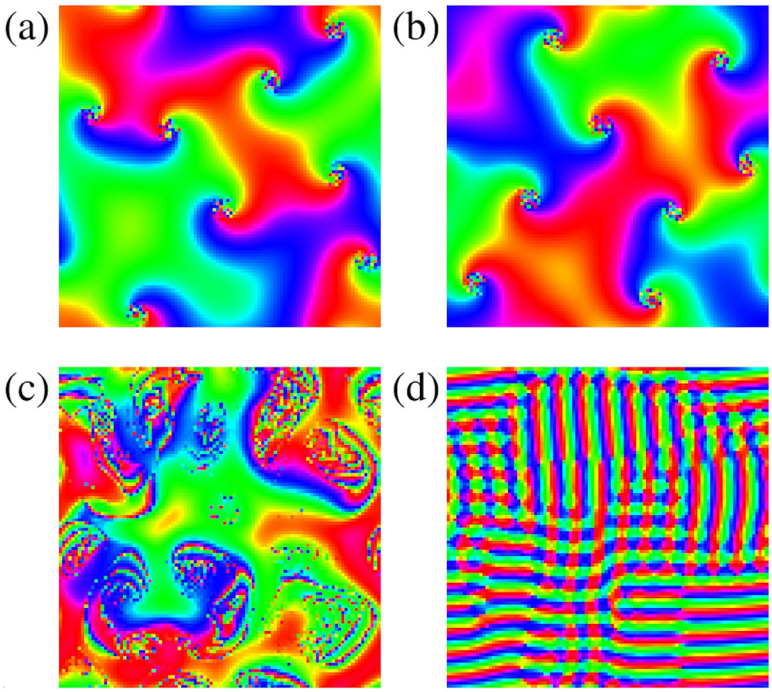

Fig. 59. Patterns in the 2D network of Eq. (133) with $R = 6$ and different α values. (a) $\alpha = 0.2\pi$: spiral chimera, (b) $\alpha = -0.2\pi$: anti-spiral chimera, (c) $\alpha = 0.4\pi$: irregular pattern, (d) $\alpha = \pi$: plane waves coexisting with square-like pinwheels.
Source: Figure reproduced with permission from [245].

introduced a finite interaction radius as realistic coupling and studied over the whole range of phase shifts with the equations below

$$\frac{d\Theta_{ij}}{d\tau} = \frac{1}{N(R)} \sum_{mn}{}' \sin(\Theta_{mn} - \Theta_{ij} - \alpha), \tag{133}$$

where $\theta_{ij} \to \omega t + \Theta_{ij}$ indicates the phase of the oscillator at position (i, j) on a two-dimensional network. ω is the natural frequency so Θ_{ij} maintains the spatial pattern as θ_{ij}, but not temporal behaviors.$\sum_{mn}{}' \equiv \sum_{mn,0<r_{mn,ij}\leq R}$, where $r_{mn,ij}$ is the distance between two oscillators located at (i, j) and (m, n). $N(R)$ shows the number of the neighbors of each oscillator within a finite distant R. $t \to \frac{\tau}{K}$ that K is the coupling strength between oscillators. α is the phase shift in a way that $|\alpha| < \pi/2$ leads to in-phasing of the two oscillators, whereas $|\alpha| > \pi/2$ leads to their anti-phasing. In this equation, α and R are the only control parameters.

The simulations of this network showed that the emerging pattern is very sensitive to the value of α, when $R = 1$. In case $R > 1$, the non-locality of interactions inflicts several changes on patterns and leads to the formation of some asynchronous parts. Fig. 59 illustrates the network patterns for $R = 6$. It is observable that non-local interactions develop (anti)spirals with a phase-randomized core (Fig. 59a,b), which are not obtained with $R = 1$. It can be observed that the long-range coupling of oscillators, which have a broad frequency range due to the gradient of effective frequency near the core, results in the incoherence in the cores. Further increasing of α, creates irregular patterns consisting of incoherent phases (Fig. 59c). For $|\alpha| > \pi/2$, plane waves and square-like pinwheels exist in the network (Fig. 59d). In conclusion, this study shows that by changing α various spatial patterns emerge, and unravel that the symmetry properties of the system play an important role in the formation of patterns.

5 years later, C. R. Laing [108] worked on the same system (Eq. (133)) with non-local interactions, while most of the previous studies of spiral waves were based on the local coupling. They used the Ott–Antonsen ansatz and derived a probability density function to define the dynamics of the network. In 2010, Martens et al. [246] studied the spiral wave chimeras analytically and computed the radius of the incoherent core and the rate of rotation by using the perturbation theory. In addition to the simple oscillatory systems, the spiral wave chimera has also been discovered in oscillators with complex and chaotic dynamics [31]. One of the general properties of the period-n spiral waves is the creation of the synchronization defect lines (SDLs), which divide the regions of different oscillation phases. An investigation of a two-dimensional network based on the Rössler model revealed that the SDLs are also available in spiral wave chimeras [247]. The SDLs can be discovered by the absolute temporal change in the X field between neighboring points of the network, where X is the first variable of the Rössler system. Fig. 60 shows the formation of spiral waves with asynchronized cores

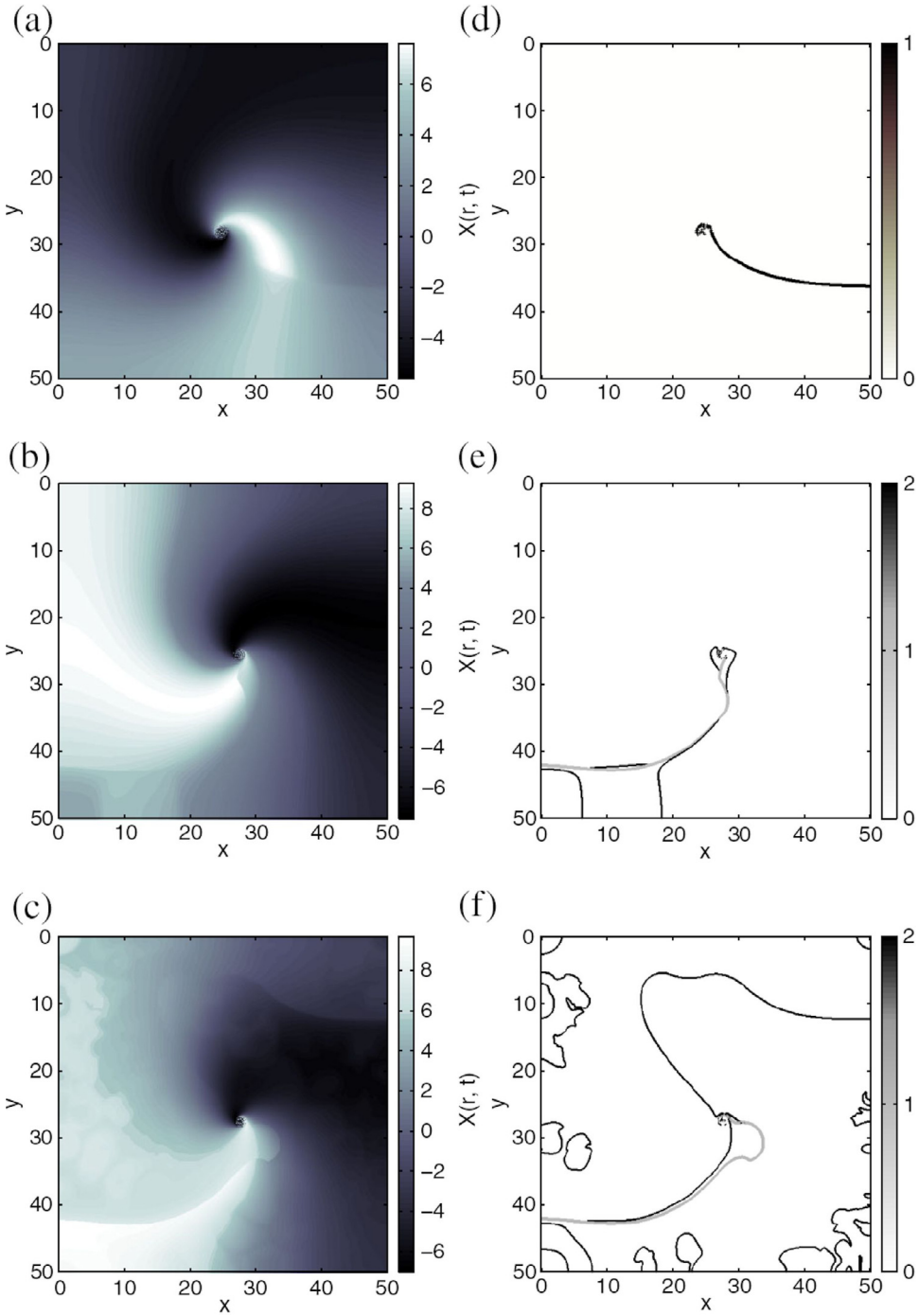

Fig. 60. The time snapshots of the X variables of the Rössler oscillators in 2D network. (a) The local dynamics of the oscillators is period-2, (b) The local dynamics of the oscillators is period-4, (c) The local dynamics of the oscillators is chaotic. (d–f) The SDLs corresponding to the parts (a–c). *Source:* Figure reproduced with permission from [247].

in the left panel, and the SDLs in the right panel. In the SDL figures, the nonzero values show the existence of the SDL between the neighboring nodes, and the integer indicates the period of the SDL. Fig. 60a shows a period-2 spiral wave, which has a period-1 SDL shown in Fig. 60d. In Fig. 60b, the spiral wave is period-4, and it has period-1 and period-2 SDLs. In Fig. 60c, the local dynamics of the nodes is chaotic. It is observed that in this case, SDLs with period-1 and period-2 exist.

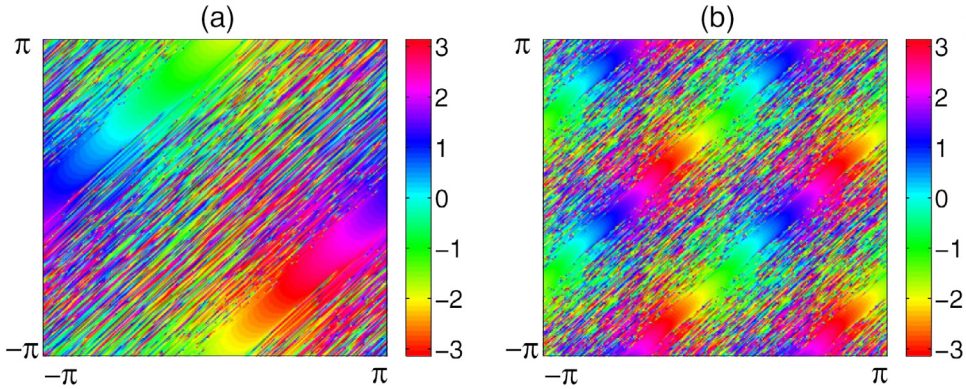

Fig. 61. Snapshots of the phase patterns of the 2D network of Eq. (134) showing the twisted chimera states with $\beta = 0.05$, $N = 256$, and random initial conditions. (a) $G_x = G_y = G_1^{(1)}$. (b) $G_x = G_y = G_2^{(1)}$.
Source: Figure reproduced with permission from [248].

5. Chimeras and network topology

Most of the studies that have been done so far in the field of chimera are on one-dimensional ring network. This is the simplest model that can be considered for the coupled oscillators. On the one hand, the network is one-dimensional, and the computational cost is less than two-dimensional or more complex networks. On the other hand, all elements are symmetric, which simplifies the expressions of the dynamic of oscillators and their connection. But it is evident that this topology is elementary and cannot provide a sufficiently accurate model of real-world phenomena. Therefore, after a while, researchers began to study the chimera state in more complex networks that can provide a more accurate model of real events, including the neural network in the human brain. In this section, we review the complex structures of networks that exhibit the chimera state.

5.1. Two-dimensional networks

Recently, the researchers have worked on the chimera state in two-dimensional arrays by different coupling functions [59,248,249]. Like one-dimensional systems, most of the studies are focused on phase oscillators. The first observations of the chimera states in two-dimensional networks refer to the discovery of spiral wave with incoherent phases in the spiral cores, which was explicitly described in the spiral wave chimera section.

One of the recent studies of chimeras in 2D networks is the investigation done by Xie et al. [248] in 2015. They studied twisted chimera states and multicore spiral chimera states on an oscillator array on a two-dimensional torus. They used the following equation for the phase $\theta(x, y, t)$

$$\frac{\partial\theta(x,y,t)}{\partial t} = -\int_{-\pi}^{\pi}\int_{-\pi}^{\pi} G(x-x', y-y') \times \sin[\phi(x,y,t) - \phi(x',y',t) + \alpha]dx'dy'. \tag{134}$$

For the system to be analytically tractable, it was supposed that the coupling kernel G is decomposed of $G(x, y) = G_x(x)+G_y(y)$ where G_x and G_y are functions representing the coupling in the x and y directions, respectively. By considering G_x and G_y as follows, the twisted chimeras and a variety of spiral wave chimeras were observed on the two-dimensional torus with random initial conditions

$$G_n^{(1)}(x) \equiv \cos(nx), \quad G_n^{(2)}(x) \equiv \cos(nx) + \cos[(n+1)x]. \tag{135}$$

The twisted chimera states are obtained when the coupling kernels are $G_x = \cos(nx)$ and $G_y = \cos(ny)$. Fig. 61 shows two examples for this type of chimera in case $n = 1, 2$ and $\beta \equiv \pi/2 - \alpha = 0.05$. In these situations, the coherent clusters form bounded stripes on a torus. Also, the phase changes monotonously along with the stripes. In Fig. 61a, there is only one strip wrap in the x (or y) direction, while Fig. 61b shows two twisted chimeras.

Furthermore, many stable configurations of multicore spiral wave chimera states are observed in this system for larger values of β. As mentioned before (in Section 4.9), spiral wave chimera is an incoherent core surrounded by spiral arms consisting of phase-locked oscillators. Fig. 62 shows three examples of spiral wave chimeras observed in the network of Eq. (134) with $G_1^{(1)}$ and different values of β.

In 2017, Schmidt et al. [250] discussed chimera patterns in two networks with different models relating to the neuronal spiking activity, FitzHugh–Nagumo (FHN) and Leaky Integrate-and-Fire (LIF) oscillators. It was assumed that the oscillators

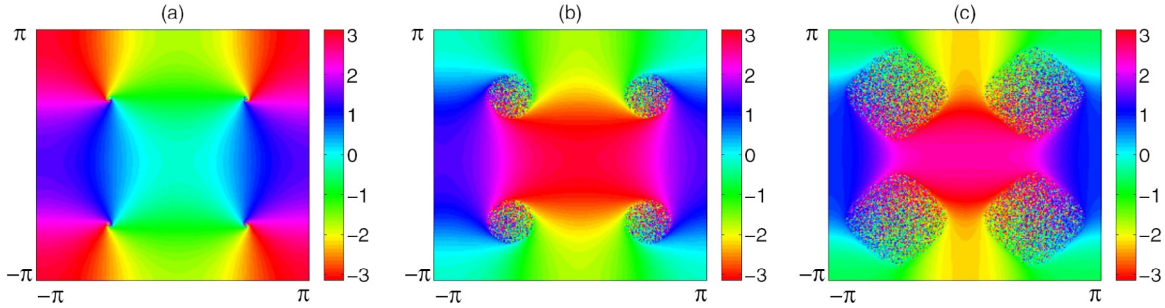

Fig. 62. Snapshots of the phase patterns of the 2D network of Eq. (134) showing the spiral chimeras. (a) $\beta = 1.5$. (b) $\beta = 1$. (c) $\beta = 0.5$. *Source:* Figure reproduced with permission from [248].

are non-locally phase coupled in two-dimensional toroidal geometry. They considered a two-dimensional $N \times N$-network with $N = 100$ nodes in a ring. The network of FHN oscillators is defined as

$$\begin{aligned} \epsilon \frac{dx_{ij}}{dt} &= x_{ij} - \frac{x_{ij}^3}{3} - y_{ij} + \frac{\sigma}{N_r - 1} \sum_{(m,n)\in B_r(i,j)} [b_{xx}(x_{ij} \\ &\quad - x_{mn}) + b_{xy}(y_{ij} - y_{mn})], \\ \frac{dy_{ij}}{dt} &= x_{ij} + a + \frac{\sigma}{N_r - 1} \sum_{(m,n)\in B_r^{FHN}(i,j)} [b_{yx}(x_{ij} - x_{mn}) \\ &\quad + b_{yy}(y_{ij} - y_{mn})], \end{aligned} \tag{136}$$

with considering $a = 0.5$, which locates the system in the oscillatory regime. The parameter ϵ, which determines the timescale separation, is fixed at $\epsilon = 0.05$ and the coupling strength at $\sigma = 0.1$. The network is considered in a way that all oscillators (x_{ij}, y_{ij}) are identical and coupled isotropically to all other oscillators in a circular neighborhood given by

$$B_r^{FHN}(i,j) = \{(m,n) : (m-i)^2 + (n-j)^2 \le r^2\}. \tag{137}$$

The coupling between the x- and y-variables is defined as follows

$$B = \begin{pmatrix} b_{xx} & b_{xy} \\ b_{yx} & b_{yy} \end{pmatrix} = \begin{pmatrix} \cos\varphi & \sin\varphi \\ -\sin\varphi & \cos\varphi \end{pmatrix}, \tag{138}$$

where the coupling phase $\varphi \in [0, 2\pi]$ allows diagonal or direct coupling, cross-coupling, and mixed-coupling scenarios. The coupling phase φ corresponds to the parameter α in the Kuramoto system, and the mapping from φ to α is by phase-reduction technique.

The LIF model is described by a single dynamical variable (u) that can be considered as a membrane potential of the cell and a threshold value (u_{th}) which the potential value is reset to the rest (u_{rest}) when reached to that. The constant value μ is $\mu \ge u_{th}$ for consistent oscillatory motion, so μ represents the maximum possible u value. There is also a refractory period (p_r) that the LIF element is held at the resting potential during that

$$\begin{aligned} &\tfrac{du}{dt} = \mu - u, \\ &\lim_{\varepsilon\to 0} u(t+\varepsilon) \to u_{rest}, \text{ when } u \ge u_{th}. \end{aligned} \tag{139}$$

They considered a two-dimensional $N \times N$ network with $N = 100$ nodes in a square of side $2R + 1$ with the equation below

$$\frac{du_{ij}}{dt} = \mu - u_{ij} + \frac{\sigma}{N_R - 1} \sum_{(m,n)\in B_R^{LIF}(i,j)} [u_{ij} - u_{mn}], \tag{140}$$

where the neighborhood of each node u_{ij} with $i, j = 1, \ldots, N$ is as follows

$$\begin{aligned} B_R^{LIF}(i,j) = \{(m,n) &: i - R \le m \le i + R \\ &\wedge j - R \le n \le j + R\}. \end{aligned} \tag{141}$$

To observe the synchronous state of the system, they used the mean phase velocity variable which is defined as $\omega_{ij} = 2\pi c_{ij}(\Delta t)/\Delta t$ where $c_{ij}(\Delta t)$ is the number of periods that the oscillator (i,j) has completed in a time interval Δt. They observed different kinds of chimera pattern in both networks, such as spots and ring patterns, stripes, and grid patterns. We bring here an example of spot chimera in the FHN system and a case of grid chimera in the LIF network.

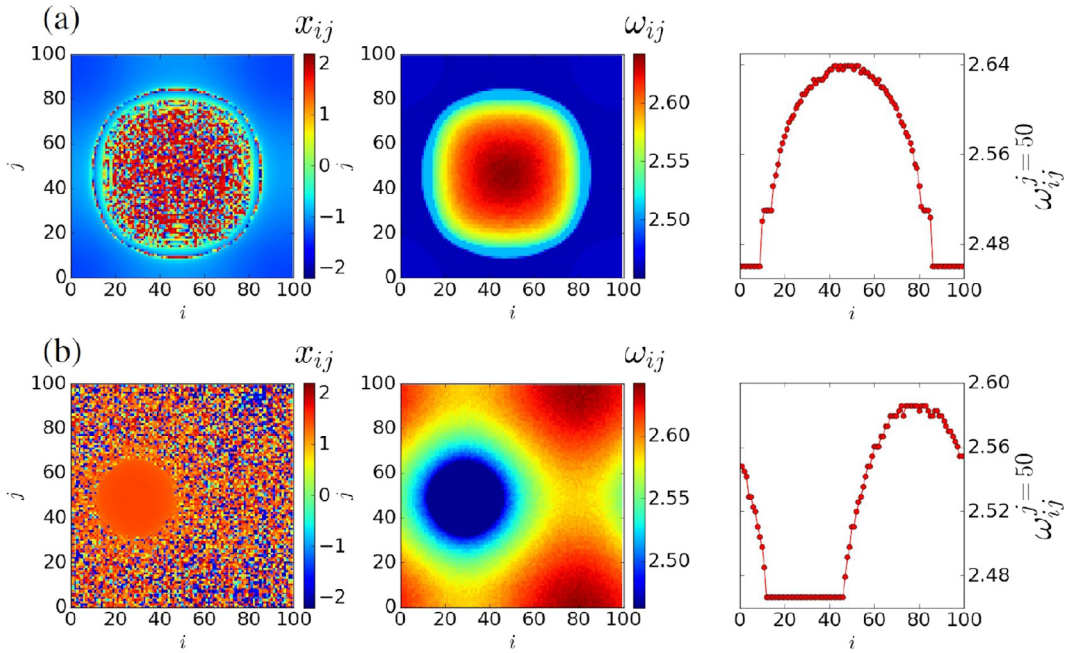

Fig. 63. Spot-pattern of chimera states in the 2D FHN network. (a) Incoherent-spot for $r = 33$, $\varphi = \pi/2 - 0.2$. (b) Coherent-spot for $r = 42$, $\varphi = \pi/2$. The left panel shows the snapshots at $t = 2000$; the center panel shows the mean phase velocity ω_{ij} and the right panel shows a horizontal cut of ω_{ij}.
Source: Figure reproduced with permission from [250].

Fig. 63 shows incoherent and coherent spot chimera state in the FHN model. Fig. 63a shows a single-headed incoherent spot surrounded by coherent oscillators. The left panel shows a snapshot of x_{ij} at $t = 2000$. The center panel and the right panel depict the mean velocity ω_{ij} over 1000 time units and a horizontal cut of ω_{ij} through the center of the spot, respectively. Another chimera spot pattern is a spot with a coherent center, which is shown in Fig. 63b. In both examples, it is obvious that the ω_{ij}-values are lower in the coherent area than in the incoherent region.

Fig. 64 shows the grid chimera patterns for high coupling values in the LIF network with random initial conditions. The left panel depicts the snapshots of u_{ij}. The corresponding mean phase velocities are shown in the middle panels, and a section of mean phase velocities is shown in the right panel. Fig. 64a illustrates a 36-headed chimera located in a $6 * 6$ square, and Fig. 64b shows a 12-headed chimera organized in two horizontal double-spotted bands, each with six incoherent regions.

This study indicated that even though the dynamics of the neurons in two networks are different, the chimera states happen in both networks in the case of non-local coupling. It seems that the characteristics of the coherent/incoherent patterns follow a general rule. For instance, by increasing the coupling range in both models, the diameter of the ring patterns grows linearly.

2D chimera pattern has also been studied in the network of neuronal systems with local coupling through the nearest-neighbor method and non-linear coupling function [251]. In [251], the authors considered a network of Stuart–Landau (SL) oscillators, a network of Hindmarsh–Rose neurons, and a network of Rulkov maps. They observed chimera phenomena in all networks by numerical simulation. Also, the occurrence of chimera in the SL oscillators' network was analytically verified through Ott–Antonsen method, which is generally used for the non-identical systems. Their study has shown that the nonlinear coupling plays a crucial role in the emergence of chimera states in 2D lattices of locally coupled oscillators and can remove the restriction of non-locality in the coupling topology.

5.2. Three-dimensional networks

Some years after the studies of two-dimensional networks, a question arose that whether the chimera states can exist in three dimensions. And, what shapes can 3D chimeras have, or how robust are they? Since many interesting chimera patterns were observed in the Kuramoto model in two-dimensional systems, some groups started studying these oscillators in three-dimension [252–254]. In 2015, Maistrenko et al. worked on non-locally coupled Kuramoto models placed in a 3D cube with periodic boundary conditions to answer these questions [253]. The Kuramoto system in three

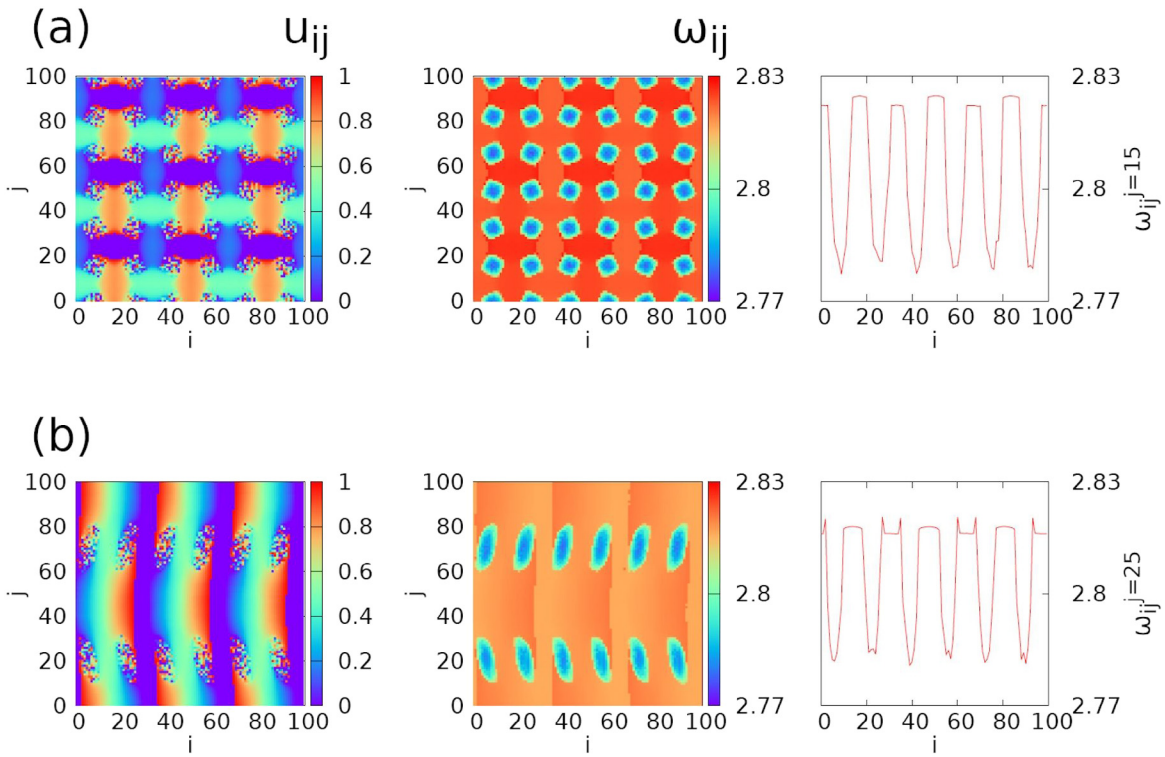

Fig. 64. Grid chimera and double-spotted chimera in the LIF system. The left panels show the snapshot of the variable u_{ij}, the center panels show the mean phase velocity of left panels, and the right panel show sections of mean phase velocities. Parameters are set at $R = 22$, $\sigma = 0.7$, $\mu = 1.0$, $N = 100$, and $p_r = 0.22T_s$, where T_s is the period between two resets.
Source: Figure reproduced with permission from [250].

dimensions is described by these equations

$$\begin{aligned} \dot{\varphi_{ijk}} &= \omega \\ &\quad + \frac{K}{P^3} \sum_{(i',j',k') \in B_p(i,j,k)} \sin(\varphi_{i'j'k'} - \varphi_{ijk} - \alpha), \\ B_p(i,j,k) &:= \{(i',j',k') : (i-i')^2 + (j-j')^2 \\ &\quad + (k-k')^2 \le P^2\}, \end{aligned} \tag{142}$$

where φ_{ijk} is the phase variable, $\omega = 0$ is the natural frequency, $K = 1$ is the coupling strength, and $\alpha \in [0, \pi/2]$ is the coupling lag. Each oscillator φ_{ijk} is coupled with equal strength K to all its nearest-neighbors $\varphi_{i'j'k'}$ within a range P to those oscillators located in a ball-like area around it. The distances $i' - i$, $j' - j$, and $k' - k$ are calculated regarding the periodic boundary conditions of the network. Here, α is one of the control parameters, and the other control parameter is the coupling radius, which is defined as $r = P/N$ and varies from $1/N$ (local coupling) to $r = 0.5$ (close to global coupling). In this model, the chimera state arises with a non-local coupling that means r should get an intermediate value between $1/N$ and 0.5. $N = 50$ is the number of oscillators in each side of the square; therefore the network size is equal to N^3 =125,000. Fig. 65 illustrates four different patterns of 3D chimera in the Kuramoto network. These patterns are an asynchronous ball (Fig. 65a) and tube (Fig. 65b) in a synchronous surrounding, and a synchronous ball (Fig. 65c) and tube (Fig. 65d) in an asynchronous surrounding. These chimera types are the three-dimensional counterparts of strip and spot chimeras in two dimensions, which were described in the previous section. They also found cross-chimeras, sandwiched-like chimeras, scroll wave chimera, and also a two-rolls chimera state in the Kuramoto network for different parameters.

The authors continued to study this network in more depth, and a little while later, they reported observation of cascade of scroll wave chimeras with multiple incoherent rolls, cascades of multiple Hopf links, and trefoils, hybrid scroll wave chimeras, single-linked and double-linked chimera states [254].

3D chimera has also been studied by Kasimatis et al. [255] on a similar network structure of LIF oscillators. They found different chimera patterns such as spheres (a generalization of the 2D spot chimera and the 1D single chimera pattern),

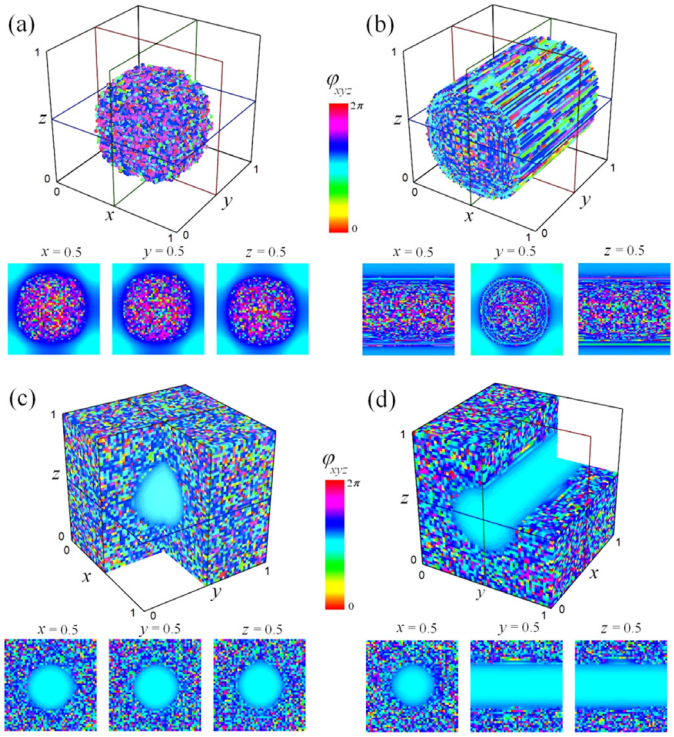

Fig. 65. Three-dimensional chimera state in Kuramoto network with random initial conditions. Snapshot of the phase distributions φ_{ijk} are shown. (a) Asynchronous ball ($\alpha = 1.15$, $r = 0.28$). (b) Asynchronous tube ($\alpha = 1.305$, $r = 0.334$). (c) Synchronous ball ($\alpha = 1.53$, $r = 0.39$). (d) Synchronous tube ($\alpha = 1.49$, $r = 0.43$). In the bottom panel the cross-sections in coordinates $x_i = i/N, y_j = j/N, z_k = k/N$ are shown.
Source: Figure reproduced with permission from [253].

layers (a generalization of the 2D single and multiple layers), and cylinder grids (a generalization of the 2D grid). Besides, they found some other patterns that do not have an equivalent in 2D networks like cylindrical and cross-layered chimeras.

Recently, Kundu et al. extended their two-dimensional network study (explained well in the previous section) [251] to 3D networks. They studied chimera phenomena in a cubic network of coupled Stuart–Landau (SL) limit cycle oscillators and Hindmarsh–Rose neuronal oscillators with local interaction topology [61]. Again, it was shown that the nonlinearity presence in the interaction function acts as an essential condition for the existence of chimera states in a network with local connections. They also demonstrated the existence of chimera state analytically through the approach of Ott–Antonsen in the SL oscillators' network.

5.3. Multilayer networks

The multilayer networks can demonstrate a variety of communications and multilevel interactions. Thus, it seems that they can provide more accurate and sophisticated models for real-world phenomena. The multilayer framework creates a platform for studying a situation in which the function of one layer gets affected by the properties of other layers. Some researchers believe that the neural network in the cortex has a multilayer structure [256]. In general, the multilayer network model consists of nodes having two types of links. The first type establishes the interaction between the nodes located in the same layer. The second one determines the intersection of dynamical elements between layers. Depending on the specific purpose of the multilayer configuration, the interconnection between layers may be quite different [257]. Studying chimera in multilayer networks has attracted a lot of attention in recent years [258–261]. In many studies, researchers have considered a framework consisting of two or three layers, where each layer is a ring of non-locally coupled identical oscillators [262–264].

We start the explanation of this part by examples of two- and three-layer networks of Kuramoto–Sakaguchi phase oscillators. The networks are considered in two cases of the homogeneous multilayer network, where all the oscillators are identical, and the heterogeneous multilayer network, where all the oscillators in each layer are identical but there exist parameter mismatches between the layers [257]. Interestingly, it was obtained that in the heterogeneous network, one layer can be in the chimera state, while the other layer is in either the coherent state or the incoherent state. If the coherent oscillators have the same indexes in all the layers, it is called "synchronous chimera state", but if the indexes are different, it is called "asynchronous chimera state". Re-emergence of synchronous chimera state or inter-layer chimera

state has also been discovered for larger inter-layer coupling. Interaction between two layers of the network has also been studied analytically by applying the Ott–Antonsen approach, and it has been shown that increasing the strength of the inter-layer coupling can prove the possibility of excitation of the inter-layer chimera state. Extending the results to a three-layer multiplexing network demonstrated an enhancement of the stability of chimera states by the inter-layer interactions [65].

One of the parameters which bring the simulation closer to reality is the time delay. Beforehand some studies have investigated the effect of time delay on the emergence of the chimera state in one-dimensional networks [265]. The intra-layer time delay in the multiplex network causes a special type of chimera, called "layer chimera state", which is unique to the delayed multiplex systems [266]. The emergence of a chimera state in these networks is dependent on the parity of the delay. One of the examples of the studies on this content is a triplex network (multiplex network with three layers) with time delay in the inter-layer coupling, where each layer consist of a ring of non-locally coupled identical FitzHugh–Nagumo (FHN) oscillators [267]. This study showed that the delay is a powerful tool for controlling the system's pattern and can be used to construct different scenarios for synchronization and chimeras.

Ghosh et al. [268] also studied the emergence of chimera states in multilayer rings. For this research, they discussed two different cases: (1) a multiplex network having two homogeneous layers with different connectivities, (2) a multiplex network consisting of one homogeneous and one inhomogeneous layer. In both cases, each layer has N nodes. They considered a discrete-time Logistic map $z_i(t+1) = \mu z_i(t)(1 - z_i(t))$ in the chaotic regime ($\mu = 4$) for describing the dynamic of each node of the network with the following equation

$$z_i(t+1) = f(z_i(t)) + \frac{\varepsilon}{(k_i+1)} \sum_{j=1}^{2N} A_{ij}[f(z_j(t)) - f(z_i(t))], \tag{143}$$

where f describes the Logistic map equation. A is the adjacency matrix that can be expressed as

$$A = \begin{pmatrix} A^{(1)} & I \\ I & A^{(2)} \end{pmatrix}, \tag{144}$$

where $A^{(1)}$ and $A^{(2)}$ are $N \times N$ dimension matrices that represent the adjacency matrix of the first and second layers, respectively, such that $A_{ij} = 1$ if the nodes i and j are connected and $A_{ij} = 0$ if they are not. I is an $N \times N$ identity matrix representing the interactions between the two layers. $k_i = \sum_{j=1}^{N} A_{ij}$ is the degree of the ith node in its own layer, and $0 \le \varepsilon \le 1$ is the overall coupling constant. The observations showed that multiplexing of these two homogeneous non-local rings results in the emergence of chimera state in the whole network, while there is no chimera in the single layer with the same parameters. Furthermore, by increasing k in the second layer (intensifying the second layer), the chimera state in the first layer is enlarged.

For identifying chimera states clearly, a normalized probability distribution function $g(|\bar{D}|)$ of the Laplacian distance measure $|\bar{D}(t)|$ was used, where $|\bar{D}(t)|$ is a vector with components

$$d_i(t) = |(z_{i+1}(t) - z_i(t)) - (z_i(t) - z_{i-1}(t))|. \tag{145}$$

They defined the correlation measure as

$$g_0(t) = \int_0^{\delta} g(|\bar{D}(t)|) d(|\bar{D}(t)|), \tag{146}$$

where the upper limit δ denotes a small positive threshold value. This measure essentially evaluates the relative size of spatially coherent regions, and ideally, an intermediate value between 0 and 1 indicates a chimera state. However, numerical results show that $0.4 \le g_0 \le 0.8$ is the best estimation of the parameter regime displaying chimera states. Fig. 66 demonstrates a diagram of the correlation measure g_0 in the plane of the node degree ($k^{(1)}$) and ε. In Fig. 66a, the node degree (k) in both layers are the same, but in Fig. 66b, the node degree of the second layer is fixed to $k^{(2)} = 64$ and only the node degree of the first layer is variable. Fig. 66b shows that for large $k^{(1)}$, where both layers are dense, the chimera state can only be found in a small range at intermediate values of ε (light color in Fig. 66b). Also, a comparison between the left part of Fig. 66a and Fig. 66b shows that in a parameter regime of large ε, when a sparse layer (low $k^{(1)}$) is multiplexed with a denser layer ($k^{(2)} = 64$) the chimera state appears, while it could not be found when both layers are sparse (Fig. 66a).

In the next step, the multiplexing of a homogeneous 1D lattice with an inhomogeneous random network has been studied. Two different types were assumed for the inhomogeneous layer: Erdös–Rényi (ER) network and scale-free (SF) network. The interesting phenomenon in this part is that unlike the case of two sparse homogeneous layers, if one layer is represented by a random connection architecture, the homogeneous layer exhibits chimera for the same connection density. It means that the sparse layer, which does not exhibit chimera upon multiplexing with a sparse homogeneous layer, starts displaying chimeras when multiplexed with a sparse inhomogeneous layer in both cases of ER and SF network. In conclusion, this study showed the effect of the connection density and the coupling architecture as control parameters on the emergence of the chimera state. Also, the effect of the changes in the mean node degree of one layer on the appearance of chimera patterns in another layer was investigated.

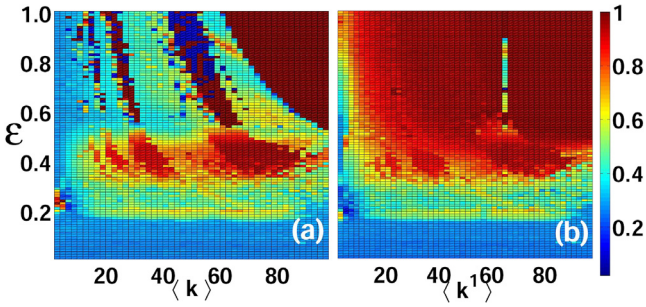

Fig. 66. The normalized correlation measure g_0 (Eq. (146)) of the first layer of the multiplex network of Logistic maps Eq. (143), in the $(k^{(1)}, \varepsilon)$ plane. (a) The node degrees of the layers are the same. (b) The node degree of the second layer is fixed at $k^{(2)} = 64$. The parameters are fixed at $N^{(1)} = N^{(2)} = 100$ and $\delta = 0.01$.
Source: Figure reproduced with permission from [268].

As mentioned in Section 2.6 neuronal networks are one of the most significant biological phenomena in which chimera has been studied. As multilayer networks can provide more accurate and sophisticated models for stimulating real-world neuronal networks, some researches focused on this concept. Ref. [269] presented a two-layer Hindmarsh–Rose neuronal network, one layer composed of N non-locally coupled and the other layer made up of N uncoupled neurons. Each isolated neuron in the uncoupled layer is connected directly with one neuron (its replica) in the coupled layer. The results show that as the intensity of the coupling between the layers increases, the neurons of each layer became more coordinated and go from the incoherent state to the chimera. Then by more increasing the coupling strength, they show cluster synchronization, and eventually, the full synchronization happens. To ensure that the network behaves as described, the strength of incoherence (SI) was performed. This measure was also used for studying a multiplex network of Hastings–Powell oscillators [270]. Moreover, a transmission delay (τ) between the layers is considered in the network, and proper delays for obtaining chimera states have been found in cases that the instantaneous interaction between layers is unable to show chimeras.

One of the other frameworks for studying chimera dynamics in multilayer neuronal networks is a bipartite network of non-locally coupled oscillatory FHN systems [271]. The bipartite network is a special type of multiplex network in which there is no interaction between nodes in the same layer. In this structure, the $2N$ identical FHN oscillators are divided into two rings, each of which having N oscillators in a way that the ith units in layers 1 and 2 are mirror units. Each oscillator in layer 1 interacts with $2R$ nearest-neighbors of its mirror oscillator in layer 2 and vice versa. The equation of the bipartite network of non-locally coupled FHN oscillators is as follows

$$\begin{aligned} \varepsilon \dot{u}_i^\alpha &= u_i^\alpha - \frac{(u_i^\alpha)^3}{3} - v_i^\alpha \\ &\quad + \frac{\sigma_\alpha}{2R_\alpha + 1} \sum_{j=i-R_\alpha}^{i+R_\alpha} [C_{uu}(u_j^\beta - u_i^\alpha) + C_{uv}(v_j^\beta - v_i^\alpha)], \\ \dot{v}_i^\alpha &= u_i^\alpha + a \\ &\quad + \frac{\sigma_\alpha}{2R_\alpha + 1} \sum_{j=i-R_\alpha}^{i+R_\alpha} [C_{vu}(u_j^\beta - u_i^\alpha) + C_{vv}(v_j^\beta - v_i^\alpha)], \end{aligned} \tag{147}$$

where the superscripts α and β indicate layers $\alpha = 1$ and $\beta = 2$. The positive parameter $\varepsilon = 0.05$ separates the time scales of the dynamics of the variables u and v. The value of the parameter a is considered $a = 0.5$, which puts the neuron in an oscillatory state. σ and R denote the strength and range of non-local coupling, respectively, which are the control parameters in this model. The coupling matrix here is considered as follows which depends on a single parameter ϕ (set at $\phi = \pi/2 - 0.1$)

$$C = \begin{pmatrix} C_{uu} & C_{uv} \\ C_{vu} & C_{vv} \end{pmatrix} = \begin{pmatrix} \cos\phi & \sin\phi \\ -\sin\phi & \cos\phi \end{pmatrix}. \tag{148}$$

To better show the chimera state on the network, they used the mean phase velocity of the FHN units. They considered two different modes for the network: homogeneous bipartite networks and heterogeneous bipartite networks. In homogeneous networks, the coupling strength (σ) and the coupling range (R) are assumed to be the same for both layers. While in heterogeneous networks, it is not necessary to establish this condition. The 1-cluster, 2-cluster, and 3-cluster chimera states can be observed for different combinations of σ and R in the homogeneous networks. Interestingly, in contrast to the synchronous chimera states in a two-layer multiplex network, the mirror units in incoherent domains can be either synchronized or unsynchronized here. It means both 'in-phase multi-cluster chimera states' and 'anti-phase

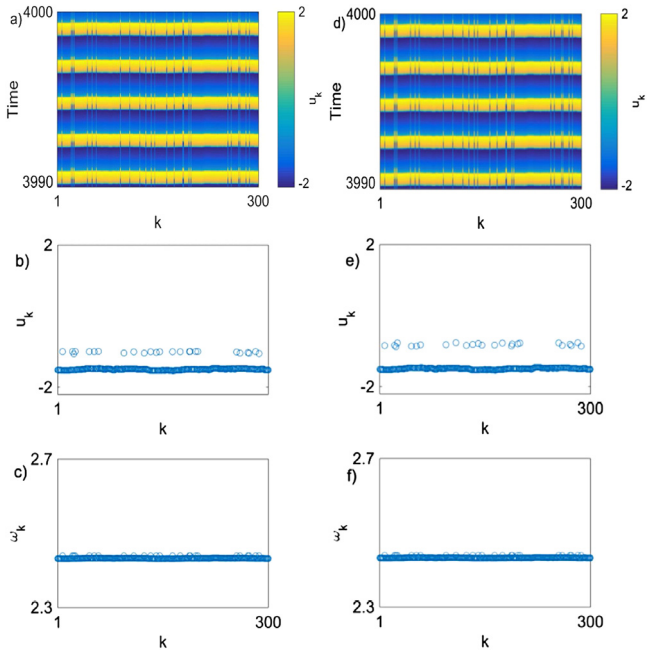

Fig. 67. The solitary state in the multiplex network of FHN oscillators with weak inter-layer coupling strength and a small mismatch in the intra-layer coupling strength. The left and right panels refer to the first and second layers, respectively. (a,d) The spatiotemporal patterns. (b,e) The time snapshots. (c,f) The mean phase velocities. The parameters are $N = 300$, $\varepsilon = 0.05$, $a = 0.5$, $r = 0.35$, $\sigma_1 = 0.4$, $\sigma_2 = 0.3$, $\phi = \pi/2 - 0.1$.
Source: Figure reproduced with permission from [274].

multi-cluster chimera states'. In the normal in-phase multi-cluster chimera state, the coherent/incoherent oscillators in the two layers have the same locations. However, in spatially anti-phase multi-cluster chimera state, the mirror FHN oscillators of coherent/incoherent domains in one layer are always incoherent/coherent in the other layer. The other type of chimera dynamics that happens here is that the numbers of coherent domains in the two layers are different, which is called 1-2-cluster chimera state. One more type is out-of-phase 2-cluster chimera state in which two coherent/incoherent domains are located in each layer.

Like homogeneous bipartite networks, the heterogeneous bipartite networks still display strong multistability, and a variety of chimera states can be observable. In addition to the types of chimera expressed in homogeneous model, another type of chimera state happening here is displaying the chimera dynamics in one layer and the coherent dynamics in the other layer.

The effect of the electromagnetic induction has also been investigated on the behavior of a multilayer Hindmarsh–Rose (HR) neural network. Neuronal memristive model was introduced by Ma et al. according to the Maxwell electromagnetic induction theorem (MEIT). This effect was also studied by considering the inter-layer coupling connections with memristive synapses and intra-layer coupling with electrical synapses [272]. The effect of the electromagnetic induction was introduced by a cubic flux controlled memristive model as a synapse. Their results showed the important role of the electromagnetic induction in regulating the dynamical behavior of the neural networks and the occurrence of chimera states.

Another partial synchronization state, similar to the chimera state, is the solitary state. The occurrence of solitary state has been reported for local, non-local, and global types of coupling in networks of Kuramoto oscillators with inertia [242,273]. Recently, it has been observed in a multiplex network of FitzHugh–Nagumo (FHN) oscillators [274]. Considering a weak coupling strength between two rings of non-locally coupled FHN oscillators can significantly influence the dynamics of the rings. When there is a mismatch in the coupling ranges of the layers, the chimera state emerges, which is not observed in the isolated rings. If the intra-layer coupling strengths have a mismatch, different behaviors such as in-phase synchronization and 2-headed chimeras can appear. In the case that the coupling strength mismatch is small, the solitary state is developed. Fig. 67 shows the dynamics of the layers in the solitary state. Moreover, with weak multiplexing, the dynamics of each layer can be controlled by adjusting the other layer's parameters.

5.4. Complex structures

The real networks constitute special properties which has led to the introduction of different structures. According to the properties of the networks, including short average distance, the clustering and the distribution of nodes' degrees,

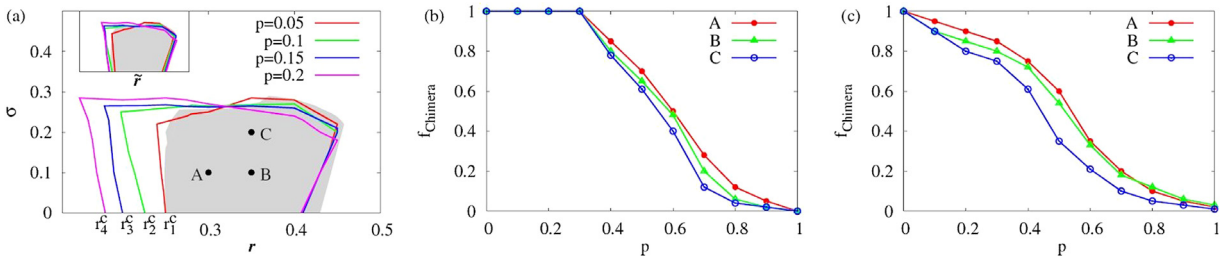

Fig. 68. (a) The stability region of the chimera state in the coupling range (r) and coupling strength (σ) plane. The gray part refers to the non-local coupling, and the color lines show the variation of the stability region by adding new links with different probabilities (p). (b) The fraction of obtaining chimera state by adding new random links from random initial conditions in 500 numerical simulations for three points of A, B, and C specified in part (a). (c) The fraction of obtaining chimera state by rewiring and adding random links from random initial conditions.
Source: Figure reproduced with permission from [218].

they can be categorized in different structures such as random, small-world, scale-free. Recently, a growing interest has been devoted to the study of the relationship between the network's topology and its behavior. As well, a number of studies have been focused on the effect of network topology on the occurrence of chimera states [275–279], which will be discussed in the following.

A few research works concentrate on the effect of network topology on synchronizability [275–278,280]. However, the concept of the space is lost on complex networks, which makes it not straightforward to figure out a chimera state [279].

Besides the regular ring networks, the chimeras can also appear in networks with star structure [281]. Considering N nodes for a network, in the star structure, there is a central hub, and all the other $N-1$ nodes are connected to this hub. Although the peripheral nodes in a star topology have identical dynamics and coupling schemes, the chimera state is observable in them. This observation is not dependent on the coupling type since it has emerged in diffusive, conjugate, and mean-field couplings.

Up to 2014, the chimera studies were devoted to the networks with regular structures. Zhu et al. [279] focused on the appearance of chimera states in scale-free and Erdös–Rényi random networks. This investigation revealed some consequences in the formation of chimera in these networks, the summary of which is given below:

- The coherent group comprises connected synchronous oscillators, and the incoherent group is formed of many asynchronous clusters, the majority of them containing one or two oscillators.
- In complex networks, the oscillators are detectable according to the number of their neighbors. This causes that the initial conditions have no effect on the coherent oscillators. Therefore, the oscillators in the coherent group are not changed by varying the initial conditions and keeping the parameters constant.
- The oscillators with a higher number of neighbors (degree) have stronger interactions with the environment. In scale-free networks, the coherent group is composed of the oscillators with a larger value of the interaction strength.

The robustness of the chimera states with respect to the adding or rewiring random links has been investigated in the ring FitzHugh–Nagumo network [218]. Firstly, it is considered that random new links with probability p are added to the non-locally coupled oscillators (no link is rewired). Fig. 68a shows the stability region of the chimera state in the coupling strength and coupling range plane, wherein the gray area belongs to the non-local network. Adding random links causes the appearance of the chimera state in smaller coupling ranges. As the probability of adding links increases, the stability region extends to lower coupling ranges. Furthermore, the fraction of obtaining the chimera state from the random initial conditions is dependent on the probability p (shown in Fig. 68b). For small p values, all the initial conditions lead to the emergence of a chimera state. When the probability increases, the chimera state is observed in less simulation. Finally, when the coupling approaches full connection, the chimera is obtained rarely. Next, the simulations are done by randomly rewiring the non-local links and adding new ones. The fraction of obtaining chimera from random initial conditions, in this case, is shown in Fig. 68c. The results show that unlike the previous example, the chimera is not formed in all simulations with the small p values.

The modular structure is one of the models presented for cortical neurons. The neurons in the cortical network have very complex connectivities. This complexity arises from different numbers of connections per neuron. It has been shown that the neurons form communities, where the density of the connections within the communities is higher than the links between the communities [282]. This structure is known as a modular network. Assuming a modular network consisting of six communities of Hindmarsh–Rose neurons, the equations of the network can be given as [283]

$$\dot{p}_i = q_i - ap_i^3 + bp_i^2 - n_i + I_{ext} + g_{el}\sum_{j=1}^{N} L_{ij}H(p_j) - g_{ch}(p_i - V_{syn})\sum_{j=1}^{N} T_{ij}S(p_j),$$

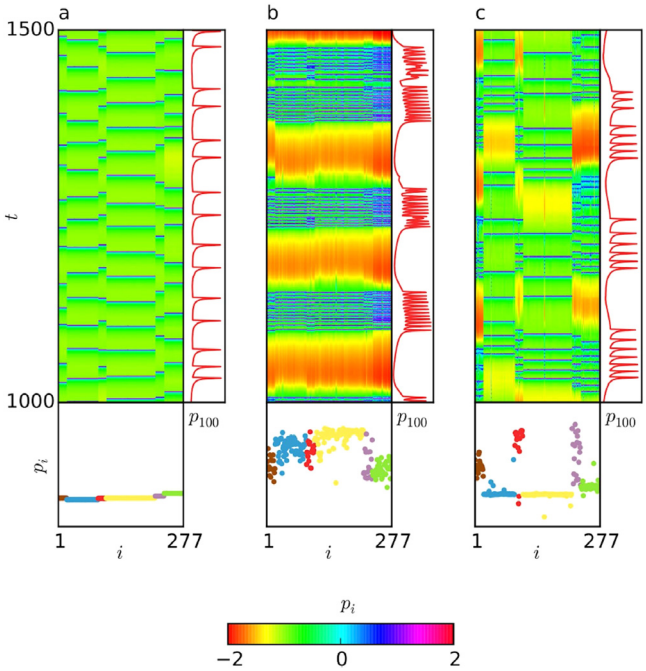

Fig. 69. The spatiotemporal pattern of the membrane potentials of the neurons in the modular network Eq. (149). The time series of the neuron $i = 100$ of community 3, and also the time snapshot of the network are also shown for each case. (a) Synchronous behavior for $g_{ch} = 0.015$ and $g_{el} = 1.7$, where both the metastability index and the chimera-like index are low. (b) Asynchronous behavior for $g_{ch} = 0.18$ and $g_{el} = 0.7$, where the metastability index is higher than the chimera-like index. (c) Chimera behavior for $g_{ch} = 0.015$ and $g_{el} = 0.5$, where the chimera-like index is higher than the metastability index.
Source: Figure reproduced with permission from [283].

$$\begin{aligned} \dot{q}_i &= c - dp_i^2 - q_i, \\ \dot{n}_i &= r[s(p_i - p_0) - n_i], \end{aligned} \tag{149}$$

where the within and between community's interactions are considered to be through electrical synapses with adjacency matrix L, and chemical synapses with adjacency matrix T. The strength of the electrical and chemical synapses are g_{el} and g_{ch}, respectively. The parameters are set at $a = 1$, $b = 3$, $c = 1$, $d = 5$, $s = 4$, $p_0 = -1.6$, $I_{ext} = 3.25$, $V_{syn} = 2$, $\theta_{syn} = -0.25$ and $\lambda = 10$, and $S(p)$ is the chemical synapse sigmoidal function. By setting these parameters, the dynamics of a single neuron is chaotic.

Two measures for evaluating the coherence and chimeric behavior of the modular networks are the metastability index and the chimera-like index. In the modular network of Eq. (149), these indices are dependent on the values of the synaptic strengths. If both indices are small, the network's synchronized behavior does not change in time, and thus, the six communities are almost synchronous. This behavior of the network is shown in Fig. 69a. In this case, the dynamics of the neurons is spiking. In the case that the metastability index is higher than the chimera-like index, the network shows a relatively regular spatial behavior. Fig. 69b represents this pattern in which the neurons are synchronous in the quiescent periods and asynchronous in bursting periods. Finally, Fig. 69c illustrates the network pattern when the chimera-like index is higher than the metastability index. It is observed that the neurons in the communities 2 and 4, which are larger, are almost synchronous, while the other communities have asynchronous firings. Thus a chimera-like behavior is formed.

In 2019, Andreev et al. [146] studied the chimera state in complex networks of bistable Hodgkin–Huxley neurons with two coexisting fixed points and limit cycle attractors. They investigated different topologies, including scale-free, small-world, and random networks, by varying the neurons' external current, which controls the dynamics of each neuron, and the synaptic strength, which affects the collective behavior. This study revealed the occurrence of a special coexistence of spiking and resting neurons in the networks, which can be called as partially spiking chimera state. Fig. 70a–c show the schematics of scale-free, small-world, and random networks, respectively. The distribution of the relative number of spiking neurons ($N'_{sp} = N_{sp}/N$, where N_{sp} is the number of the spiking neurons, and N is the number of the neuron in the network) is illustrated in Fig. 70d-f, in the parameter plane. Comparing these figures show that the appearance of the chimera state is robust to the network topology. However, the regions of the existence of chimera state in three networks are different, such that the chimera region in a scale-free network is the smallest and in the random network is the largest. The reason is that the small-world and random networks have lower connectivities and are regulated slowly, which leads

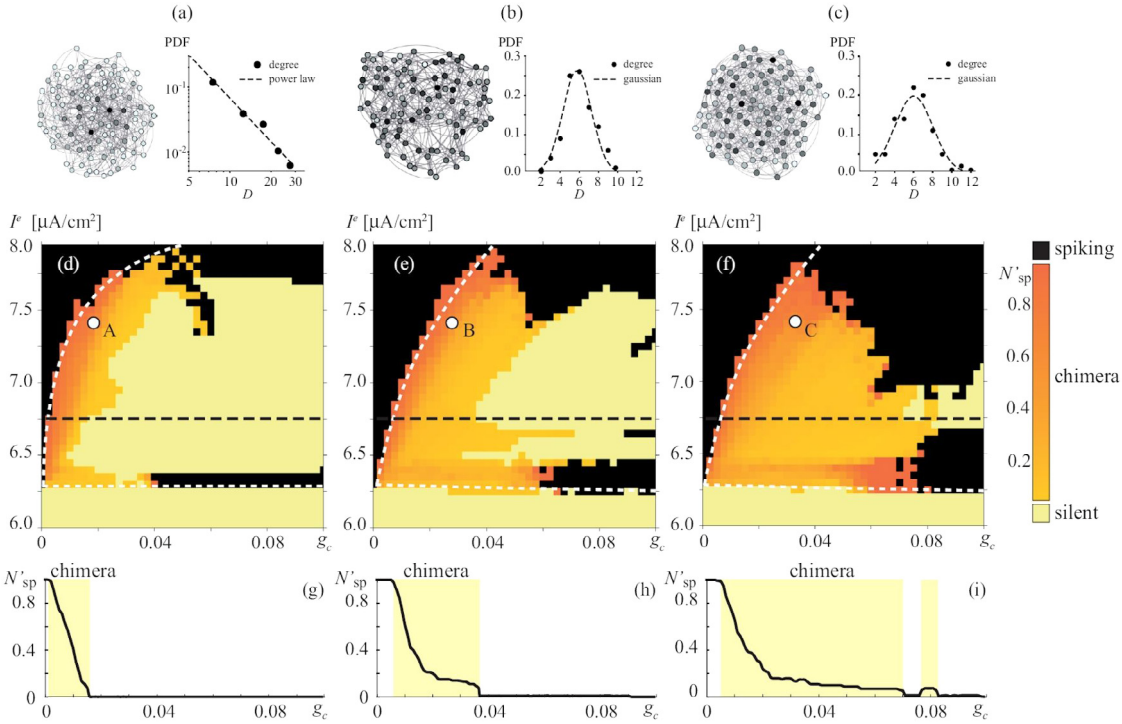

Fig. 70. The regions of partially spiking chimera states in complex networks. (a–c) The probability density functions (PDFs) of the scale-free, small-world, and random networks. (d–f) Distribution of the relative number of spiking neurons (N'_{sp}) in the parametric plane of coupling strength (g_c) and external current (I_e). White dashed lines show the regions of different states. The silent mode is shown by yellow, the chimera state by orange, and the spiking mode by black. (g-i) The relative number of spiking neurons with respect to g_c at $I_e = 6.75$.
Source: Figure reproduced with permission from [146].

to a smooth change in the network's collective behavior. In contrast, the scale-free network has higher connectivities, which leads to the sudden change in the quality of the network's dynamics near a critical point.

In reality, some networks are composed of interconnected subnetworks with different scales of topologies, which are called multiscale networks. To reveal the effect of the multiscale structure on the emergence of chimera states, Makarov et al. [284] considered a network of interconnected networks consisting of Kuramoto–Sakaguchi oscillators. The structure they used for their network was a non-locally coupled global ring, where each node was also a member of another ring of oscillators. Fig. 71 shows the schematic of the considered structure. The network was investigated by varying the coupling of the subnetworks from local to non-local. The dynamics of each node (φ_i^j) of the network is described by the following equations

$$\frac{d\varphi_i^j}{dt} = \begin{cases} \omega_i^j - \lambda \sum_{k=i-R_N}^{i+R_N} \sin(\varphi_i^j - \varphi_k^j + \alpha), & i \neq 1 \\ \omega_i^j - \lambda \sum_{k=i-R_N}^{i+R_N} \sin(\varphi_i^j - \varphi_k^j + \alpha) & \\ -\lambda \sum_{k=i-R_N}^{i+R_N} \sin(\varphi_i^j - \varphi_i^k + \alpha), & i = 1 \end{cases} \tag{150}$$

where α is the phase lag, ω_i^j is the natural frequency of the ith oscillator of the jth subnetwork, λ is the coupling strength, and R_N and R_M are the coupling range of the subnetwork and the global ring, respectively.

To evaluate the emergence of chimera states, the strength of incoherence (SI) has been used. To represent the level of synchronization in two scales of the network, the authors have calculated the classic order parameter for the global ring, and the average order parameter for the subnetworks. Fig. 72 illustrates different behaviors of the network, wherein the first row shows the SI; the second row shows the local order parameter of the global ring, and the third row shows the average order parameter of the subnetworks in the parameter plane (α, λ). The left column of this figure refers to a classic non-locally coupled ring ($N = 1$). It is observed that the one scale network exhibits chimera state in a thin region, and

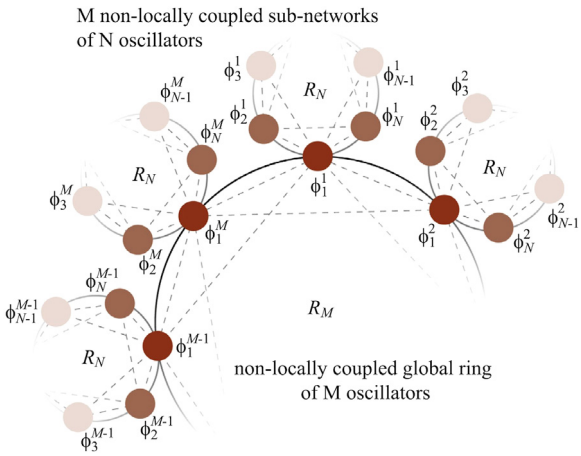

Fig. 71. The schematic of a multiscale network consisting of M subnetworks. The global ring has M nodes with coupling radius R_M, and the subnetworks consist of N nodes with coupling radius R_N. φ_i^j represent the dynamics of the ith oscillator in the jth subnetwork. Since the dark red nodes belong to two networks with different topologies, a multiscale network is formed.
Source: Figure reproduced with permission from [284].

when the order parameter of the global ring is near 0.7. The middle column shows the results when the subnetworks are extended to $N = 20$ locally coupled nodes. In this case, the chimera state is appeared in a larger region, with the global ring order parameter near 0.7, but very small values of average order parameter for subnetworks. Then the subnetworks are considered to have non-local coupling with $R_N = 5$, and the results are shown in the right column of Fig. 72. It is observed that the transition from incoherence to coherence happens in lower α values, and the existence of the chimera state is dependent on the value of the λ. Therefore, the existence and robustness of the chimera states are influenced by the topology of the subnetworks. These numerical results have been confirmed analytically by using the Ott–Antonsen ansatz. Furthermore, the authors have also checked the results numerically in a multiscale network of Hindmarsh–Rose neurons.

5.5. Coupling schemes

Early studies of chimeras were based on the assumption that the chimera state is only achieved in the case of non-local interactions between the units. Therefore, non-locality was the basis of the network coupling in several primary studies. Later investigations revealed the appearance of chimera in networks with global or local couplings [285]. Also, the further analysis uncovered the possibility of the emergence of chimera in the population of oscillators with time-varying, hierarchical, and fractal topologies. In this subsection, our concentration is on the effects of different coupling schemes on the chimera states.

5.5.1. Global coupling

In globally coupled identical oscillators, all of the units are homogeneous and under the same force. Since the chimera is a symmetry-breaking state, the initial impression was that the global coupling cannot exhibit chimera. In 2014, Sethia et al. [286] showed the opposite of this conception by observation of the amplitude-mediated chimera in the globally coupled complex Ginzburg–Landau equations. Former, they had demonstrated the existence of amplitude-mediated chimera as a result of the coexistence of one fixed point and a limit cycle attractor or a spiral attractor, in these oscillators with non-local coupling [234]. After that, Yeldesbay et al. [287] investigated the globally coupled Kuramoto–Sakaguchi type oscillators. They demonstrated that the chimera can emerges in the global coupling due to the bistability. This bistability can arise from the internal time-delay feedback in the oscillators, which were basically monostable. The existence of chimera state in globally coupled systems has also been observed experimentally in [30,288].

The intensity-dependent self-interaction can also lead to the multistability. The intensity causes the increment of the fixed points and thus, increasing the multistable attractors. The stability of these attractors depends on the coupling strength between the elements. Motivated by this, Chandrasekar et al. [289] discussed the emergence of chimera state in the globally coupled oscillators with intensity self-interaction. The network of van der Pol oscillators with additional intensity-dependent frequency terms is described as follows

$$\begin{aligned}\ddot{x}_i &= b(1-x_i^2)\dot{x}_i - (\omega_0^2 + \alpha_1 x_i^2 + \alpha_2 x_i^4)x_i \\ &\quad + \epsilon(\dot{X} - \dot{x}_i) + \eta(X - x_i), i = 1, \ldots, N,\end{aligned} \tag{151}$$

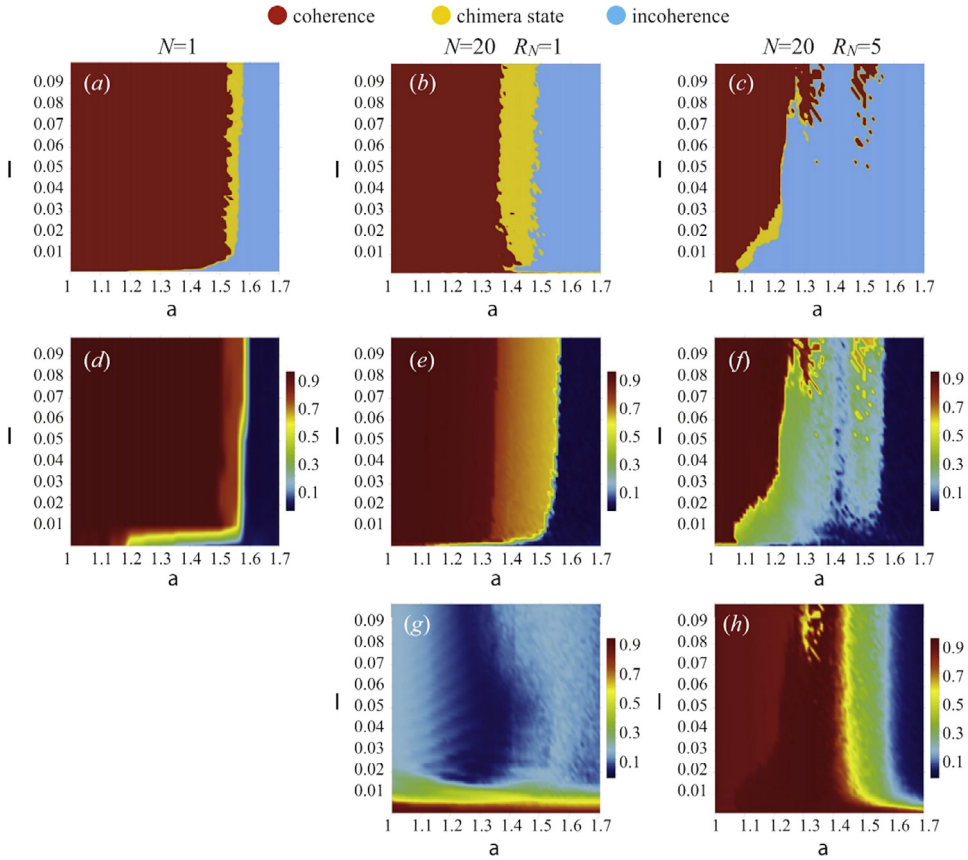

Fig. 72. Dynamics of the multiscale network in the parameter plane (α, λ) for different subnetworks structures (the left column: $N = 1$, the middle column: $N = 20$ and $R_N = 1$, the right column: $N = 20$ and $R_N = 5$). (a–c) Different behaviors of the global ring (coherent, chimera, and incoherent). (d–f) The order parameter of the global ring. (g,h) The average order parameter of the subnetworks.
Source: Figure reproduced with permission from [284].

where α_1 and α_2 are the intensity parameters, ϵ and η are the coupling strength between $\dot{x}$ and x variables and $X = 1/N \sum_{i=1}^{N} x_i$, $\dot{X} = 1/N \sum_{i=1}^{N} \dot{x}_i$. In the absence of the intensity parameters, the van der Pol oscillators can only show chimera state in the non-local coupling. The network of Eq. (151) is investigated in four different conditions according to the values of the α_1, α_2, ϵ, η. To characterize different behaviors of the network, the strength of incoherence (SI) is used.

Firstly, the network is considered with no intensity ($\alpha_1 = \alpha_2 = 0$) and $\epsilon \neq 0$, $\eta = 0$. In this case, the network transits from asynchronization to synchronization by increasing ϵ, and the chimera is not formed. This is shown in Fig. 73a by (*i*). Secondly, $\alpha_1 = 2.15$, $\alpha_2 = \eta = 0$ are considered. Similar to the previous case, the chimera state does not emerge in this condition, too. The SI of this case is shown in Fig. 73a by (ii). Next, the value of α_1 is increased to $\alpha_1 = 4$ and η is set at $\eta = 0.1$ ($\alpha_2 = 0$). The variation of SI for this condition, which is shown in Fig. 73a by (iii), represents that for a specified range of ϵ, the chimera is formed. Finally, for $\alpha_1 = 2.18$, $\alpha_2 = 2.15$, $\eta = 0.1$, the network's dynamics changes from asynchronization to chimera and then to synchronization (shown in Fig. 73a by (iv)). These results confirm that the chimera is the result of the intensity interactions. Fig. 73b shows the time series of the oscillators in the chimera state, where the black time series refers to the coherent group of chimera. The time snapshots of oscillators, in this case, is shown in Fig. 73c. The time series of the oscillators in the synchronized state is illustrated in Fig. 73d.

As mentioned, the reason for the existence of the chimera state in the global coupling is the multistability induced by the intensity. To represent the multistability of the oscillators, Fig. 74 is presented. The oscillation period of the oscillators in the absence of the coupling $\alpha_1 = \alpha_2 = \epsilon = 0$, is illustrated in Fig. 74a and its phase space is depicted in Fig. 74e with A_1. If the intensity parameters are changes to $\alpha_1 = 2.18$, $\alpha_2 = 2.15$, the additional fixed points are created, but the oscillators have only one synchronized attractor, as shown in Fig. 74b and Fig. 74e by B_1. In the case when the intensity parameters are zero but there is a coupling strength, again, there exists a synchronized attractor. This case is depicted in Fig. 74c,f. Finally, when there are both coupling strength and intensity parameters, the network exhibits chimera state, whose time series are illustrated in Fig. 74d and the phase spaces are shown in Fig. 74g. The existence of multistability is clear in these figures, where the synchronized and asynchronized oscillators are shown in black and brown, respectively.

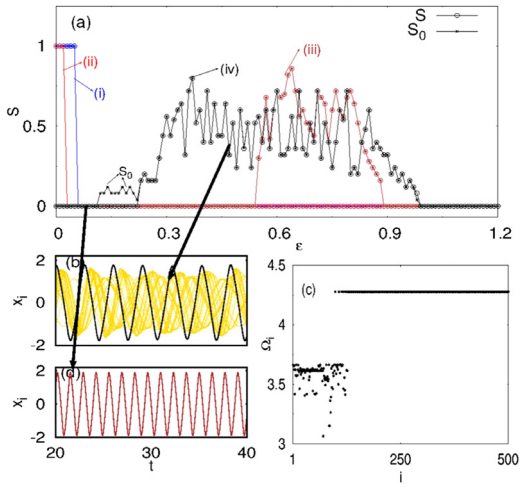

Fig. 73. The network of van der Pol oscillators with intensity-dependent self-interaction. (a) The strength of incoherence with respect to ϵ, for different parameter values: (i) $\alpha_1 = \alpha_2 = \eta = 0$, (ii) $\alpha_1 = 2.15$, $\alpha_2 = \eta = 0$, iii) $\alpha_1 = 4$, $\alpha_2 = 0$, $\eta = 0.1$. iv) $\alpha_1 = 2.18$, $\alpha_2 = 2.15$, $\eta = 0.1$. (b) The time series of the oscillators in the chimera state, where the black and gold refer to the synchronized and asynchronized groups, respectively. (c) The time snapshots of the oscillators in the chimera state. (d) The time series of the oscillators in the synchronized state.
Source: Figure reproduced with permission from [289].

One sufficient condition for the chimera state is a clustering mechanism. This clustering can split the oscillators into different groups and break the symmetry of the uniform global coupling. Schmidt and Krischer [290] reported that this clustering could be attained by a nonlinear coupling, which reflects the nonlinear amplitude effects. To represent this concept, they used a network of Stuart–Landau oscillators with the nonlinear global coupling as follows

$$\frac{d}{dt}W_k = W_k - (1+ic_2)|W_k|^2 W_k - (1+i\nu)\langle W\rangle + (1+ic_2)\langle |W|^2 W\rangle, \tag{152}$$

where $\langle W\rangle = \sum_{k=1}^{N} W_k/N$ is the arithmetic mean of the oscillators, and can be described by the following equation

$$\frac{d}{dt}\langle W\rangle = -i\nu\langle W\rangle \Rightarrow \langle W\rangle = \eta e^{-i\nu t}. \tag{153}$$

The behavior of this network is dependent on the parameters ν, η, c_2. There are two types of clustering dynamics in this network. The first one is the amplitude clusters (shown in Fig. 75a), in which there are two groups of oscillators with different amplitudes and rather different phases. The second type is the modulated amplitude clusters (shown in Fig. 75f). In this clustering, the groups not only have the mean-field oscillations but also oscillate around their mean-field [291]. This can lead to a quasiperiodic dynamic. Each of these clustering mechanisms can give rise to the chimera state, which inherits the characteristics of the original clusters. The chimera state originated from the first type that is shown in Fig. 75b, is an intermediate state between the cluster state in Fig. 75a and the synchronous state in Fig. 75c. In this chimera state, the oscillators with the smaller amplitude are asynchronous, and the ones with the larger amplitude are synchronous. The second chimera state is caused by the modulated amplitude clusters with similar properties to this clustering. This type of chimera is shown in Fig. 75e and is between the asynchronous state in Fig. 75d and the modulated amplitude clusters in Fig. 75f. The experimental observation of chimera in global coupling has been reported in [292].

It has been shown that the combination of attractive and repulsive coupling can also break the symmetry of global coupling [293,294]. For the oscillators with dynamics $\dot{X}_i = F(X_i)$, this coupling can be described by $\dot{X}_i = F(X_i) + KAB$, where K is the coupling strength, $A = \begin{bmatrix} a_{11} & a_{12} \\ a_{21} & a_{22} \end{bmatrix}$ is a real matrix and $B = \begin{bmatrix} \bar{x} - x_i \\ \bar{y} - y_i \end{bmatrix}$ is the mean-field diffusions matrix. Different configurations of the matrix A gives rise to different couplings, which are described below:

1. $a_{11} = 1$, $a_{12} = a_{21} = a_{22} = 0$: The x variable has a mean-field self-feedback coupling.
2. $a_{11} = a_{12} = 0$, $a_{21} = \epsilon$, $a_{22} = 1$: The y variable has a self-feedback and also cross feedback of the x variable. The cross-feedback coupling can be attractive or repulsive.
3. $a_{11} = \epsilon$, $a_{12} = a_{21} = 0$, $a_{22} = 1$: Both variables have self-feedback coupling. There is no cross-feedback coupling.
4. $a_{11} \neq 0$, $a_{12} \neq 0$, $a_{21} \neq 0$, $a_{22} \neq 0$: The variables have both self-feedback and cross-feedback couplings. In this case, the coupling is more complicated than previous ones.

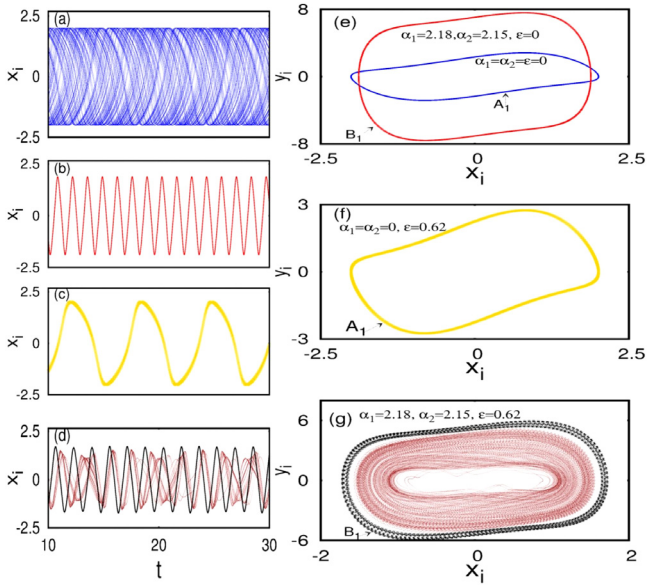

Fig. 74. The time series of the oscillators of Eq. (151) for different parameters. (a) $\alpha_1 = \alpha_2 = \epsilon = 0$. (b) $\alpha_1 = 2.18$, $\alpha_2 = 2.15$, $\epsilon = 0$. (c) $\alpha_1 = \alpha_2 = 0$, $\epsilon = 0.62$. (d) $\alpha_1 = 2.18$, $\alpha_2 = 2.15$, $\epsilon = 0.62$. (e) The corresponding attractor of part a (A_1) and part b (B_1). (f) The corresponding attractor of part c. (g) The corresponding attractor of part d. There exists multistability in the chimera state.
Source: Figure reproduced with permission from [289].

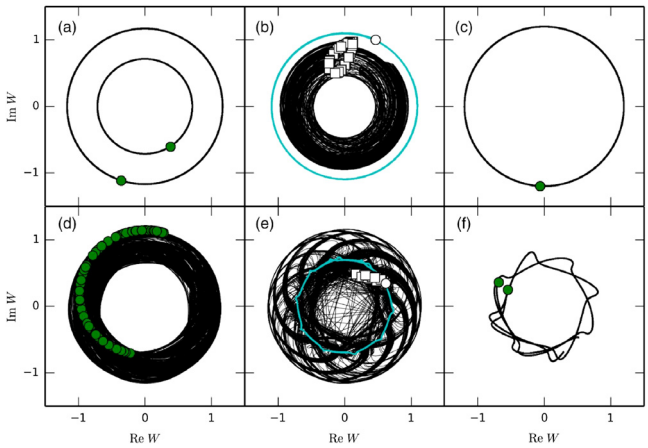

Fig. 75. The trajectories (lines) and the snapshot (symbols) of the Stuart–Landau oscillators with the nonlinear global coupling Eq. (152) in the complex plane. The top row shows the first clustering mechanism for $c_2 = 0.58$, $\nu = 1.49$: (a) Amplitude clusters, $\eta = 0.9$. (b) Chimera state, $\eta = 1.02$. (c) Synchronization, $\eta = 1.2$. The bottom row shows the second clustering mechanism for $c_2 = -0.6$, $\eta = 0.7$: (d) Irregular oscillations, $\nu = -0.1$. (e) Chimera state, $\nu = 0.02$. (f) Modulated amplitude clusters, $\nu = 0.1$.
Source: Figure reproduced with permission from [290].

Mishra et al. [293] represented the existence of chimera in globally coupled oscillators with considering the above second and third coupling schemes. For example, the Liénard network with the second type of coupling is as follows

$$\begin{aligned} \dot{x}_i &= y_i, \\ \dot{y}_i &= -\alpha x_i y_i - \beta x_i^3 - \gamma x_i + K[(\bar{y} - y_i) + \epsilon(\bar{x} - x_i)], \end{aligned} \tag{154}$$

where the parameters are set at $\alpha = 0.45$, $\beta = 0.5$, $\gamma = -0.5$, and $N = 100$. By this setting, the Liénard system is bistable. Varying the coupling parameters (K, ϵ) results in various collective behaviors in the network, including one-, two-, three- and four-cluster states, and the chimera states. The observed chimera states in different coupling parameters have different properties and can be divided into two types. In the first type, both the coherent and incoherent groups of the oscillators behave chaotically, although the isolated system oscillates periodically. The time snapshot in the polar coordinate and the spatiotemporal behavior of the oscillators in this chimera type are represented in the first row of

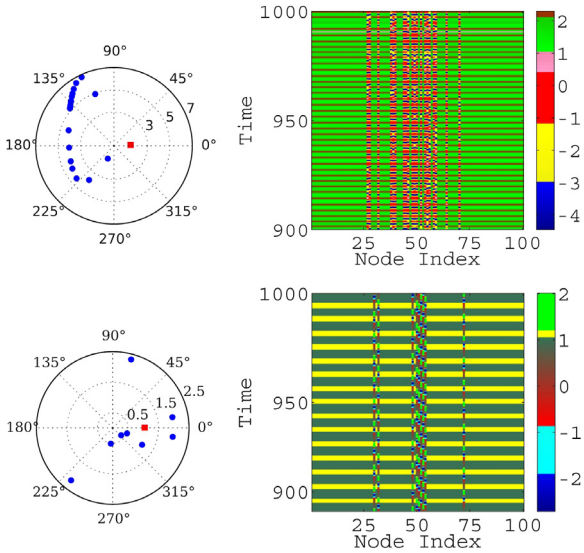

Fig. 76. The chimera states observed in the network of globally coupled Liénard systems (Eq. (154)). The first and second rows show the first and second types of observed chimeras. The left panel: the snapshots in the polar coordinate. The right panel: the spatiotemporal patterns.
Source: Figure reproduced with permission from [293].

Fig. 76. In the polar snapshot, the asynchronous oscillators are shown by blue circles, and the synchronous group is shown by the red square. The second type of chimera is composed of a desynchronized group of periodic oscillations and a synchronized group that has irregular oscillation. The second row of Fig. 76 shows the snapshot of the oscillators and the spatiotemporal evolution of the network. It is evident that the asynchronous oscillators have both amplitude and phase differences.

5.5.2. Local coupling

The local coupling is in the opposite of the global coupling. After the discovery of the emergence of chimeras in non-local and global connections, the question was whether they could appear in the local coupling. Laing [295] demonstrated the existence of chimera in purely locally coupled oscillators for the first time in 2015. To reveal this possibility, three different systems were investigated under the nearest-neighbor diffusive coupling. The first system was a general reaction–diffusion equation, whose network exhibited chimera state with coherent and incoherent phases. As the second system, the Stuart–Landau oscillator was considered, which has an amplitude variable in comparison to the first system. Finally, an oscillator model with a real variable and an angular variable with the Winfree oscillator form was examined. It was shown that the chimera state is formed in all three networks for a specific range of parameters.

The requisites for the occurrence of chimera state in local coupling was investigated by Clerc et al. [296] in the network of nonlinear oscillators without time scales. This model shows the coexistence of a uniform steady-state and an incoherent state, which is the result of the homoclinic bifurcation. Weak local coupling between the oscillators leads to the inability of the incoherent state to overcome the coherent state. Thus, the chimera states, which are followed by a homoclinic snaking bifurcation diagram, can appear.

The existence of chimera has also been studied in locally coupled chaotic and limit cycle oscillators with nonlinear coupling function [46]. Considering a network of Hindmarsh–Rose neurons with only local electrical synapses (simple diffusive nearest-neighbor), it is not possible to find the chimera state. But if the coupling function changes from electrical synapse to chemical one, which is nonlinear, the chimera and multi-chimera are observed. In this case, the coupling term (added to the x variable of the Hindmarsh–Rose model) is $\epsilon(v_s - x_i)\Gamma(x_{i+1}(t)) + \Gamma(x_{i-1}(t))$, where ϵ is the synaptic strength, $v_s = 2$ is the reversal potential, $\Gamma(x)$ is the sigmoidal function (Eq. (166)) with $\lambda = 10$ and $\theta_s = -0.25$. Fig. 77 shows the transition of the network with local chemical synapses between different behaviors. It is clear that by increasing the coupling strength (ϵ), the dynamics of the network changes from asynchronization to multi-chimera, then to chimera state, and finally, to complete synchronization. The right panel of Fig. 77 demonstrates the corresponding mean phase velocities.

Next, the effect of time-delay in the chemical synapses was investigated. Thus, the coupling term is changed to $\epsilon(v_s - x_i)\Gamma(x_{i+1}(t-\tau)) + \Gamma(x_{i-1}(t-\tau))$, where the parameters are the same as before. Fig. 78 shows the phase diagram in the (ϵ, τ) plane by calculating the strength of incoherence. This figure represents that increasing the time delay from a definite threshold leads to the disappearance of the complete synchronization in the network.

The chimeras induced by the nonlinear coupling function have also been confirmed in the locally coupled Mackey–Glass oscillators and locally coupled van der Pol oscillators. Therefore, the emergence of chimera with local coupling can be generalized to the other systems with the proper selection of the nonlinear coupling function.

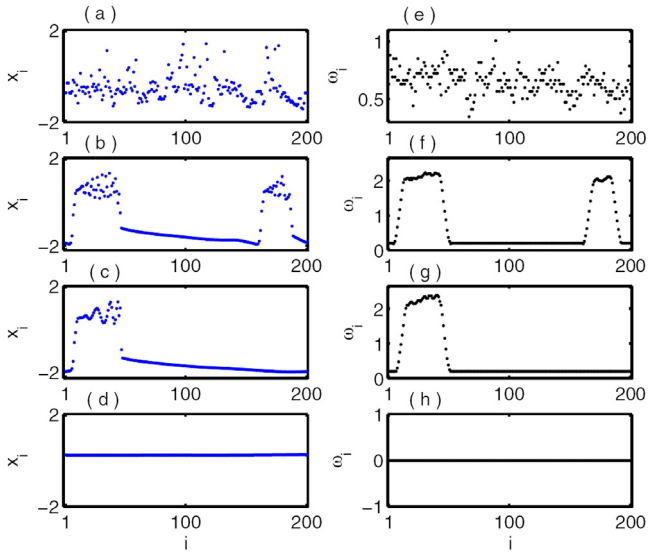

Fig. 77. The time snapshot (left panel) and mean phase velocity (right panel) of the Hindmarsh–Rose neurons with the local chemical synapses. (a) Asynchronization for $\epsilon = 0.18$. (b) Multi-chimera state for $\epsilon = 0.63$. (c) Chimera state for $\epsilon = 0.67$. (d) Synchronization for $\epsilon = 2$.
Source: Figure reproduced with permission from [46].

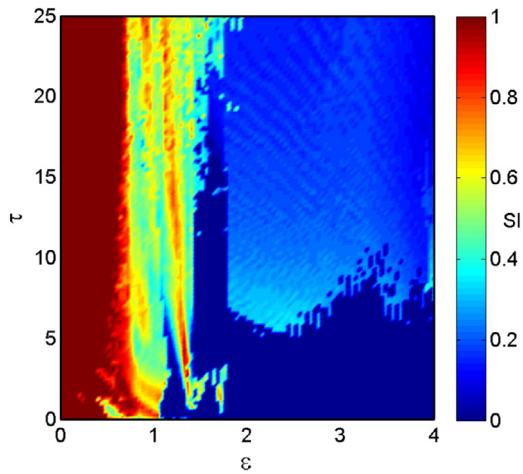

Fig. 78. Phase diagram of the locally coupled Hindmarsh–Rose neurons with time delay in the (ϵ, τ) plane. The strength of incoherence is calculated and shown by color.
Source: Figure reproduced with permission from [46].

It has been revealed that the dynamics of the delayed feedback system is close to the one-dimensional spatially extended system [219]. One property leading to this similarity is the asymmetry in the coupling, which can be applied by unidirectional couplings. Since the chimera state has been observed in the oscillators with delayed feedback [297,298], it could also be possible in a ring network with local unidirectional interactions. Shepelev et al. [219] examined this hypothesis in a ring of linear dissipative oscillators with local and nonlinear coupling. The equations of this network are given as

$$\begin{cases} \dot{x}_j = -\alpha x_j - \omega_0^2 y_j + \sigma f(x_{j-1}) + \gamma(x_{j-1} + x_{j+1} - 2x_j) \\ \dot{y}_j = x_j \\ x_{j+N} = x_j \\ y_{j+N} = y_j \end{cases} \tag{155a}$$

$$f(x) = \frac{\beta}{1 + A\sin^2(x + \Phi)}, \tag{155b}$$

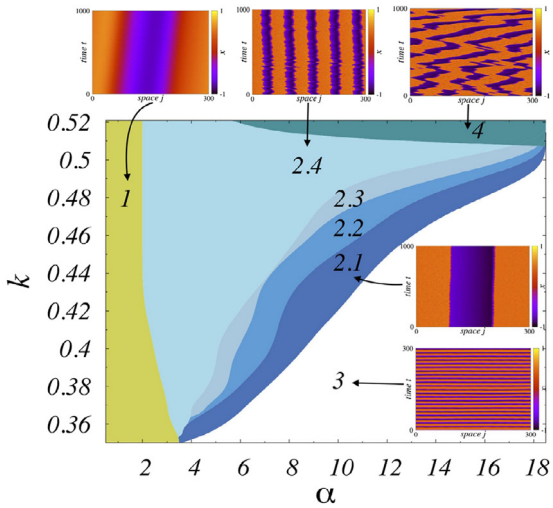

Fig. 79. The phase diagram of the network Eq. (155a) in the parameter plane (α, k). The insets show the spatiotemporal pattern in each case in a co-moving frame. Region 1: Coherent traveling wave. Region 2: Chimera states with one or multiple heads. Region 3: Intermittency between coherent and chaotic behavior in time. Region 4: Irregular behavior.
Source: Figure reproduced with permission from [219].

where α and ω_0 are the oscillators' parameters, σ is the strength of the unidirectional coupling with nonlinear function as $f(x)$, and γ is the strength of the local dissipative coupling. For the stationary oscillations in the network, the unidirectional coupling needs to be a ratio of parameter α as $\sigma = k\alpha$.

The network is investigated by setting the constant parameters at $\omega_0 = 1$, $N = 300$, $A = 4.7$, $\beta = 4$, $\phi = 0.4$, and varying the parameters α and k. To consider the most asymmetry, the dissipative coupling strength is set at zero ($\gamma = 0$). The simulation results revealed different spatiotemporal patterns in the parameter plane, including the traveling chimera. The regimes of these behaviors are defined in Fig. 79. For small α values, that is marked by number 1, the coherent traveling waves appear in the network. In the region marked by 3, the coherent and chaotic behavior intermittent in time. The region marked by 2 contains the chimera states with one, two, three, and four heads. In some regions, these multi-headed chimeras coexist. The chimera states are no longer observed as the parameters move to region 4.

The traveling chimera obtained in network Eq. (155a) is not restricted to the coupling function given in Eq. (155b). In fact, other nonlinear functions with at least one maximum, that is transferred from zero value, can result in the same results. For example, the following equations have the same chimera patterns like the one described in Eq. (155b) [219]:

1. The shifted Gaussian function:
   $f(x) = A + B\exp\{-\frac{(x-\mu)^2}{2\sigma}\}$, $A = 0.5$, $B = 3.5$, $\mu = 0.35$, $\sigma = 0.15$
2. The shifted Lorentzian function:
   $f(x) = \frac{1}{\beta^2+(x-A)^2}$, $\beta = 0.5$ and $A = 0.4$

5.5.3. Time-varying coupling

One of the essential properties of complex systems is the self-organization. In the majority of the real networks, the interactions are adopted in time in such a way that the network reaches the desirable state. This adaptation can be considered in networks through either the time-varying topology or time-varying coupling strength. The time-varying interactions can be observed in social, communication, ecological, and biological networks. Most of the chimera studies have been done on static networks. However, a few have considered the time-varying connections or weights [299,300].

The simple Kuramoto network with static couplings produces a chimera state by choosing random initial conditions. If the coupling weights of this network become adaptive with the following equations

$$\dot{\theta}_i = \omega - \frac{\sigma}{N}\sum_{j=1}^{N} k_i \sin(\theta_i - \theta_j),$$
$$\dot{k}_i = \frac{\eta}{N}\sum_{j=1}^{N} \cos(\theta_i - \theta_j), i = 1, 2, \ldots, N \tag{156}$$

then, a two-clustered state emerges instead of chimera state for the same parameter set and conditions [300]. The two-clustered state is composed of two anti-phase synchronized groups. Furthermore, the adaptive coupling leads to a stable state in a shorter time.

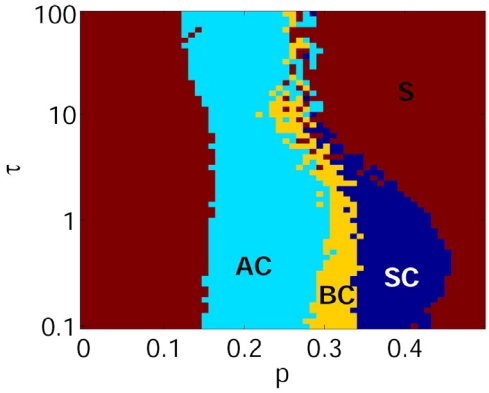

Fig. 80. Different collective behaviors of two populations of Kuramoto oscillators with time-varying inter-population links (Eq. (157)) in the (p, τ) plane. The parameters are $N_1 = N_2 = 100$, $\mu = 0.6$, $\omega = 1$ and $\alpha = 1.5$. The regions are S: synchronization, BC: breathing chimera, AC: alternating chimera, SC: stable chimera.
Source: Figure reproduced with permission from [212].

Considering the time-varying links between two populations of the Kuramoto oscillators causes the formation of different chimera types in the network. Buscarino et al. [212] assumed that each population of the network is globally coupled with constant coupling strength. While the inter-population links can be either on or off with the probability p. Thus, the equations of this network can be described by

$$\frac{d}{dt}\theta_i^{\sigma} = \omega + \sum_{\sigma'=1}^{2} \frac{1}{N_{\sigma'}} \sum_{j=1}^{N_{\sigma'}} K_{ij}^{\sigma\sigma'}(t) \sin(\theta_j^{\sigma'} - \theta_i^{\sigma} - \alpha), \tag{157}$$

where $K_{ij}^{11}(t) = K_{ij}^{22}(t) = \mu$ is the intra-population coupling strength and $K_{ij}^{12}(t) = K_{ji}^{21}(t) = s_{ij}(q)$ are time-dependent inter-population coupling strength, which takes the values zero or one randomly at each time interval τ as

$$s_{ij}(q) = \begin{cases} 1 \text{ with probability } p \\ 0 \text{ with probability } 1-p \end{cases}, (q-1)\tau < t < q\tau. \tag{158}$$

The behavior of this network is entirely dependent on the probability p and the time interval τ. Fig. 80 shows different collective behaviors of the network by varying p in $[0, 0.5]$ and τ in $[0.1, 100]$. For the low and high values of p, both populations are synchronized. In the intermediate values of p, the alternating chimera is formed. In this case, the synchrony and asynchrony alternate between two populations in time. For larger p values, in a small region, breathing chimera is observed. In this state, one population is synchronized, while the phase coherence of the asynchronized population changes periodically. For a specific region in the (p, τ) plane, the chimera state is stable, with one coherent and one incoherent population. The appearance of the alternating chimera is a consequence of the time-varying structure, since it cannot be obtained in this network with static links.

Adaptive coupling is also a new idea in studying chimera states in multilayer networks. The effect of this variation of coupling has been studied in a network of Kuramoto-type oscillators with the equations [301]

$$\begin{aligned} \frac{d\phi_i}{dt} &= 1 - \frac{1}{N}\sum_{j=1}^{N} \kappa_{ij} \sin(\phi_i - \phi_j + \alpha), \\ \frac{d\kappa_{ij}}{dt} &= -\varepsilon[\sin(\phi_i - \phi_j + \beta) + \kappa_{ij}], \end{aligned} \tag{159}$$

where the dynamics of the coupling is slower than the phase dynamics, and this is reflected by a small parameter $\varepsilon \ll 1$. Here, the control parameters are α and β. Initial conditions of the phase ϕ_i are chosen randomly in the interval $[0, 2\pi]$ and the coupling strength κ_{ij} is in $[-1, 1]$. Regardless of the specific characteristics of the final states of the network, a sequential hierarchical formation of new densely connected subnetworks is observable in all the networks. This determines the common feature of their formation mechanisms. These features are apparent in all the networks, despite the dynamic of each subnetwork, which can be coherence, cluster, traveling wave, or incoherence. These subnetworks arise on different time scales, and their size decreases at each subsequent stage of the network evolution. Fig. 81 illustrates a series of snapshots of the coupling matrix κ_{ij} calculated at different stages of the formation of the chimera state to display the hierarchical formation of chimera. In order to identify the synchronization patterns and the coupling structure, the average frequency of each oscillator was calculated after a sufficiently long transient time. It can be seen that in this situation, the formation of synchronous groups terminates at some stage, and the remaining oscillators stay

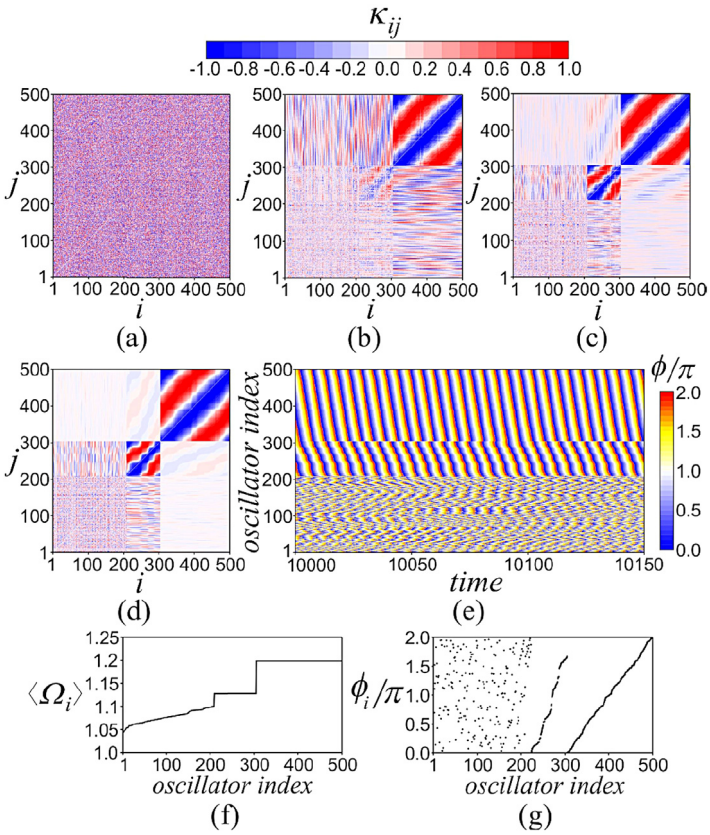

Fig. 81. The generation of the chimera state in the multilayer network with coupling. Parts (a–d) show the development of coupling matrix κ_{ij} at different times: (a) $t = 0$, (b) $t = 350$, (c) $t = 1500$, (d) $t = 10{,}000$. Part (e) shows the final evolution of the phases $\phi_i(t)$. Part (f) is the average frequencies of oscillators, and part (g) demonstrates the snapshot of the phases at $t = 10{,}050$, representing the traveling waves within the two coherent clusters. The parameters are set at $\varepsilon = 0.01$, $\alpha = 0.3\pi$, $\beta = 0.3\pi$, $N = 500$.
Source: Figure reproduced with permission from [301].

unsynchronized, so the chimera phenomenon happens. Fig. 81e demonstrates the differences in the relative phase in oscillators in the coherent and incoherent groups. While the relative phase in the coherent part and resulting traveling waves remain stable with time, the oscillators' phase in the incoherent part changes irregularly. A similar structure can explain the formation of chimera states: while the coupling strength within a group of oscillators is strong, it decreases among the others. It can be concluded that a variety of adaptation functions and network connectivities can lead to the self-organized groups with different local synchronous behaviors. Subsequently, in the final state, the network can be in the multi-cluster synchronized states or different types of chimera states.

The next step is studying the synchronization constructed by the unidirectional and mutual nonlinear non-adaptive couplings between the layers, which indicate chimera states with different properties. This research is a result of a discussion about various aspects of the organization of interactions in the multiplex network with adaptive couplings [302]. In order to study this issue in more depth, a two-layer network of the interacting phase oscillators is considered that in each layer, $N = 200$ coupled oscillators interact with each other relative to their phase difference. Inter-layer interaction between the elements of different layers with the same indices was invariant. The phase dynamic of the ith oscillator within the layer l ($l = 1, 2$) is described by the following equation

$$\dot{\phi}_i^{(l)} = \omega_i^{(l)} - \frac{1}{N}\sum_{j=1}^{N}\kappa_{ij}^{(l)}\sin(\phi_i^{(l)} - \phi_j^{(l)} + \alpha_l) - \\ - \sum_{k=1,k\neq l}^{2}\sigma_{lk}\sin(\phi_i^{(l)} - \phi_i^{(k)}), \tag{160}$$

where $\omega_i^{(l)}$ denotes the natural frequency of the ith oscillator in the lth layer, σ_{lk} defines the inter-layer coupling strength from the oscillators of the layer k to the layer l, and α_l is the phase lag in the coupling between the oscillators in layer l.

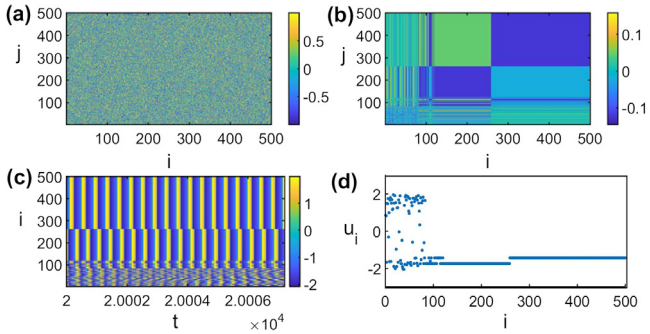

Fig. 82. The formation of chimera state in the adaptive FitzHugh–Nagumo network with fully connected topology. (a) The initial coupling strength matrix $\lambda_{ij}(0)$. (b) The adopted coupling strength matrix $\lambda_{ij}(t)$. (c) The spatiotemporal pattern of the network. (d) The time snapshot of the u variables of the oscillators.
Source: Figure reproduced with permission from [303].

$\kappa_{ij}^{(l)}$ indicates the coupling strength from the jth to the ith oscillator in layer l and is considered the same as Eq. (159). The parameter $0 < \beta_l < 2\pi$ controls the adaptation properties of the intra-layer couplings. Since $0 < \varepsilon \ll 1$, if the initial value of the $\kappa_{ij}^{(l)}$ is considered in the range of $[-1, 1]$, it will remain in this range forever. It can also be understood from Eq. (160) that if the oscillators i and j are in-phase synchronized ($\Delta\phi_{ij}^{(l)}(t) = \phi_i^{(l)}(t) - \phi_j^{(l)}(t) = 0$), the coupling strength between them should be equal to $\kappa_{ij}^{(l)} = -\sin\beta$ and if they are anti-phase synchronized ($\Delta\phi_{ij}^{(l)}(t) = \pi$), the coupling strength will be $\kappa_{ij}^{(l)} = \sin\beta$. In this research, the parameters were assumed in a way that the layers demonstrate different chimera states in the absence of inter-layer couplings.

First, the synchronization and chimera state were considered in a two-layer system with unidirectional coupling from the master layer's elements to the slave layer's elements ($\sigma_{12} = 0$, $\sigma_{21} \neq 0$). This mode always ensures the forced synchronization of chimera states. Next, the network with mutual coupling in layers ($\sigma_{12} = \sigma_{21} = \sigma$) was studied. In this case, the results showed that for weak coupling strength, the network is in incoherent state, and the formation of multi-cluster state needs a significantly strong inter-layer interaction. The results also showed that the dynamical behavior of the system is significantly dependent on the parameter σ.

In the neuronal ensembles, the synaptic strength and connections evolve in time regularly. In order to model a realistic neuronal network, Huo et al. [303] considered adaptive coupling strength with the following equation in coupled FitzHugh–Nagumo oscillators

$$\dot{\lambda}_{ij} = -\gamma[\sin(u_j - u_i + \beta) + \lambda_{ij}], \tag{161}$$

with $\gamma = 0.01$. The excitatory and inhibitory synapses are reflected by the positive and negative λ_{ij}, respectively. This network was studied under fully connected, random, and scale-free structures. The initial conditions of the oscillators and the initial coupling strength $\lambda_{ij}(0)$ are selected randomly. Fig. 82 shows the evolution of the network to a chimera state for fully connected topology. The initial and the stable coupling strength values are illustrated in Fig. 82a,b, respectively. It is observed that although $\lambda_{ij}(0)$ are distrusted randomly in $[-1, 1]$, the network evolution leads to the adaptation of $\lambda_{ij}(t)$ to take smaller values in $[-0.15, 0.15]$. Furthermore, the values of λ_{ij} for the synchronized group reaches a stabilized value, while for the asynchronized group changes randomly. The spatiotemporal pattern and the time snapshot of the network are depicted in Fig. 82c,d, respectively.

By changing the network structure to random ER or scale-free topologies, the chimera state is still organized, but with different evolution of the coupling strength matrix. Comparing the behaviors of the network in the case of static coupling with the adaptive coupling reveals that the adaptive coupling is essential for the emergence of chimera in the fully connected network. In comparison, it is a supporting factor in the random and scale-free networks.

The alternations in the synaptic strength and weights are known as plasticity. During different neuronal activities, the synapses become stronger or weaker for short or long time intervals. Various rules have been presented for the synaptic plasticity. One of these rules, which have been investigated in the chimera state, is the burst-timing-dependent plasticity (BTDP) [304]. This plasticity is dependent on the timing of the pre- and post-synaptic bursts in a way that short and long latencies result in potentiation and depression, respectively. For this study, the two-variable integrate-and-fire (IF) model of Izhikevich has been considered

$$\begin{cases} \dot{v}_i = 0.04v_i^2 + 5v_i + 140 - u_i + I + I_i^{syn} \\ \dot{u}_i = a(bv_i - u_i) \\ \text{if } v_i > 30 \text{ mv, then} \begin{cases} v_i \leftarrow c \\ u_i \leftarrow u_i + d \end{cases} \end{cases}, \tag{162}$$

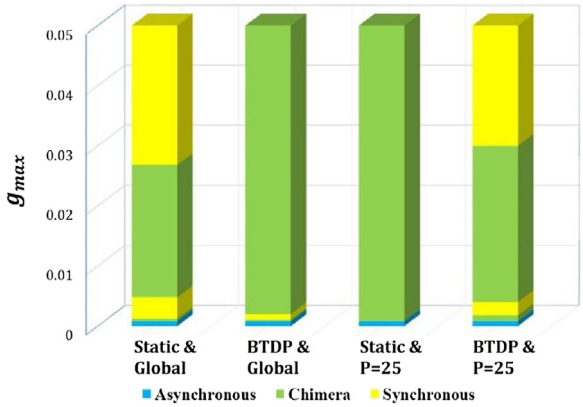

Fig. 83. Different behaviors of the network of Izhikevich neurons Eqs. (162) and (163) by choosing g_{max} in the range $[0, 0.05]$. The effects of global and non-local coupling and the static and BTDP synapses are shown. The asynchronization, chimera, and synchronization are represented by blue, green, and yellow colors.
Source: Figure reproduced with permission from [304].

where v and u are the membrane potential and the recovery variables, respectively. I^{syn} is the synaptic current obtained by

$$\begin{aligned} I_i^{syn} &= -\sum_{1(i\neq j)}^{N} g_{ji}C_{ji}s_j(v_i - v_{v_{[syn]}}), \\ \dot{s}_j &= \alpha(v_j)(1-s_j) - s_j/\tau, \\ \alpha(v_j) &= \alpha_0/(1+e^{-v_j/v_{shp}}), \end{aligned} \tag{163}$$

where s_j is the synaptic variable and is approximated by $\dot{s}_j = -\beta s_j$, if the pre-synaptic neuron is in the silent state, otherwise, it acts on the post-synaptic neuron with the value equal to one. Thus, the function $\alpha(v_j)$ can be estimated by a Heaviside function. The connectivity of the neurons is determined by the matrix C, such that $C_{ij} = 1$, if neurons i and j are connected, and $C_{ij} = 0$ otherwise, and $C_{ii} = \sum_{j=1(i\neq j)}^{N} C_{ij}$. The synaptic strength from jth to ith neuron is g_{ji}, which is refined by the BTDP rule

$$F(\Delta t) = \begin{cases} 18.2 - 25.8|\Delta t| & \text{if } |\Delta t| < 1, \\ -7.6 & \text{if } |\Delta t| \geq 1, (\%s^{-1}). \end{cases} \tag{164}$$

In this function, Δt is the time difference between the beginning of the post-synaptic and pre-synaptic bursts. *A* specific range is also considered for the synaptic strength to remain in the interval $[0, g_{max}]$.

Fig. 83 shows the dynamical behaviors of the network for static and BTDP synapses, with considering global and non-local connections. If the neurons are globally coupled, the BTDP leads to the extension of the chimera region to the parameter values in which the static network exhibits synchronization. In the non-local coupling, the results are inverse. As the static synapses are replaced with the BTDP, the synchronization is converted to the chimera for higher g_{max} values. Therefore, both the connection type (global or non-local) and the synaptic weight play significant roles in the network behavior. Furthermore, the stabilized synaptic strengths are different in the synchronized, asynchronized, and chimera states.

5.5.4. Hierarchical connections

Studies in neuroscience have drawn attention to another peculiar aspect in the topology of the networks' coupling. Hierarchical geometry in the connectivity matrix between oscillators causes qualitative changes of chimera state and induces nested coherent and incoherent regions. A hierarchical pattern is the finite form of the fractal pattern. This idea comes from diffusion tensor magnetic resonance imaging (DT-MRI) studies that have revealed an intricate architecture in the neuronal interconnectivity in the human and mammalian brain. This connection has already been used in simulations [305]. The analysis of DT-MRI images has shown that the connectivity of the neurons' axons represents a hierarchical geometry with fractal dimensions varying between 2.3 and 2.8. This variation is due to the local properties, on the subject, and on the noise reduction threshold [306].

For analyzing different networks with hierarchical connectivity, the "clustering coefficient" variable was defined by Watts and Strogatz [307]. The clustering coefficient describes the number of neighboring links relative to the maximum number of possible links. For observing the effect of varying the number of hierarchical steps on the emergence of different

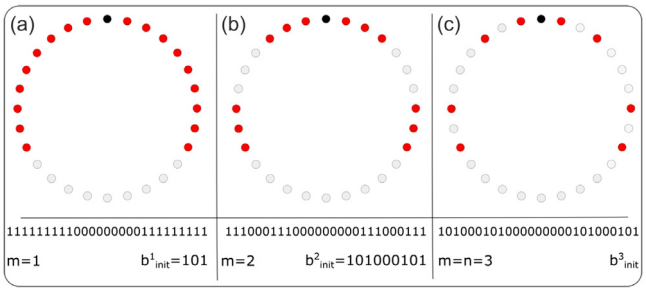

Fig. 84. Formation of the hierarchical coupling from the non-local coupling, with the initial base pattern of b_{init}=(101), the hierarchical level of $n = 3$ and $N = b^n + 1 = 28$. The reference, connected, and disconnected nodes are shown by black, red, and gray, respectively. (a) The first step of the hierarchical formation that is a non-local coupling with $R = 9$ nearest-neighbors at each side. In this step the clustering coefficient is $C(101, 3, 1) = 0.705882$ and the link density is $\rho = 0.64$. (b) The second step of the hierarchical formation with $C(101, 3, 2) = 0.409091$, and $\rho = 0.428$. (c) The final step of the hierarchical formation with $C(101, 3, 3) = 0$, and $\rho = 0.286$.
Source: Figure reproduced with permission from [308].

types of chimera states, a ring network of N van der Pol oscillators is considered in [308]. The dynamical equations for the 2-dimensional phase space variable $x_k = (u_k, \dot{u}_k)^T = (u_k, v_k)^T \in R^2$ are

$$\dot{x}_i(t) = \mathbf{F}(x_i(t)) + \frac{\sigma}{g}\sum_{j=1}^{N} G_{ij}\mathbf{H}(x_j - x_i), \tag{165}$$

with $i \in 1, \ldots, N$, and

$$\mathbf{F} = \begin{pmatrix} v \\ \varepsilon(1-u^2)v - u \end{pmatrix}, \tag{166}$$

where $\varepsilon > 0$ denotes the bifurcation parameter, and σ is the coupling strength. $g = \sum_{j=1}^{N} G_{ij}$ is the number of links for each node and $\mathbf{H} = \begin{pmatrix} 0 & 0 \\ b_1 & b_2 \end{pmatrix}$ is the local coupling matrix, which specifies the local interaction. $b_1 = 1.0$ and $b_2 = 0.1$ are interaction parameters that allow us to observe chimera states in non-locally coupled systems.

A classical Cantor construction algorithm for a fractal set is used for generating hierarchical geometry. The algorithm starts with assuming a base pattern or initiation string b_{init} of length b, where each element represents either a link ('1') or a gap ('0'). c_1 is defined as the number of links in b_{init} that each of these links is replaced by an initial base pattern in each iterative step, while each gap is replaced by b gaps. So the length of the bit pattern in the nth iteration will be equal to $N = b^n$. By using the resulting string as the fundamental row of the circulant adjacency matrix G, a hierarchical ring network of $N = b^n + 1$ nodes will be generated. The link density in the network is defined by $\rho = \frac{c_1^n}{N}$ and the fractal dimension is explained as $d_f = \frac{\ln c_1}{\ln b}$.

By considering a stepwise iteration process, the transition between non-local and hierarchical topology is observable. A base pattern (b_{init}) for both networks with non-local and hierarchical topology is a string of length b that contains an equal number of links (1) only at its beginning and end, and the other elements are zero (for instance (101) or (110011)). The stepwise transition between non-local and hierarchical topologies is as follows: First, by m times iteration of b_{init} according to the Cantor construction process, a pattern of size b^m is generated. Then this pattern expends to its final size N, by replacing each element with $\frac{N-1}{b^m}$ copies of itself. Fig. 84 shows a schematic view of the coupling topology with mth Cantor iterations of b before the expansion, which is defined as a hierarchical step. Each hierarchical step modifies the compactness and the total number of links of the final topology.

The simplest example of a chimera state in the above network (Eq. (165)) with hierarchical topology is constructed from the base pattern (101). The first step of the hierarchical network shows a two-headed chimera pattern, and in the 2-step, an eight-headed chimera pattern is formed. For a 3-step hierarchical network, the chimera state disappears and is not constructed again up to the 6th iteration. This observation shows the effect of the coupling radius and strength on the system's behavior that has also been studied before in [226].

The Logistic maps with $a = 3.8$ have also been used for studying chimera state in a ring network with hierarchical connectivity [309]. As the network of van der Pol oscillators, the results show that increasing the hierarchical level of iteration affects the spatiotemporal pattern of the system. This network can be described with the following equation

$$z_i^{t+1} = f(z_i^t) + \frac{\sigma}{c_{n,m}}\sum_{j=0}^{N-1} C_{ij}[f(z_j^t) - f(z_i^t)], \tag{167}$$

where f refers to the Logistic map, σ is the coupling strength, and $c_{n,m}$ denotes the number of links in the topology. Since it is assumed that the chimera state is more likely to occur in networks with higher clustering coefficient, in this work,

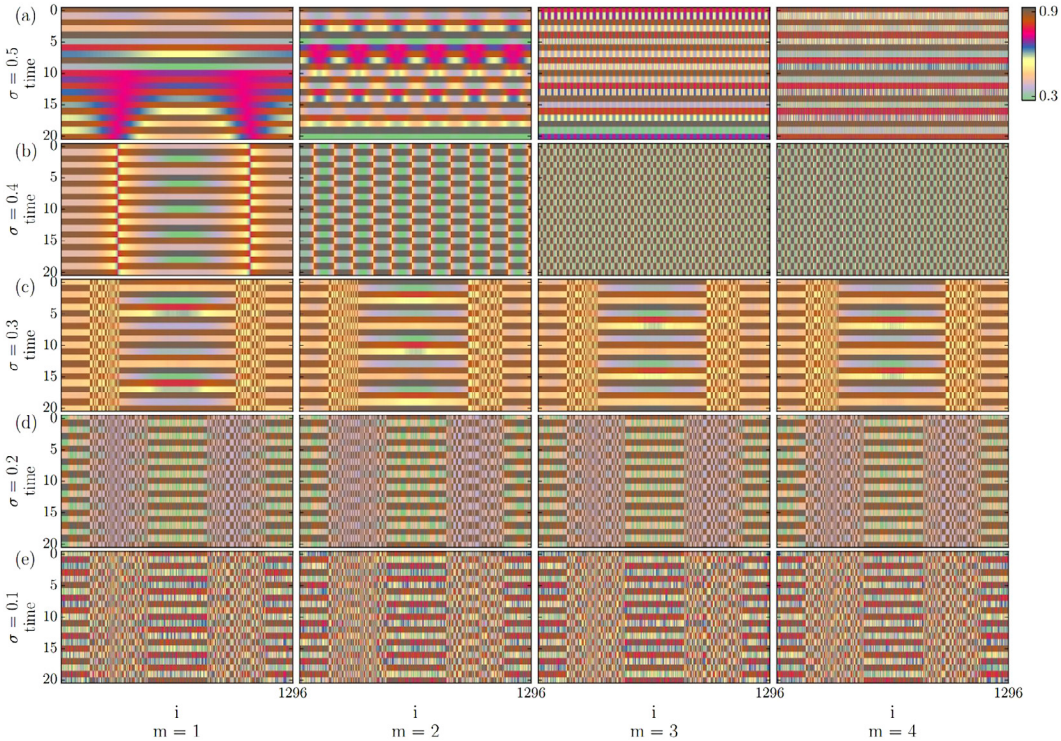

Fig. 85. Spatiotemporal patterns of the hierarchical Logistic network with considering $b_{init} = 110011$, $n = 4$, $N = 1297$, $a = 3.8$ for different hierarchical steps m (the columns) and coupling strength σ (the rows).
Source: Figure reproduced with permission from [309].

the base patterns of length $b = 6$ with at least $c_1 = 3$ links are considered. The hierarchical level is set at $n = 4$, so the number of nodes will be $N = b^n + 1 = 1297$. The network topology, bifurcation parameter of the Logistic map, coupling strength, initial condition, symmetry, and hierarchical step, all affect the dynamics of the system. The results show that with a fixed bifurcation parameter ($a = 3.8$), various phase and amplitude chimera patterns with multiple incoherent domains can be obtained from the network. Fig. 85 illustrates the dynamics of the network with base pattern 110011 for $m = 1, 2, 3, 4$. Twenty space–time plots are shown for different coupling strengths at each step. For all hierarchical steps, a transition to a chimera state with two incoherent domains is observable.

The comparison between the dynamics of two exemplary networks with symmetric and asymmetric base patterns (110011 and 011100, respectively) illustrated that symmetry and specially prepared initial conditions are critical for the observation of regular chimera patterns. While the asymmetric base pattern and the specific selection of the initial conditions lead to chimeras with small amplitudes and more complicated nests.

For the next step, researchers studied the effect of time delay on hierarchical networks [310]. For this purpose, a ring network of van der Pol oscillators Eqs. (165) and (166) with the base pattern $b_{init} = 11011$ after four iterative steps was considered. The results demonstrated that chimera state occurs in hierarchical networks with a high clustering coefficient. To investigate the effect of time-delay on this system, the network parameter was fixed at $b_{init} = 11011$, $n = 4$, $N = 5^4 + 1 = 626$, and $\varepsilon = 0.1$, where the network without delay demonstrated chimera pattern. The coupling strength σ and the time delay τ were considered as control parameters. The behaviors of the network in the parameter plane are demonstrated in Fig. 86. It is evident that for weak coupling strength ($\sigma < 0.3$), a small time-delay can immediately eliminate the chimera pattern and turn the behavior of the system from chimera to asynchronous. However, for larger values of coupling strength ($\sigma > 0.3$), chimera states are more stable and do not disappear by consideration of a small time-delay. By increasing the time delay, only some small tongue-like regions in the $\sigma - \tau$ plane show the chimera state, and the other parts exhibit coherent structures (fully synchronized state and traveling waves). The size of the chimera tongues is reduced as the time delay increases. As well, the coupling strength threshold at which the chimera is observable is lessened.

Another example that has been studied in this content is a complex network of FitzHugh–Nagumo oscillators with the below equations with $\varepsilon = 0.05$ and the threshold parameter $|a| < 1$, which locate the system in the oscillatory

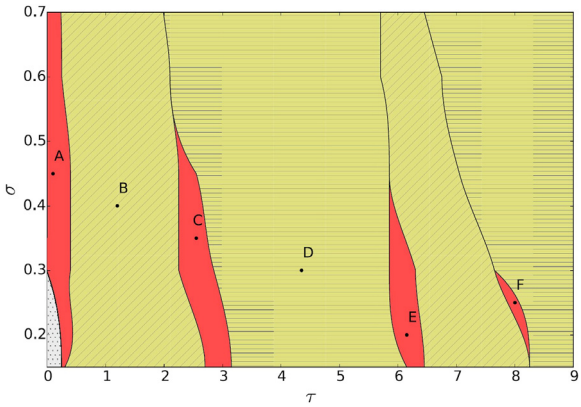

Fig. 86. Dynamical behaviors of the hierarchical van der Pol oscillators with time delay in the (σ, τ) plane with $b_{init} = 11011$, $n = 4$, $N = 626$, $\varepsilon = 0.1$. The tongue-like regions represent the regions of the chimeras within the coherent regime (in-phase synchronization or coherent traveling wave).
Source: Figure reproduced with permission from [310].

regime [311]

$$\begin{aligned} \varepsilon \frac{du_k}{dt} &= u_k - \frac{u_k^3}{3} - v_k \\ &\quad + \sigma \sum_{j=1}^{N} G_{kj}[b_{uu}(u_j - u_k) + b_{uv}(v_j - v_k)], \\ \varepsilon \frac{dv_k}{dt} &= u_k + a \\ &\quad + \sigma \sum_{j=1}^{N} G_{kj}[b_{vu}(u_j - u_k) + b_{vv}(v_j - v_k)], \end{aligned} \tag{168}$$

where the topology of the network is defined by the adjacency matrix G. In Ref. [311], two different topologies have been considered for this matrix. The first one is a symmetric structural neural connectivity G_{emp}, which has been derived from diffusion-weighted MRI images and models the brain network of a healthy human subject. The second is a mathematically constructed topology with modular fractal connectivity, G_{mod}. In both cases, the adjacency matrix G is weighted and undirected. The local interaction B is the same as C matrix in Eq. (148) with the fixed coupling phase $\phi = \pi/2 - 0.1$. In both cases, the chimera state can be observed for weak coupling strength, and further increasing the coupling strength leads the system toward a completely coherent state. In the empirical structural connectivity mode, frequency synchronized state can be obtained, and in the modular fractal connectivity mode, a completely synchronous state is achievable. Between these two states, the solitary state is seen where only single oscillators have different frequencies among the others. Since the node removal can eliminate the synchrony of the nodes, the hierarchical FitzHugh–Nagumo network model, has the ability to simulate epileptic seizures where the increased coupling strength leads to pathological synchrony, initiated or terminated via chimera states. Omelchenko et al. [218] studied a similar network of FHN oscillators with a construction base $b = 6$, and $n = 4$ iteration of the hierarchical step. Their results also indicated that increment of the links' number can decrease the chimera's multiplicity. Besides, they showed that the hierarchical distribution of the links leads to chimera states with complex nested asynchronous regions. For the next part, they used fractal dimension and local structure of the connectivity matrix as the control parameters for determining the multiplicity or the pattern of the chimera state. It was also investigated that different initiation strings, producing the same fractal dimension, give rise to different chimera patterns.

One of the other interesting aspects of the networks with hierarchical coupling topologies is their ability to show traveling multi-chimera states [214]. This phenomenon has been observed in a ring network of reduced form of Lattice Limit Cycle (LLC) model, which is devised for a cyclic reaction–diffusion process with predator–prey interactions among three particles X, Y, and S. The equations of the LLC model are as follows

$$\begin{aligned} \frac{dx}{dt} &= 2p_1x^2y^2 + p_2x(1 - x - y), \\ \frac{dy}{dt} &= p_1x^2y^2 - p_3y(1 - x - y), \end{aligned} \tag{169}$$

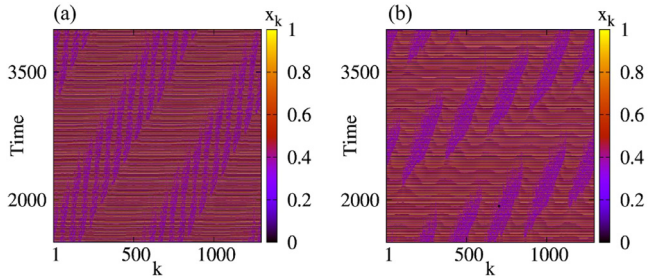

Fig. 87. Traveling chimeras observed in the hierarchical Lattice Limit Cycle network. (a) $d_f = \ln 4/\ln 6 = 0.774$, $b_{init} = 001111$. (b) $d_f = \ln 5/\ln 6 = 0.898$, $b_{init} = 110111$.
Source: Figure reproduced with permission from [214].

where p_1 is a control parameter, $p_2 = 0.5$, and $p_3 = 0.8$ are interaction rates. For constructing the hierarchical network, they considered the base size $b = 6$ and $n = 4$ iteration steps producing a system of size $N = 64 = 1296$. Two different initiation strings were assumed for stimulations: $S =$ "001111" and $S =$ "110111". So the connectivity patterns consisted of 256 and 625 times the symbol 1 and 1040 and 671 times the symbol 0, respectively. Fig. 87 shows the space–time plots of the mobility of the coherent/incoherent regions in traveling chimeras. It can be understood from this figure that each part of the ring network is continuously translated from coherent to the incoherent group.

The effect of fractal connectivity has also been investigated in a network of Leaky Integrate-and-Fire (LIF) elements [312]. The hierarchical topology leads the network to exhibit nested chimera state and transit between multi-chimera states with different multiplicities. Ref. [312] studied a ring of LIF oscillators with both non-local and hierarchical coupling with initiation string as "110011", the base size and the iteration steps as $b = 6$ and $n = 4$, respectively. It was attained that for the low value of the coupling strength in the case of hierarchical connectivity, the coherent regions have always lower mean phase velocities than the incoherent ones, irrespective of the refractory period. On the other hand, with a small refractory period, low values of coupling strength lead to the emergence of nested chimeras in a way that the incoherent and coherent regions are traveling around the ring. Their results showed that increasing the coupling strength merge the incoherent regions together and construct a larger incoherent region.

6. Control of chimeras

As mentioned in the previous sections, the chimera state in finite size networks is mostly transient and collapse to a coherent state after a defined time. Furthermore, in most of the cases, the chimera states are formed from the random initial conditions. Thus, the positions of the coherent and incoherent clusters are variant and depending on the initial conditions. While in some applications it is vital to control the lifetime of chimera or the clusters' spatial positions. Recently, some control techniques have been applied in this regard to stabilize the existence of chimeras or adjust the spatial locations [313–319]. Some of these proposed methods are reviewed in the following.

6.1. Proportional feedback

In 2014, Sieber et al. [211] presented a control approach based on the classical proportional control for the chimera state. To describe this method, they considered the network of coupled phase oscillators as

$$\frac{d\theta_k}{dt} = \omega - \frac{2\pi}{N}\sum_{j=1}^{N} G_{kj}\sin(\theta_k - \theta_j + \alpha),\ k = 1, \ldots, N, \tag{170}$$

with the coupling matrix

$$G_{kj} = G(x_k - x_j) = \frac{1}{2\pi}[1 + A\cos(x_k - x_j)], \tag{171}$$

with $x_k = 2k\pi/N - \pi$ being the position of the kth oscillator in the ring. As described in Section 3.1, the continuum limit equation of the network is as follows

$$\frac{dz}{dt} = i\omega z + \frac{1}{2}e^{-i\alpha}\mathcal{G}z - \frac{1}{2}e^{i\alpha}z^2\mathcal{G}\bar{z}, \tag{172}$$

where $z(x, t)$ is the complex local order parameter and

$$(\mathcal{G}\varphi)(x) := \int_{-\pi}^{\pi} G(x - y)\varphi(y)dy. \tag{173}$$

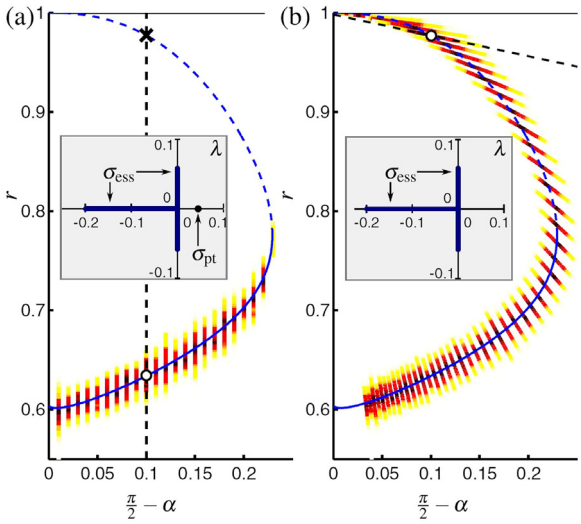

Fig. 88. The chimera solutions in the (α, r) plane for the uncontrolled (a) and controlled (b) cases. The continuum limit solution is shown by the blue curve, where the stable part is solid, and the unstable is dashed. The densities of the global order parameter are shown by the colored shades. The insets show the spectra of the linearized continuum limit.
Source: Figure reproduced with permission from [211].

Thus, the chimera state is the uniform rotating solution as

$$z(x,t) = a(x)e^{i\Omega t}, \tag{174}$$

where $a(x)$ is a spatial profile representing the coherent state by $|a(x)| = 1$ and the incoherent state by $|a(x)| < 1$ and Ω is a fixed frequency. The chimera solution of the continuum limit is demonstrated in Fig. 88 with the blue curve, showing the stable part with a solid line and the unstable part with the dashed line. Fig. 88a shows that the chimera state becomes unstable by decreasing α from $\pi/2 - 0.22$. The unstable solution continues until reaching the coherent state at $\alpha = \pi/2$, $r = 1$. In the case of finite size network, the stationary profile of the chimera state has some variations in time or space. In Fig. 88, the densities of the global order parameter are shown by the colored shades.

To control the unstable branch, the proportional control as follows has been suggested

$$\alpha(t) = \alpha_0 + K(r(t) - r_0), \tag{175}$$

where (α_0, r_0) is the reference point, and K is the control gain. In the uncontrolled case ($K = 0$), a straight line is created in the (α, r) plane (shown by the dashed line in Fig. 88a). The controlled system is developed along this line. In Fig. 88b, the reference point is chosen at $(\pi/2 + 0.01, 1)$, and it is observed that the chimera state becomes stable throughout the continuum limit branch. The insets in Fig. 88 indicate the spectra of the linearized continuum limit, representing that the unstable eigenvalue disappears by controlling.

The proposed control scheme also improves the collapse of the chimera to the coherent state in small networks. The destroyed chimera state in the uncontrolled network is shown in Fig. 89a for $N = 20$. By applying the controller, the lifetime of chimera is increased with raising the control gain up to $K = 0.5$. For $K > 0.5$, the chimera collapse is not observed anymore in the simulation time. Eventually, with increase of the gain from $K = 0.67$, the collapse is completely suppressed and the network reaches chimera state from all of the initial conditions. The chimera's lifetime and also the basin of attraction of the chimera state with increasing K is shown in Fig. 89c. The chimera's solution and the control lines with different gains are shown in Fig. 89b. Here, the reference point has been selected to support the chimera state for all K values.

6.2. Gradient dynamics

To control the spatial positions in chimera state, Bick and Martens et al. [313] proposed a control scheme based on the gradient control. They considered a network of phase oscillators described by

$$\partial_t \varphi(x,t) = \omega - \int_0^1 h(d(x,y)) \sin(\varphi(x,t) - \varphi(y,t) + \alpha) dy, \tag{176}$$

where the spatial position of an oscillator is denoted by x, the oscillator's phase at time t by $\varphi(x,t)$, and the coupling kernel by h. Assuming Q to be an observable of the system, the solution of Eq. (176), $\varphi(x,t)$, is termed as Q-traveling,

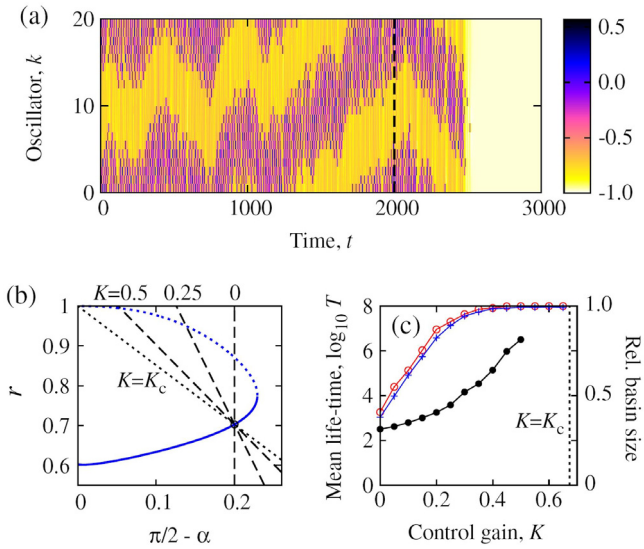

Fig. 89. (a) The uncontrolled chimera state for $N = 20$. The controller is switched off at $t = 2000$, which leads to chimera collapse. (b) The chimera solution in the continuum limit and the control lines with increasing control gain K. (c) The averaged lifetime of chimera with increasing control gain K for $N = 20$ (black), and the chimera's basin of attraction (blue: $N = 100$ and red: $N = 20$).
Source: Figure reproduced with permission from [211].

if the functions $y(t)$ and q exist in such a way that for all t, the equality $Q(x, \varphi_t) = q(x - y(t))$ is met. The function y(t) represents the spatial position of φ_t according to Q, and q is a differentiable function where all of its critical points are either minimum or maximum. The Q-traveling solution has a fixed speed v in space for all t, if $Q(x, \varphi_t) = q(x - vt)$.

Assuming that the desired position is x_*, this method aims to control the development of φ_t such that Q becomes maximum at x_*. In other words, by modifying the system parameter, $y(t)$ should be changed in a way that maximizes the term $q_{x_*}(y) := q(x_* - y)$. Further, it is supposed that the kernel functions h_a and a continuous invertible map ν exist such that φ_t is Q-traveling with speed $\dot{y} = \nu(a)$. Thus for constant a, the observable Q is as $Q(x, \varphi_t) = q(x - \nu(a)t)$, and therefore, φ_t travels with constant speed. Finally, the controller based on the gradient dynamics can be implemented by proper selection of the parameter a. By applying the gradient dynamics, one can find $\dot{y} = \gamma \partial_y q_{x_*}(y)$, which results in maximized $q_{x_*}(y)$ for $\gamma > 0$. Since $\partial_y q_{x_*}(y) = -q\prime(x_* - y) = -\partial_x q(x - y)|_{x_*}$, in the case of the following equality

$$\dot{y} = -\gamma \partial_x q(x - y)\Big|_{x_*} = -\gamma \partial_x Q(x, \varphi_t)\Big|_{x_*}, \tag{177}$$

$x = x_*$ will be a maximum of the observable Q. With considering $\dot{y} = \nu(a(t))$, the parameter $a(t)$ can be used as a control parameter

$$a(t) = \nu^{-1}\left(-\gamma \partial_x Q(x, \varphi_t)\Big|_{x_*}\right). \tag{178}$$

Therefore, selecting the parameter $a(t)$ according to Eq. (178), the traveling solution, in which x_* is the maximum of Q, will exist.

For controlling chimera states, the proposed control method is applied to the absolute value R of the local-order parameter. The reason is that the local order parameter provides a measure for the local synchronization. Thus, finding an R-traveling solution for the network which maximizes the local order parameter, leads to the transition of the synchronized part to the desired position x_*. With considering the kernel functions such that the R-traveling solutions have nonzero speed $\nu(a)$, then the control parameter is obtained by

$$a(t) = \nu^{-1}\left(-\gamma \partial_x R(x, \varphi_t)\Big|_{x_*}\right). \tag{179}$$

In the chimera state with one coherent cluster within the incoherent one, the local order parameter has a global maximum, while in multi-headed chimera, the local order parameter at the desired position is locally minimized.

To represent the control efficiency numerically, the following network is considered

$$\dot{\varphi}_k = \omega_k - \frac{1}{N}\sum_{j=1}^{N} h(d(\iota(k), \iota(j)))\sin(\varphi_k - \varphi_j + \alpha), \tag{180}$$

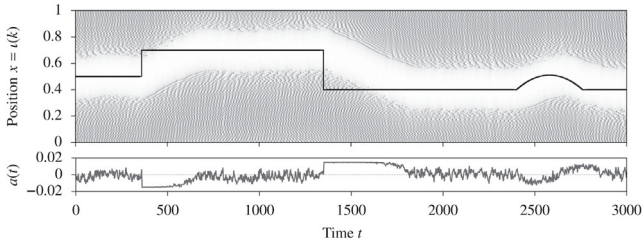

Fig. 90. Controlling the chimera position with the gradient coupling in $N = 256$ phase oscillators. The desired position is shown by the black line in the space–time plot. The lower panel shows the variation of the asymmetry parameter $a(t)$ with considering $a_{max} = 0.015$.
Source: Figure reproduced with permission from [313].

where $\iota = k/N$ denotes the oscillators' locations in the ring, and $d(x, y) = \left(\left(x - y + \frac{1}{2}\right) \mod 1\right) - \frac{1}{2}$ is a signed distance function in space. To induce the drifting clusters in the network, the asymmetric coupling kernel is used as

$$h_a(x) = \begin{cases} \exp(-\kappa(1-a)|x|) & \text{if } x < 0 \\ \exp(-\kappa(1+a)|x|) & \text{if } x \geq 0, \end{cases} \tag{181}$$

where $a \in (-1, 1)$ defines the symmetry, this kernel function causes the asymmetry and the traveling speed to have a monotonic correlation $\nu(a)$. For very small values of a ($a < 0.015$), $\nu(a)$ is almost linear at $a = 0$, and thus, the chimera state can be considered as an R-traveling solution with constant speed. By applying the controller Eq. (179) works as feedback control. The mechanism is as follows: when the coherent part is far from the desired position, the nonzero asymmetry leads to the motion of the coherent part respecting the desired position. As the desired position is obtained, the asymmetry is reduced and helps in the persisting of the chimera in space. The result of the controlled chimera state is illustrated in Fig. 90, wherein the desired position x_* is time-varying (shown with black line). It is observed that the controller effectively influences the coherent cluster to follow the desired position in the ring. The asymmetry parameter $a(t)$ changes to direct the chimera toward the desired position. As soon as the desired position is attained, $a(t)$ variation is declined to zero.

6.3. Modification of system parameters

In a network with fixed couplings, substituting one or some of the oscillatory units with excitable ones can be used for controlling the position of the incoherent cluster [314]. In the FitzHugh–Nagumo model, by changing the parameter a, the system can exhibit either oscillatory dynamics ($a < 1$) or excitable one ($a > 1$). Therefore, in a ring of non-locally coupled FHN oscillators, the dynamics of the units can be adjusted by varying this parameter. To investigate the influence of the excitable units in the network, it is considered that b of N FHN oscillators are in the excitatory state, while others are in the oscillatory state

$$a_i = \begin{cases} a_{osc} & \text{for } i > b \\ a_{exc} & \text{for } i \leq b. \end{cases} \tag{182}$$

Therefore, a barrier of excitable units exists in the network, with the barrier border b and the barrier height a_{exc}. In a large homogeneous network of FHN oscillators with $N = 1000$ and $a_i = a_{osc} = 0.5$, a stable chimera state emerges for the coupling strength $\sigma = 0.2$ and the coupling range $R = 350$. In this case, the positions of the coherent and incoherent oscillators are fixed and dependent on the initial conditions. In the same parameter values and initial conditions, by introducing a barrier of excitable units, the incoherent cluster is attracted by the barrier. Fig. 91 illustrates an example of this case where a barrier with width $b = 5$ and height $a_{exc} = 1.3$ is located at the center of the ring ($i = 500$). At first, the chimera state with the coherent part almost in the center is formed (Fig. 91a). As time passes, the coherent and incoherent groups move in space such that the barrier is finally in the middle of the incoherent group (Fig. 91b).

An interesting event in this control method is that after the attraction of the incoherent domain, by returning the excitable units to oscillatory, the position of the incoherent cluster remains the same. Fig. 92a illustrates the stability of the incoherent cluster by removing the barrier. Firstly, the network's nodes are homogeneously in the oscillatory state, and a chimera state is formed. Then, a single node at the network's center is changed to the excitable unit (at $t = 0$, shown by a dashed white line in the figure), and attracts the incoherent domain. After 5000 time-units (demonstrated by the second dashed white line), the barrier is removed, and the network returns to the previous homogeneous oscillatory units. It is observed that the incoherent location is preserved and does not return to its previous location. If the width and height of the barrier increase, then the speed of the drifting increases accordingly, and thus the barrier is placed at the incoherence center faster. In Fig. 92b, a wider barrier with $b = 100$ and the height $a_{exc} = 1.5$ is used alternatively at two different locations of the ring (placed within the white dashed lines). Consequently, the coherent and incoherent domains change alternatively. As a result, one can locate the incoherent cluster at the desired position by defining a specific barrier of excitable units in the network. Furthermore, the presence of the excitable units can lead to the emergence of a chimera state from a completely coherent network.

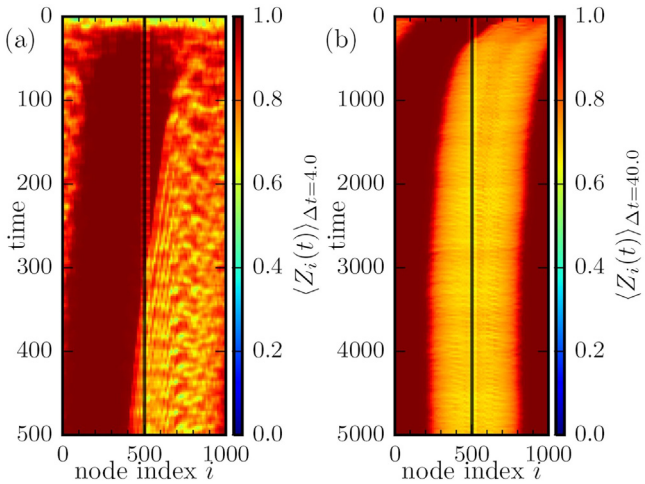

Fig. 91. The local order parameter of the FHN network ($N = 1000$) with a barrier of excitable units with width $b = 5$ and height $a_{exc} = 1.3$. (a) $t \in (0, 500)$, (b) $t \in (0, 5000)$. The black vertical line shows the barrier.
Source: Figure reproduced with permission from [314].

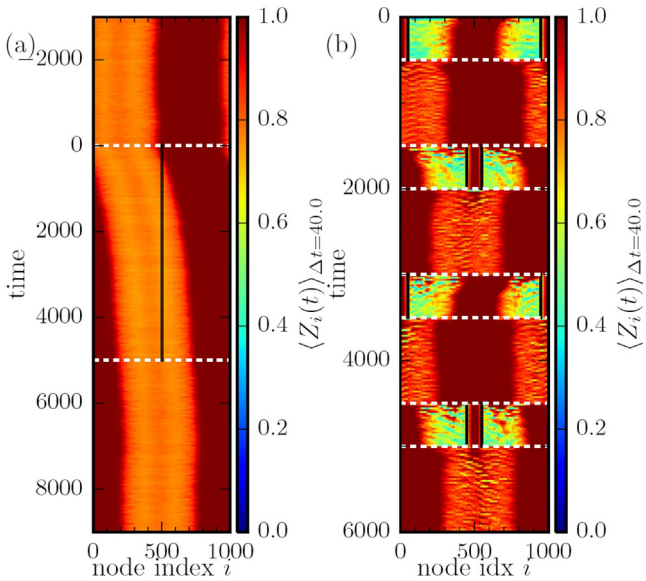

Fig. 92. The local order parameter of the FHN network with excitable units barrier. (a) The barrier with $b = 1$ and $a_{exc} = 1.1$ is applied from $t = 0$ to $t = 5000$. (b) The barrier with $b = 100$ and $a_{exc} = 1.5$ is applied alternatively at two different locations within the white dashed lines.
Source: Figure reproduced with permission from [314].

6.4. Pinning control

In the networks of coupled oscillators, the pinning control is defined by applying the controller only to specific nodes of the network, which are called pinned nodes. Generally, the pinning control has been used to force all of the network's nodes to have a completely coherent oscillation. However, it has also been successful in partial synchronization to control the positions of the coherent and incoherent clusters [315]. This method excels when there is access only to some of the oscillators of the network.

To examine the pinning control, a ring network of non-locally coupled oscillators is considered. Then a certain number of oscillators (N_p) are imposed by a controller ($u_i, i = 1, \ldots, N_p$). Designing the controller depends on whether the purpose is to adjust the coherent cluster or the incoherent cluster. To control the position of the coherent domain, the controller is defined as follows

$$\mathbf{u}_i(t) = w\delta_i(\Theta(t) - \Theta(t - t_c))\mathbf{H}_c(x_r, x_i), \tag{183}$$

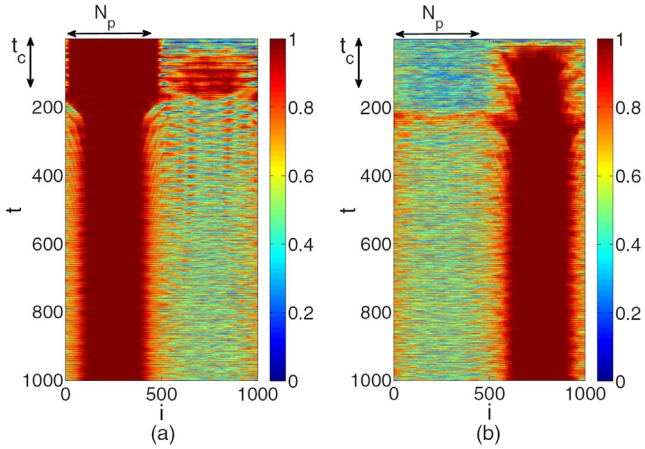

Fig. 93. The result of applying the pinning control on the FHN network with $N = 1000$, $P = 350$, $\sigma = 0.15$, $\beta = 1.47$, $\varepsilon = 0.05$, $a = 0.5$, $N_p = 500$, $t_c = 150$. The local order parameter of the oscillators is shown. (a) Applying the coherent control with $w = 0.25$, $\varepsilon_r = 0.06$, $a_r = 0.5$. (b) Applying the incoherent control with $D = 0.125$.
Source: Figure reproduced with permission from [315].

where w is the controller strength, Θ is the Heaviside function, $\delta_i = 1$ for $i = 1, \ldots, N_p$ and $\delta_i = 0$ for $i = N_p + 1, \ldots, N$. The time of applying the controller is t_c, and $\mathbf{H}_c$ is the coupling function between the pinned nodes (x_i) and the reference trajectory (x_r). The reference oscillator (x_r) is to direct the pinned systems in a synchronized motion. In order to prevent a complete synchronization state, the reference oscillator is the same as the network's oscillators, but with a small difference in parameters. Therefore, the pinning control drives the pinned nodes toward a coherent state, while the other nodes are incoherent, and subsequently, a chimera state with a controlled coherent domain is formed.

In the case when the purpose is controlling the incoherent domain, the controller can be determined as

$$\mathbf{u}_i(t) = \delta_i(\Theta(t) - \Theta(t - t_c))\sqrt{2D}\mathbf{H}_n\xi_i(t), \tag{184}$$

where $\xi_i(t)$ is the white Gaussian noise with intensity D. The matrix $\mathbf{H}_n$ determines the variable that is added with noise. In this case, the pinned nodes are led to behave incoherently. In pinning control, the controller is applied for an interval (t_c), and then it is turned off, and the coherent and incoherent domains remain stable. Thus the period of applying controller is an important factor. The other parameters affecting the controller result are the strength of the controller (w) or noise intensity (D), and the fraction of the pinned nodes to the total nodes (N_p/N). The error of control is defined by the difference between the local order parameter of the pinned nodes and their desired local order parameter

$$E = \frac{1}{N_p}\sum_{j=1}^{N_p} |\langle R_i\rangle_T - R_d|, \tag{185}$$

where the desired local order parameter in the coherent control is $R_d = 1$, and in the incoherent control is assumed to be $R_d = 0.5$.

To demonstrate the effect of pinning control, a network of non-locally coupled FitzHugh–Nagumo oscillators is considered. The parameters of the network are fixed at $N = 1000$, $\sigma = 0.15$, $P = 350$, $\varepsilon = 0.05$, $a = 0.5$, and $\beta = 1.47$. For coherent control, the coupling matrix is $\mathbf{H}_c(x_r, x_i) = \begin{pmatrix} 1 & 0 \\ 0 & 1 \end{pmatrix}(x_r - x_i)$, and the reference oscillator has the equations of FHN oscillator with $a_r = 0.5$ and $\varepsilon_r = 0.06$. For the incoherent control, $\mathbf{H}_n$ is considered as $\mathbf{H}_n = \begin{pmatrix} 1 & 0 \\ 0 & 1 \end{pmatrix}$. The results are shown in Fig. 93. In Fig. 93a,b, the pinned oscillators are enforced to be coherent and incoherent, respectively. In both cases, the initial conditions are the same, and the number of pinned nodes is $N_p = 500$ with $t_c = 150$ time units. It is observed that the effect of initial conditions is suppressed, and the coherent (or incoherent) clusters are located at the desired position and are stable after switching off the controller.

The efficiency of the pinning control depends on the controller parameters (N_p/N, t_c, w, or D) simultaneously. For example, when the controller strength (w) is small, the coherent cluster locates properly for a large fraction of pinned nodes. As the strength increases, a smaller number of pinned nodes is required. More increasing of w leads to the appearance of complete synchronization in the network. The synchronization may also be obtained when the fraction of pinned nodes exceeds 0.5. The variation of the control error with w is represented in Fig. 94a. Similarly, in incoherent control, the method is effective for intermediate values of D. For small intensities, the effect of noise is not considerable, and the initial conditions define the clusters' positions. In contrast, very large noises and also pinned fraction increase uncertainty in the network. The effect of D on the control error for $N_p/N = 0.4$ is shown in Fig. 94b.

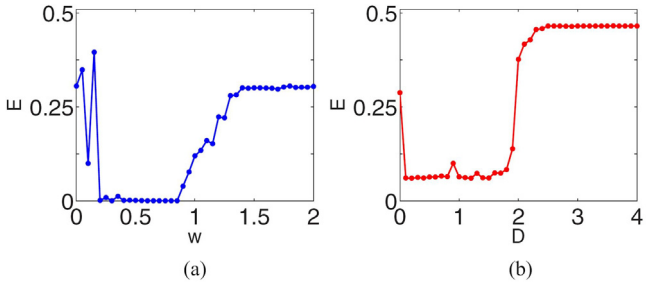

Fig. 94. The error of the pinning control concerning the controller strength w for $N_p/N = 0.15$ in (a), and the noise intensity D for $N_p/N = 0.4$ in (b).
Source: Figure reproduced with permission from [315].

To deal with the problem of drifting of clusters in the small networks, the pinning control can be applied in a closed-loop scheme. In this case, the error is computed by

$$E(t) = \frac{1}{N_p}\sum_{j=1}^{N_p}\left|R_d - \frac{1}{\Delta T}\int_{t-\Delta T}^{t} R_i(\tau)d\tau\right|, \tag{186}$$

where $\frac{1}{\Delta T}\int_{t-\Delta T}^{t} R_i(\tau)d\tau$ is the moving average local order parameter in the interval $[t-\Delta T, t]$. After applying the controller on the network for the period t_c, the error is observed continuously. The drifting is detected by an increase in the error. In this case, the controller is applied again for the t_c period.

6.5. Tweezer control

In 2016, a tweezer control method was presented for stabilizing chimeras in small networks [316]. Similar to the tweezer, which has two levers, the tweezer control aims to provide two efficient mechanisms for preventing chimera collapses and also fixing the incoherent part position. To describe this control scheme, the coupled van der Pol oscillators with the following equation is considered

$$\begin{aligned}\ddot{x}_k &= (\varepsilon - x_k^2)\dot{x}_k - x_k \\ &\quad + \frac{1}{R}\sum_{j=1}^{R}[a_-(x_{k-j} - x_k) + b_-(\dot{x}_{k-j} - \dot{x}_k)] \\ &\quad + \frac{1}{R}\sum_{j=1}^{R}[a_+(x_{k+j} - x_k) + b_+(\dot{x}_{k+j} - \dot{x}_k)],\end{aligned} \tag{187}$$

where R is the coupling range, and a_-, a_+ and b_-, b_+ are the coupling strength of the position and velocity variable to the left and right neighbors, respectively. For simplicity, the coupling of the position variable is assumed to be symmetric as: $a_- = a_+ = a$, and the coupling of the velocity variable is asymmetric as: $b_- = a\sigma_-$, $b_+ = a\sigma_+$. Also, the desired position of the incoherent state is assumed to be at the center of oscillators. The control method must find the optimum σ_- and σ_+ for stabilizing chimera. The method is started by introducing the following complex order parameters

$$\begin{aligned}Z_1(t) &= \frac{1}{[N/2]}\sum_{k=1}^{[N/2]} e^{i\phi_k(t)}, \\ Z_2(t) &= \frac{1}{[N/2]}\sum_{k=1}^{[N/2]} e^{i\phi_{N-k+1}(t)},\end{aligned} \tag{188}$$

where $\phi_k(t)$ denotes the geometric phase of the kth oscillator, given by

$$e^{i\phi_k(t)} = (x_k^2(t) + \dot{x}_k^2(t))^{-1/2}(x_k(t) + i\dot{x}_k(t)). \tag{189}$$

Subsequently, the tweezer feedback control is designed as

$$\sigma_\pm = K_s\left(1 - \frac{1}{2}|Z_1 + Z_2|\right) \pm K_a(|Z_1| - |Z_2|). \tag{190}$$

The control term is divided into two symmetric and asymmetric parts with strengths K_s and K_a, respectively. The term $(Z_1 + Z_2)/2$ is equivalent to the complex global order parameter. Thus K_s controls the collapse of the chimera to

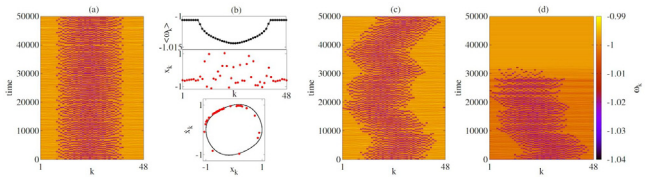

Fig. 95. Applying the tweezer chimera method on the network Eq. (187) with $N = 48$ oscillators. (a) A stable chimera state is obtained for $K_s = 0.5$ and $K_a = 2$. (b) The mean phase velocity, the snapshot of x variables, and the phase portrait of oscillators corresponding to part a. (c) A drifting chimera state obtained for $K_s = 0.5$ and $K_a = 0$. (d) A collapse chimera state obtained for constant σ_- and σ_+. Other parameters of the network are $R = 16$, $\varepsilon = 0.2$, $a = 0.02$.
Source: Figure reproduced with permission from [316].

the coherent state. In the second term, $|Z_1| - |Z_2|$ indicates the distance of the incoherent part from the center of the oscillators. Therefore, regulating K_a leads to the centering of the incoherent domain.

The results of applying the tweezer control on the network Eq. (187) with $N = 48$ oscillators are shown in Fig. 95. In Fig. 95a, both of the symmetric and asymmetric terms of the control Eq. (190) are applied and regulated. Thus, a stable chimera state with a fixed incoherent part is produced. The averaged mean phase velocity of the oscillators, the snapshot of the x variables and phase portrait of the oscillators are shown in part b. Next, only the symmetric control term is considered, and the asymmetric term is ignored ($K_a = 0$). This setting leads to the formation of a chimera state with drifting domains (Fig. 95c). Finally, with no consideration of both control terms and adjusting the σ_- and σ_+ at the effective time-averaged of σ_- and σ_+ obtained for case a, a transient chimera state emerges and after a while the network becomes coherent (Fig. 95d). This control strategy is also effective in networks with smaller oscillator numbers.

Varying the control gains (K_s and K_a) indeed affects the obtained chimera state. Therefore, finding the range of gains for the optimum control of the network is necessary [320]. To evaluate the chimera state, the standard deviation of the mean phase velocity can be used

$$\Delta_\omega = \sqrt{\frac{1}{N}\sum_{k=1}^{N}(\langle\omega_k\rangle - \Omega)^2}, \qquad \Omega = \frac{1}{N}\sum_{k=1}^{N}\langle\omega_k\rangle\,. \tag{191}$$

The profile of ω in the case of chimera state is arc-like, where arc-part shows the incoherent part, and the flat part shows the coherent part. Thus, larger Δ_ω shows a chimera state and $\Delta_\omega = 0$ illustrates the coherent state. Another measure for the network's pattern can be the size of the coherent part of chimera. Fig. 96 represents these two measures by varying the control gains for $N = 24$ coupled van der Pol oscillators (Eq. (187)). Since the dynamics of the isolated oscillator affects the control's results, the analysis has been done on three different oscillator's dynamics by choosing $\varepsilon = 0.2, 1, 5$. The corresponding results are shown in the left, middle, and right panels of Fig. 96, respectively. The diagrams of Δ_ω show that the optimum control is obtained for intermediate values of K_s. In contrast, the asymmetric gain (K_a) influences on Δ_ω in very small values. As K_a increases from a threshold, the network's behavior remains the same, and thus, the position control is saturated. The second row of Fig. 96 shows the size of the coherent part corresponding to parts a–c. Except for very small K_s values, with the increment of K_s, the size of the coherent part is increased, while Δ_ω is decreased. Therefore, the chimera state with larger Δ_ω (higher difference between the mean phase velocities of coherent and incoherent parts) has a smaller coherent part.

The dynamical regions near the limits $K_s \longrightarrow 0$ and $K_a \longrightarrow 0$ are different, although having the same colors in the diagrams of Fig. 96. For $K_s = 0$, the global order parameter is close to one, and the network is completely synchronous. While in $K_a = 0$, the global order parameter is between zero and one. But due to the high drifting of the incoherent part, the pattern cannot be named chimera state. In conclusion, tweezer control is an effective tool for the stabilization of chimera state in the networks especially with a small number of oscillators. Through this method, the stabilized chimera with the desired coherent size can be attained with proper selection of the control gains. Furthermore, this approach is applicable for chimera states with multiple incoherent groups.

In many applications of multilayer networks, there is no access to some of the layers. Therefore, finding a mechanism for controlling the non-accessible layer is essential. Omelchenko et al. [321] presented that the tweezer control scheme has well performance in multilayer structures, such that by applying the controller on one layer, the other layer is also controllable. To this aim, they considered a two-layer multiplex network of coupled van der Pol oscillators, where each layer can be described by Eq. (187). The layers are identical, and the inter-layer coupling is bidirectional and has a constant value. Then, the tweezer control is only applied to the first layer. The inter-layer coupling strength plays an important role in the control of the second layer. When the layers are coupled weakly (small inter-layer coupling strength), only the first layer has a stable chimera state, and the second layer reaches a coherent state. As the inter-layer coupling strength increases, it allows for the controlled chimera in the second layer. This control scheme is also applicable in networks with non-identical rings (having different coupling ranges).

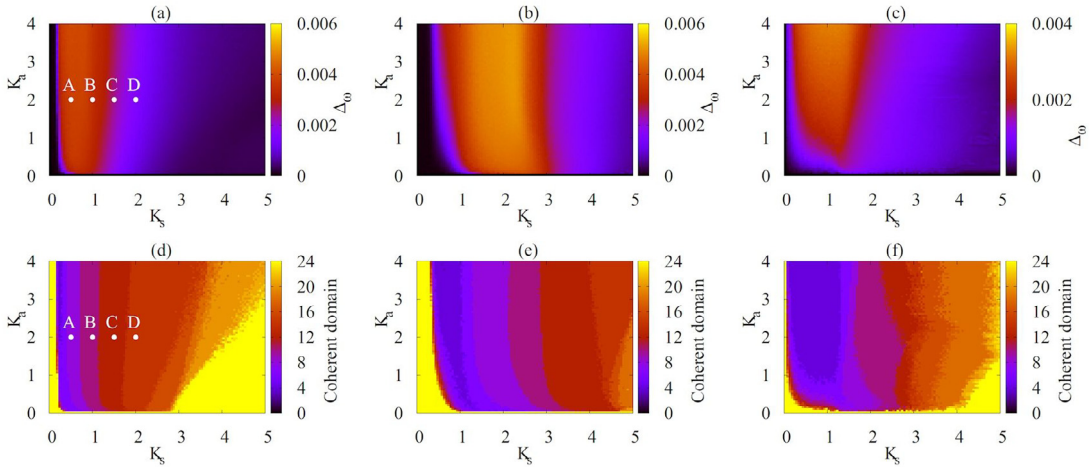

Fig. 96. The standard deviation of the mean phase velocity (first row) and the size of the coherent part of chimera (second row) of the van der Pol oscillators Eq. (187) by varying the tweezer control gains. The parameters are $N = 24$, $R = 8$, $a = 0.02$. (a,d) $\varepsilon = 0.2$. (b,e) $\varepsilon = 1$. (c,f) $\varepsilon = 5$.
Source: Figure reproduced with permission from [320].

6.6. Time-delayed coupling

It has been shown that using the time delay in the coupling can help in controlling the stability of the networks. As well, the time-delayed coupling can considerably influence the behavior of the network, and also on the lifetime of chimeras. As mentioned in Section 4, the network of non-locally coupled Stuart–Landau (SL) oscillators exhibits amplitude chimera and also chimera death in a particular range of parameters. The amplitude chimeras in this network are transient and change to the coherent states after a specified time. However, using the time delay in the coupling of SL oscillators can increase the lifetime of amplitude chimera [318]. The network of SL oscillators with time-delayed coupling is as follows

$$\dot{z}_j = [\lambda + i\omega - |z_j|^2]z_j + \frac{\sigma}{2P}\sum_{k=j-P}^{j+P}[\mathrm{Re}(D[z_k(t)]) - \mathrm{Re}(z_j(t))], \tag{192}$$

where D is the delay operator, such that $D_1[z(t)] = z(t-\tau)$ denotes the constant delay, $D_2[z(t)] = z(t-\tau(t))$ represents the time-varying delay, and $D_3[z(t)] = \int_0^\infty G(t')z(t-t')dt'$ shows the distributed delay. The top row in Fig. 97 shows the lifetime of the amplitude chimera by the variation of the coupling range (P) and the time delay (τ). This diagram indicates that the time delays effect on the chimera's lifetime in low values of the coupling range significantly. As the coupling range increases, the time delay effect is decreased. The lifetime of chimera versus time delay for different coupling strengths and for $P = 2$, $P = 3$, and $P = 4$ are illustrated in Fig. 97 bottom row. The increment of the lifetime by increasing time delay is obvious in these figures. Furthermore, the larger coupling strength results in a longer lifetime. Therefore, the lifetime of amplitude chimera is controllable by using time delay in the coupling.

The delayed coupling can also change the dynamical pattern of the network and induce other partially coherent patterns [318]. The observed spatiotemporal patterns include symmetric and asymmetric amplitude chimeras, partial amplitude chimera, partial oscillation death, and multi-cluster chimeras. Some of the patterns relating to the multi-cluster amplitude chimeras are shown in Fig. 98. Consequently, by changing the time delay, one can obtain the desired amplitude chimera pattern. If the constant time delay is changed to the time-varying or distributed ones, the modulation of the time-varying delay or the type and parameters of the distributed delay can be considered as the control parameters.

The other factor which can control the lifetime of amplitude chimera is the noise [322]. The Stuart–Landau network with the presence of noise is given by

$$\dot{z}_j = f(z_j) + \frac{\sigma}{2P}\sum_{k=j-P}^{j+P}(\mathrm{Re}(z_k) - \mathrm{Re}(z_j)) + \sqrt{2D}\xi_j(t), \tag{193}$$

where $\xi_j(t)$ is additive Gaussian white noise, and D is its intensity.

In the presence of noise, the network still exhibits the amplitude chimera, though with shorter lifetime. The left panel of Fig. 99 represents the lifetime of amplitude chimera versus the noise intensity for different coupling strengths. The diagrams are plotted by averaging the results of 50 sets of initial conditions and different noise distributions. It is obvious that the lifetime decreases linearly with increasing the noise in the logarithmic scale. The relation between the lifetime

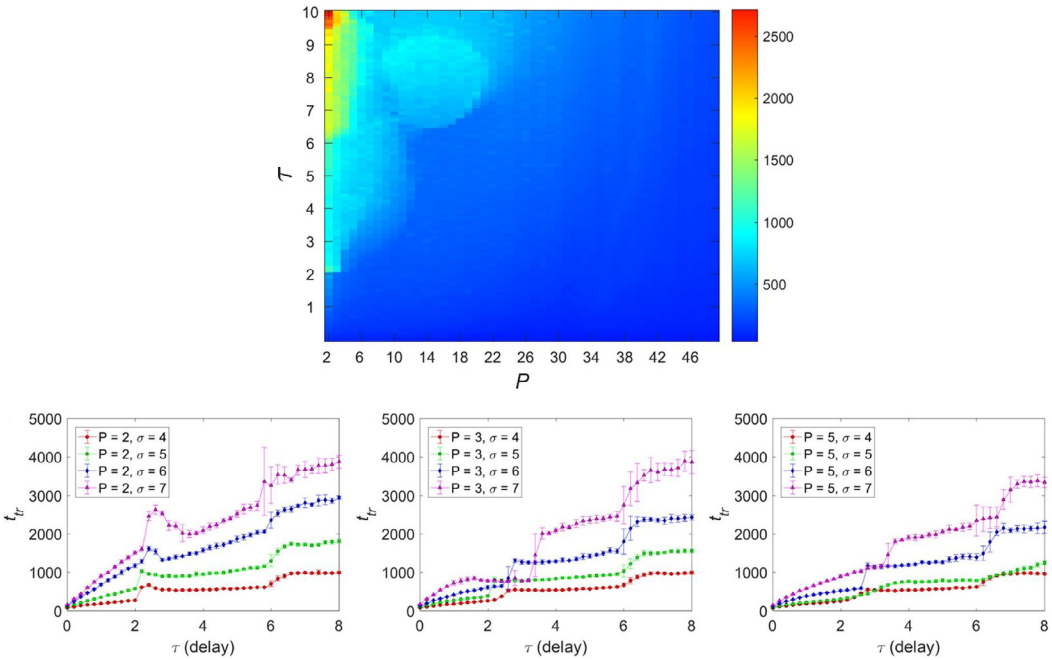

Fig. 97. The lifetime of the amplitude chimera in the network of delayed-coupled Stuart–Landau oscillators (Eq. (192)). Top row: The plane of coupling range (P) and the time delay (τ) for $\sigma = 5$. Bottom row: The lifetime vs. time delay for $\sigma = 4, 5, 6, 7$ and $P = 2, 3, 5$. The parameters of the network are $\lambda = 1$, $\omega = 2$, $N = 100$.
Source: Figure reproduced with permission from [318].

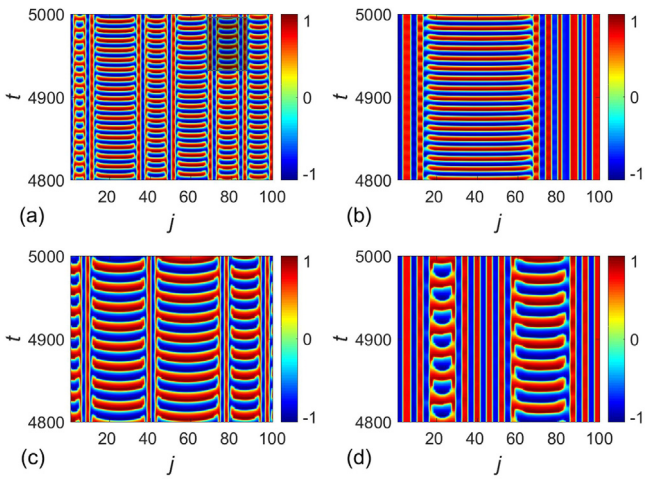

Fig. 98. Some of the multi-cluster amplitude chimeras induced by the delayed coupling in the Stuart–Landau oscillators (Eq. (192)). (a) $\sigma = 13$, $P = 2$, $\tau = \pi/4$. (b) $\sigma = 14$, $P = 5$, $\tau = \pi/4$. (c) $\sigma = 11$, $P = 2$, $\tau = \pi$. (d) $\sigma = 12$, $P = 5$, $\tau = \pi$.
Source: Figure reproduced with permission from [318].

and noise intensity can be described by $t_{tr} = -\frac{1}{\mu}\ln D + \eta$, where $-\frac{1}{\mu}$ is the slope of the lines, and η is the axis intercept. In contrast to the noise, the strengthening of the coupling leads to an increase of lifetime. Furthermore, the spread of the lifetimes is less for lower coupling strength and larger noise.

The noise also affects the dynamical regions of the network. In the absence of noise, by varying the coupling strength and range, the network behavior changes between coherent state and chimera death states with different clusters. When the noise is added, the regions of these behaviors are affected. However, the noise does not influence on the borders of the different cluster chimera death states. But the border between the synchronous state and the chimera death states depends on the noise intensity, such that it is moved toward higher coupling strength as the noise increases. The borders

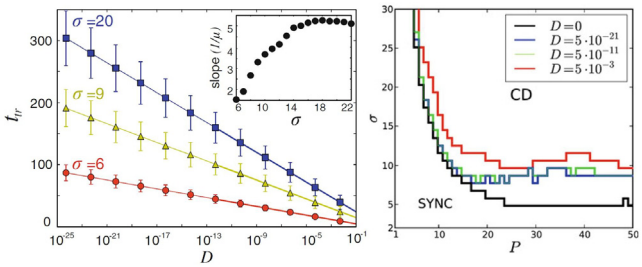

Fig. 99. Left panel: The amplitude chimera's lifetime vs. the intensity of the noise in the logarithmic scale for $\sigma = 6, 9, 20$. The results of 50 different initial conditions have been averaged. The inset shows the slope vs. the coupling strength. The parameters of the network are $\lambda = 1$, $\omega = 2$, $N = 100$, $P = 4$. Right panel: The borders between the synchronous oscillations (SYNC) and the chimera death states (CD) for different noise intensities (D) in the (P, σ) plane.
Source: Figure reproduced with permission from [322].

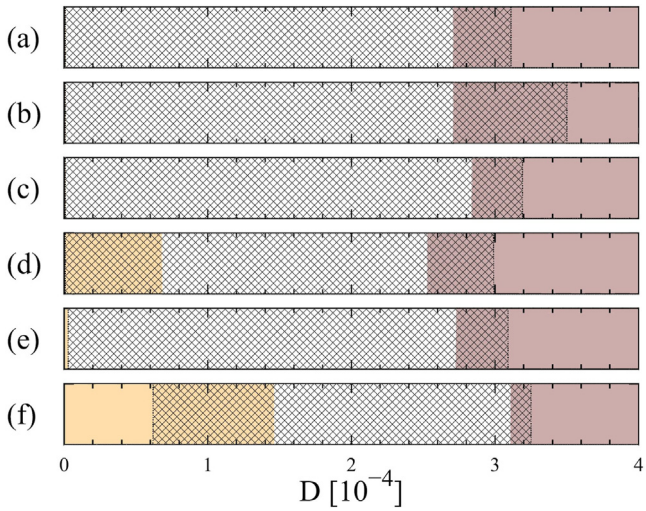

Fig. 100. Dynamical regions of the noisy FHN network with delayed feedback according to the noise intensity (D). the yellow, pink and hatching regions show the steady-state, incoherence and coherence-resonance chimera, respectively. The values of the time delays are (a) $\tau = 9.52$, (b) $\tau = 6$, (c) $\tau = 4.76$, (d) $\tau = 1.8$, (e) $\tau = 0.8$, (f) $\tau = 0$. The parameters used for the simulations are $N = 500$, $\varepsilon = 0.05$, $a = 1.001$, $\phi = \pi/2 - 0.1$, $r = 0.2$, $\sigma = 0.4$.
Source: Figure reproduced with permission from [323].

between the coherent oscillations and the chimera death state for different noise intensities are shown in the right panel of Fig. 99. Thus, the region of the chimera death state is lessened by increasing noise.

Adjusting the time-delay and strength of the feedback in the network of non-locally coupled FHN oscillators with additive noise can regulate the dynamical regime of the coherence-resonance chimeras [323]. The coherence-resonance chimera is noise-induced and occurs for certain values of the noise intensity and also the system's parameters. By applying the delayed feedback, the ranges of the noise intensity leading to coherence-resonance chimera are modified. An example of these changes is shown in Fig. 100 for some time delay values and the feedback strength of 0.2. In this diagram, the steady-state, the incoherent, and the coherence-resonance chimera regions are shown by yellow, pink, and hatching, respectively. It is observed that by increasing the time delay, the steady-state region is lessened, and the left boundary of the chimera region is shifted to the lower noise intensities. Thus, the coherence-resonance chimera can be formed even in the absence of the noise (Fig. 100a,b,c). Furthermore, the right boundary is also changed to either stronger (Fig. 100b) or weaker noises (Fig. 100a,d,e). If the time delay is set near the intrinsic period of oscillators, the right boundary does not change (Fig. 100c). Consequently, with the modification of the time-delayed feedback, one can obtain the coherence-resonance chimera for both cases of no additive noise and strong noise, which were not attained without delay.

One feature of the coherence-resonance chimera without time delay is the periodic alternation of the coherent and incoherent domains. Therefore, in each period of the oscillations, the position of the incoherent part on the ring is changed. Considering the delayed feedback, the period of this alternation is doubled, and the incoherent position alters after two cycles of spiking. This event is represented in Fig. 101. The chimera pattern, in this case, is called period-two coherence-resonance chimera.

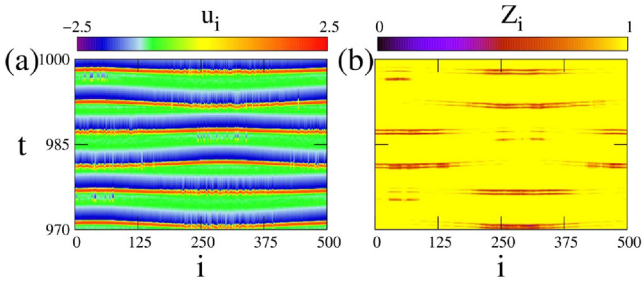

Fig. 101. The period-two coherence-resonance chimera in which the alternation of the coherent and incoherent parts occurs with every second spiking of neurons. (a) The spatiotemporal pattern of the network. (b) The local order parameter.
Source: Figure reproduced with permission from [323].

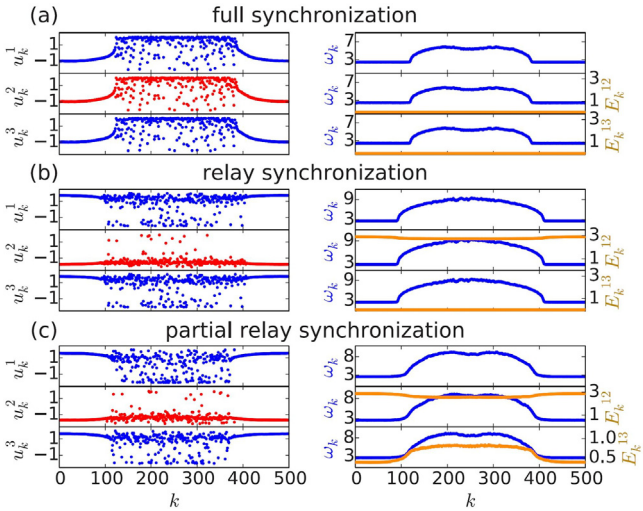

Fig. 102. The dynamics of the 3-layer network of FHN oscillators with inter-layer time delay. The left panel shows the time snapshots of the layers, and the right panel shows the mean phase velocities (blue) together with the inter-layer errors (orange). (a) All layers are synchronous for $\tau = 2.4$. (b) The first and third layers are synchronous. Thus, the pattern is relay synchronization for $\tau = 5.5$. (c) Only the coherent parts of the chimeras in the first and third layers are synchronous. Thus, the pattern is a double chimera for $\tau = 0.4$.
Source: Figure reproduced with permission from [267].

The time delay can also be used for controlling the coherent regions of chimeras in multilayer networks [267]. In a multilayer structure, remote or relay synchronization is referred to the synchronization of two layers with indirect connections. The simple structure which can support this behavior is a three-layer multiplex network wherein the first and third layers have no direct links and are only connected to the middle layer (relay layer). Considering time delay in the inter-layer couplings causes the transition of the network's behavior between different relay synchronization states. In this regard, Sawicki et al. [267] investigated a 3-layer network of FHN oscillators. They observed that for the inter-layer time delays near the period of the isolated oscillator (T) and its integer multiples, the layers have complete inter-layer synchronization. This state is illustrated in Fig. 102a, in which the snapshots of the neurons in three layers and their mean phase velocities are shown in the left and right panels, respectively. When the time delay is set at half-integer multiples of T, the relay synchronization is formed, as shown in Fig. 102b. In this case, the first and third layers are synchronized, while are anti-phase synchronized with the middle layer. For specified time delay values, the coherent parts of the chimera in the first and third layers are synchronous, while the incoherent parts are not. This state, which is demonstrated in Fig. 102c, is called partial relay inter-layer synchronization or double chimera. Therefore, proper selection of the inter-layer time delay leads to obtaining the desired synchronization pattern and also fixing the position of the coherent domain in disconnected layers.

6.7. Coupling modifications

The modification of the connections of a network acts as a controller for inducing the chimera state from a completely coherent state and also adjusting the position of the incoherent part of chimera [319]. In comparison to the closed-loop techniques, this method is open-loop and, thus, is useful when there is restricted access to the system. In a non-local

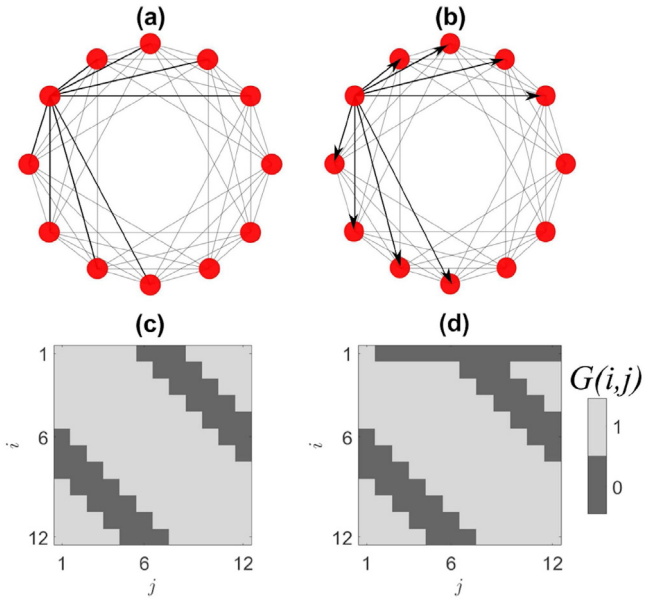

Fig. 103. (a,c) Schematic of a non-local network and its corresponding coupling matrix. (b,d) Schematic of a network with one pacemaker oscillator (the one with unidirectional links) and the corresponding coupling matrix.
Source: Figure reproduced with permission from [319].

ring, this control strategy is applicable through two mechanisms. The first one is to create a pacemaker oscillator in the network by changing the links of a node to unidirectional ones. Thus, the pacemaker oscillator affects the other nodes without getting affected by them. The second one is a symmetry-breaking mechanism of connections opposite to the pacemaker oscillator. The schematic of a network with a pacemaker oscillator is shown in Fig. 103. The non-local network and its corresponding coupling matrix are shown in Fig. 103a,c. Fig. 103b,d illustrate the network with the pacemaker oscillator (the first node), which is connected to its nearest-neighbors with unidirectional links.

To investigate the effects of the existence of the pacemaker oscillator on the network's behavior, a network of non-locally coupled phase oscillators with the following equation is considered in [319]

$$\dot{\phi}_j(t) = \omega - \frac{1}{2b}\sum_{k=1}^{N} G(j,k)\sin(\phi_j(t) - \phi_k(t) + \alpha), \tag{194}$$

where the parameters of the oscillators are set at $\omega = 0$ and $\alpha = 1.46$, and G is the coupling matrix. Fig. 104a–c show three different patterns of this network with non-local coupling, by fixing the total number of the oscillators at $N = 35$ and the number of nearest-neighbors at 12. In Fig. 104a, a chimera state is formed in which the incoherent part is drifting. This movement is known as the Brownian motion and occurs typically in small networks. Fig. 104b represents another chimera state that is not stable and converts to a completely coherent state after a certain time. Finally, in Fig. 104c, the chimera state is not formed, and the coherence appears shortly. The corresponding high coherence group (HCG) and low coherence group (LCG) of Fig. 104a–c are demonstrated in the left second panel (Fig. 104d–f).

Next, the connections of the network are changed such that the oscillator i=18 acts as a pacemaker oscillator. Therefore, this node oscillates with a constant frequency as $\dot{\phi}_i(t) = -\sin\alpha$ and the neighboring nodes are influenced by this frequency. The results of this case are shown in Fig. 104g–I, with the same initial conditions as in Fig. 104a–c. Fig. 104g shows that the incoherent part of a chimera is attracted by the pacemaker oscillator, and the drifting is stopped. Fig. 104h indicates that the existence of the pacemaker oscillator causes the stability of the chimera state, and it is not collapsed by the synchronous state anymore. Finally, Fig. 104i represents that due to the presence of pacemaker oscillator, the chimera state is formed from the initial conditions, which led to a synchronous state in the non-local connections. The patterns in Fig. 104j–l show the network's behavior with the conditions when the pacemaker oscillator is triggered on after 150 time-units. To apply fewer changes in the network connections, the pacemaker can also be implemented by fewer intensities. The pacemaker intensity is defined as the ratio of the cut links to the primary bidirectional links in the non-local configuration. The pacemaker oscillators with low intensity also lead to the formation of chimera state. Moreover, the results of the pacemaker oscillators with the intensity equal to 0.5 has very close results to the full pacemaker oscillator.

For the second mechanism, one of the oscillators is selected, and all of its outgoing links are removed. The results have shown that this mechanism acts the same as the pacemaker oscillator. Thus the symmetry breaking of the coupling can be considered as another controller for the chimera state.

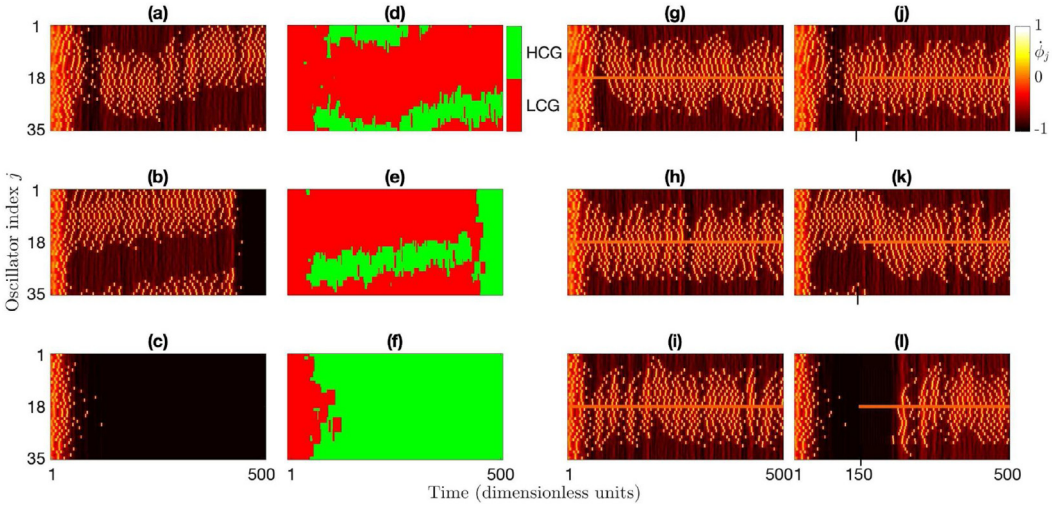

Fig. 104. Control of the drift and collapse of chimera state via the pacemaker oscillator. (a–c) Three patterns of the network Eq. (194) with non-local connections: (a) the incoherent part is drifting, (b) the chimera collapses to the synchronous state, (c) no chimera is formed. (d–f) The corresponding high coherence group (HCG) and low coherence group (LCG) of parts a–c. (g–i) The network's behaviors with the same parameters and initial conditions as parts a–c, when a pacemaker oscillator is implemented in the position $i = 18$. (j–l) The pacemaker oscillator is implemented after 150 time-units.
Source: Figure reproduced with permission from [319].

6.8. Control of virtual chimeras

The studies have shown a similarity between the behavior of the networks of coupled systems and the time-delayed systems. Larger et al. [297] showed that the Ikeda time-delayed model exhibits chimera state if its temporal dynamics is mapped into a virtual space–time description. The temporal dynamics of this model is composed of an alternation of the regular and chaotic intervals, which is shown in Fig. 105a,b (parts a and b show the numerical and experimental results, respectively). The system can be virtually converted to the space–time scheme by considering $t = \tau_c(n + \sigma)$, where n is integer and $\sigma < 1$ is a real positive number. τ_c is introduced as $\tau_D(1 + \gamma)$, where τ_D is the time delay of the model, and γ is a small value that is obtained such that the virtual space–time patterns are stationary in space σ. The obtained space–time plots that are shown in Fig. 105c,d, demonstrate a chimera-like behavior.

The virtual chimera state can be controlled with an external periodic forcing [324]. A time-delay system similar to the Ikeda model with negative time-delayed feedback is as follows

$$\begin{cases} \varepsilon\dot{x} = -y - gx - f(x(t-\tau)), \\ \dot{y} = x - S(y), \\ f(x(t-\tau)) = \frac{x(t-\tau)}{ax^2(t-\tau)+b}, \\ S(y) = \begin{cases} -m_1 y, & y < 0 \\ -m_2 y, & y \geq 0, \end{cases} \end{cases} \tag{195}$$

where τ is the time delay, and ε, g, a, b, m_1, m_2 are constant positive parameters. This system is able to exhibit the same temporal dynamics as the Ikeda model shown in Fig. 105a. Therefore, the chimera state is obtained by implementing the virtual space–time plots.

Next, an external force with amplitude A and frequency f_{ext} is applied to the time-delayed system. The influence of the external force parameters on the space–time pattern is shown in Fig. 106a. For the small amplitudes, the chimera state is destroyed (shown by point 1 in the figure), except for $f_{ext} = 1/\eta_0$ which leads to appearance of the chimera. Near the frequency $f_{ext} = 1/\eta_0$, the chimera state is observed for large amplitudes (shown by point 2 in the figure). But in this case, the period of the variations of the regular and chaotic intervals in the temporal dynamics is changed from $\eta = \eta_0$ to $\eta = 1/f_{ext}$. The chimera domains in the parameter plane are similar to the Arnold tongues, where within the tongues, the chimeras emerge and outside the tongues are suppressed as a result of the elimination of regular dynamics in the system's time series. In the subsequent tongues, the chimeras with multiple clusters are formed (shown by point 3 in the figure). For the frequency of the force equal to $f_{ext} = k/\eta_0$, the number of the clusters is $k = \eta f_{ext}$. Fig. 106b,c show the multi-chimera states for $k = 4$ and $k = 5$. In the outside of the tongues, the chimera can be induced by adding a white Gaussian noise with specific noise intensity to the force amplitude.

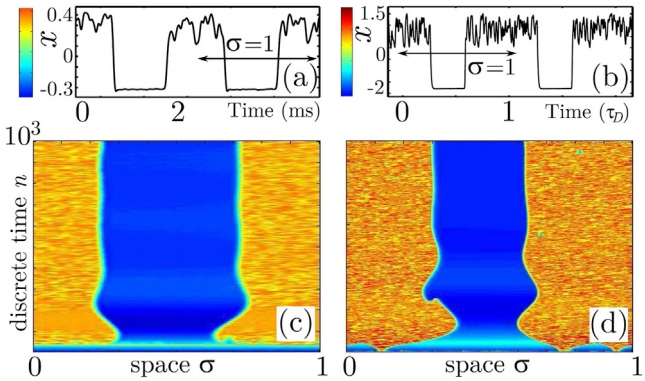

Fig. 105. The behavior of the Ikeda time-delayed model. (a) The numerically obtained time series. (b) The experimentally obtained time series. (c,d) The virtual chimera state obtained by constructing the space–time plots from numerical (c) and experimental (d) time series.
Source: Figure reproduced with permission from [297].

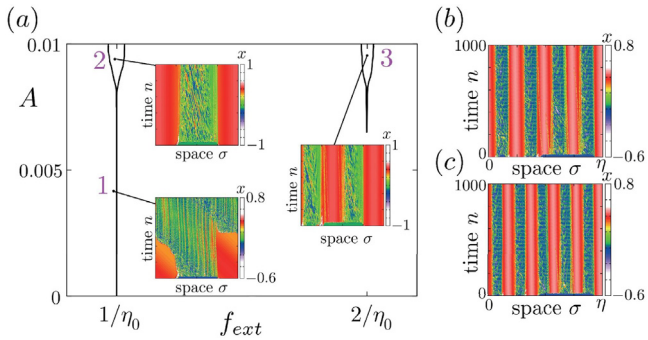

Fig. 106. (a) The regions of the virtual chimera in the plane of external force amplitude and frequency. The space–time plots in different domains are shown in the insets. (b) The four-cluster chimera state for $A = 0.008$ and $f_{ext} = 4/\eta_0$. (c) The five-cluster chimera state for $A = 0.008$ and $f_{ext} = 5/\eta_0$. The other parameters are $\varepsilon = 0.005$, $g = 0.1$, $a = 200$, $b = 0.2$, $m_1 = 7$, $m_2 = 1$, $\tau = 200$, $\eta_0 = 200.202$.
Source: Figure reproduced with permission from [324].

7. Summary

We have presented a systematic review of the chimera state in dynamical networks to understand this peculiar collective behavior in complex systems. In general, it can be said that oscillators' collective behaviors have always been of interest to researchers. However, as a special case in which one or some clusters of oscillators oscillate synchronously and the others asynchronously, the chimera state has received particular attention in recent years. In the Introduction, we have described the definition of coupled oscillators network, the chimera state, the history of its foundation, and why it was discovered so late. We have also outlined different types of synchrony in coherent clusters, which are useful for categorizing different types of chimera.

In Section 2, we have first studied the chimera phenomenon in phase oscillators. The reason is that the first observation of the chimera state was in coupled phase oscillators, which have various applications in different fields. Since the oscillators of a network in the real world are never entirely homogeneous, and there are some differences between them, to provide a more realistic model, various heterogeneities, for example, in phase lags or frequencies of the oscillators, have been considered in some simulations. The effects of changing coupling strength and scheme on the network behavior have also been studied. Then, we brought a review of mechanical, chemical, and optical dynamical systems that the chimera state has been observed in them. The first observation of the chimera in experiments refers to a mechanical network of coupled metronomes. Many interesting phenomena, such as the chimera state, have been observed in this network by varying the spring strengths. In continuation, we have discussed the existence of the chimera state in discrete-time systems (Map lattices). At the end of Section 2, we have emphasized the neuronal networks and the importance of the chimera in healthy and unhealthy modes.

In Section 3, we have introduced the chimera states' mathematics and investigated the theoretical and mathematical methods used for stability analysis of phase oscillators and characterizing chimeras in dynamical systems. The continuum limit and Ott–Antonsen approach are used as the reduction methods for invariant manifolds when the system's steady-state dynamics are more critical than the transient dynamics. These methods have been used for analyzing the stability

of the chimera states. The stability analysis has also been done considering different factors, such as the heterogeneity, which were discussed briefly. In the last part of this section, we investigated the indexes and indicators for chimera measurements in time and phase space.

We evaluated and described different types of chimera by looking at various oscillatory systems in Section 4. One of the essential factors for classifying chimera is the stationarity in time. Commonly, the chimera states have static coherent, and incoherent clusters in time. But in some cases, the position of these two domains may vary in time, which is called as the "breathing chimera" in general. In special cases, if the coherent and incoherent groups change their spatial position alternatively in time, it is named as "alternating chimera" state. While if the chimera's coherent group moves in time with a constant speed, it will be referred to as "traveling chimera". Moreover, the chimera studies' extension to various dynamical systems led to the foundation of other chimera types, such as the "amplitude mediated chimera" and "amplitude chimera". In these chimera states, the amplitude has more significance than the phase. Other chimera types are "chimera death", "imperfect chimera", and "spiral wave chimera" that were described by details at the end of Section 4.

In the continuation, we have then described a critical factor on the collective behavior of oscillators in Section 5. Network topology and coupling scheme are influential features in network behavior that their impact cannot be ignored in any way. We first reviewed different structures that the chimera state has been observed in them, including two and three dimensions, multilayered and complex network structures. Then we focused on the effect of various coupling schemes on the chimera state, which include global coupling, local coupling, time-varying coupling, and hierarchical connection. Lastly, in Section 6, we discussed the existing techniques for controlling chimeras. These controlling methods have been presented with different purposes, including controlling the existence and lifetime of chimera, determining the position of clusters, and preventing the drifting.

8. Future research and outlook

The discovery and study of dynamical systems have brought about dramatic changes in the modeling and predicting nature's behavior in recent years. These new insights had significant effects on various majors, including physics, chemistry, medicine, mechanics, optics, biology, etc. However, the investigation of a single element can never give comprehensive information about the entire system's behavior. Therefore, the study of collective behaviors seems necessary. The chimera state is one of the particular interesting collective behaviors observed in many natural systems, and there are still many unknowns about this phenomenon. It seems that further understanding of this phenomenon requires more experiments in natural systems to obtain more information about the transient time of the system before the chimera phenomenon and also the behavior of synchronous and asynchronous groups during the occurrence of the chimera state. For example, the available laboratory data on chimera related brain diseases are insufficient. Thus, it cannot be used to extract a comprehensive model for neurons' behavior during the disease. For this issue, the chimera state in neuronal networks should be depicted in the microscopic view to be able to make a fantastic process on the exploration of chimera related diseases.

It can be said that there is not yet a unit mathematical definition that can cover all types of chimeras and determine the possibility of occurrence of this behavior in a network before performing numerical calculations. While this review can be considered a modest step in the clearance of this particular state's mathematics, it likely still looks like there are many questions in this area with no answer for them. Although the chimera's stability has been discussed in some studies, the proposed analytical methods are exclusive to phase oscillators and in the continuum limit. Therefore, no analytical method has been presented to study the chimera in other dynamical systems, so far. Besides, some techniques similar to those used to evaluate the synchronization's stability, such as the master stability function (MSF), which determines the requisites for the stable synchronous manifold, are not provided for the chimera state. In general, there are not many theoretical studies on the emergence and stability of the chimera state. Thus, it is expected to have extensive research in this field and find sufficient and necessary conditions for the chimera's appearance.

One of the other non-complete subjects in chimera studies is the network structure. Over time, the scientists have turned their attention to more complex and realistic systems. This issue has also been in consideration of chimera researchers during recent years. However, there is still a long way from real networks that have adaptation, coevolution, and self-organization. Considering any of these features in the investigations is a step in bringing the scientific studies closer to reality.

In terms of controlling the chimera state, all of the proposed control methods have been investigated only in networks with non-local interactions, and it is necessary to study other structures as well. More precisely, all the practical factors on the system's behavior, including network topology and scheme, initial conditions, bifurcation parameters, etc., need to be considered to develop controlling methods for the chimera state. Furthermore, there is no actual evidence for the applicability of the current theoretical methods. The presented techniques have only been investigated in theoretical and mathematical models. Thus, verifying these methods' performance in natural and biological systems is a fundamental problem that should be noticed in future research. Proper operation of control methods can have significant effects in the neuroscience field in the direction of treating or controlling patients with epilepsy, Parkinson's, schizophrenia, etc.

Declaration of competing interest

The authors declare that they have no known competing financial interests or personal relationships that could have appeared to influence the work reported in this paper.

Acknowledgments

We gratefully acknowledge Mohadeseh Shafiei Kafraj for her much appreciated help. Zhen Wang was supported by the National Natural Science Foundation of China (Grant Nos. 81961138010, U1803263, and 11931015), by the Fundamental Research Funds for the Central Universities, China (Grant No. 3102019PJ006), by the Key Area Research and Development Program of Guangdong Province, China (Grant No. 2019B010137004), and by the Key Area Research and Development Program of Shaanxi Province, China (Grant No. 2019ZDLGY17-07). Matjaž Perc was supported by the Slovenian Research Agency (Grant Nos. P1-0403, J1-2457, J4-9302, and J1-9112).

References

[1] S. Boccaletti, V. Latora, Y. Moreno, M. Chavez, D.-U. Hwang, Complex networks: Structure and dynamics, Phys. Rep. 424 (2006) 175–308.
[2] S. Boccaletti, G. Bianconi, R. Criado, C.I. Del Genio, J. Gómez-Gardenes, M. Romance, I. Sendina-Nadal, Z. Wang, M. Zanin, The structure and dynamics of multilayer networks, Phys. Rep. 544 (2014) 1–122.
[3] S.H. Strogatz, Exploring complex networks, Nature 410 (2001) 268–276.
[4] R. Albert, A.-L. Barabási, Statistical mechanics of complex networks, Rev. Modern Phys. 74 (2002) 47.
[5] M. Kivelä, A. Arenas, M. Barthelemy, J.P. Gleeson, Y. Moreno, M.A. Porter, Multilayer networks, J. Complex Netw. 2 (2014) 203–271.
[6] E. Estrada, The Structure of Complex Networks: Theory and Applications, Oxford University Press, Oxford, U.K., 2012.
[7] H.A. Simon, The organization of complex systems, in: Models of Discovery, Springer, 1977, pp. 245–261.
[8] S. Boccaletti, J. Kurths, G. Osipov, D. Valladares, C. Zhou, The synchronization of chaotic systems, Phys. Rep. 366 (2002) 1–101.
[9] A. Pikovsky, J. Kurths, M. Rosenblum, J. Kurths, Synchronization: A Universal Concept in Nonlinear Sciences, Cambridge University Press, Cambridge, U.K., 2003.
[10] M. Chavez, D.-U. Hwang, S. Boccaletti, Synchronization processes in complex networks, Eur. Phys. J. Spec. Top. 146 (2007) 129–144.
[11] S. Boccaletti, A.N. Pisarchik, C.I. Del Genio, A. Amann, Synchronization: From Coupled Systems To Complex Networks, Cambridge University Press, Cambridge, U.K., 2018.
[12] G.M. Mahmoud, E.E. Mahmoud, Complete synchronization of chaotic complex nonlinear systems with uncertain parameters, Nonlinear Dynam. 62 (2010) 875–882.
[13] C. Yao, Q. Zhao, J. Yu, Complete synchronization induced by disorder in coupled chaotic lattices, Phys. Lett. A 377 (2013) 370–377.
[14] X. He, C. Li, J. Huang, L. Xiao, Generalized synchronization of arbitrary-dimensional chaotic systems, Optik 126 (2015) 454–459.
[15] A. Ouannas, L. Jouini, O. Zehrour, On new generalized hybrid synchronization in chaotic and hyperchaotic discrete-time dynamical systems, J. Appl. Nonlinear Dyn. 8 (2019) 435–445.
[16] D.J. DeShazer, R. Breban, E. Ott, R. Roy, Detecting phase synchronization in a chaotic laser array, Phys. Rev. Lett. 87 (2001) 044101.
[17] X. Li, Generalized projective synchronization using nonlinear control method, Int. J. Nonlinear Sci. 8 (2009) 79–85.
[18] X.-F. Li, A.C.-S. Leung, X.-P. Han, X.-J. Liu, Y.-D. Chu, Complete (anti-) synchronization of chaotic systems with fully uncertain parameters by adaptive control, Nonlinear Dynam. 63 (2011) 263–275.
[19] G.V. Osipov, A.S. Pikovsky, M.G. Rosenblum, J. Kurths, Phase synchronization effects in a lattice of nonidentical Rössler oscillators, Phys. Rev. E 55 (1997) 2353.
[20] F. Parastesh, H. Azarnoush, S. Jafari, B. Hatef, M. Perc, R. Repnik, Synchronizability of two neurons with switching in the coupling, Appl. Math. Comput. 350 (2019) 217–223.
[21] L.M. Pecora, T.L. Carroll, Synchronization of chaotic systems, Chaos 25 (2015) 097611.
[22] I.V. Belykh, V.N. Belykh, M. Hasler, Blinking model and synchronization in small-world networks with a time-varying coupling, Physica D 195 (2004) 188–206.
[23] S.K. Bhowmick, C. Hens, D. Ghosh, S.K. Dana, Mixed synchronization in chaotic oscillators using scalar coupling, Phys. Lett. A 376 (2012) 2490–2495.
[24] E. Bolhasani, Y. Azizi, A. Valizadeh, M. Perc, Synchronization of oscillators through time-shifted common inputs, Phys. Rev. E 95 (2017) 032207.
[25] S.N. Chowdhury, S. Majhi, M. Ozer, D. Ghosh, M. Perc, Synchronization to extreme events in moving agents, New J. Phys. 21 (2019) 073048.
[26] L. Pecora, T. Carroll, G. Johnson, D. Mar, K.S. Fink, Synchronization stability in coupled oscillator arrays: Solution for arbitrary configurations, Internat. J. Bifur. Chaos 10 (2000) 273–290.
[27] Z. Shahriari, M. Small, Permutation entropy of state transition networks to detect synchronization, Internat. J. Bifur. Chaos 30 (2020) 2050154.
[28] Y. Kuramoto, D. Battogtokh, Coexistence of coherence and incoherence in nonlocally coupled phase oscillators, Nonlinear Phenom. Complex Syst. 5 (2002) 380–385.
[29] D.M. Abrams, S.H. Strogatz, Chimera states for coupled oscillators, Phys. Rev. Lett. 93 (2004) 174102.
[30] M.R. Tinsley, S. Nkomo, K. Showalter, Chimera and phase-cluster states in populations of coupled chemical oscillators, Nat. Phys. 8 (2012) 662–665.
[31] S. Nkomo, M.R. Tinsley, K. Showalter, Chimera states in populations of nonlocally coupled chemical oscillators, Phys. Rev. Lett. 110 (2013) 244102.
[32] K. Schönleber, C. Zensen, A. Heinrich, K. Krischer, Pattern formation during the oscillatory photoelectrodissolution of n-type silicon: turbulence, clusters and chimeras, New J. Phys. 16 (2014) 063024.
[33] S. Nkomo, M.R. Tinsley, K. Showalter, Chimera and chimera-like states in populations of nonlocally coupled homogeneous and heterogeneous chemical oscillators, Chaos 26 (2016) 094826.
[34] E.A. Martens, S. Thutupalli, A. Fourrière, O. Hallatschek, Chimera states in mechanical oscillator networks, Proc. Natl. Acad. Sci. 110 (2013) 10563–10567.
[35] T. Bountis, V.G. Kanas, J. Hizanidis, A. Bezerianos, Chimera states in a two–population network of coupled pendulum–like elements, TEur. Phys. J. Spec. Top. 223 (2014) 721–728.
[36] H. Yin, Chimera states in three populations of pendulum-like elements with inertia, Am. J. Phys. Appl. 7 (2019) 27.
[37] E. Viktorov, T. Habruseva, S. Hegarty, G. Huyet, B. Kelleher, A continuous chimera state in an optical comb, in: The European Conference on Lasers and Electro-Optics, Optical Society of America, 2013, p. CB_3_4.

[38] F. Böhm, A. Zakharova, E. Schöll, K. Lüdge, Amplitude-phase coupling drives chimera states in globally coupled laser networks, Phys. Rev. E 91 (2015) 040901.
[39] J. Shena, J. Hizanidis, V. Kovanis, G.P. Tsironis, Turbulent chimeras in large semiconductor laser arrays, Sci. Rep. 7 (2017) 42116.
[40] L.V. Gambuzza, A. Buscarino, S. Chessari, L. Fortuna, R. Meucci, M. Frasca, Experimental investigation of chimera states with quiescent and synchronous domains in coupled electronic oscillators, Phys. Rev. E 90 (2014) 032905.
[41] T. Banerjee, P.S. Dutta, A. Zakharova, E. Schöll, Chimera patterns induced by distance-dependent power-law coupling in ecological networks, Phys. Rev. E 94 (2016) 032206.
[42] L. Bauer, J. Bassett, P. Hövel, Y.N. Kyrychko, K.B. Blyuss, Chimera states in multi-strain epidemic models with temporary immunity, Chaos 27 (2017) 114317.
[43] Z. Shahriari, F. Parastesh, M. Jalili, V. Berec, J. Ma, S. Jafari, The role of coupling factors on the emergence of synchronization and chimera patterns in network of non-locally coupled pancreatic β-cells, Europhys. Lett. 125 (2019) 60001.
[44] J. Khouhak, Z. Faghani, J.L. Laugesen, S. Jafari, The emergence of chimera states in a network of nephrons, Chin. J. Phys. 63 (2020) 402–409.
[45] S. Majhi, B.K. Bera, D. Ghosh, M. Perc, Chimera states in neuronal networks: A review, Phys. Life Rev. 28 (2019) 100–121.
[46] B.K. Bera, D. Ghosh, M. Lakshmanan, Chimera states in bursting neurons, Phys. Rev. E 93 (2016) 012205.
[47] I.A. Shepelev, T.E. Vadivasova, A. Bukh, G. Strelkova, V. Anishchenko, New type of chimera structures in a ring of bistable Fitzhugh–Nagumo oscillators with nonlocal interaction, Phys. Lett. A 381 (2017) 1398–1404.
[48] L. Khaleghi, S. Panahi, S.N. Chowdhury, S. Bogomolov, D. Ghosh, S. Jafari, Chimera states in a ring of map-based neurons, Physica A 536 (2019) 122596.
[49] S. Majhi, M. Perc, D. Ghosh, Chimera states in uncoupled neurons induced by a multilayer structure, Sci. Rep. 6 (2016) 39033.
[50] M. Shafiei, S. Jafari, F. Parastesh, M. Ozer, T. Kapitaniak, M. Perc, Time delayed chemical synapses and synchronization in multilayer neuronal networks with ephaptic inter-layer coupling, Commun. Nonlinear Sci. Numer. Simul. 84 (2020) 105175.
[51] A.V. Andreev, M.V. Ivanchenko, A.N. Pisarchik, A.E. Hramov, Stimulus classification using chimera-like states in a spiking neural network, Chaos Solitons Fractals 139 (2020) 110061.
[52] P. Vázquez-Guerrero, J. Gómez-Aguilar, F. Santamaria, R. Escobar-Jiménez, Synchronization patterns with strong memory adaptive control in networks of coupled neurons with chimera states dynamics, Chaos Solitons Fractals 128 (2019) 167–175.
[53] F. Yue-E, L. Hai-Hong, The dependence of chimera states on initial conditions, Chin. Phys. Lett. 32 (2015) 060502.
[54] E.A. Martens, M.J. Panaggio, D.M. Abrams, Basins of attraction for chimera states, New J. Phys. 18 (2016) 022002.
[55] S. Rakshit, B.K. Bera, M. Perc, D. Ghosh, Basin stability for chimera states, Sci. Rep. 7 (2017) 1–12.
[56] P. Kalle, J. Sawicki, A. Zakharova, E. Schöll, Chimera states and the interplay between initial conditions and non-local coupling, Chaos 27 (2017) 033110.
[57] Z. Faghani, Z. Arab, F. Parastesh, S. Jafari, M. Perc, M. Slavinec, Effects of different initial conditions on the emergence of chimera states, Chaos Solitons Fractals 114 (2018) 306–311.
[58] V. Dos Santos, F.S. Borges, K.C. Iarosz, I.L. Caldas, J. Szezech, R.L. Viana, M.S. Baptista, A.M. Batista, Basin of attraction for chimera states in a network of Rössler oscillators, Chaos 30 (2020) 083115.
[59] O.E. Omel'chenko, M. Wolfrum, S. Yanchuk, Y.L. Maistrenko, O. Sudakov, Stationary patterns of coherence and incoherence in two-dimensional arrays of non-locally-coupled phase oscillators, Phys. Rev. E 85 (2012) 036210.
[60] Y. Liu, A.J.M. Khalaf, S. Jafari, I. Hussain, Chimera state in a two-dimensional network of coupled genetic oscillators, Europhys. Lett. 127 (2019) 40001.
[61] S. Kundu, B.K. Bera, D. Ghosh, M. Lakshmanan, Chimera patterns in three-dimensional locally coupled systems, Phys. Rev. E 99 (2019) 022204.
[62] V. Maistrenko, O. Sudakov, O. Osiv, Chimeras and solitary states in 3d oscillator networks with inertia, Chaos 30 (2020) 063113.
[63] S. Ghosh, S. Jalan, Emergence of chimera in multiplex network, Internat. J. Bifur. Chaos 26 (2016) 1650120.
[64] M. Goremyko, V. Maksimenko, V. Makarov, D. Ghosh, B. Bera, S. Dana, A. Hramov, Interaction of chimera states in a multilayered network of nonlocally coupled oscillators, Tech. Phys. Lett. 43 (2017) 712–715.
[65] M.V. Goremyko, V.A. Maksimenko, V.V. Makarov, D. Ghosh, B.K. Bera, S.K. Dana, A.E. Hramov, Numerical analysis of the chimera states in the multilayered network model, in: Dynamics and Fluctuations in Biomedical Photonics XIV, Vol. 10063, International Society for Optics and Photonics, 2017, p. 100631J.
[66] S. Jalan, S. Ghosh, B. Patra, Is repulsion good for the health of chimeras? Chaos 27 (2017) 101104.
[67] F. Parastesh, C.-Y. Chen, H. Azarnoush, S. Jafari, B. Hatef, Synchronization patterns in a blinking multilayer neuronal network, Eur. Phys. J. Spec. Top. 228 (2019) 2465–2474.
[68] X. Li, T. Xu, J. Li, Synchronization and chimera states in a multilayer neuronal network with unidirectional interlayer links, Eur. Phys. J. Spec. Top. 228 (2019) 2419–2427.
[69] L. Kang, C. Tian, S. Huo, Z. Liu, A two-layered brain network model and its chimera state, Sci. Rep. 9 (2019) 1–12.
[70] N. Lotfi, A.H. Darooneh, et al., Existence of chimera-like state in community structured networks, Internat. J. Modern Phys. C 31 (2020) 1–11.
[71] A.V. Andreev, N.A. Malova, E.I. Borovkova, N.S. Frolov, Interaction of bistable neurons leading to the complex network dynamics, in: Saratov Fall Meeting 2019: Computations and Data Analysis: From Nanoscale Tools To Brain Functions, Vol. 11459, International Society for Optics and Photonics, 2020, p. 114590V.
[72] C. Tian, H. Bi, X. Zhang, S. Guan, Z. Liu, Asymmetric couplings enhance the transition from chimera state to synchronization, Phys. Rev. E 96 (2017) 052209.
[73] H. Cheng, Q. Dai, N. Wu, Y. Feng, H. Li, J. Yang, Chimera states in nonlocally coupled phase oscillators with biharmonic interaction, Commun. Nonlinear Sci. Numer. Simul. 56 (2018) 1–8.
[74] G.B. Soh, P. Louodop, R. Kengne, R. Tchitnga, Chimera dynamics in an array of coupled Fitzhugh-Nagumo system with shift of close neighbors, Heliyon 6 (2020) e03739.
[75] T. Njougouo, G.R. Simo, P. Louodop, H. Fotsin, P.K. Talla, Effects of intermittent coupling on synchronization, Chaos Solitons Fractals 139 (2020) 110082.
[76] E.A. Martens, Chimeras in a network of three oscillator populations with varying network topology, Chaos 20 (2010) 043122.
[77] W.-H. Wang, Q.-L. Dai, H.-Y. Cheng, H.-H. Li, J.-Z. Yang, Chimera dynamics in nonlocally coupled moving phase oscillators, Front. Phys. 14 (2019) 43605.
[78] D. Dudkowski, K. Czołczyński, T. Kapitaniak, Traveling chimera states for coupled pendula, Nonlinear Dynam. 95 (2019) 1859–1866.
[79] F. Parastesh, S. Jafari, H. Azarnoush, Traveling patterns in a network of memristor-based oscillators with extreme multistability, Eur. Phys. J. Spec. Top. 228 (2019) 2123–2131.
[80] F. Parastesh, S. Jafari, H. Azarnoush, B. Hatef, A. Bountis, Imperfect chimeras in a ring of four-dimensional simplified Lorenz systems, Chaos Solitons Fractals 110 (2018) 203–208.
[81] K. Sathiyadevi, V. Chandrasekar, D. Senthilkumar, M. Lakshmanan, Imperfect amplitude mediated chimera states in a nonlocally coupled network, Front. Appl. Math. Stat. 4 (2018) 58.
[82] U.K. Verma, G. Ambika, Amplitude chimera and chimera death induced by external agents in two-layer networks, Chaos 30 (2020) 043104.

[83] Y. Suda, K. Okuda, Emergence of second coherent regions for breathing chimera states, Phys. Rev. E 101 (2020) 062203.
[84] Z. Wei, F. Parastesh, H. Azarnoush, S. Jafari, D. Ghosh, M. Perc, M. Slavinec, Nonstationary chimeras in a neuronal network, Europhys. Lett. 123 (2018) 48003.
[85] A.V. Slepnev, A.V. Bukh, T.E. Vadivasova, Stationary and non-stationary chimeras in an ensemble of chaotic self-sustained oscillators with inertial nonlinearity, Nonlinear Dynam. 88 (2017) 2983–2992.
[86] N. Semenova, A. Zakharova, V. Anishchenko, E. Schöll, Coherence-resonance chimeras in a network of excitable elements, Phys. Rev. Lett. 117 (2016) 014102.
[87] A. Alvarez-Socorro, M. Clerc, M. Ferré, Wandering walk of chimera states in a continuous medium, Chaos Solitons Fractals 140 (2020) 110169.
[88] A. Bukh, V. Anishchenko, Spiral and target wave chimeras in a 2d network of nonlocally coupled van der pol oscillators, Chaos Solitons Fractals 131 (2020) 109492.
[89] E. Omel'chenko, M. Wolfrum, Y.L. Maistrenko, Chimera states as chaotic spatiotemporal patterns, Phys. Rev. E 81 (2010) 065201.
[90] M. Wolfrum, O.E. Omel'chenko, S. Yanchuk, Y.L. Maistrenko, Spectral properties of chimera states, Chaos 21 (2011) 013112.
[91] M. Wolfrum, E. Omel'chenko, Chimera states are chaotic transients, Phys. Rev. E 84 (2011) 015201.
[92] Y. Zhu, Y. Li, M. Zhang, J. Yang, The oscillating two-cluster chimera state in non-locally coupled phase oscillators, Europhys. Lett. 97 (2012) 10009.
[93] C.R. Laing, K. Rajendran, I.G. Kevrekidis, Chimeras in random non-complete networks of phase oscillators, Chaos 22 (2012) 013132.
[94] M.J. Panaggio, D.M. Abrams, Chimera states on a flat torus, Phys. Rev. Lett. 110 (2013) 094102.
[95] Z. Yun, Z. Zhi-Gang, Y. Jun-Zhong, Four-cluster chimera state in non-locally coupled phase oscillator systems with an external potential, Chin. Phys. B 22 (2013) 100505.
[96] S.R. Ujjwal, R. Ramaswamy, Chimeras with multiple coherent regions, Phys. Rev. E 88 (2013) 032902.
[97] M.J. Panaggio, D.M. Abrams, Chimera states on the surface of a sphere, Phys. Rev. E 91 (2015) 022909.
[98] N. Yao, Z.-G. Huang, C. Grebogi, Y.-C. Lai, Emergence of multicluster chimera states, Sci. Rep. 5 (2015) 1–12.
[99] X. Jiang, D.M. Abrams, Symmetry-broken states on networks of coupled oscillators, Phys. Rev. E 93 (2016) 052202.
[100] L. Smirnov, G. Osipov, A. Pikovsky, Chimera patterns in the Kuramoto–Battogtokh model, J. Phys. A 50 (2017) 08LT01.
[101] Y. Suda, K. Okuda, Breathing multichimera states in nonlocally coupled phase oscillators, Phys. Rev. E 97 (2018) 042212.
[102] P. Ashwin, O. Burylko, Weak chimeras in minimal networks of coupled phase oscillators, Chaos 25 (2015) 013106.
[103] Y. Suda, K. Okuda, Persistent chimera states in nonlocally coupled phase oscillators, Phys. Rev. E 92 (2015) 060901.
[104] M. Wolfrum, O.E. Omel'chenko, J. Sieber, Regular and irregular patterns of self-localized excitation in arrays of coupled phase oscillators, Chaos 25 (2015) 053113.
[105] Y.L. Maistrenko, A. Vasylenko, O. Sudakov, R. Levchenko, V.L. Maistrenko, Cascades of multiheaded chimera states for coupled phase oscillators, Internat. J. Bifur. Chaos 24 (2014) 1440014.
[106] E.A. Martens, C. Bick, M.J. Panaggio, Chimera states in two populations with heterogeneous phase-lag, Chaos 26 (2016) 094819.
[107] C.-U. Choe, R.-S. Kim, J.-S. Ri, Chimera and modulated drift states in a ring of nonlocally coupled oscillators with heterogeneous phase lags, Phys. Rev. E 96 (2017) 032224.
[108] C.R. Laing, The dynamics of chimera states in heterogeneous Kuramoto networks, Physica D 238 (2009) 1569–1588.
[109] C.R. Laing, Chimera states in heterogeneous networks, Chaos 19 (2009) 013113.
[110] N. Frolov, V. Maksimenko, S. Majhi, S. Rakshit, D. Ghosh, A. Hramov, Chimera-like behavior in a heterogeneous Kuramoto model: The interplay between attractive and repulsive coupling, Chaos 30 (2020) 081102.
[111] J. Xie, H.-C. Kao, E. Knobloch, Chimera states in systems of nonlocal nonidentical phase-coupled oscillators, Phys. Rev. E 91 (2015) 032918.
[112] E. Omel'chenko, Y.L. Maistrenko, P.A. Tass, Chimera states induced by spatially modulated delayed feedback, Phys. Rev. E 82 (2010) 066201.
[113] L. Schmidt, K. Krischer, Chimeras in globally coupled oscillatory systems: From ensembles of oscillators to spatially continuous media, Chaos 25 (2015) 064401.
[114] S.A. Loos, J.C. Claussen, E. Schöll, A. Zakharova, Chimera patterns under the impact of noise, Phys. Rev. E 93 (2016) 012209.
[115] K. Premalatha, V. Chandrasekar, M. Senthilvelan, M. Lakshmanan, Chimeralike states in two distinct groups of identical populations of coupled Stuart-Landau oscillators, Phys. Rev. E 95 (2017) 022208.
[116] F.P. Kemeth, S.W. Haugland, K. Krischer, Symmetries of chimera states, Phys. Rev. Lett. 120 (2018) 214101.
[117] K. Sathiyadevi, V. Chandrasekar, D. Senthilkumar, Stable amplitude chimera in a network of coupled Stuart-Landau oscillators, Phys. Rev. E 98 (2018) 032301.
[118] K. Premalatha, V. Chandrasekar, M. Senthilvelan, M. Lakshmanan, Stable amplitude chimera states in a network of locally coupled Stuart-Landau oscillators, Chaos 28 (2018) 033110.
[119] L. Gambuzza, L. Minati, M. Frasca, Experimental observations of chimera states in locally and non-locally coupled Stuart-Landau oscillator circuits, Chaos Solitons Fractals 138 (2020) 109907.
[120] K. Premalatha, V. Chandrasekar, M. Senthilvelan, M. Lakshmanan, Impact of symmetry breaking in networks of globally coupled oscillators, Phys. Rev. E 91 (2015) 052915.
[121] K. Premalatha, V. Chandrasekar, M. Senthilvelan, M. Lakshmanan, Imperfectly synchronized states and chimera states in two interacting populations of nonlocally coupled Stuart-Landau oscillators, Phys. Rev. E 94 (2016) 012311.
[122] K. Blaha, R.J. Burrus, J.L. Orozco-Mora, E. Ruiz-Beltrán, A.B. Siddique, V. Hatamipour, F. Sorrentino, Symmetry effects on naturally arising chimera states in mechanical oscillator networks, Chaos 26 (2016) 116307.
[123] T. Kapitaniak, P. Kuzma, J. Wojewoda, K. Czolczynski, Y. Maistrenko, Imperfect chimera states for coupled pendula, Sci. Rep. 4 (2014) 6379.
[124] J. Wojewoda, K. Czolczynski, Y. Maistrenko, T. Kapitaniak, The smallest chimera state for coupled pendula, Sci. Rep. 6 (2016) 1–5.
[125] D. Dudkowski, Y. Maistrenko, T. Kapitaniak, Occurrence and stability of chimera states in coupled externally excited oscillators, Chaos 26 (2016) 116306.
[126] P.R. Carvalho, M.A. Savi, Synchronization and chimera state in a mechanical system, Nonlinear Dynam. (2020) 1–19.
[127] M. Wickramasinghe, I.Z. Kiss, Spatially organized dynamical states in chemical oscillator networks: Synchronization, dynamical differentiation, and chimera patterns, PLoS One 8 (2013) e80586.
[128] D.M. Abrams, S.H. Strogatz, Chimera states in a ring of nonlocally coupled oscillators, Internat. J. Bifur. Chaos 16 (2006) 21–37.
[129] N.M. Awal, D. Bullara, I.R. Epstein, The smallest chimera: Periodicity and chaos in a pair of coupled chemical oscillators, Chaos 29 (2019) 013131.
[130] A.M. Hagerstrom, T.E. Murphy, R. Roy, P. Hövel, I. Omelchenko, E. Schöll, Experimental observation of chimeras in coupled-map lattices, Nat. Phys. 8 (2012) 658–661.
[131] E.A. Viktorov, T. Habruseva, S.P. Hegarty, G. Huyet, B. Kelleher, Coherence and incoherence in an optical comb, Phys. Rev. Lett. 112 (2014) 224101.
[132] D. Dudkowski, Y. Maistrenko, T. Kapitaniak, Different types of chimera states: An interplay between spatial and dynamical chaos, Phys. Rev. E 90 (2014) 032920.

[133] I. Omelchenko, Y. Maistrenko, P. Hövel, E. Schöll, Loss of coherence in dynamical networks: spatial chaos and chimera states, Phys. Rev. Lett. 106 (2011) 234102.
[134] I. Omelchenko, B. Riemenschneider, P. Hövel, Y. Maistrenko, E. Schöll, Transition from spatial coherence to incoherence in coupled chaotic systems, Phys. Rev. E 85 (2012) 026212.
[135] S.A. Bogomolov, A.V. Slepnev, G.I. Strelkova, E. Schöll, V.S. Anishchenko, Mechanisms of appearance of amplitude and phase chimera states in ensembles of nonlocally coupled chaotic systems, Commun. Nonlinear Sci. Numer. Simul. 43 (2017) 25–36.
[136] A.-K. Malchow, I. Omelchenko, E. Schöll, P. Hövel, Robustness of chimera states in nonlocally coupled networks of nonidentical logistic maps, Phys. Rev. E 98 (2018) 012217.
[137] P. Chandran, R. Gopal, V. Chandrasekar, N. Athavan, Chimera states in coupled logistic maps with additional weak nonlocal topology, Chaos 29 (2019) 053125.
[138] S. Bogomolov, G. Strelkova, E. Schöll, V. Anishchenko, Amplitude and phase chimeras in an ensemble of chaotic oscillators, Tech. Phys. Lett. 42 (2016) 765–768.
[139] E.V. Rybalova, D.Y. Klyushina, V.S. Anishchenko, G.I. Strelkova, Impact of noise on the amplitude chimera lifetime in an ensemble of nonlocally coupled chaotic maps, Regul. Chaotic Dyn. 24 (2019) 432–445.
[140] C.R. Nayak, N. Gupte, Chimera states in coupled sine-circle map lattices, in: AIP Conference Proceedings, Vol. 1339, American Institute of Physics, 2011, pp. 172–180.
[141] J. Singha, N. Gupte, Chimera states in globally coupled sine circle map lattices: Spatiotemporal intermittency and hyperchaos, Phys. Lett. A 384 (2020) 126225.
[142] N. Semenova, A. Zakharova, E. Schöll, V. Anishchenko, Does hyperbolicity impede emergence of chimera states in networks of nonlocally coupled chaotic oscillators? Europhys. Lett. 112 (2015) 40002.
[143] N.I. Semenova, E.V. Rybalova, G.I. Strelkova, V.S. Anishchenko, Coherence–incoherence transition in ensembles of nonlocally coupled chaotic oscillators with nonhyperbolic and hyperbolic attractors, Regul. Chaotic Dyn. 22 (2017) 148–162.
[144] E. Rybalova, N. Semenova, G. Strelkova, V. Anishchenko, Transition from complete synchronization to spatio-temporal chaos in coupled chaotic systems with nonhyperbolic and hyperbolic attractors, Eur. Phys. J. Spec. Top. 226 (2017) 1857–1866.
[145] W. Evans, Cell communication across gap junctions: a historical perspective and current developments, Biochem. Soc. Trans. 43 (2015) 450.
[146] A. Andreev, N. Frolov, A. Pisarchik, A. Hramov, Chimera state in complex networks of bistable Hodgkin-Huxley neurons, Phys. Rev. E 100 (2019) 022224.
[147] D. Mears, H.B. Pollard, Network science and the human brain: using graph theory to understand the brain and one of its hubs, the amygdala, in health and disease, J. Neurosci. Res. 94 (2016) 590–605.
[148] S.F. Muldoon, D.S. Bassett, Network and multilayer network approaches to understanding human brain dynamics, Philos. Sci. 83 (2016) 710–720.
[149] D. Poli, V.P. Pastore, P. Massobrio, Functional connectivity in vitro neuronal assemblies, Front. Neural Circuits 9 (2015) 57.
[150] M.N. Moussa, C.D. Vechlekar, J.H. Burdette, M.R. Steen, C.E. Hugenschmidt, P.J. Laurienti, Changes in cognitive state alter human functional brain networks, Front. Hum. Neurosci. 5 (2011) 83.
[151] T. Arodz, D. Bonchev, Identifying influential nodes in a wound healing-related network of biological processes using mean first-passage time, New J. Phys. 17 (2015) 025002.
[152] O. Sporns, Structure and function of complex brain networks, Dialogues Clin. Neurosci. 15 (2013) 247.
[153] K.W. Thee, H. Nisar, C.S. Soh, Graph theoretical analysis of functional brain networks in healthy subjects: visual oddball paradigm, IEEE Access 6 (2018) 64708–64727.
[154] M.D. Humphries, K. Gurney, T.J. Prescott, The brainstem reticular formation is a small-world, not scale-free, network, Proc. R. Soc. B 273 (2006) 503–511.
[155] C.-C. Hilgetag, G.A. Burns, M.A. O'Neill, J.W. Scannell, M.P. Young, Anatomical connectivity defines the organization of clusters of cortical areas in the macaque and the cat, Philos. Trans. Royal Soc. Lond. B 355 (2000) 91–110.
[156] O. Sporns, G. Tononi, G.M. Edelman, Theoretical neuroanatomy: relating anatomical and functional connectivity in graphs and cortical connection matrices, Cereb. Cortex 10 (2000) 127–141.
[157] E. Bullmore, O. Sporns, Complex brain networks: graph theoretical analysis of structural and functional systems, Nat. Rev. Neurosci. 10 (2009) 186–198.
[158] A. Mheich, M. Hassan, O. Dufor, M. Khalil, C. Berrou, F. Wendling, Spatiotemporal analysis of brain functional connectivity, in: 6th European Conference of the International Federation for Medical and Biological Engineering, Springer, 2015, pp. 934–937.
[159] C.J. Stam, Modern network science of neurological disorders, Nat. Rev. Neurosci. 15 (2014) 683–695.
[160] B.W. Connors, M.A. Long, Electrical synapses in the mammalian brain, Annu. Rev. Neurosci. 27 (2004) 393–418.
[161] M.V. Bennett, Gap junctions as electrical synapses, J. Neurocytol. 26 (1997) 349–366.
[162] S.G. Hormuzdi, M.A. Filippov, G. Mitropoulou, H. Monyer, R. Bruzzone, Electrical synapses: a dynamic signaling system that shapes the activity of neuronal networks, Biochim. Biophys. Acta 1662 (2004) 113–137.
[163] A.E. Pereda, Electrical synapses and their functional interactions with chemical synapses, Nat. Rev. Neurosci. 15 (2014) 250–263.
[164] F. Schmitz, A. Königstorfer, T.C. Südhof, Ribeye, A component of synaptic ribbons: a protein's journey through evolution provides insight into synaptic ribbon function, Neuron 28 (2000) 857–872.
[165] M.E. Yamakou, P.G. Hjorth, E.A. Martens, Optimal self-induced stochastic resonance in multiplex neural networks: electrical versus chemical synapses, Front. Comput. Neurosci. 14 (2020) 2002.
[166] V. Coutinho, T. Knöpfel, Book review: metabotropic glutamate receptors: electrical and chemical signaling properties, Neuroscientist 8 (2002) 551–561.
[167] N. Zandi-Mehran, S. Jafari, S.M.R.H. Golpayegani, F. Nazarimehr, M. Perc, Different synaptic connections evoke different firing patterns in neurons subject to an electromagnetic field, Nonlinear Dynam. 100 (2020) 1809–1824.
[168] J.I. Nagy, A.E. Pereda, J.E. Rash, Electrical synapses in mammalian cns: past eras, present focus and future directions, Biochim. Biophys. Acta 1860 (2018) 102–123.
[169] A. Vüllings, J. Hizanidis, I. Omelchenko, P. Hövel, Clustered chimera states in systems of type-i excitability, New J. Phys. 16 (2014) 123039.
[170] A. Calim, P. Hövel, M. Ozer, M. Uzuntarla, Chimera states in networks of type-i Morris-Lecar neurons, Phys. Rev. E 98 (2018) 062217.
[171] S. Petkoski, V.K. Jirsa, Transmission time delays organize the brain network synchronization, Philos. Trans. Royal Soc. Lond. A 377 (2019) 20180132.
[172] C.-H. Tian, X.-Y. Zhang, Z.-H. Wang, Z.-H. Liu, Diversity of chimera-like patterns from a model of 2d arrays of neurons with nonlocal coupling, Front. Phys. 12 (2017) 128904.
[173] K. Usha, P. Subha, Star-coupled Hindmarsh–Rose neural network with chemical synapses, Internat. J. Modern Phys. C 29 (2018) 1850023.
[174] M.S. Santos, P.R. Protachevicz, K.C. Iarosz, I.L. Caldas, R.L. Viana, F.S. Borges, H.-P. Ren, J.D. Szezech Jr, A.M. Batista, C. Grebogi, Spike-burst chimera states in an adaptive exponential integrate-and-fire neuronal network, Chaos 29 (2019) 043106.

[175] T. Fang, J. Zhang, S. Huang, F. Xu, M. Wang, H. Yang, Synchronous behavior among different regions of the neural system induced by electromagnetic radiation, Nonlinear Dynam. 98 (2019) 1267–1274.
[176] H. Bao, Y. Zhang, W. Liu, B. Bao, Memristor synapse-coupled memristive neuron network: synchronization transition and occurrence of chimera, Nonlinear Dynam. 100 (2020) 937–950.
[177] C. Tian, L. Cao, H. Bi, K. Xu, Z. Liu, Chimera states in neuronal networks with time delay and electromagnetic induction, Nonlinear Dynam. 93 (2018) 1695–1704.
[178] S. Wang, S. He, K. Rajagopal, A. Karthikeyan, K. Sun, Route to hyperchaos and chimera states in a network of modified Hindmarsh-Rose neuron model with electromagnetic flux and external excitation, Eur. Phys. J. Spec. Top. 229 (2020) 929–942.
[179] O. Sporns, G. Tononi, G.M. Edelman, Connectivity and complexity: the relationship between neuroanatomy and brain dynamics, Neural netw. 13 (2000) 909–922.
[180] A. Calim, J.J. Torres, M. Ozer, M. Uzuntarla, Chimera states in hybrid coupled neuron populations, Neural Netw. 126 (2020) 108–117.
[181] M. Bolotov, G. Osipov, A. Pikovsky, Marginal chimera state at cross-frequency locking of pulse-coupled neural networks, Phys. Rev. E 93 (2016) 032202.
[182] V. Kaminker, R. Wackerbauer, Alternating activity patterns and a chimeralike state in a network of globally coupled excitable Morris-Lecar neurons, Chaos 29 (2019) 053121.
[183] Z. Wang, Z. Liu, A brief review of chimera state in empirical brain networks, Front. Physiol. 11 (2020) 724.
[184] P. Hövel, A. Vüllings, I. Omelchenko, J. Hizanidis, Chimera states in neuronal systems of excitability type-i, in: Proceedings of ECCS 2014, Springer, 2016, pp. 247–258.
[185] N.C. Rattenborg, Do birds sleep in flight? Sci. Nat. 93 (2006) 413–425.
[186] N.C. Rattenborg, S.L. Lima, C.J. Amlaner, Half-awake to the risk of predation, Nature 397 (1999) 397–398.
[187] C.G. Mathews, J.A. Lesku, S.L. Lima, C.J. Amlaner, Asynchronous eye closure as an anti-predator behavior in the western fence lizard (sceloporus occidentalis), Ethology 112 (2006) 286–292.
[188] N.C. Rattenborg, C. Amlaner, S. Lima, Behavioral, neurophysiological and evolutionary perspectives on unihemispheric sleep, Neurosci. Biobehav. Rev. 24 (2000) 817–842.
[189] T.A. Glaze, S. Lewis, S. Bahar, Chimera states in a Hodgkin-Huxley model of thermally sensitive neurons, Chaos 26 (2016) 083119.
[190] P.J. Uhlhaas, W. Singer, Neural synchrony in brain disorders: relevance for cognitive dysfunctions and pathophysiology, Neuron 52 (2006) 155–168.
[191] C.A. Frantzidis, A.-K.I. Ladas, A.B. Vivas, M. Tsolaki, P.D. Bamidis, Cognitive and physical training for the elderly: evaluating outcome efficacy by means of neurophysiological synchronization, Int. J. Psychophysiol. 93 (2014) 1–11.
[192] A. Schnitzler, C. Münks, M. Butz, L. Timmermann, J. Gross, Synchronized brain network associated with essential tremor as revealed by magnetoencephalography, Mov. Disord. 24 (2009) 1629–1635.
[193] P. Khanna, J.M. Carmena, Beta band oscillations in motor cortex reflect neural population signals that delay movement onset, Elife 6 (2017) e24573.
[194] R.G. Andrzejak, C. Rummel, F. Mormann, K. Schindler, All together now: Analogies between chimera state collapses and epileptic seizures, Sci. Rep. 6 (2016) 23000.
[195] C. Lainscsek, N. Rungratsameetaweemana, S.S. Cash, T.J. Sejnowski, Cortical chimera states predict epileptic seizures, Chaos 29 (2019) 121106.
[196] S. Huo, C. Tian, M. Zheng, S. Guan, C.S. Zhou, Z. Liu, Spatial multi-scaled chimera states of cerebral cortex network and its inherent structure-dynamics relationship in human brain, Natl. Sci. Rev.
[197] J. Hizanidis, V.G. Kanas, A. Bezerianos, T. Bountis, Existence and control of chimera states in networks of nonlocally coupled models of neuron oscillators, in: 2014 13th International Conference on Control Automation Robotics & Vision (ICARCV), IEEE, 2014, pp. 243–246.
[198] M. Santos, J. Szezech, F. Borges, K. Iarosz, I. Caldas, A. Batista, R. Viana, J. Kurths, Chimera-like states in a neuronal network model of the cat brain, Chaos Solitons Fractals 101 (2017) 86–91.
[199] N. Semenova, Chimera states in ensembles of excitable Fitzhugh-Nagumo systems, 2019, arXiv:1911.01862.
[200] A. Zakharova, N. Semenova, V. Anishchenko, E. Schöll, Noise-induced chimera states in a neural network, in: International Conference on Patterns of Dynamics, Springer, 2016, pp. 44–63.
[201] K. Bansal, J.O. Garcia, S.H. Tompson, T. Verstynen, J.M. Vettel, S.F. Muldoon, Cognitive chimera states in human brain networks, Sci. Adv. 5 (2019) eaau8535.
[202] O.E. Omel'chenko, The mathematics behind chimera states, Nonlinearity 31 (2018) R121.
[203] E. Ott, T.M. Antonsen, Low dimensional behavior of large systems of globally coupled oscillators, Chaos 18 (2008) 037113.
[204] E. Ott, T.M. Antonsen, Long time evolution of phase oscillator systems, Chaos 19 (2009) 023117.
[205] O.E. Omel'chenko, Coherence–incoherence patterns in a ring of non-locally coupled phase oscillators, Nonlinearity 26 (2013) 2469.
[206] T. Kotwal, X. Jiang, D.M. Abrams, Connecting the Kuramoto model and the chimera state, Phys. Rev. Lett. 119 (2017) 264101.
[207] C.R. Laing, Dynamics and stability of chimera states in two coupled populations of oscillators, Phys. Rev. E 100 (2019) 042211.
[208] P. Clusella, A. Politi, Between phase and amplitude oscillators, Phys. Rev. E 99 (2019) 062201.
[209] M.J. Panaggio, D.M. Abrams, P. Ashwin, C.R. Laing, Chimera states in networks of phase oscillators: the case of two small populations, Phys. Rev. E 93 (2016) 012218.
[210] G. Bordyugov, A. Pikovsky, M. Rosenblum, Self-emerging and turbulent chimeras in oscillator chains, Phys. Rev. E 82 (2010) 035205.
[211] J. Sieber, E. Omel'chenko, M. Wolfrum, Controlling unstable chaos: stabilizing chimera states by feedback, Phys. Rev. Lett. 112 (2014) 054102.
[212] A. Buscarino, M. Frasca, L.V. Gambuzza, P. Hövel, Chimera states in time-varying complex networks, Phys. Rev. E 91 (2015) 022817.
[213] B.K. Bera, D. Ghosh, T. Banerjee, Imperfect traveling chimera states induced by local synaptic gradient coupling, Phys. Rev. E 94 (2016) 012215.
[214] J. Hizanidis, E. Panagakou, I. Omelchenko, E. Schöll, P. Hövel, A. Provata, Chimera states in population dynamics: networks with fragmented and hierarchical connectivities, Phys. Rev. E 92 (2015) 012915.
[215] T. Girnyk, M. Hasler, Y. Maistrenko, Multistability of twisted states in non-locally coupled Kuramoto-type models, Chaos 22 (2012) 013114.
[216] R. Gopal, V. Chandrasekar, A. Venkatesan, M. Lakshmanan, Observation and characterization of chimera states in coupled dynamical systems with nonlocal coupling, Phys. Rev. E 89 (2014) 052914.
[217] I. Omelchenko, E. Omel'chenko, P. Hövel, E. Schöll, When nonlocal coupling between oscillators becomes stronger: patched synchrony or multichimera states, Phys. Rev. Lett. 110 (2013) 224101.
[218] I. Omelchenko, A. Provata, J. Hizanidis, E. Schöll, P. Hövel, Robustness of chimera states for coupled Fitzhugh-Nagumo oscillators, Phys. Rev. E 91 (2015) 022917.
[219] I.A. Shepelev, A. Zakharova, T.E. Vadivasova, Chimera regimes in a ring of oscillators with local nonlinear interaction, Commun. Nonlinear Sci. Numer. Simul. 44 (2017) 277–283.
[220] I. Shepelev, T. Vadivasova, Inducing and destruction of chimeras and chimera-like states by an external harmonic force, Phys. Lett. A 382 (2018) 690–696.
[221] T. Vadivasova, G. Strelkova, S. Bogomolov, V. Anishchenko, Correlation characteristics of phase and amplitude chimeras in an ensemble of nonlocally coupled maps, Tech. Phys. Lett. 43 (2017) 118–121.

[222] A.E. Botha, Characteristic distribution of finite-time lyapunov exponents for chimera states, Sci. Rep. 6 (2016) 29213.
[223] F.P. Kemeth, S.W. Haugland, L. Schmidt, I.G. Kevrekidis, K. Krischer, A classification scheme for chimera states, Chaos 26 (2016) 094815.
[224] D.M. Abrams, R. Mirollo, S.H. Strogatz, D.A. Wiley, Solvable model for chimera states of coupled oscillators, Phys. Rev. Lett. 101 (2008) 084103.
[225] M.I. Bolotov, L.A. Smirnov, G.V. Osipov, A.S. Pikovsky, Breathing chimera in a system of phase oscillators, JETP Lett. 106 (2017) 393–399.
[226] I. Omelchenko, A. Zakharova, P. Hövel, J. Siebert, E. Schöll, Nonlinearity of local dynamics promotes multi-chimeras, Chaos 25 (2015) 083104.
[227] P. Jaros, L. Borkowski, B. Witkowski, K. Czolczynski, T. Kapitaniak, Multi-headed chimera states in coupled pendula, Eur. Phys. J. Spec. Top. 224 (2015) 1605–1617.
[228] N. Tsigkri-DeSmedt, J. Hizanidis, P. Hövel, A. Provata, Multi-chimera states in the leaky integrate-and-fire model, Procedia Comput. Sci. 66 (2015) 13–22.
[229] R. Ma, J. Wang, Z. Liu, Robust features of chimera states and the implementation of alternating chimera states, Europhys. Lett. 91 (2010) 40006.
[230] S. Majhi, D. Ghosh, Alternating chimeras in networks of ephaptically coupled bursting neurons, Chaos 28 (2018) 083113.
[231] S.W. Haugland, L. Schmidt, K. Krischer, Self-organized alternating chimera states in oscillatory media, Sci. Rep. 5 (2015) 1–5.
[232] J. Xie, E. Knobloch, H.-C. Kao, Multicluster and traveling chimera states in nonlocal phase-coupled oscillators, Phys. Rev. E 90 (2014) 022919.
[233] A. Mishra, S. Saha, D. Ghosh, G.V. Osipov, S.K. Dana, Traveling chimera pattern in a neuronal network under local gap junctional and nonlocal chemical synaptic interactions, Opera Med. Physiol. 3 (2017) 14–18.
[234] G.C. Sethia, A. Sen, G.L. Johnston, Amplitude-mediated chimera states, Phys. Rev. E 88 (2013) 042917.
[235] R. Mukherjee, A. Sen, Amplitude mediated chimera states with active and inactive oscillators, Chaos 28 (2018) 053109.
[236] A. Zakharova, M. Kapeller, E. Schöll, Chimera death: Symmetry breaking in dynamical networks, Phys. Rev. Lett. 112 (2014) 154101.
[237] A. Zakharova, M. Kapeller, E. Schöll, Amplitude chimeras and chimera death in dynamical networks, J. Phys. Conf. Ser. 727 (2016) 010218.
[238] L. Tumash, A. Zakharova, J. Lehnert, W. Just, E. Schöll, Stability of amplitude chimeras in oscillator networks, Europhys. Lett. 117 (2017) 20001.
[239] T. Banerjee, D. Biswas, D. Ghosh, E. Schöll, A. Zakharova, Networks of coupled oscillators: From phase to amplitude chimeras, Chaos 28 (2018) 113124.
[240] T. Banerjee, B. Bandyopadhyay, A. Zakharova, E. Schöll, Filtering suppresses amplitude chimeras, Front. Appl. Math. Stat. 5 (2019) 8.
[241] G. Xiao, W. Liu, Y. Lan, J. Xiao, Stable amplitude chimera states and chimera death in repulsively coupled chaotic oscillators, Nonlinear Dynam. 93 (2018) 1047–1057.
[242] P. Jaros, Y. Maistrenko, T. Kapitaniak, Chimera states on the route from coherence to rotating waves, Phys. Rev. E 91 (2015) 022907.
[243] Y. Kuramoto, S. i. Shima, Rotating spirals without phase singularity in reaction–diffusion systems, Prog. Theor. Exp. Phys. 150 (2003) 115–125.
[244] S. i. Shima, Y. Kuramoto, Rotating spiral waves with phase-randomized core in nonlocally coupled oscillators, Phys. Rev. E 69 (2004) 036213.
[245] P.-J. Kim, T.-W. Ko, H. Jeong, H.-T. Moon, Pattern formation in a two-dimensional array of oscillators with phase-shifted coupling, Phys. Rev. E 70 (2004) 065201.
[246] E.A. Martens, C.R. Laing, S.H. Strogatz, Solvable model of spiral wave chimeras, Phys. Rev. Lett. 104 (2010) 044101.
[247] C. Gu, G. St-Yves, J. Davidsen, Spiral wave chimeras in complex oscillatory and chaotic systems, Phys. Rev. Lett. 111 (2013) 134101.
[248] J. Xie, E. Knobloch, H.-C. Kao, Twisted chimera states and multicore spiral chimera states on a two-dimensional torus, Phys. Rev. E 92 (2015) 042921.
[249] S. Guo, Q. Dai, H. Cheng, H. Li, F. Xie, J. Yang, Spiral wave chimera in two-dimensional nonlocally coupled Fitzhugh–Nagumo systems, Chaos Solitons Fractals 114 (2018) 394–399.
[250] A. Schmidt, T. Kasimatis, J. Hizanidis, A. Provata, P. Hövel, Chimera patterns in two-dimensional networks of coupled neurons, Phys. Rev. E 95 (2017) 032224.
[251] S. Kundu, S. Majhi, B.K. Bera, D. Ghosh, M. Lakshmanan, Chimera states in two-dimensional networks of locally coupled oscillators, Phys. Rev. E 97 (2018) 022201.
[252] H.W. Lau, J. Davidsen, Linked and knotted chimera filaments in oscillatory systems, Phys. Rev. E 94 (2016) 010204.
[253] Y. Maistrenko, O. Sudakov, O. Osiv, V. Maistrenko, Chimera states in three dimensions, New J. Phys. 17 (2015) 073037.
[254] V. Maistrenko, O. Sudakov, O. Osiv, Y. Maistrenko, Multiple scroll wave chimera states, Eur. Phys. J. Spec. Top. 226 (2017) 1867–1881.
[255] T. Kasimatis, J. Hizanidis, A. Provata, Three-dimensional chimera patterns in networks of spiking neuron oscillators, Phys. Rev. E 97 (2018) 052213.
[256] G.M. Shepherd, The Synaptic Organization of the Brain, Oxford University Press, Oxford, U.K., 2004.
[257] V.A. Maksimenko, V.V. Makarov, B.K. Bera, D. Ghosh, S.K. Dana, M.V. Goremyko, N.S. Frolov, A.A. Koronovskii, A.E. Hramov, Excitation and suppression of chimera states by multiplexing, Phys. Rev. E 94 (2016) 052205.
[258] A. Dmitrichev, D. Shchapin, V.I. Nekorkin, Cloning of chimera states in a multiplex network of two-frequency oscillators with linear local couplings, JETP Lett. 108 (2018) 543–547.
[259] N.S. Frolov, V.A. Maksimenko, V.V. Makarov, D.V. Kirsanov, A.E. Hramov, J. Kurths, Macroscopic chimeralike behavior in a multiplex network, Phys. Rev. E 98 (2018) 022320.
[260] J. Sawicki, I. Omelchenko, A. Zakharova, E. Schöll, Synchronization scenarios of chimeras in multiplex networks, Eur. Phys. J. Spec. Top. 227 (2018) 1161–1171.
[261] G.I. Strelkova, T.E. Vadivasova, V.S. Anishchenko, Synchronization of chimera states in a network of many unidirectionally coupled layers of discrete maps, Regul. Chaotic Dyn. 23 (2018) 948–960.
[262] R.G. Andrzejak, G. Ruzzene, I. Malvestio, Generalized synchronization between chimera states, Chaos 27 (2017) 053114.
[263] A. Bukh, E. Rybalova, N. Semenova, G. Strelkova, V. Anishchenko, New type of chimera and mutual synchronization of spatiotemporal structures in two coupled ensembles of nonlocally interacting chaotic maps, Chaos 27 (2017) 111102.
[264] R.G. Andrzejak, G. Ruzzene, I. Malvestio, K. Schindler, E. Schöll, A. Zakharova, Mean field phase synchronization between chimera states, Chaos 28 (2018) 091101.
[265] M. Shafiei, F. Parastesh, M. Jalili, S. Jafari, M. Perc, M. Slavinec, Effects of partial time delays on synchronization patterns in izhikevich neuronal networks, Eur. Phys. J. B 92 (2019) 36.
[266] S. Ghosh, A. Kumar, A. Zakharova, S. Jalan, Birth and death of chimera: Interplay of delay and multiplexing, Europhys. Lett. 115 (2016) 60005.
[267] J. Sawicki, I. Omelchenko, A. Zakharova, E. Schöll, Delay controls chimera relay synchronization in multiplex networks, Phys. Rev. E 98 (2018) 062224.
[268] S. Ghosh, A. Zakharova, S. Jalan, Non-identical multiplexing promotes chimera states, Chaos Solitons Fractals 106 (2018) 56–60.
[269] S. Majhi, M. Perc, D. Ghosh, Chimera states in a multilayer network of coupled and uncoupled neurons, Chaos 27 (2017) 073109.
[270] S. Kundu, S. Majhi, D. Ghosh, From asynchronous to synchronous chimeras in ecological multiplex network, Eur. Phys. J. Spec. Top. 228 (2019) 2429–2439.
[271] Z.-M. Wu, H.-Y. Cheng, Y. Feng, H.-H. Li, Q.-L. Dai, J.-Z. Yang, Chimera states in bipartite networks of Fitzhugh–Nagumo oscillators, Front. Phys. 13 (2018) 130503.
[272] F. Xu, J. Zhang, M. Jin, S. Huang, T. Fang, Chimera states and synchronization behavior in multilayer memristive neural networks, Nonlinear Dynam. 94 (2018) 775–783.

[273] P. Jaros, S. Brezetsky, R. Levchenko, D. Dudkowski, T. Kapitaniak, Y. Maistrenko, Solitary states for coupled oscillators with inertia, Chaos 28 (2018) 011103.
[274] M. Mikhaylenko, L. Ramlow, S. Jalan, A. Zakharova, Weak multiplexing in neural networks: Switching between chimera and solitary states, Chaos 29 (2019) 023122.
[275] B.K. Bera, S. Rakshit, D. Ghosh, J. Kurths, Spike chimera states and firing regularities in neuronal hypernetworks, Chaos 29 (2019) 053115.
[276] A. Rothkegel, K. Lehnertz, Irregular macroscopic dynamics due to chimera states in small-world networks of pulse-coupled oscillators, New J. Phys. 16 (2014) 055006.
[277] E. Schöll, Synchronization patterns and chimera states in complex networks: Interplay of topology and dynamics, Eur. Phys. J. Spec. Top. 225 (2016) 891–919.
[278] J. Tang, J. Zhang, J. Ma, J. Luo, Noise and delay sustained chimera state in small world neuronal network, Sci. China Technol. Sci. 62 (2019) 1134–1140.
[279] Y. Zhu, Z. Zheng, J. Yang, Chimera states on complex networks, Phys. Rev. E 89 (2014) 022914.
[280] A. Bandyopadhyay, S. Kar, Impact of network structure on synchronization of Hindmarsh–Rose neurons coupled in structured network, Appl. Math. Comput. 333 (2018) 194–212.
[281] C. Meena, K. Murali, S. Sinha, Chimera states in star networks, Int. J. Bifurcation Chaos 26 (2016) 1630023.
[282] C.A. Moreira, M.A. de Aguiar, Modular structure in c. elegans neural network and its response to external localized stimuli, Physica A 533 (2019) 122051.
[283] J. Hizanidis, N.E. Kouvaris, G. Zamora-López, A. Díaz-Guilera, C.G. Antonopoulos, Chimera-like states in modular neural networks, Sci. Rep. 6 (2016) 19845.
[284] V.V. Makarov, S. Kundu, D.V. Kirsanov, N.S. Frolov, V.A. Maksimenko, D. Ghosh, S.K. Dana, A.E. Hramov, Multiscale interaction promotes chimera states in complex networks, Commun. Nonlinear Sci. Numer. Simul. 71 (2019) 118–129.
[285] B.K. Bera, S. Majhi, D. Ghosh, M. Perc, Chimera states: Effects of different coupling topologies, Europhys. Lett. 118 (2017) 10001.
[286] G.C. Sethia, A. Sen, Chimera states: the existence criteria revisited, Phys. Rev. Lett. 112 (2014) 144101.
[287] A. Yeldesbay, A. Pikovsky, M. Rosenblum, Chimeralike states in an ensemble of globally coupled oscillators, Phys. Rev. Lett. 112 (2014) 144103.
[288] J.D. Hart, K. Bansal, T.E. Murphy, R. Roy, Experimental observation of chimera and cluster states in a minimal globally coupled network, Chaos 26 (2016) 094801.
[289] V. Chandrasekar, R. Gopal, A. Venkatesan, M. Lakshmanan, Mechanism for intensity-induced chimera states in globally coupled oscillators, Phys. Rev. E 90 (2014) 062913.
[290] L. Schmidt, K. Krischer, Clustering as a prerequisite for chimera states in globally coupled systems, Phys. Rev. Lett. 114 (2015) 034101.
[291] L. Schmidt, K. Krischer, Two-cluster solutions in an ensemble of generic limit-cycle oscillators with periodic self-forcing via the mean-field, Phys. Rev. E 90 (2014) 042911.
[292] L. Schmidt, K. Schönleber, K. Krischer, V. García-Morales, Coexistence of synchrony and incoherence in oscillatory media under nonlinear global coupling, Chaos 24 (2014) 013102.
[293] A. Mishra, C. Hens, M. Bose, P.K. Roy, S.K. Dana, Chimeralike states in a network of oscillators under attractive and repulsive global coupling, Phys. Rev. E 92 (2015) 062920.
[294] C. Hens, A. Mishra, P. Roy, A. Sen, S. Dana, Chimera states in a population of identical oscillators under planar cross-coupling, Pramana 84 (2015) 229–235.
[295] C.R. Laing, Chimeras in networks with purely local coupling, Phys. Rev. E 92 (2015) 050904.
[296] M. Clerc, S. Coulibaly, M. Ferré, M. García-Ñustes, R. Rojas, Chimera-type states induced by local coupling, Phys. Rev. E 93 (2016) 052204.
[297] L. Larger, B. Penkovsky, Y. Maistrenko, Virtual chimera states for delayed-feedback systems, Phys. Rev. Lett. 111 (2013) 054103.
[298] L. Larger, B. Penkovsky, Y. Maistrenko, Laser chimeras as a paradigm for multistable patterns in complex systems, Nature Commun. 6 (2015) 1–7.
[299] H. Wang, X. Li, Synchronization and chimera states of frequency-weighted Kuramoto-oscillator networks, Phys. Rev. E 83 (2011) 066214.
[300] V. Chandrasekar, J.H. Sheeba, B. Subash, M. Lakshmanan, J. Kurths, Adaptive coupling induced multi-stable states in complex networks, Physica D 267 (2014) 36–48.
[301] D. Kasatkin, S. Yanchuk, E. Schöll, V. Nekorkin, Self-organized emergence of multilayer structure and chimera states in dynamical networks with adaptive couplings, Phys. Rev. E 96 (2017) 062211.
[302] D. Kasatkin, V. Nekorkin, Synchronization of chimera states in a multiplex system of phase oscillators with adaptive couplings, Chaos 28 (2018) 093115.
[303] S. Huo, C. Tian, L. Kang, Z. Liu, Chimera states of neuron networks with adaptive coupling, Nonlinear Dynam. 96 (2019) 75–86.
[304] Z. Wang, S. Baruni, F. Parastesh, S. Jafari, D. Ghosh, M. Perc, I. Hussain, Chimeras in an adaptive neuronal network with burst-timing-dependent plasticity, Neurocomputing 406 (2020) 117–126.
[305] V. Vuksanović, P. Hövel, Functional connectivity of distant cortical regions: role of remote synchronization and symmetry in interactions, NeuroImage 97 (2014) 1–8.
[306] P. Katsaloulis, J. Hizanidis, D. Verganelakis, A. Provata, Complexity measures and noise effects on diffusion magnetic resonance imaging of the neuron axons network in the human brain, Fluct. Noise Lett. 11 (2012) 1250032.
[307] D.J. Watts, S.H. Strogatz, Collective dynamics of 'small-world' networks, Nature 393 (1998) 440–442.
[308] S. Ulonska, I. Omelchenko, A. Zakharova, E. Schöll, Chimera states in networks of van der pol oscillators with hierarchical connectivities, Chaos 26 (2016) 094825.
[309] A. zur Bonsen, I. Omelchenko, A. Zakharova, E. Schöll, Chimera states in networks of logistic maps with hierarchical connectivities, Eur. Phys. J. B 91 (2018) 65.
[310] J. Sawicki, I. Omelchenko, A. Zakharova, E. Schöll, Chimera states in complex networks: interplay of fractal topology and delay, Eur. Phys. J. Spec. Top. 226 (2017) 1883–1892.
[311] T. Chouzouris, I. Omelchenko, A. Zakharova, J. Hlinka, P. Jiruska, E. Schöll, Chimera states in brain networks: Empirical neural vs. modular fractal connectivity, Chaos 28 (2018) 045112.
[312] N. Tsigkri-DeSmedt, J. Hizanidis, P. Hövel, A. Provata, Multi-chimera states and transitions in the leaky integrate-and-fire model with nonlocal and hierarchical connectivity, Eur. Phys. J. Spec. Top. 225 (2016) 1149–1164.
[313] C. Bick, E.A. Martens, Controlling chimeras, New J. Phys. 17 (2015) 033030.
[314] T. Isele, J. Hizanidis, A. Provata, P. Hövel, Controlling chimera states: The influence of excitable units, Phys. Rev. E 93 (2016) 022217.
[315] L.V. Gambuzza, M. Frasca, Pinning control of chimera states, Phys. Rev. E 94 (2016) 022306.
[316] I. Omelchenko, E. Omel'chenko, A. Zakharova, M. Wolfrum, E. Schöll, Tweezers for chimeras in small networks, Phys. Rev. Lett. 116 (2016) 114101.
[317] I. Shepelev, T. Vadivasova, External localized harmonic influence on an incoherence cluster of chimera states, Chaos Solitons Fractals 133 (2020) 109642.
[318] A. Gjurchinovski, E. Schöll, A. Zakharova, Control of amplitude chimeras by time delay in oscillator networks, Phys. Rev. E 95 (2017) 042218.

[319] G. Ruzzene, I. Omelchenko, E. Schöll, A. Zakharova, R.G. Andrzejak, Controlling chimera states via minimal coupling modification, Chaos 29 (2019) 051103.
[320] I. Omelchenko, E. Omel'chenko, A. Zakharova, E. Schöll, Optimal design of tweezer control for chimera states, Phys. Rev. E 97 (2018) 012216.
[321] I. Omelchenko, T. Hülser, A. Zakharova, E. Schöll, Control of chimera states in multilayer networks, Front. Appl. Math. Stat. 4 (2019) 67.
[322] A. Zakharova, S.A. Loos, J. Siebert, A. Gjurchinovski, J.C. Claussen, E. Schöll, Controlling chimera patterns in networks: interplay of structure, noise, and delay, in: Control of Self-Organizing Nonlinear Systems, Springer, 2016, pp. 3–23.
[323] A. Zakharova, N. Semenova, V. Anishchenko, E. Schöll, Time-delayed feedback control of coherence resonance chimeras, Chaos 27 (2017) 114320.
[324] V. Semenov, A. Zakharova, Y. Maistrenko, E. Schöll, Deterministic and stochastic control of chimera states in delayed feedback oscillator, AIP Conf. Proc. 1738 (2016) 210013.